



University of Kentucky
UKnowledge

Theses and Dissertations--Mechanical
Engineering

Mechanical Engineering

2012

AERODYNAMICS AND CONTROL OF A DEPLOYABLE WING UAV FOR AUTONOMOUS FLIGHT

Michael Thamann

University of Kentucky, matham2@uky.edu

[Right click to open a feedback form in a new tab to let us know how this document benefits you.](#)

Recommended Citation

Thamann, Michael, "AERODYNAMICS AND CONTROL OF A DEPLOYABLE WING UAV FOR AUTONOMOUS FLIGHT" (2012). *Theses and Dissertations--Mechanical Engineering*. 18.
https://uknowledge.uky.edu/me_etds/18

This Master's Thesis is brought to you for free and open access by the Mechanical Engineering at UKnowledge. It has been accepted for inclusion in Theses and Dissertations--Mechanical Engineering by an authorized administrator of UKnowledge. For more information, please contact UKnowledge@lsv.uky.edu.

STUDENT AGREEMENT:

I represent that my thesis or dissertation and abstract are my original work. Proper attribution has been given to all outside sources. I understand that I am solely responsible for obtaining any needed copyright permissions. I have obtained and attached hereto needed written permission statements(s) from the owner(s) of each third-party copyrighted matter to be included in my work, allowing electronic distribution (if such use is not permitted by the fair use doctrine).

I hereby grant to The University of Kentucky and its agents the non-exclusive license to archive and make accessible my work in whole or in part in all forms of media, now or hereafter known. I agree that the document mentioned above may be made available immediately for worldwide access unless a preapproved embargo applies.

I retain all other ownership rights to the copyright of my work. I also retain the right to use in future works (such as articles or books) all or part of my work. I understand that I am free to register the copyright to my work.

REVIEW, APPROVAL AND ACCEPTANCE

The document mentioned above has been reviewed and accepted by the student's advisor, on behalf of the advisory committee, and by the Director of Graduate Studies (DGS), on behalf of the program; we verify that this is the final, approved version of the student's dissertation including all changes required by the advisory committee. The undersigned agree to abide by the statements above.

Michael Thamann, Student

Dr. Suzanne Weaver Smith, Major Professor

Dr. James McDonough, Director of Graduate Studies

AERODYNAMICS AND CONTROL OF A DEPLOYABLE
WING UAV FOR AUTONOMOUS FLIGHT

THESIS

A thesis submitted in partial fulfillment of the requirements
for the degree of Master of Science in Mechanical Engineering
the College of Engineering at the University of Kentucky

By

Michael Andrew Thamann

Lexington, Kentucky

Co-Director: Dr. Suzanne Weaver Smith, Donald and Gertrude Lester
Professor of Mechanical Engineering
and Dr. Sean Bailey, Professor of Mechanical Engineering

Lexington, Kentucky

2012

Copyright © Michael Andrew Thamann 2012

ABSTRACT OF THESIS

AERODYNAMICS AND CONTROL OF A DEPLOYABLE WING UAV FOR AUTONOMOUS FLIGHT

UAV development and usage has increased dramatically in the last 15 years. In this time frame the potential has been realized for deployable UAVs to the extent that a new class of UAV was defined for these systems. Inflatable wing UAVs provide a unique solution for deployable UAVs because they are highly packable (some collapsing to 5 – 10% of their deployed volume) and have the potential for the incorporation of wing shaping. In this thesis, aerodynamic coefficients and aileron effectiveness were derived from the equations of motion of aircraft as necessary parameters for autonomous flight. A wind tunnel experiment was performed to determine the aerodynamic performance of a bumpy inflatable wing airfoil for comparison with the baseline smooth airfoil from which it was derived. Results showed that the bumpy airfoil has improved aerodynamics over the smooth airfoil at low-Re. The results were also used to create aerodynamic performance curves to supplement results of aerodynamic modeling with a smooth airfoil. A modeling process was then developed to calculate the aileron effectiveness of a wing shaping demonstrator aircraft. Successful autonomous flight tests were then performed with the demonstrator aircraft including in-flight aileron doublets to validate the predicted aileron effectiveness, which matched within 8%.

KEYWORDS: Unmanned Aerial Vehicle, Inflatable Wing, Bumpy Airfoil, Wing Shaping, Autonomous Flight

Michael A. Thamann

November 29, 2012

AERODYNAMICS AND CONTROL OF A DEPLOYABLE
WING UAV FOR AUTONOMOUS FLIGHT

By

Michael Andrew Thamann

Dr. Suzanne Weaver Smith

Co-Director of Thesis

Dr. Sean Bailey

Co-Director of Thesis

Dr. James McDonough

Director of Graduate Studies

11/29/12

Acknowledgements

I would first like to extend my thanks to my parents for their continuous support and appreciation for my work. This is especially true for my mother who, although I have been designing and building aircraft for approximately 4 years, is continuously amazed at how aircraft can actually fly. I would also like to thank those people who have helped to fuel my interest in aircraft design, and helped me realize that someone without an aeronautical engineering degree can design aircraft. Dr. Raymond Lebeau was the first to help me realize this when I had the privilege of taking his aircraft design course as an undergraduate. This list would also include Dr. Jamey Jacob who has always been available to lend a helping hand and advice, or even help diagnose plane crashes from only a blurry video and story.

Special thanks also go to Dr. Suzanne Smith and Dr. Sean Bailey. Dr. Smith was the one who made this experience possible. When I graduated from my undergrad at UK in 2010 the economy had just gone south and she recognized my skill set and offered me the fellowship which has supported me during this work. Not only has she managed to provide monetary support for this work but she also provided me with many other great opportunities over these last few years like being able to say that I have sent something to space, or seeing the last shuttle launch. Dr. Bailey has always been available throughout this research effort to provide guidance with anything fluids, much needed sanity checks, the expert knuckle tap to make an electronic device work again, and even rapid turnaround on thesis edits only weeks after having a child.

I would also like to thank some friends that have helped me through the years. This would be the other members of the lab, first and foremost, for the camaraderie during our respective research. It was always comforting to have someone there to share the pain and our always enjoyable “lab outings”. This is especially true for my colleague Brady Doepke. After

working so closely for so long, it will be quite strange working on aircraft in the future without you. Don't worry though, I'll be sure to call you after not sleeping for two days and leave you a voicemail – since you never answer your phone – just like the old days. We've quite literally been back and forth across the country together through 15 of the lower 48 together (13 of those by car) which have led to some unforgettable moments. Wichita and Tucson, for example; it's still hard to tell those stories without falling over from laughter. Or when we had to teach those city kids from Rutgers how guys from Kentucky camp – all while becoming honorary members of their autonomous aircraft club. Then there was the rocket launch and even the shuttle launch... I feel like I could nearly write a thesis on the memories and experiences from the last few years. Even though there were several occasions where we wanted to kill each other (hey, there's a reason I chose my desk at the opposite end of the lab), I appreciate all those moments.

Very special thanks are extended to Brittany Adam (soon to be Dr. Adam) for feeding me so often, providing excuses for getting out of the lab, and our existential and philosophical conversations over piles of fluids textbooks. One of these days we will figure out what the Galerkin procedure is. I would also like to thank my ex-girlfriend. She once told me I should quit because I was so stressed out. Every time I was feeling overwhelmed I thought of that conversation and that kept me going because it reminded me I had to keep going, if for nothing else, on principal alone. I have stayed with it and have been able to accomplish and experience things that I have dreamt about since childhood – as cliché as that sounds.

The list could go on, but I will keep it brief by saying: to all my other friends, if they are reading this they know who they are, and if not probably still know who they are, that I could not have done this without having you around. You have stuck with me through my brushes

with insanity and being so exhausted I could barely stand up, yet you drug me out and forced back to the real world. Trust me; I appreciate that more than you will know.

It was nice finally being able to write something in the first person. I've missed it.

Table of Contents

Acknowledgements.....	v
Table of Contents.....	viii
List of Tables	x
List of Figures	xi
Nomenclature	xv
Chapter 1 Introduction	1
1.1 Motivation.....	1
1.2 Objectives	3
1.3 Overview of Thesis.....	4
Chapter 2 Literature Review	5
2.1 Deployable Wings	5
2.2 Wing Shaping	17
Chapter 3 Introduction to Parameters Flight	25
3.1 Piccolo II Autopilot Systems.....	29
Chapter 4 Determination of Aerodynamic Coefficients of Inflatable Airfoils	33
4.1 Experimental Methodology	34
4.2 Experimental Setup.....	36
4.2.1 Airfoil Models.....	37
4.2.2 Drag Rake	43
4.2.3 Pressure Measurement.....	47
4.3 Results.....	48
4.3.1 Smooth Airfoil Results.....	48
4.3.2 Bumpy Airfoil Results	53
4.3.3 Smooth to Bumpy Airfoil Correction.....	57
4.3.4 Lift Hysteresis.....	62
4.3.5 Laminar Separation Bubble.....	65
Chapter 5 Autopilot Programming for Wing Shaping.....	68
5.1 Modeling of Standard Wing.....	68
5.2 Modeling Wing Shaping	69
5.3 Performance of Model in Simulations	73
5.4 Flight Performance of Autonomous Wing Shaping	76
Chapter 6 Summary, Conclusions, and Future Work.....	82
6.1 Summary and Conclusions.....	82
6.2 Future Work.....	83
6.2.1 Wind Tunnel Testing	83
6.2.2 Wing Shaping & Autopilot Programming.....	84
Appendix A Smooth Airfoil Results.....	85
A.1 $Re = 25,000$	85

A.2	Re = 50,000	88
A.3	Re = 100,000	92
A.4	Re = 150,000	95
A.5	Re = 200,000	97
A.6	Re = 250,000	102
A.7	Re = 300,000	106
A.8	Re = 500,000	111
Appendix B	Bumpy Airfoil Results	116
B.1	Re = 25,000	116
B.2	Re = 50,000	119
B.3	Re = 100,000	122
B.4	Re = 150,000	126
B.5	Re = 200,000	129
B.6	Re = 250,000	134
B.7	Re = 300,000	138
B.8	Re = 500,000	143
Appendix C	MATLAB Code	148
C.1	Smooth Airfoil Integration Code Re < 500 <i>k</i>	148
C.2	Smooth Airfoil Integration Code Re = 500 <i>k</i>	153
C.3	Bumpy Airfoil Integration Code Re < 500 <i>k</i>	159
C.4	Bumpy Airfoil Integration Code Re = 500 <i>k</i>	164
References	169
Vita	173

List of Tables

Table 2.1	Approximate chordwise location of flow separation from simulations [22]	16
Table 3.1	Normalized forces, moments, and rates of flight	27
Table 4.1	Comparison of Eppler 398 airfoil to NACA 4318 airfoil (dimensions in percent chord)	33
Table 4.2	Test matrix	34
Table 4.3	Construction technique pros and cons	39
Table 4.4	Pressure tap specifications for the smooth and bumpy airfoils	41
Table 4.5	Pitot-tube locations from top of the test section	47
Table 4.6	Effects of the bumps on the lift curve at varying Re	60
Table 4.7	Effects of the bumps on the drag polar	61
Table 4.8	Summary of separation and reattachment angles of attack from lift hysteresis results	65
Table 5.1	a_{eff} calculation comparison	69
Table 5.2	Specifications of the twisting wing	70
Table 5.3	Summary of aileron effectiveness calculation for wing shaping	72
Table 5.4	Summary of aileron effectiveness from various wing configurations	73
Table 5.5	Summary of model performance during simulations	75
Table 5.6	Flight test process	77
Table 5.7	Summary of model performance during flight	80

List of Figures

Figure 1.1 UAV flight hours since 1996, adapted from Winnefeld and Kendall [5]	1
Figure 1.2 Examples of deployable UAV's <i>top left</i>) Raven [6], <i>top right</i>) Wasp [6], <i>bot left</i>) Dragon Eye [6], <i>bot right</i>) tube launched Coyote II [7]	2
Figure 1.3 Packability of inflatable wings demonstrated.....	3
Figure 2.1 NASA ARES Mar's glider <i>top left</i>) first stage of concept deployment, <i>top right</i>) second stage of concept deployment, <i>bot left</i>) concept in flight, and <i>right</i>) test flight photo after high altitude deployment (images courtesy of NASA)	5
Figure 2.2 Left) Goodyear Inflateoplane stowed, and <i>right</i>) deployed in flight	6
Figure 2.3 Inflatable wing UAVs developed by ILC dover: <i>Left</i>) Apterion, and <i>right</i>) backpackable demonstration UAV with coated nylon inflatable wings (images courtesy of ILC Dover [16]) ..	7
Figure 2.4 Deployment sequence of the NASA Dryden I2000 inflatable wing UAV, total elapsed time approximately 0.33 seconds (images courtesy of NASA)	7
Figure 2.5 I2000 wing structure [17].....	8
Figure 2.6 <i>Left</i>) BBI/BBII aircraft, <i>mid</i>) BBIII/BBIV aircraft, <i>right</i>) BBV aircraft [17].....	9
Figure 2.7 E398 airfoil used in the inflatable-rigidizable wings and the ideal smooth shape [27].	9
Figure 2.8 Smoke wire visualizations of <i>left</i>) smooth E398 and <i>right</i>) bumpy E398 at $Re = 50k$, $\alpha = 4^\circ$ [27]	10
Figure 2.9 Bumpy E398 experimental results compared to XFOIL [25, 26] smooth airfoil predictions at $Re = 156k$ (adapted from Usui [24]) <i>Left</i>) lift curve, <i>right</i>) drag polar.....	10
Figure 2.10 PIV streamline results and vorticity contours at $Re = 36k$ [27] for <i>top left</i>) smooth, $\alpha = 7^\circ$, <i>top right</i>) smooth, $\alpha = 10^\circ$, <i>bot left</i>) bumpy, $\alpha = 7^\circ$, <i>bot right</i>) bumpy, $\alpha = 10^\circ$...	11
Figure 2.11 Visualization of flow over a dragon fly wing showing recirculation regions between the bumps yielding a “smooth airfoil” profile around the wing [28]	11
Figure 2.12 E398 experimental [24] and CFD [29] results at $Re = 200k$ <i>left</i>) lift curve, <i>right</i>) drag polar (adapted from Usui [24] and Reasor [29])	12
Figure 2.13 Comparison of experimental [27] and CFD [29] streamlines for the E398 airfoil at $Re = 25k$. <i>Top left</i>) smooth $\alpha = 0^\circ$, <i>top right</i>) bumpy $\alpha = 0^\circ$, <i>mid left</i>) smooth, laminar model $\alpha = 7^\circ$, <i>mid right</i>) bumpy, laminar model $\alpha = 7^\circ$, <i>bot left</i>) bumpy, transitional model $\alpha = 7^\circ$, <i>bot right</i>) bumpy, turbulent model $\alpha = 7^\circ$	13
Figure 2.14 <i>Left, mid</i>) recirculation shown by PIV with vorticity contours at $Re = 36k$, $\alpha = 7^\circ$ [27], <i>right</i>) recirculation shown by CFD with u/U_∞ contours at $Re = 18k$, $\alpha = 7^\circ$ [30]	14
Figure 2.15 Velocity profiles of $u^* = u/U_\infty$ for the E398 bumpy and smooth airfoil at various chord locations, $Re = 18k$, $\alpha = 7^\circ$ [30].....	14
Figure 2.16 CFD Pressure distributions of smooth and bumpy E398 at $Re = 36k$, $\alpha = 7^\circ$ [30]..	15
Figure 2.17 CFD results of NACA 4-digit smooth and bumpy airfoil shapes at $Re = 300k$ (XXXXs denotes smooth, XXXXb denotes bumpy). <i>Left</i>) lift curve, and <i>right</i>) drag polar (adapted from Innes [34]).....	17
Figure 2.18 Morphing concepts from, <i>top right</i>) Nextgen Aeronautics [35], and <i>bot right</i>) Lockheed Martin [35]	18
Figure 2.19 Concept of Virginia Polytechnic Institute RC extendable wing UAV [38]	18

Figure 2.20 Festo Smartbird <i>top</i>) in flight <i>bot</i>) sequence of flaping motion [44]	19
Figure 2.21 Wing shaping techniques <i>left</i>) total camber change, <i>mid</i>) local camber change, and <i>right</i>) twist [45]	19
Figure 2.22 1903 Wright flyer showing wing twist for roll control	20
Figure 2.23 Top) wind tunnel models to measure the increase in circulation due to wing warping, <i>bot left</i>) circulation distribution from unwarped model, $Re = 100k$, $\alpha = 4^\circ$, <i>bot right</i>) circulation distribution of model warped 17° , $Re = 100k$, $\alpha = 4^\circ$ [23]	21
Figure 2.24 UAV outfitted with pulley mechanism for wing twist for roll control [17]	22
Figure 2.25 Local camber change used for RC wing shaping flight control [17]	22
Figure 2.26 Left) Virginia Polytechnic Institute's UAV with MFC actuators, <i>right</i>) deflection models of MFC actuated aircraft [55]	23
Figure 2.27 Recently developed wing shaping demonstrator used in this study	24
Figure 3.1 Left) Body frame Right) Aerodynamic frame	25
Figure 3.2 Forces and moments of flight <i>left</i>) the body frame <i>right</i>) the aerodynamic frame	26
Figure 3.3 Cloud Cap Technology Piccolo II autopilot [63]	29
Figure 3.4 Block diagram of autopilot bank angle control loops	30
Figure 4.1 Left) Eppler 398 airfoil smooth and bumpy shape, <i>right</i>) NACA 4318 airfoil smooth and bumpy shape	33
Figure 4.2 Typical pressure distribution over an airfoil	35
Figure 4.3 Typical velocity profile aft of an object	36
Figure 4.4 Block diagram of experimental set up	37
Figure 4.5 University of Kentucky low speed wind tunnel	37
Figure 4.6 Model dimensions and wind tunnel clearances	38
Figure 4.7 Airfoil wing section ProE models <i>left</i>) smooth profile with 25 taps, <i>right</i>) bumpy profile with 49 taps	40
Figure 4.8 Finished SLA wing sections with fully assembled model	40
Figure 4.9 Top <i>left</i>) side view of smooth airfoil, <i>bot left</i>) Side view of bumpy airfoil, <i>right</i>) pressure tap geometry (dimensions in inches)	41
Figure 4.10 Pressure rake geometry and orientation <i>top left</i>) smooth profile, <i>top right</i>) bumpy profile, <i>bot</i>) SLA test section with internal pressure lines	42
Figure 4.11 End plate geometry (dimensions in inches)	43
Figure 4.12 Wake measurement locations	44
Figure 4.13 Drag rake and Pitot tube configuration	45
Figure 4.14 Wind tunnel test section setup	45
Figure 4.15 Left) worst case data: $Re = 25k$, $\alpha = 3.2^\circ$, <i>right</i>) typical data: $Re = 250k$, $\alpha = 3.5^\circ$	49
Figure 4.16 Top Left) low α C_p distribution with interpolation, <i>top right</i>) high α C_p distribution with interpolation, <i>bot left</i>) lift curve without interpolation, and <i>bot right</i>) lift curve with interpolation.	50
Figure 4.17 Top) drag polars and <i>bot</i>) lift curves for the smooth NACA 4318 airfoil	51
Figure 4.18 Top <i>left</i>) drag polars from XFOIL, <i>top right</i>) drag polars from experiment, <i>bot left</i>) lift curves from XFOIL, and <i>bot right</i>) lift curves from experiment	53

Figure 4.19 <i>Left)</i> low α pressure distribution, <i>right)</i> high α pressure distribution $Re = 250k$...	54
Figure 4.20 <i>Top)</i> drag polars and <i>bot)</i> lift curves for the bumpy NACA 4318 airfoil	55
Figure 4.21 <i>Left)</i> smooth airfoil drag polars and lift curves, <i>right)</i> bumpy airfoil drag polars and lift curves	56
Figure 4.22 <i>Left)</i> smooth airfoil L/D vs α , <i>right)</i> bumpy airfoil L/D vs α	57
Figure 4.23 Lift curve comparison, $Re = 50k$	57
Figure 4.24 Drag polar comparison, $Re = 50k$	57
Figure 4.25 Lift curve comparison, $Re = 100k$	57
Figure 4.26 Drag polar comparison, $Re = 100k$	57
Figure 4.27 Lift curve comparison, $Re = 150k$	58
Figure 4.28 Drag polar comparison, $Re = 150k$	58
Figure 4.29 Lift curve comparison, $Re = 200k$	58
Figure 4.30 Drag polar comparison, $Re = 200k$	58
Figure 4.31 Lift curve comparison, $Re = 250k$	58
Figure 4.32 Drag polar comparison, $Re = 250k$	58
Figure 4.33 Lift curve comparison, $Re = 300k$	59
Figure 4.34 Drag polar comparison, $Re = 300k$	59
Figure 4.35 Lift curve comparison, $Re = 500k$	59
Figure 4.36 Drag polar comparison, $Re = 500k$	59
Figure 4.37 Approximated lift curve for use with the autopilot system with experimental data	61
Figure 4.38 Approximated drag polar for use in the autopilot system with experimental data..	62
Figure 4.39 Wake shapes at various α for <i>left)</i> $Re = 50k$ and <i>right)</i> $Re = 250k$	63
Figure 4.40 Smooth airfoil lift hysteresis for <i>left)</i> $Re = 150k$, and <i>right)</i> $Re = 250k$	64
Figure 4.41 Bumpy airfoil lift hysteresis for <i>left)</i> $Re = 150k$, and <i>right)</i> $Re = 250k$	64
Figure 4.42 Indication of the laminar separation bubble $Re = 250k$	65
Figure 4.43 <i>Left)</i> Low- Re airfoil performance [9, 10, 17], <i>right)</i> demonstrated airfoil performance	66
Figure 4.44 <i>Left)</i> Bumpy pressure distribution, <i>right)</i> smooth pressure distribution $Re = 250k$	67
Figure 5.1 AVL model of a standard Hobbico® NexSTAR™ compared to the autonomous NexSTAR™.....	68
Figure 5.2 Twisting wing used in this study, $\delta\alpha = -15^\circ$	69
Figure 5.3 AVL model of the twisting wing, $\delta\alpha = -15^\circ$	71
Figure 5.4 C_l vs $\delta\alpha$ in degrees.....	72
Figure 5.5 AVL model used for the Piccolo flight simulator.....	73
Figure 5.6 Block diagram of SiL set up	73
Figure 5.7 Screen capture from SiL. <i>Top)</i> Piccolo Command Center (PCC), <i>Bot Left)</i> Simulator display, <i>Bot Right)</i> Piccolo flight simulator	74
Figure 5.8 Analysis of first SiL doublet	75
Figure 5.9 Analysis of second SiL doublet	75
Figure 5.10 Block diagram of the HiL set up	76
Figure 5.11 Wing warping aircraft during HiL simulation	76

Figure 5.12 Mission plan for light testing of the wing shaping aircraft	78
Figure 5.13 Warping wing preparing for take off	78
Figure 5.14 Ground track and flight path from one autonomous test flight (green indicates autonomous control)	79
Figure 5.15 Wing warping aircraft in flight under autonomous control.....	79
Figure 5.16 Analysis of first in-flight doublet, manual control taken at ~ 4.25 s	80
Figure 5.17 Analysis of second in-flight doublet.....	80
Figure 5.18 Analysis of third in-flight doublet.....	81
Figure 5.19 Analysis of fourth in-flight double	81

Nomenclature

a_{eff}	Aileron effectiveness	F_{zb}	Body fixed z component of the force vector
a	Dimensionless coefficient	fps	Feet per second
b	Wing span	ft (')	Foot
CFD	Computational Fluid Dynamics	GTOW	Gross Takeoff Weight
C_d	Drag coefficient	g	Gravity
C_L	Lift coefficient for the wing	Hp	Horsepower
C_l	Lift coefficient for the airfoil	I_{xxb}	Body fixed Moment of inertia about the x axis
$C_{l,\alpha}$	Lift curve slope	I_{zzb}	Body fixed Moment of inertia about the x and z axes
$C_{l,max}$	Maximum lift coefficient	I_{yyb}	Body fixed Moment of inertia about the y axis
C_ℓ	Rolling moment coefficient	I_{zzb}	Body fixed Moment of inertia about the z axis
$C_{\ell,\bar{p}}$	Change in C_ℓ with respect to \bar{p}	in (")	Inch
$C_{\ell,\bar{r}}$	Change in C_ℓ with respect to \bar{r}	k	$\times 1,000$
$C_{\ell,\beta}$	Change in C_ℓ with respect to \bar{p}	k	Induced drag coefficient
C_{ℓ,δ_a}	Change in C_ℓ with respect to δ_a	kg	Kilogram
C_{ℓ,δ_r}	Change in C_ℓ with respect to δ_r	km/h	Kilometers per hour
C_m	Pitching moment coefficient	kPa	KiloPascals
C_n	Yawing moment coefficient	kW	Kilowatt
$C_{n,\bar{p}}$	Change in C_n with respect to \bar{p}	L	Lift Force
$C_{n,\bar{r}}$	Change in C_n with respect to \bar{r}	L/D	Lift-to-drag ratio
$C_{n,\beta}$	Change in C_n with respect to \bar{p}	\mathcal{L}	Rolling moment
C_{n,δ_a}	Change in C_n with respect to δ_a	lb	Pound
C_{n,δ_r}	Change in C_n with respect to δ_r	ℓ	Pressure tap depth
C_p	Coefficient of pressure	\mathcal{M}	Pitching moment
C_X	Axial force coefficient	M_{xb}	Body fixed x component of the moment vector
C_Y	Side force coefficient	M_{yb}	Body fixed y component of the moment vector
$C_{Y,\bar{p}}$	Change in C_Y with respect to \bar{p}	M_{zb}	Body fixed z component of the moment vector
$C_{Y,\bar{r}}$	Change in C_Y with respect to \bar{r}	m	Meter
$C_{Y,\beta}$	Change in C_Y with respect to \bar{p}	mm	Millimeter
C_{Y,δ_a}	Change in C_Y with respect to δ_a	mph	Miles per hour
C_{Y,δ_r}	Change in C_Y with respect to δ_r	m/s	Meters per second
C_Z	Vertical force coefficient	\mathcal{N}	Yawing moment
C_θ	Notation for $\cos(\theta)$	PCC	Piccolo Command Center
C_ϕ	Notation for $\cos(\phi)$	Pa	Pascal
C_ψ	Notation for $\cos(\psi)$	p	Roll rate
c	Chord length	\dot{p}	Roll acceleration
D	Drag force	\bar{p}	Dimensionless roll rate
DAQ	Data acquisition system	psi	Pounds per square inch
DMLS	Direct metal laser sintering		
d	Pressure tap depth		
F_{xb}	Body fixed x component of the force vector		
F_{yb}	Body fixed y component of the force vector		

q	Dynamic pressure	x_0	Reference x location
\dot{q}	Pitch rate	\dot{x}_f	Earth fixed x velocity
\ddot{q}	Pitch acceleration	Y	Side force
q_∞	Free stream dynamic pressure	y_0	Reference y location
r	Yaw rate	\dot{y}_f	Earth fixed y velocity
\dot{r}	Yaw acceleration	\dot{z}_f	Earth fixed z velocity
\bar{r}	Dimensionless yaw rate	α	Angle of attack
r^2	Coefficient of determination	$\alpha_{C_l=0}$	Zero lift angle of attack
Re	Reynolds number	α_{stall}	Stall angle
$R_{\ell, \bar{p}}$	Dimensionless coefficient	β	Sideslip angle
R_{ℓ, δ_a}	Dimensionless coefficient	$\Delta \bar{p}$	Disturbance in \bar{p}
S	Wing area	$\Delta \hat{\bar{p}}$	Dimensionless rate of change $\Delta \bar{p}$
S_θ	Notation for $\sin(\theta)$	$\Delta \bar{r}$	Disturbance in \bar{r}
S_ϕ	Notation for $\sin(\phi)$	$\Delta \hat{\bar{r}}$	Dimensionless rate of change $\Delta \bar{r}$
S_ψ	Notation for $\sin(\psi)$	$\Delta \beta$	Disturbance in β
SLA	Sterolithography	$\Delta \hat{\beta}$	Dimensionless rate of change $\Delta \beta$
T	Thrust Force	$\Delta \delta_a$	Disturbance in δ_a
t	Time	$\Delta \delta_r$	Disturbance in δ_r
U_∞	Air Velocity	δ_a	Aileron deflection
UAV	Unmanned aerial vehicle	δ_r	Rudder deflection
UV	Ultra violet	θ	Euler elevation angle
u	Velocity component in x	$\dot{\theta}$	Time rate of change of θ
u_a	Aileron actuator input signal	μ	Dynamic viscosity
V_0	Airspeed	ν	Kinematic viscosity
V_{wx_f}	Earth fixed x component constant wind vector	ρ	Air density
V_{wy_f}	Earth fixed y component constant wind vector	σ_r	Roll damping rate
V_{wz_f}	Earth fixed z component constant wind vector	τ_y	Dimensionless time
v	Velocity component in y	ϕ	Euler bank angle
W	Weight	ϕ_c	Commanded bank angle
W	Wind disturbance (controller)	$\dot{\phi}$	Time rate of change of ϕ
W	Watt (motor power)	ψ	Euler heading angle
w	Velocity component in z	$\dot{\psi}$	Time rate of change of ψ
		$\%c$	Percent chord
		$^\circ$	Degree

Chapter 1 Introduction

1.1 Motivation

Within the last 15 years Unmanned Aerial Vehicles (UAVs) have become an integral part of the aerospace industry, becoming a tool to complete the “dull,” “dirty” and “dangerous” missions. These are the missions where the human becomes the limiting factor in performing the mission [1-5]. In early 2010 UAVs had accumulated over one million total flight hours, most of which had accrued in the last 10 years [5] as shown in Figure 1.1.

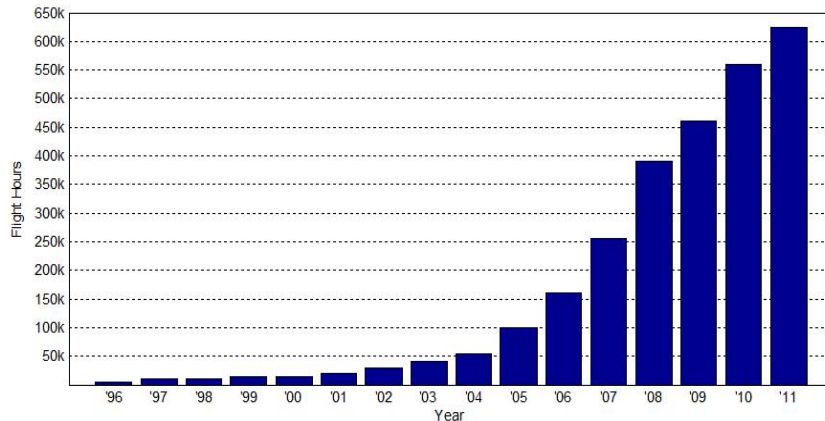


Figure 1.1 UAV flight hours since 1996, adapted from Winnefeld and Kendall [5]

In the initial years of UAV usage, the vehicles were categorized into 4 groups (or classes) based on aircraft gross takeoff weight (GTOW) and usage translating into the capability needs of the various combatant commanders (COCOMs) [1, 2]. These groups are:

- Small: GTOW < 55 *lbs*,
- Tactical: GTOW 55 – 1320 *lbs*,
- Theater: GTOW > 1320 *lbs*,
- Combat: GTOW > 1320 *lbs* and designed as a strike platform.

This classification system continued until approximately 2009 when flight altitude was added as an extra classification criteria and another group designation was added [3-5]. The new classification system is:

- Group 1: GTOW 0 – 20 *lbs*,
Flight altitude < 1,200 *ft*,
- Group 2: GTOW 21 – 55 *lbs*,
Flight altitude < 3,500 *ft*
- Group 3: GTOW < 1320 *lbs*,
Flight altitude < 18,000 *ft*,
- Group 4: GTOW > 1320 *lbs*,
Flight altitude < 18,000 *ft*,

- Group 5: GTOW > 1320 lbs,
Flight altitude > 18,000 ft.

This new grouping system also added a fifth group to accommodate a rapidly growing class of UAV: the 0 – 20 lbs GTOW range. As the popularity of UAVs grew their size began to shrink, opening a vast opportunity for instant strategic use of the vehicle to provide reconnaissance instead of waiting for an aircraft to become available and get on station. They have proven to be an invaluable tool to soldiers in theatre for gathering intelligence and even providing air support. These smaller UAVs have become known as “deployable” UAVs because of their ability to be packed away into a soldier’s gear and deployed when needed. Figure 1.2 shows a few examples of these types of UAVs.



Figure 1.2 Examples of deployable UAV's *top left*) Raven [6], *top right*) Wasp [6], *bot left*) Dragon Eye [6], *bot right*) tube launched Coyote II [7]

Inflatable wings have been able to fill a special niche of these deployable UAVs. Having wings that can deflate and be stowed in an extremely small container is beneficial when considering deployability. Some inflatable wings can pack to as low as 5 – 10% of their deployed volume [8] as illustrated by Figure 1.3. These high packing ratios allow for the integration of heavier payloads with more sophisticated sensors into an aircraft, normally requiring larger wings, while retaining the ability to fit into the same package as a smaller UAV. Harris [8] provides a detailed review of the various forms inflatable wings can take including purely inflatable structures or hybrid mechanical/inflatables.



Figure 1.3 Packability of inflatable wings demonstrated

The manufacturing process of many of these inflatable wings, like those shown in Figure 1.3, creates a unique bumpy shape. These bumps are predicted to improve the aerodynamic characteristics of the wings at low Reynolds numbers (Re) [9, 10]. This is beneficial for slow flying aircraft, the flight regime of most deployable aircraft, or aircraft flying in low density (high altitudes or in other atmospheres).

Although inflatable wings come with many advantages, there are still several challenges to overcome. There is limited knowledge about the true effects of the presence of the bumps on aerodynamic performance. Initial research into the exact effects has been conducted using both wind tunnel tests and computational fluid dynamics (CFD). Results from these studies indicate potential aerodynamic benefits are gained from the bumpy inflatable geometry at low Re , however, these studies were only able to examine a limited number of flight conditions. This prompted the need for a more comprehensive study of varying flight parameters. Without knowing the specifics of the aerodynamic performance of a bumpy airfoil shape, it becomes difficult to size the aircraft's wings appropriately during the design phase of an inflatable wing UAV. This typically translates into oversizing the vehicle, adding unnecessary weight and making inefficient use of the packability of the wings.

Another inherent challenge is producing roll authority. Many inflatable wings are made to retain rigidity and do not have built in ailerons. External ailerons can be added, and have been in some cases, but these external control surfaces remove packability from the wings since they are usually rigid. In general, these inflatable wing UAVs have been flown using strictly tail control, with either elevons or a combination of rudder and wing dihedral for roll control. These roll control methods lead to low maneuverability, and narrow the mission capability of the aircraft. However, by reducing the inflation pressure of the inflatable wings the torsional stiffness can be reduced, thus adding the potential for the addition of wing shaping for roll authority. Instances of both forms of flight control are discussed in Chapter 2.

1.2 Objectives

There are two main objectives of this thesis. The first objective of this study is to provide insight into the aerodynamic characteristics of the inflatable form of the NACA 4318 airfoil. This provides necessary data for sizing and optimization of wings for deployable aircraft with inflatable wings. Wind tunnel tests are performed to determine these characteristics, and a lift curve and drag polar were developed that can be used in the modeling process for autonomous control. Since smooth airfoils are typically required in the aerodynamic models for commercial autopilots, the aerodynamic performance curves developed from the wind tunnel results can also be used to replace the smooth airfoil's characteristics resulting from the modeling process.

The second objective of this thesis was to introduce the concept of wing warping and show its potential as a viable source of roll control for deployable inflatable wing UAVs. A process was developed for creating aerodynamic models to determine how the warping wings roll an aircraft. Using this modeling technique, a method was found to determine the necessary parameters used to program a commercial autopilot system and achieve successful autonomous flight using wing shaping for roll control.

1.3 Overview of Thesis

Chapter 2 of this thesis discusses previous research on deployable wings and wing shaping. This covers types and their potential uses of both deployable wings and wing shaping, as well as prior research performed to determine the aerodynamic effects of the bumps that appear in inflatable airfoil shapes. Chapter 3 introduces the important flight parameters used for this work. Chapter 4 outlines the experimental setup used to determine the aerodynamic characteristics of the inflatable NACA 4318 airfoil. The results of these experiments are also presented and discussed. Chapter 5 shows the modeling process used to determine the aerodynamic properties required to program a commercial autopilot to fly using wing shaping. The results of both simulations and flight testing using the predicted flight control parameters are discussed as well. Chapter 6 summarizes the work done and outlines potential future research directions, and the appendices provide detailed results of the experiments.

Copyright © Michael Andrew Thamann 2012

Chapter 2 Literature Review

2.1 Deployable Wings

The ability to easily transport aircraft to strategic locations near their operating zones can be beneficial. This ability can decrease operating costs and allow the operator to utilize more of the aircraft's endurance in the operating zone, since there is less distance to the targeted area. Furthermore, in some cases this is the only way to get to the operational zone. For example, when considering a UAV for data collection about the Martian surface and atmosphere, the aircraft must be able to be compactly stored into a rocket in order to get to its operational zone. This concept was demonstrated with the Aerial Regional-scale Environmental Survey (ARES) Mars Scout airplane. The aircraft could be stowed into the 8.5 ft (2.6 m) diameter aeroshell of the rocket, then deploy its 20.5 ft (6.25 m) wingspan and 14.6 ft (4.45 m) overall length and fly its mission [11]. Successful high altitude flight testing demonstrated the potential capabilities of deployable Mars aircraft. Figure 2.1 shows the stages of deployment for the ARES glider as well as an image from the high altitude flight test in 2002.

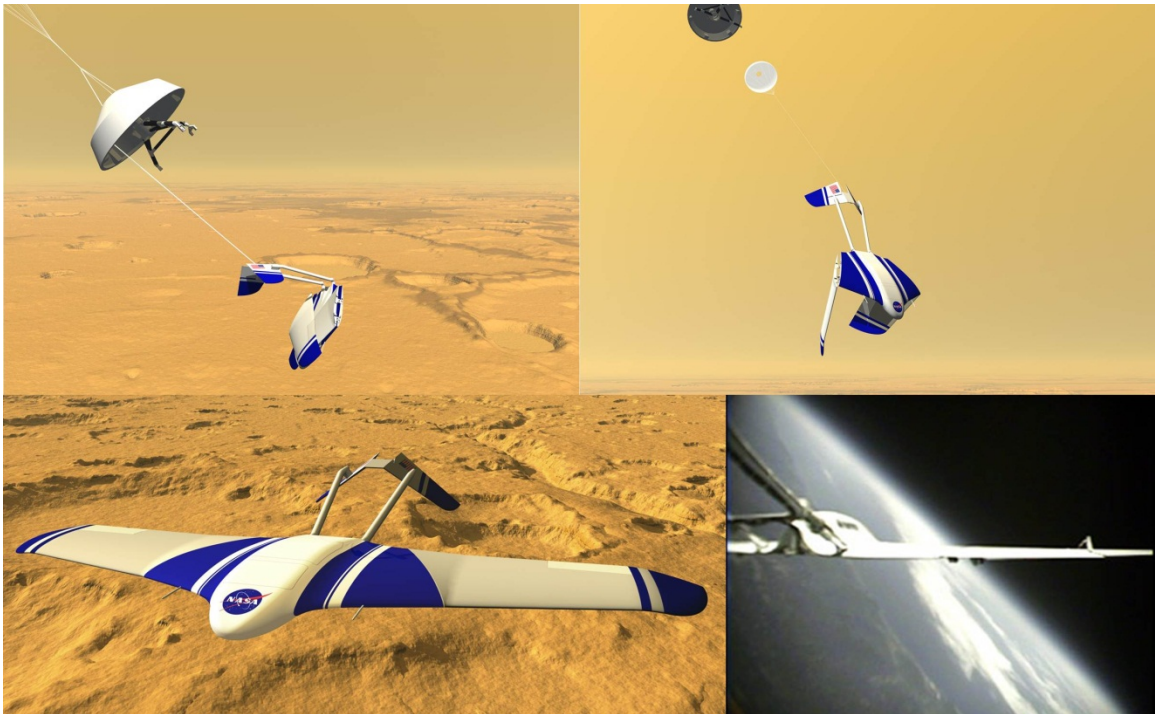


Figure 2.1 NASA ARES Mar's glider *top left*) first stage of concept deployment, *top right*) second stage of concept deployment, *bot left*) concept in flight, and *right*) test flight photo after high altitude deployment (images courtesy of NASA)

The ARES glider was not the first demonstrated deployable aircraft, however. The potential was first considered as early as 1933 when inflatable structures were starting to be recognized for their deployable characteristics, and a concept for an inflatable airplane was developed by McDaniel [12]. Then in the 1950's another inflatable aircraft concept was developed, built, and tested by the Goodyear Aerospace Corporation called the Inflatoplane [13]. This aircraft was developed to be small and light weight and have a stowed configuration

that could be parachuted to the location of a downed pilot. The downed pilot would then be able to unpack and inflate the aircraft and fly themselves back to safety. Figure 2.2 shows both the packed configuration and the deployed and operational configuration of this aircraft. It was the first successfully demonstrated deployable aircraft, as well as the first demonstrated inflatable wing aircraft. However, the aircraft could not perform any maneuvers that caused a load greater than $2g$'s because it was susceptible to sudden wing buckling at load factors just over 2 [14]. It had a maximum speed of 70 mph (112.65 km/h) because once the aircraft reached 71 mph (114.26 km/h) the wing would buckle at an angle of attack of just 5° . Therefore the aircraft had an operational Reynolds number (defined in Chapter 4) of $Re = 1.6 \cdot 10^6 - 3.1 \cdot 10^6$. Note the smooth airfoil shape shown in the right side of Figure 2.2. Approximately 12 of these aircraft were built through the mid 1960's and development continued until the cancelation of the project in the early 1970's.

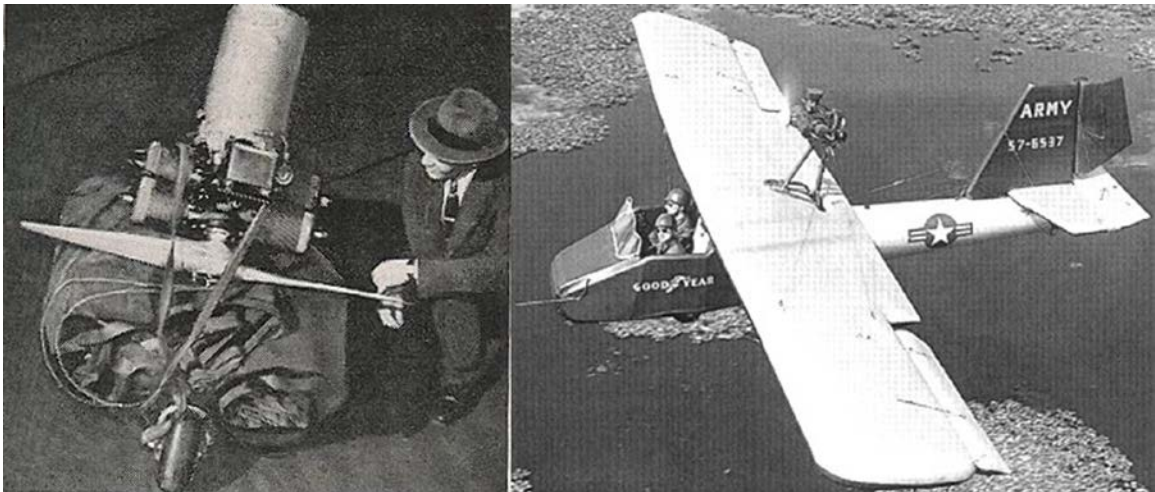


Figure 2.2 Left) Goodyear Inflateoplane stowed, and right) deployed in flight

It was in the mid 1970's that inflatable wings began being considered for use in UAVs. This started with the development of the Apterion UAV by ILC Dover [15]. This small UAV could be packed and taken to any location for deployment and is shown in Figure 2.3. The construction of the Apterion's inflatable wing generated a bumpy profile of the airfoil shape, which can be seen in Figure 2.3. It had a 5.1 ft (1.554 m) wingspan, weighed only 7 lb (3.175 kg), and used elevons for flight control. ILC Dover continues to develop inflatable wing technology, and has since developed several generations of inflatable wing technologies including rigidizable inflatable wings, and wings made from a coated nylon fabric which require much lower inflation pressures, and are lighter weight than other forms of non-rigidizable inflatable wings. An example of these nylon wings is also shown in Figure 2.3.

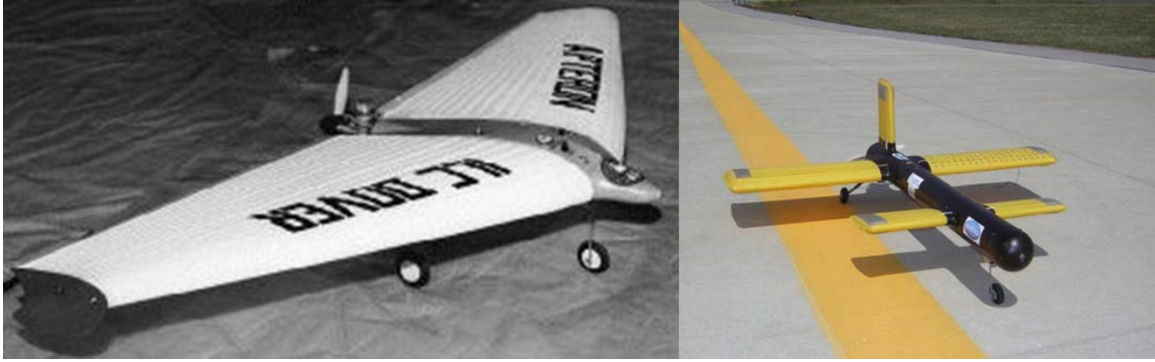


Figure 2.3 Inflatable wing UAVs developed by ILC Dover: *Left*) Apterion, and *right*) backpackable demonstration UAV with coated nylon inflatable wings (images courtesy of ILC Dover [16])

In 2001 NASA's Dryden Flight Research Center developed and flew an inflatable wing UAV, the I2000. This UAV was dropped from a carrier aircraft, as shown in the top left photograph of Figure 2.4, and the wings inflated in approximately one-third of a second. The wings used on the I2000 were developed for a gun-launched observation vehicle, and required high inflation pressures of 200 – 250 *psi* (1380 – 1725 *kPa*) using an onboard nitrogen bottle. It was constructed of 5 parallel inflatable spars that were covered with crushable foam to give the aerodynamic shape, and then skinned with rip-stop nylon [17]. The internal details of the wings can be seen in Figure 2.5.

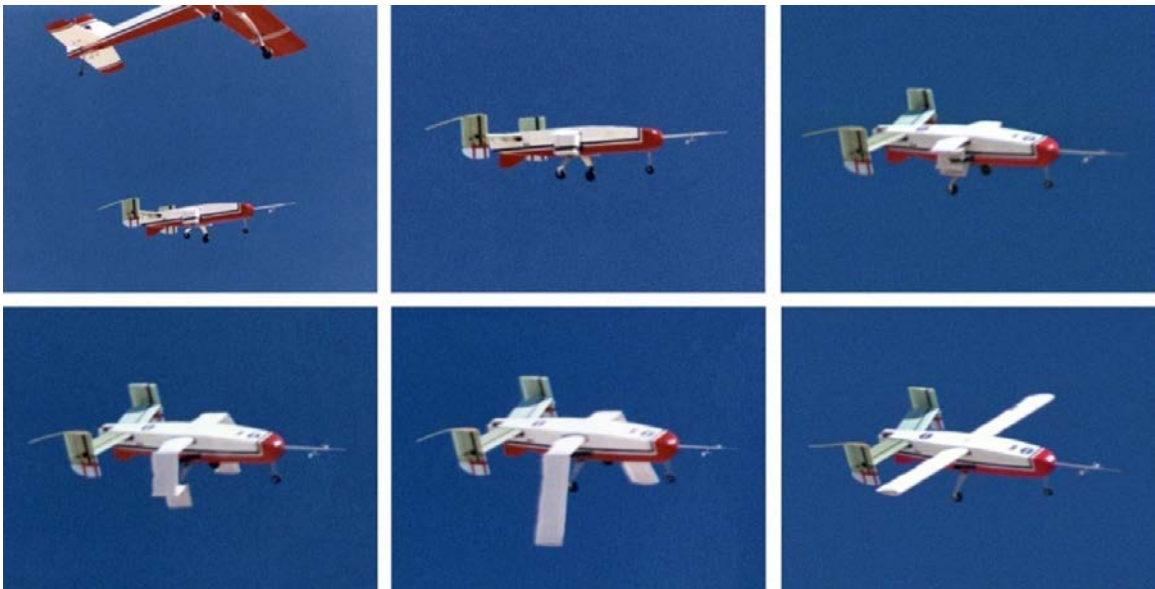


Figure 2.4 Deployment sequence of the NASA Dryden I2000 inflatable wing UAV, total elapsed time approximately 0.33 seconds (images courtesy of NASA)

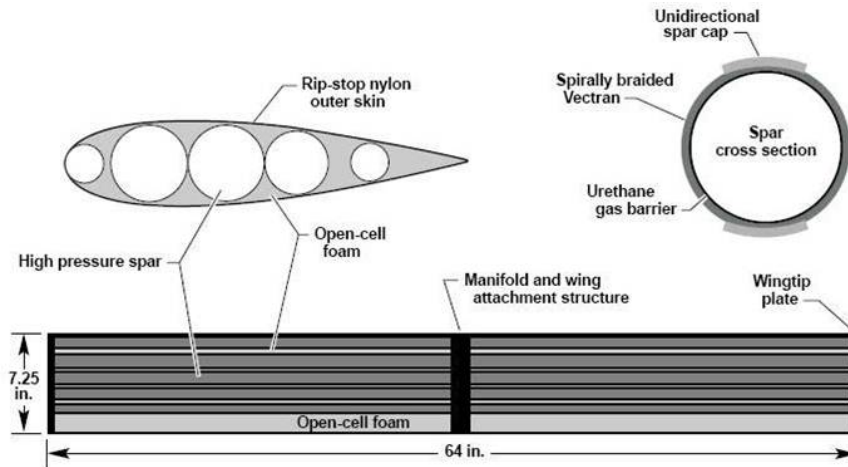


Figure 2.5 I2000 wing structure [17]

In 2002, The University of Kentucky began a collaboration with ILC Dover on inflatable wing development and feasibility. Inspired by the Mars glider and the Dryden I2000, this research was focused on demonstrating the feasibility of an inflatable wing vehicle for flight in low density environments such as Mars and was dubbed BIG BLUE (“Baseline Inflatable Glider Balloon Launch Unmanned Experiment”). The first two years (BBI and BBII) of the project started with a focus on inflatable-rigidizable wings. An example of these wings can be seen in the far left photo of Figure 2.6. These wings were made of fiberglass fabric, and coated in a UV curing resin that hardened when deployed and exposed to sunlight to maintain the wing’s shape. These wings were used in several low altitude flight tests as well as high altitude deployments detailed elsewhere [17-24]. These tests accomplished the first rigidization of an inflatable wing, and demonstrated the potential for use of inflatable wings for a Mars glider.

Years three and four (BBIII and BBIV) of the project used another form of inflatable wings made out of vectran, which was not impregnated with the UV curing resin. This material was chosen due to its heritage as Mars airbag material and its potential for future wing shaping. Shown in the middle photo of Figure 2.6, these wings were test flown at low altitudes and used in high altitude deployment testing [17-24]. Since these wings did not rigidize, a pressure regulation system was required for the wings to maintain strength after the deployment. The success of the flight tests and high altitude deployments demonstrated that this technique was viable. The final year of the project (BBV) focused on other aspects of the Mars glider problem. More emphasis was placed on the required autopilot integration to verify the capability of the autopilot to operate the sub-systems of the aircraft (i.e. pressure regulation, picture taking, parachute deployment, etc.) as well as maintaining communication at altitudes of 100,000 *ft* (30480 *m*) [17]. Another goal was to reduce the aircraft weight compared to the aircraft used in BBIII/BBIV to allow for high altitude balloon deployments. In order for high altitude balloon testing to be cost effective, the aircraft weight would need to be between 13 – 17 *lbs* (5.9 – 7.7 *kg*). To do this, polyurethane coated nylon wings replaced the vectran wings requiring lower inflation pressure, and thus a smaller inflation system. This and other changes dropped the gross takeoff weight (GTOW) from nearly 40 *lbs* (14.14 *kg*) in BBIII/BBIV

to under 15 *lbs* (6.8 *kg*). The BBV vehicle can be seen in the far right photo of Figure 2.6, and more detail can found elsewhere [17-24].



Figure 2.6 *Left*) BBI/BBII aircraft, *mid*) BBIII/BBIV aircraft, *right*) BBV aircraft [17]

The design of the inflatable-rigidizable wings used in BBI and BBII is outlined in Usui [24]. The airfoil selection analysis was performed using the baseline smooth airfoils, and then optimized for manufacturability. This process led to the use of the Eppler 398 (E398) airfoil shown in Figure 2.7. Once the airfoil was selected, the effects of the bumps on the aerodynamic properties needed to be quantified, so stereo-lithographic (SLA) models of the smooth and bumpy airfoil shapes were made for wind tunnel testing. The models were mounted to a pyramidal force and moment balance to measure lift, drag, and pitching moments, and smoke-wire visualizations were used to show flow separation, as seen in Figure 2.8.

Flow visualization with the smoke-wire was performed at $Re = 25k, 50k,$ and $100k$ each at few angles of attack. The flow visualizations indicated that the presence of the bumps on the airfoil surface delays flow separation from the surface at these lower Re . Aerodynamic forces were then measured for $Re = 156k, 200k,$ and $250k$ for the bumpy airfoil only, because smooth airfoil test results were not completed [24]. The result of one of these test cases is shown in Figure 2.9. Since no experimental comparison was made to the smooth airfoil, to better understand the effect of the bumps on the aerodynamic performance, the results from the airfoil selection process's XFOIL [25, 26] analysis were used to quantify the effects of the bumps on the aerodynamic properties. This comparison is shown in Figure 2.9. At this Re it appeared that presence of bumps reduces the max lift, increases the drag of the airfoil, and delays stall.

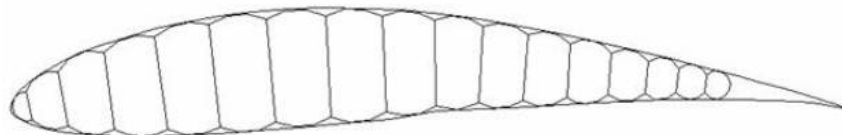


Figure 2.7 E398 airfoil used in the inflatable-rigidizable wings and the ideal smooth shape [27]

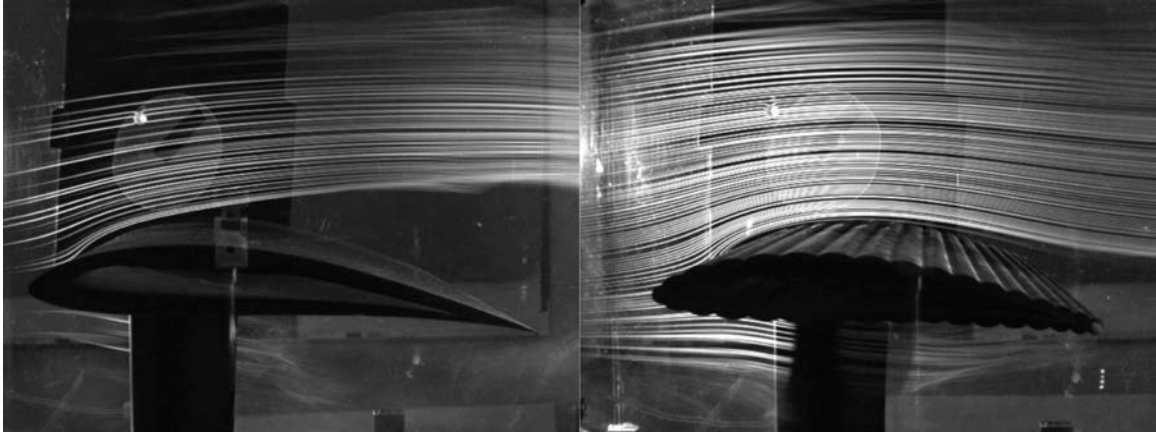


Figure 2.8 Smoke wire visualizations of *left*) smooth E398 and *right*) bumpy E398 at $Re=50k$, $\alpha = 4^\circ$ [27]

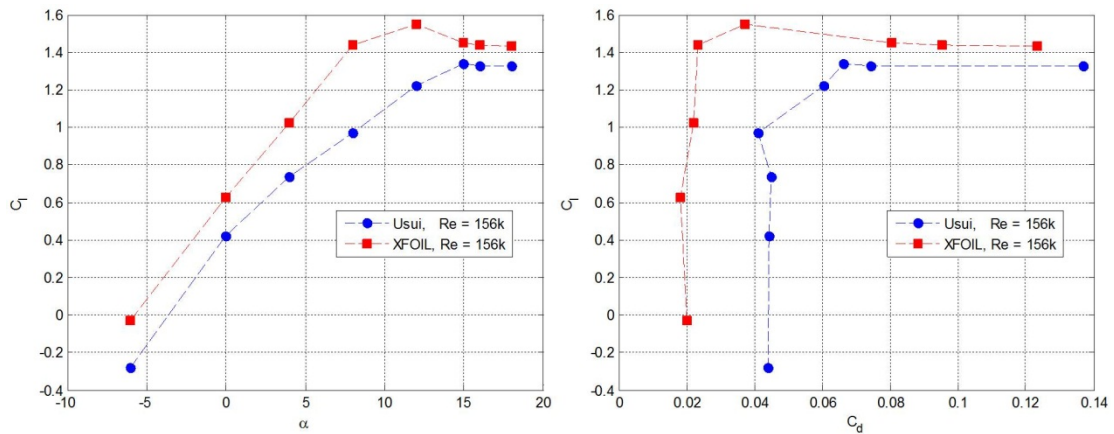


Figure 2.9 Bumpy E398 experimental results compared to XFOIL [25, 26] smooth airfoil predictions at $Re = 156k$ (adapted from Usui [24]) *Left*) lift curve, *right*) drag polar

Then Santhanakrishnan and Jacob [27] strove to get a better understanding of the effects of the bumps on the flow around the airfoil at low Re . To do this, PIV measurements were performed on the same SLA models used in Usui [24], as well as an ideal airfoil shape with a single bump at the $10\%c$ location. Only cases of $Re = 18k, 36k$, and $50k$ were run because these lower Re improve smoke visibility for seed particles required to perform the PIV measurements. Vorticity contours from the averaged $Re = 36k$ PIV runs are shown in Figure 2.10 for the regions indicating separation (the remaining results can be found elsewhere [27]). It was found that the flow over the bumpy airfoil stays attached longer than for the smooth airfoils. Figure 2.10 also illustrates how small recirculation regions form in the valleys between the bumps which assist in maintaining attachment of the flow. This effect is similar to what is found on the corrugated surface of a dragonfly wing as shown in Figure 2.11 from Sparks [28].

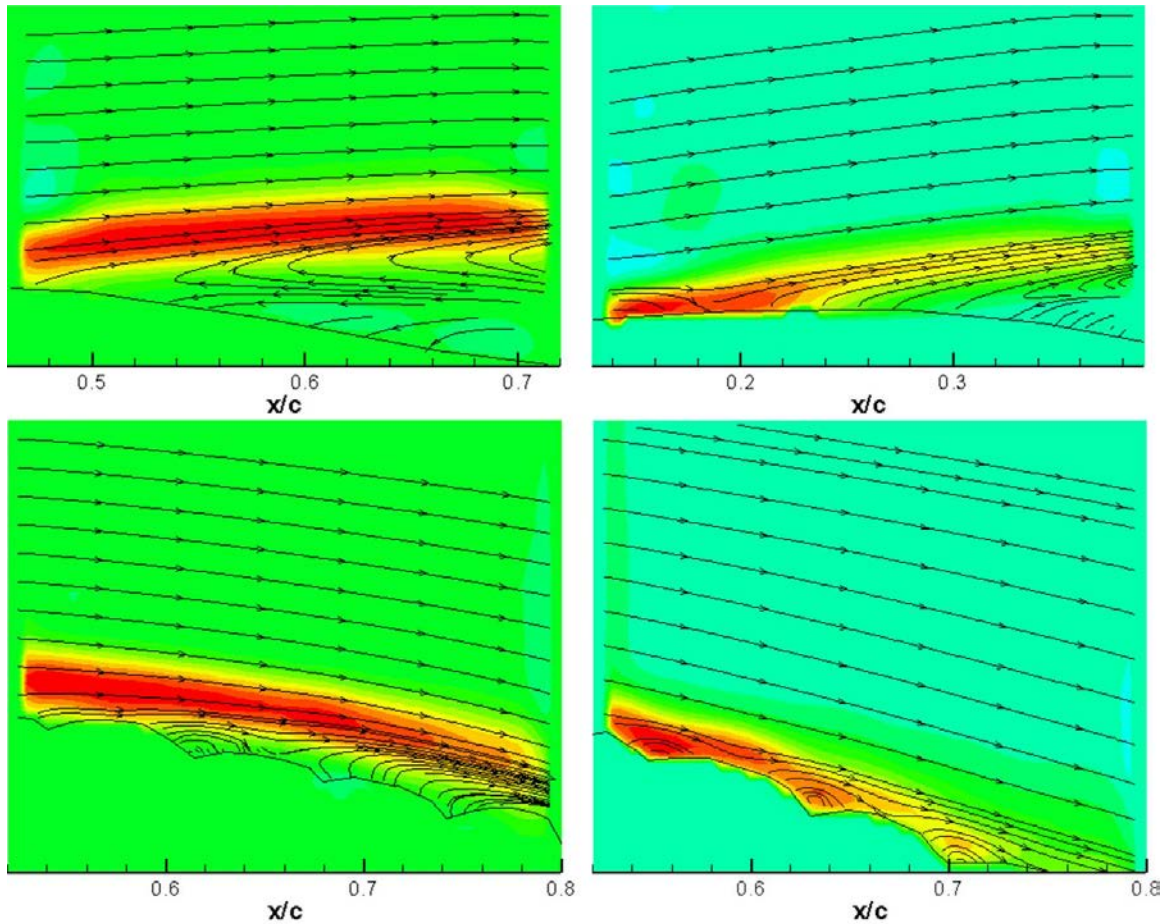


Figure 2.10 PIV streamline results and vorticity contours at $Re=36k$ [27] for *top left*) smooth, $\alpha = 7^\circ$, *top right*) smooth, $\alpha = 10^\circ$, *bot left*) bumpy, $\alpha = 7^\circ$, *bot right*) bumpy, $\alpha = 10^\circ$

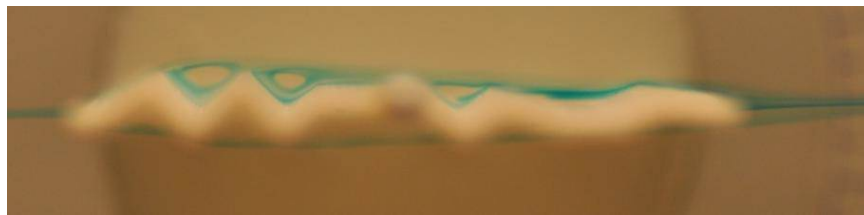


Figure 2.11 Visualization of flow over a dragon fly wing showing recirculation regions between the bumps yielding a “smooth airfoil” profile around the wing [28]

Reasor [29] analyzed computational models which complemented the experimental work performed on the E398 airfoil. An in house CFD code called GHOST was used to perform the analysis. GHOST gives the option to run a fully laminar simulation, a Suzen-Huang transitional simulation, or a fully turbulent simulation. The turbulence is modeled using a one-equation Spalart-Allmaras (SA) or a two-equation Shear Stress Transport (SST) Reynolds Averaged Navier-Stokes (RANS) model [30]. In Reasor [29] laminar, transitional, and SST turbulence simulations were run for $Re = 25k$ and $200k$ in both cases running an angle of attack (α) sweep from small negative α up to $\alpha = 20^\circ$. The lift and drag coefficients were then calculated from the resulting pressure distributions calculated from the CFD results. The results

from the $Re = 200k$ simulations are shown in Figure 2.12 along with the measured data from Usui [24]. In the CFD simulations the presence of bumps again resulted in a loss of lift and a delay in stall. The streamlines from the simulations also show similar patterns as the flow visualization from Usui [24], and also suggest that the fully turbulent model gives the best predictions for the effects of the bumps.

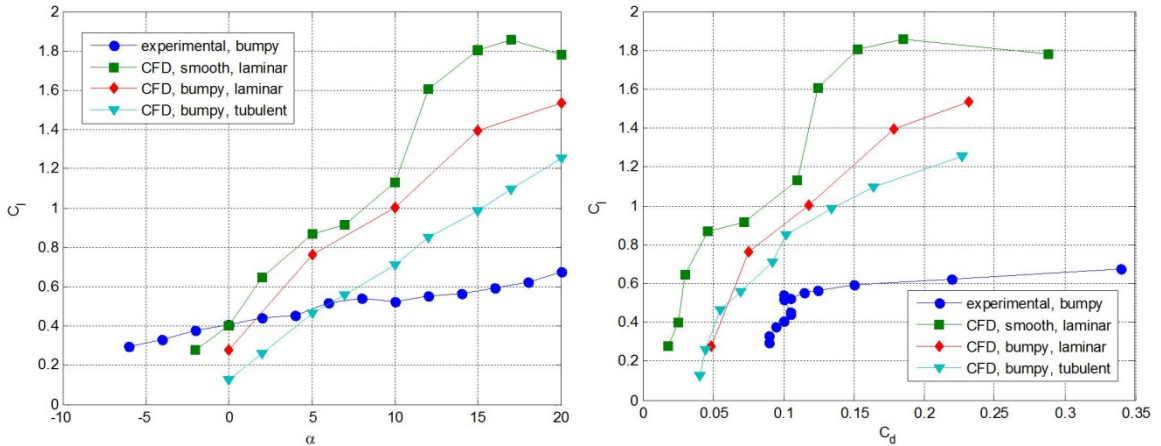


Figure 2.12 E398 experimental [24] and CFD [29] results at $Re = 200k$ (*left*) lift curve, (*right*) drag polar (adapted from Usui [24] and Reasor [29])

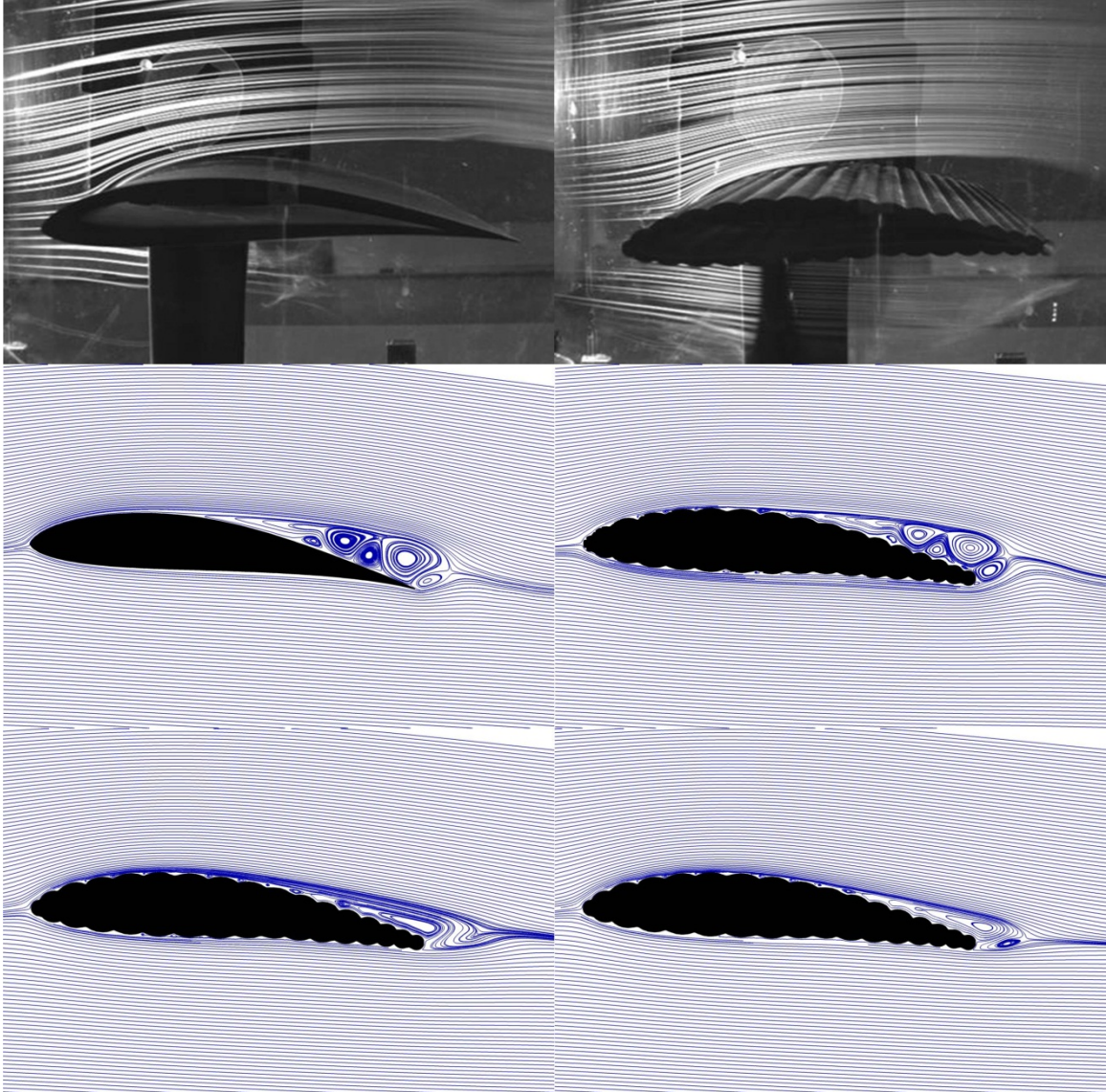


Figure 2.13 Comparison of experimental [27] and CFD [29] streamlines for the E398 airfoil at $Re = 25k$. *Top left*) smooth $\alpha = 0^\circ$, *top right*) bumpy $\alpha = 0^\circ$, *mid left*) smooth, laminar model $\alpha = 7^\circ$, *mid right*) bumpy, laminar model $\alpha = 7^\circ$, *bot left*) bumpy, transitional model $\alpha = 7^\circ$, *bot right*) bumpy, turbulent model $\alpha = 7^\circ$

In Reasor and Lebeau [30] further CFD simulations were completed that complimented the PIV experiments of Santhanakrishnan and Jacob [27], and comparison of the results is given in Reasor et al [22]. These simulations utilize the one-equation SA turbulence model instead of the two-equation SST model used in Reasor [29]. The focus of some of the CFD studies [22, 30] was to examine the interaction of the flow with surface of the airfoils, specifically to examine the flow between the bumps and their effect on flow separation, therefore, little aerodynamic data is provided. Figure 2.14 shows the indication of recirculation regions between the bumps in both experimental and CFD results, and Figure 2.15 shows the normalized velocity profiles of the bumpy and smooth E398 at various chord locations. Figure 2.15 indicates that the smooth

airfoil experiences adverse pressure gradients much sooner than the bumpy airfoil, thus separating earlier on the airfoil. Another interesting result from the CFD studies [22, 30] is the predicted effect of the bumps on the pressure distribution shown in Figure 2.16.

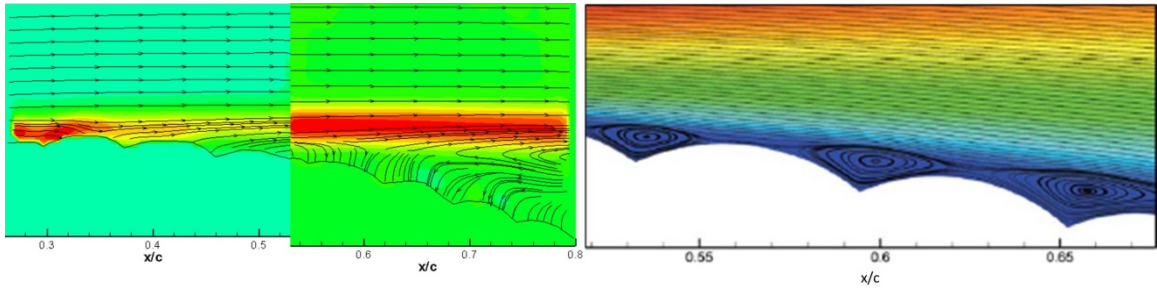


Figure 2.14 *Left, mid*) recirculation shown by PIV with vorticity contours at $Re = 36k, \alpha = 7^\circ$ [27], *right*) recirculation shown by CFD with u/U_∞ contours at $Re = 18k, \alpha = 7^\circ$ [30]

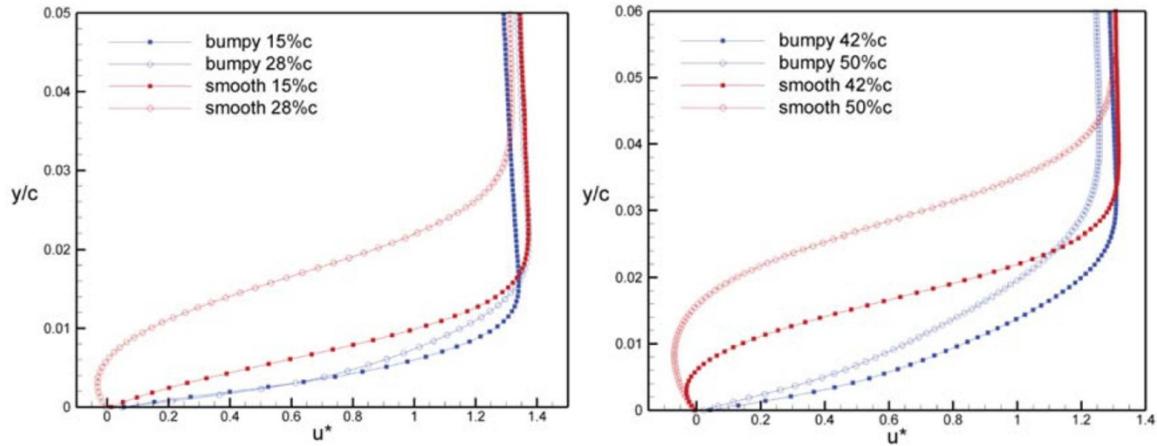


Figure 2.15 Velocity profiles of $u^* = u/U_\infty$ for the E398 bumpy and smooth airfoil at various chord locations, $Re = 18k, \alpha = 7^\circ$ [30]

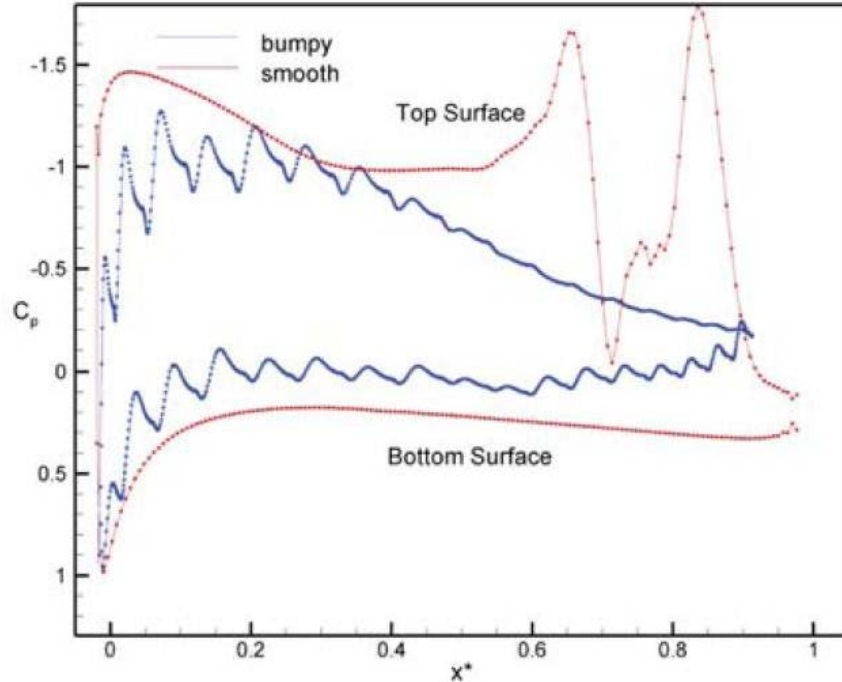


Figure 2.16 CFD Pressure distributions of smooth and bumpy E398 at $Re = 36k$, $\alpha = 7^\circ$ [30] To the author's knowledge, to date no experimental data has been collected for the inflatable NACA 4318 airfoil shape, which is the airfoil used in the inflatable wings of BBIII-BBV, and inflatable wings currently available at the University of Kentucky. However, there have been some CFD simulations performed [22, 31, 32]. These simulations used the same CFD code as was used to analyze the E398, and the same turbulence models. Simulations were run at $Re = 10k$ up to $Re = 500k$, giving a wide range of flight regimes. The results show that in laminar flow the inflatable airfoils generally displayed higher lift and higher drag than the smooth counterpart. However, the fully turbulent simulations show the smooth airfoils have higher lift and significantly lower drag at lower Re , and at higher Re the difference in lift becomes negligible. Reasor et al [22] tabulates the difference in flow separation as indicated by the various simulations shown in Table 2.1.

Table 2.1 Approximate chordwise location of flow separation from simulations [22]

Airfoil	Re	α	%c
E398 smooth	18k	7°	38%
E398 Bumpy	18k	7°	81%
E398 smooth	18k	10°	23%
E398 Bumpy	18k	10°	58%
E398 smooth	36k	7°	37%
E398 Bumpy	36k	7°	84%
E398 smooth	36k	10°	17%
E398 Bumpy	36k	10°	74%
NACA 4318 Smooth	10k	0°	53%
NACA 4318 Bumpy	10k	0°	91%
NACA 4318 Smooth	10k	10°	24%
NACA 4318 Bumpy	10k	10°	30%
NACA 4318 Smooth	200k	0°	none
NACA 4318 Bumpy	200k	0°	95%
NACA 4318 Smooth	200k	10°	81%
NACA 4318 Bumpy	200k	10°	52%

Other works employ CFD to analyze inflatable airfoil shapes, as well. For example, Johansen [33] combined CFD with a genetic algorithm (GA) code to optimize the size, number, and shape of the bumps on the E398 airfoil. The open source CFD code OpenFOAM was utilized to calculate the lift to drag ratio (L/D) while the GA optimized the bumps to maximize the L/D of the airfoil shape. Innes [34] used the commercial CFD solver Fluent to perform simulations of four separate National Advisory Committee for Aeronautics (NACA) 4-digit airfoil shapes: 0010, 1412, 2411, and 4415. These four shapes were then analyzed both in their ideal smooth shapes, and in their inflatable forms. Fully turbulent $Re = 300k$ flow was modeled using the one-equation SA turbulence model. The resulting aerodynamic performance is shown in Figure 2.17. In all cases, the presence of the bumps reduced the lift curve slope as well as the maximum lift coefficient and increased drag.

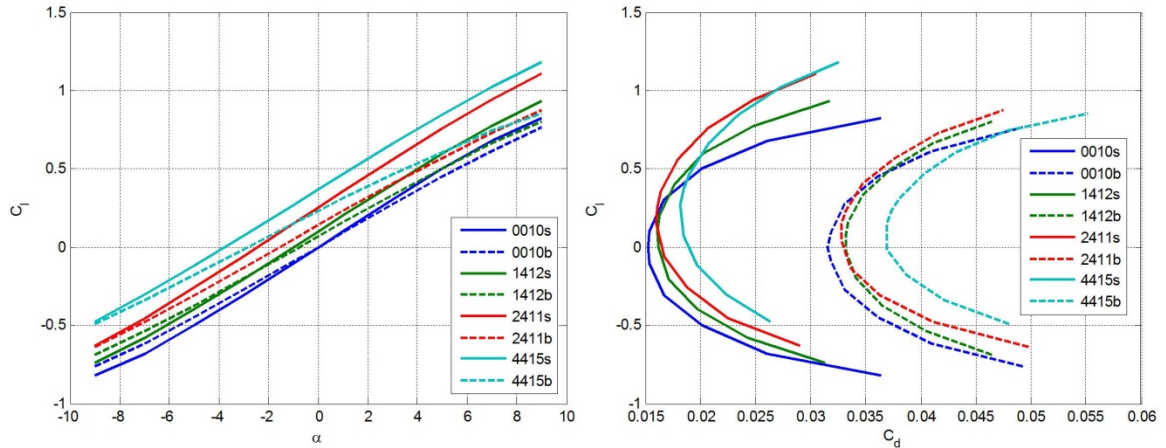


Figure 2.17 CFD results of NACA 4-digit smooth and bumpy airfoil shapes at $Re = 300k$ (XXXXs denotes smooth, XXXXb denotes bumpy). *Left*) lift curve, and *right*) drag polar (adapted from Innes [34])

2.2 Wing Shaping

Wing shaping can take many forms such as planform change, wing optimization, or roll control. Wing planform change is generally (and in this thesis) considered wing morphing. In the case of wing morphing the wing of the vehicle can be re-shaped to accommodate an optimum shape for each segment of a given mission. Typically this takes the form of highly swept or delta wings for high speed and maneuverable flight, and increased wingspan and aspect ratio for more efficient, slower flying. Figure 2.18 illustrates two wing morphing concepts from NextGen Aeronautics and Lockheed Martin [35]. The concept from Virginia Tech was built into a wind tunnel model and the effects of the planform change on various characteristics of the aircraft were measured [36]. Seigler [35] and Seigler et al [37] derive the equations of motion for such an aircraft as well as control schemes to control the motion of the structure during all phases of flight. To determine the feasibility of these type of concepts, Virginia Tech also built a remote control (RC) wing morphing aircraft, the concept is shown in Figure 2.19 [38]. This aircraft was built with a delta wing configuration with servo controlled wing extensions that could be extended symmetrically for improved endurance, or asymmetrically for roll control.

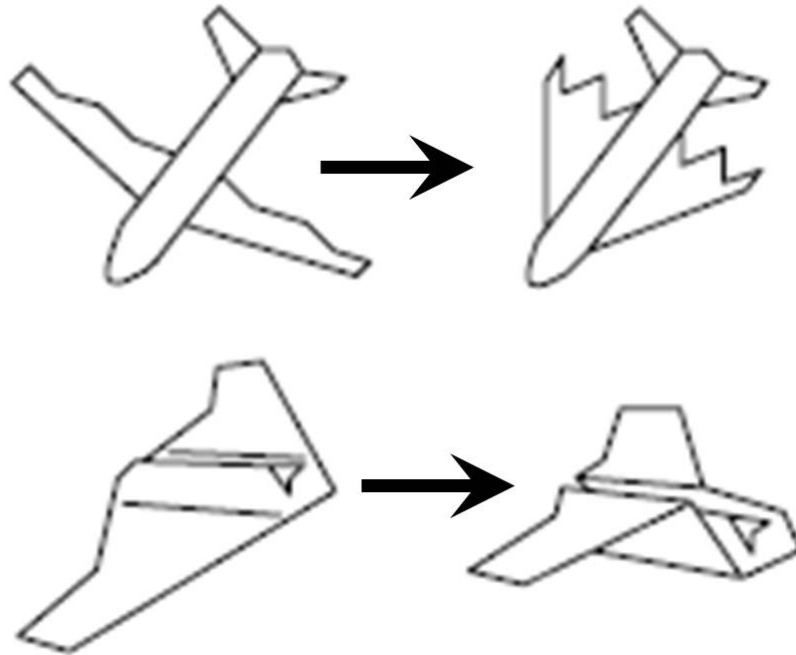


Figure 2.18 Morphing concepts from, *top right*) Nextgen Aeronautics [35], and *bot right*) Lockheed Martin [35]

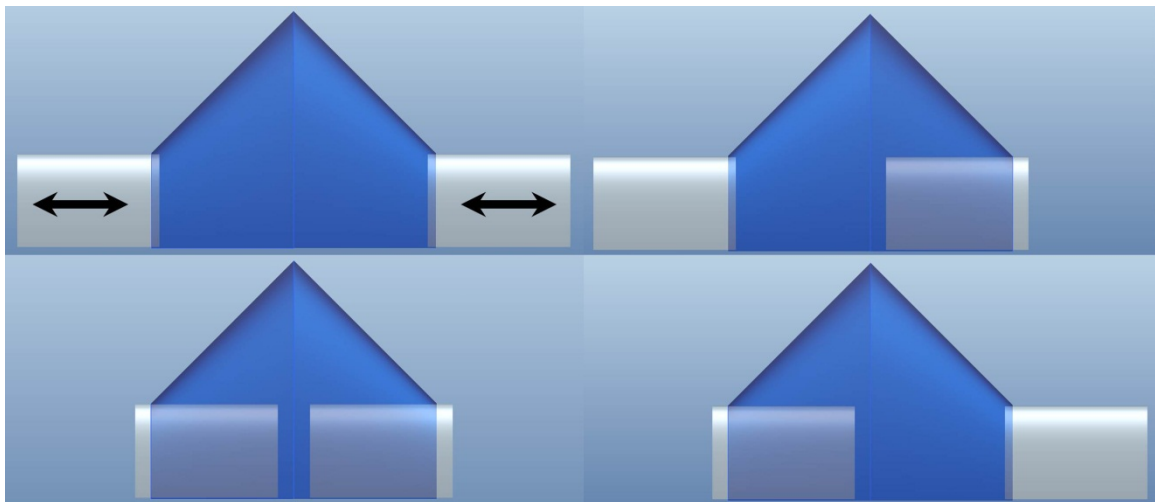


Figure 2.19 Concept of Virginia Polytechnic Institute RC extendable wing UAV [38]

Another potential application of wing shaping is for aerodynamic optimization of a wing by geometric twist or airfoil change. For example, Phillips [39, 40] discusses the use of lifting line theory to optimize a wing by introducing either geometric twist or camber change. Jacob [41] discusses the potential for incorporating adaptive airfoils for flight optimization of flight characteristics as well.

Other researchers are using wing shaping to try and recreate biologically inspired aircraft. Krashanitsa et al [42] discusses a model developed to measure the flight dynamics of an ornithopter. This flapping wing vehicle was both wind tunnel tested and flight tested under

manual and autonomous control. The vehicle was reported to have successfully tracked way points during autonomous control. The automation company Festo [43] has also recently been inspired by biology, and their Bionic Learning Network developed a mechatronic vehicle mimicking the actions of a bird called the “SmartBird” [44]. The SmartBird combines active torsion with flapping motion, as well as a tilting tail and head to closely mimic the flight of birds. Figure 2.20 demonstrates the flapping motion of the SmartBird as well as photos from successful flight testing.

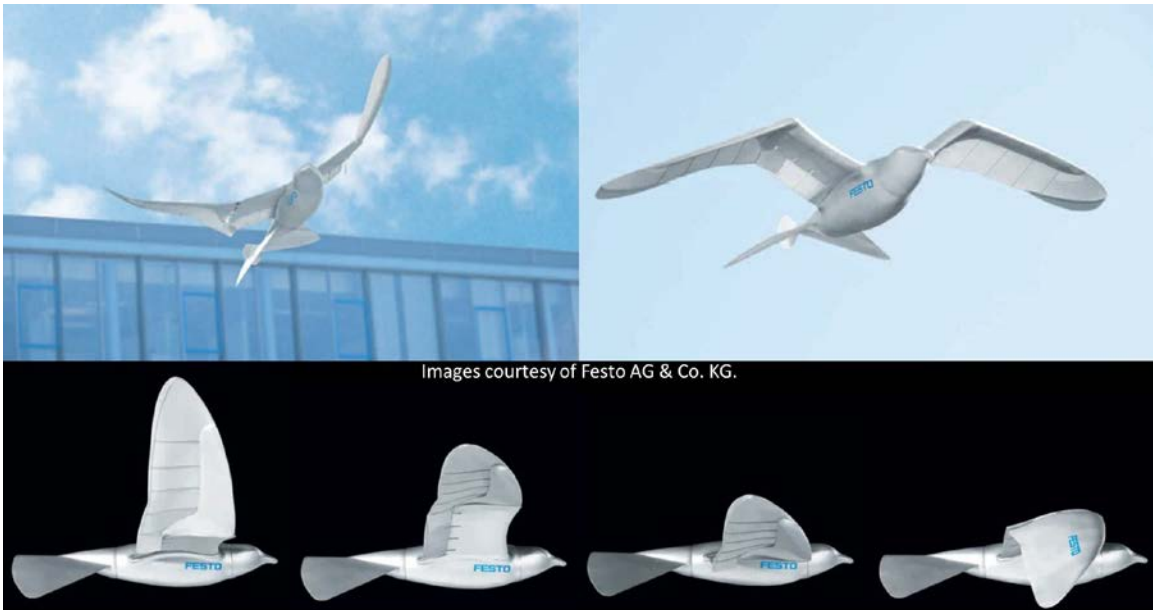


Figure 2.20 Festo Smartbird *top*) in flight *bot*) sequence of flaping motion [44]

The last way to implement wing shaping is for adding roll authority to an aircraft. This is the primary goal of the wing shaping investigated in this thesis. There are four main ways to implement roll authority via wing shaping: 1) total camber change, 2) local camber change, 3) twist, and 4) wing shape change. The first three of these concepts are illustrated in Figure 2.21 [45]. The last option involves asymmetric planform change to generate the necessary rolling moments for flight control (i.e. Figure 2.19).

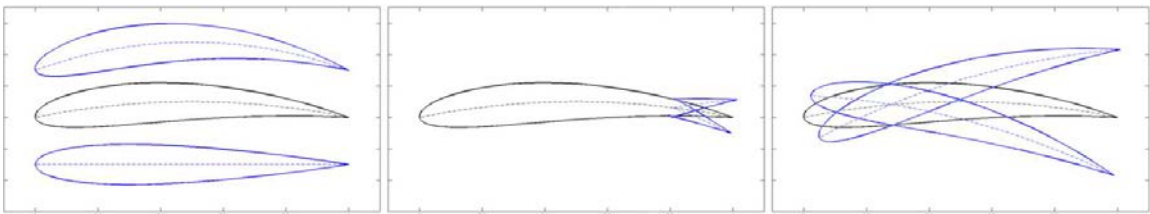


Figure 2.21 Wing shaping techniques *left*) total camber change, *mid*) local camber change, and *right*) twist [45]

Using wing twist for roll control has existed since prior to even the existence of powered flight. It was the incorporation of wing twist that allowed the first successful flight of the 1903 Wright Flyer [46, 47]. The Wright’s wing twisting mechanism was tested and perfected during

the flights of the 1902 glider [47, 48] and the asymmetric wing twist used to achieve their monumental first flight is shown in Figure 2.22.

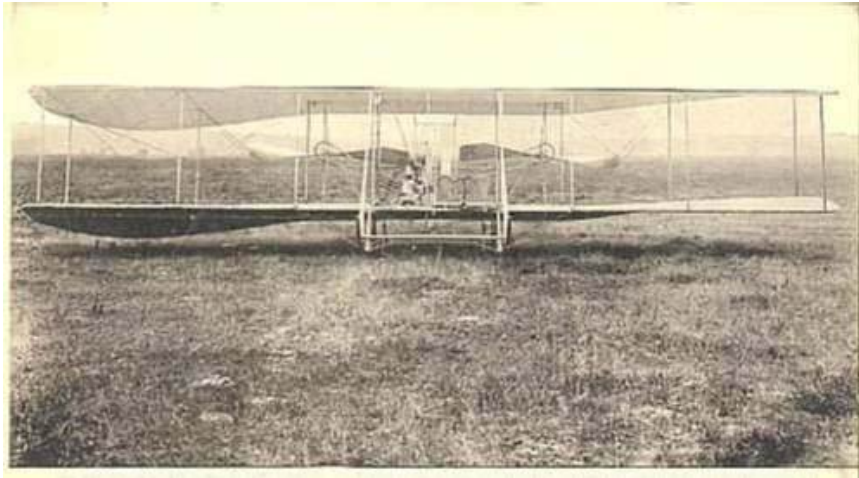


Figure 2.22 1903 Wright flyer showing wing twist for roll control

The University of Kentucky has been conducting research in the use of wing twisting for flight control since the BIG BLUE project. The potential to incorporate wing twisting into inflatable wings has always been a possible benefit to their use in addition to their packability. In the beginning stages of this research wind tunnel models were built to determine the effect of twisting the wings [23]. Scaled models of the BBIII/BBIV wings were rapid prototyped with various degrees of twist, then PIV measurements were taken of the resulting circulation to calculate the resulting increase in lift. The models and sample circulation distributions are shown in Figure 2.23. The blue curve in Figure 2.23 is the circulation calculated directly from the velocity data from the PIV, and the red curve was calculated from the vorticity. The testing showed that the fully twisted wing generated approximately four times the lift as the untwisted wing, indicating that wing twisting could provide adequate roll authority.

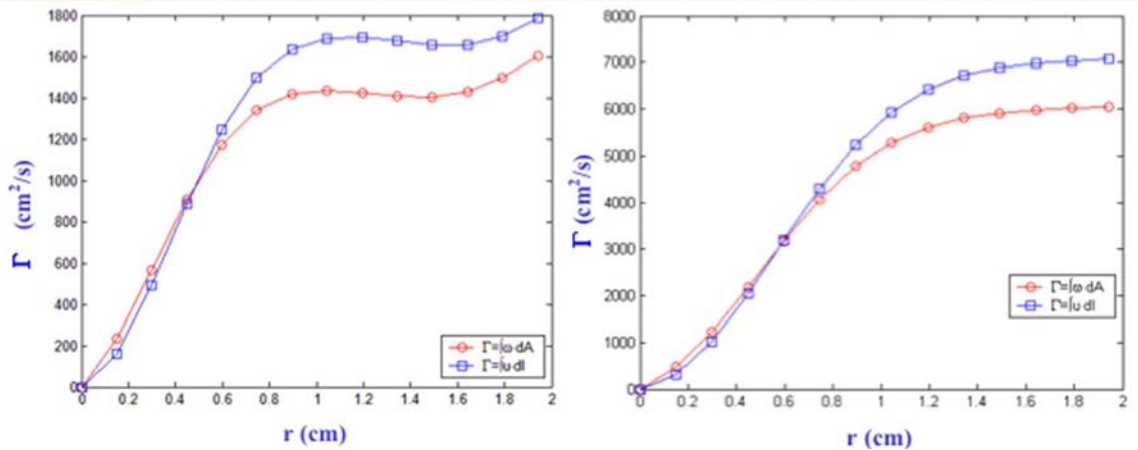
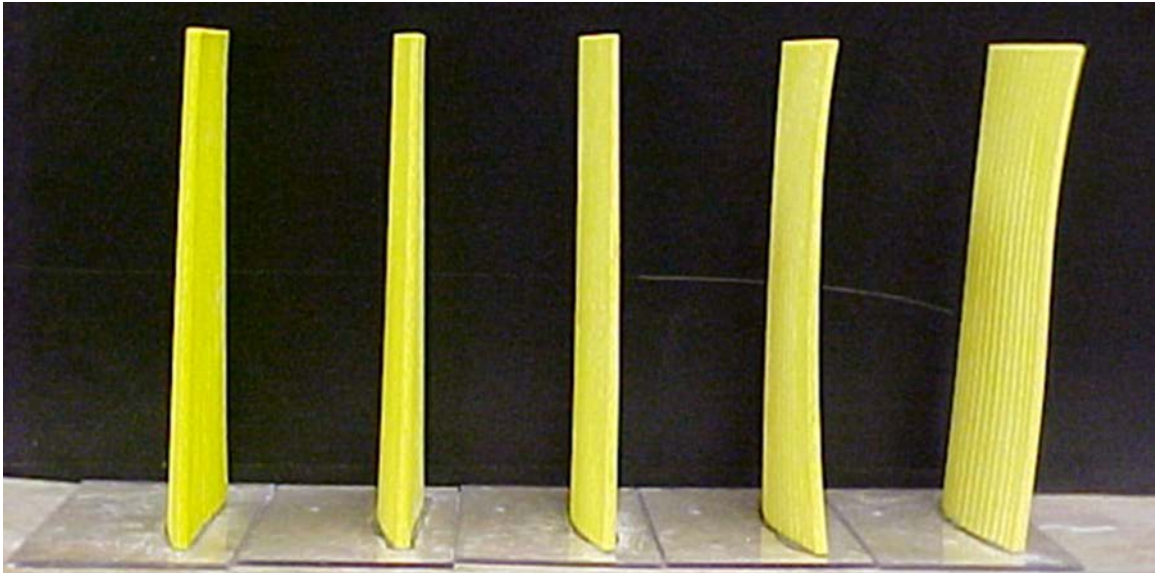


Figure 2.23 Top) wind tunnel models to measure the increase in circulation due to wing warping, *bot left*) circulation distribution from unwarped model, $Re = 100k$, $\alpha = 4^\circ$, *bot right*) circulation distribution of model warped 17° , $Re = 100k$, $\alpha = 4^\circ$ [23]

Flight test models were then developed to incorporate this wing twist for roll control [17, 19-21, 23, 49] under piloted remote control (RC). To do this a pulley system was developed which was controlled by a single servo such that, when rotated, one wing tip was pulled downward thus twisting the wing as shown by Figure 2.24. When using this technique only one side of the wing was deflected at a time, but it was found to provide adequate roll authority for aircraft control. Later flight tests of this vehicle incorporated a roll rate and servo position sensors allowing in flight data collection. The results from some of these tests are documented in [17, 19, 20].

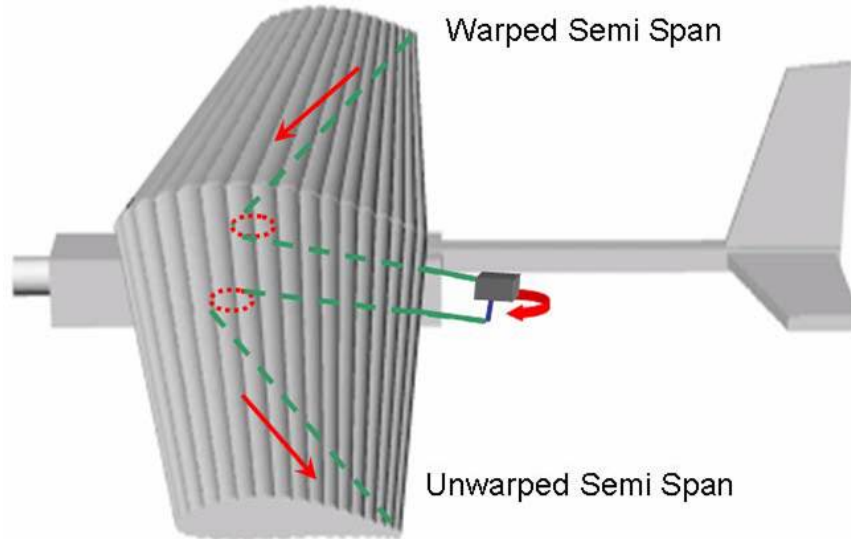


Figure 2.24 UAV outfitted with pulley mechanism for wing twist for roll control [17]

Other wing shaping methods were tested as well. These included servo actuators [17, 23] (shown in Figure 2.25) as well as shape memory alloys [17-21, 23, 49]. The shape memory alloys were never successfully flight tested because the air flowing over the externally mounted actuators inhibited their performance, and they had a slow response time for actuation [17]. However, the servo actuated wings have undergone both wind tunnel and flight testing [17, 23]. The resultant wing shaping from both of these methods was local camber change, illustrated by Figure 2.25. All flight tests with local camber change were performed under RC control only, and the technique was claimed to also provide adequate roll authority.

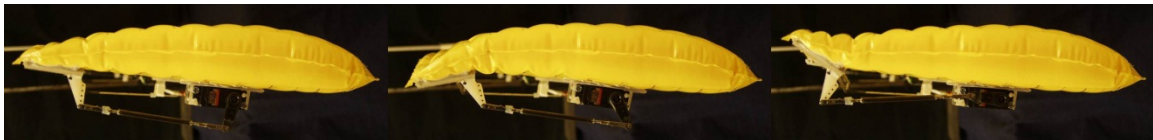


Figure 2.25 Local camber change used for RC wing shaping flight control [17]

The University of Florida has been researching the use of wing shaping to control micro air vehicles (MAVs) with membrane wings [50-54]. This research first used a flexible wing with Kevlar thread connected to the wing tip. The other end of the thread was connected to a servo head which would curl the wing to change the planform for roll control. The original curling design did not sufficiently change the roll trim to control the aircraft, therefore, another thread was connected to the trailing edge, thus adding twist to the curling motion [50]. In this configuration only one wing was deflected at a time. According to Garcia et al [54], the model was so responsive in the lateral directions during the RC flight tests that a stability augmentation system was recommended to reduce pilot work load.

Another MAV with a membrane wing was retro fitted with a twisting mechanism and RC flight tested as well [50, 51]. This mechanism allowed incorporation of bi-directional control of the deformation unavailable in the curling aircraft. This anti-symmetric twist reduced the

adverse yaw coupling that was noticed RC during flight tests with the curling wing, and also greatly improved the response of the MAV to the pilot's command inputs [50]. Models of both of these aircraft, as well as other biologically inspired MAVs, have been developed with the intent of developing controllers for both stability augmentation and autonomous control [50-54], however, the author is unaware of any implementation of any such controllers to date.

Virginia Tech has developed a UAV that uses total camber change to provide roll control [55, 56]. This was accomplished using macro-fiber composite (MFC) actuators incorporated into the upper and lower surfaces of the wing as shown in Figure 2.26. These actuators can be excited either symmetrically for a flap effect, or asymmetrically for roll control. The MFC aircraft was both wind tunnel and RC flight tested to test the effectiveness of the camber control [55]. The aircraft flight tests indicated a lower roll rate than predicted by the wind tunnel testing due to damage to the actuators, but the aircraft demonstrated stable flight characteristics and sufficient control authority. Other methods of aerodynamic control via camber and thickness change have also been studied [56] at Virginia Tech, as well as wing shape change [38].

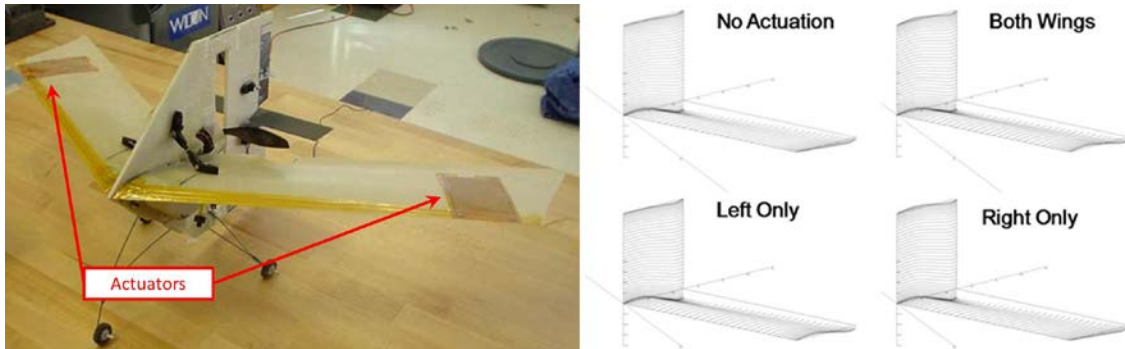


Figure 2.26 Left) Virginia Polytechnic Institute's UAV with MFC actuators, right) deflection models of MFC actuated aircraft [55]

Recently the University of Kentucky has revisited the concept of wing shaping for flight control with two objectives: 1) develop a rapidly prototypable wing shaping concept, and 2) incorporate autonomous control using wing shaping for primary roll authority. Doepke [45] outlines the development of such a wing, and this thesis discusses the implementation of autonomous control. The wing used in this research utilizes interchangeable warping inserts that mount to the end of a rigid wing section. These warping sections contain flexible foam which allows the section to twist, thus providing roll control. This aircraft had been flown under manual RC control to demonstrate the concept's ability to provide roll authority for the aircraft [45]; the autopilot integration leading to autonomous flight of the aircraft is outlined in Chapter 5 of this thesis. Figure 2.27 shows the wing shaping demonstrator aircraft used by Doepke [45] and this thesis.



Figure 2.27 Recently developed wing shaping demonstrator used in this study

Copyright © Michael Andrew Thamann 2012

Chapter 3 Introduction to Parameters Flight

When considering the topics being discussed in this thesis, it is important to note the origin of the terms being used, and why these terms are important. This thesis deals with two major topics of aircraft design: 1) the aerodynamic forces generated by the aircraft's wing, and 2) stability derivatives required to control the aircraft. In dealing with these topics one must recognize that the analyses performed to determine these characteristics occur in different coordinate systems. For example, when performing a stability analysis on an aircraft you can orient the three coordinate axes in a manner called the "body fixed axes" or the "stability axes," however, when performing an aerodynamic analysis the coordinate axes are re-oriented into the "aerodynamic axes." These orientations are shown in Figure 3.1 and are also referred to as reference frames. Only the body fixed axes are shown in this thesis and discussed because they are used in stability treatments. In this thesis the term "body frame" will be used to denote the body fixed axes orientation, and "aerodynamic frame" will be for aerodynamic axes orientation.

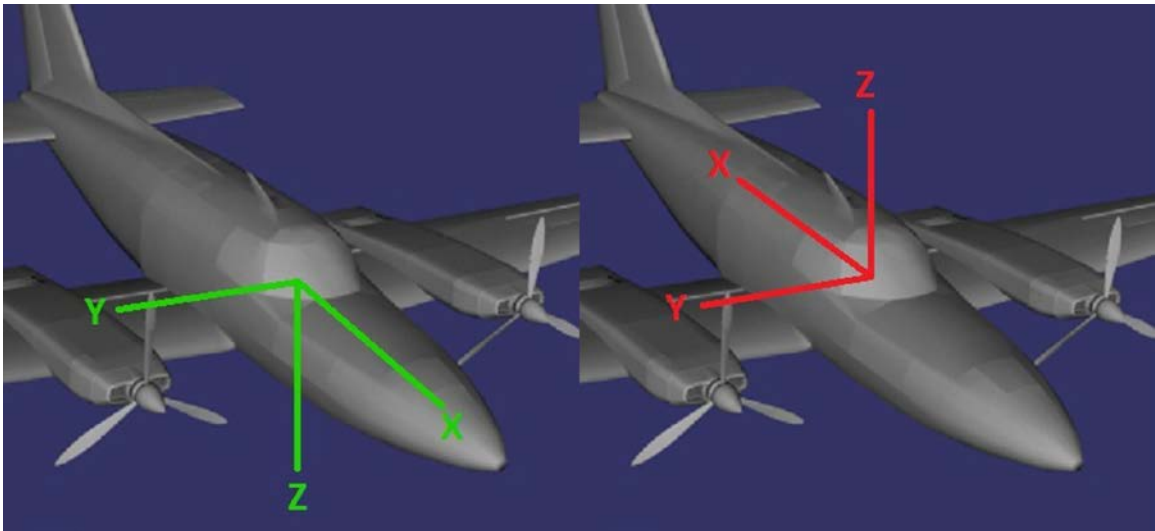


Figure 3.1 *Left)* Body frame *Right)* Aerodynamic frame

It is important to note the axis orientation in an analysis because this directly effects how the forces of flight are defined on the aircraft. For example, in the aerodynamic frame, a lift force is a positive force in the z -direction, but in the body frame the same lift would be a negative force in the z -direction. This difference is important because in one axis a $F_z < 0$ means the aircraft cannot fly, while in the other $F_z > 0$ means the aircraft cannot fly. A similar situation occurs with x -direction forces. This translates to $F_x > 0$ being a thrust force in the body frame, while being a drag force in the aerodynamic frame. Even though the x and z direction forces and moments will have different definitions, the forces and moments in the y -direction (F_y, M_y) will be the same in both analyses. This permits the calculation of pitch stability properties during the aerodynamic analysis allowing, for example, the designer to properly size the tail of the aircraft. Figure 3.2 shows how these definitions relate to the different reference frames.

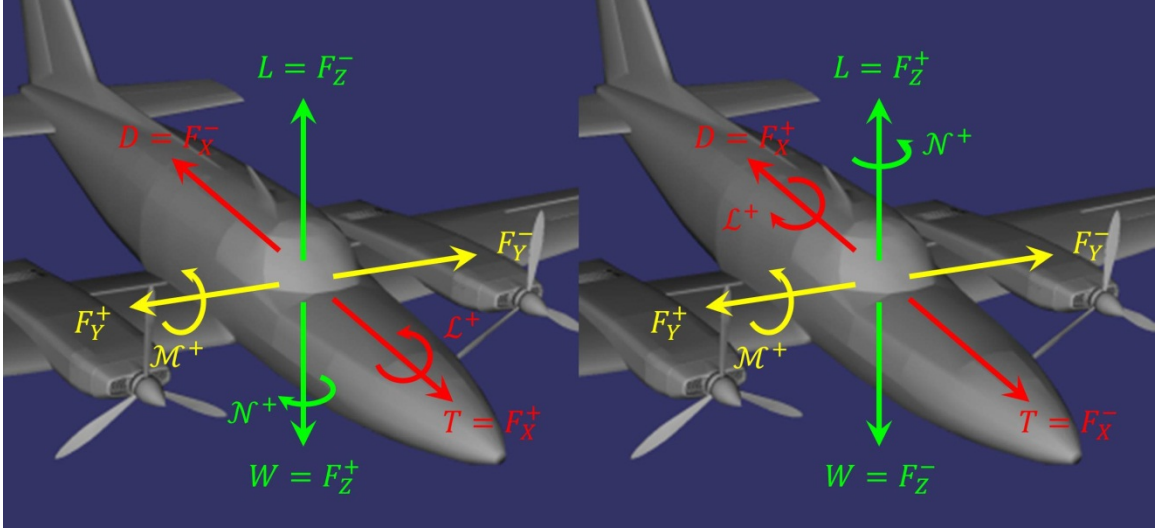


Figure 3.2 Forces and moments of flight *left*) the body frame *right*) the aerodynamic frame

Once the reference frame is chosen and the forces are defined, it is possible to determine the equations of motion for the aircraft. The full set of coupled, six degree of freedom equations of motion are given as Equation 3.1. The variables and symbols used in Equation 3.1 are defined in the Nomenclature section. These are the twelve equations that govern the motion of the aircraft. It should be noted that the equations in this set are coupled, meaning that the variables that are being solved for appear in multiple equations. For example it can be seen that the roll, pitch, and yaw rates, p , q , and r respectively, appear in nine of the twelve equations. It should also be noted that these equations are non-linear. These two facts make it difficult to analyze the equations of motion for aircraft.

$$\begin{aligned}
 \begin{Bmatrix} \dot{u} \\ \dot{v} \\ \dot{w} \end{Bmatrix} &= \frac{g}{W} \begin{Bmatrix} F_{x_b} \\ F_{y_b} \\ F_{z_b} \end{Bmatrix} + g \begin{Bmatrix} -S_\theta \\ S_\phi C_\theta \\ C_\phi C_\theta \end{Bmatrix} + \begin{Bmatrix} rv - qw \\ pw - ru \\ qu - pv \end{Bmatrix} \\
 \begin{Bmatrix} \dot{p} \\ \dot{q} \\ \dot{r} \end{Bmatrix} &= \begin{bmatrix} I_{xx_b} & 0 & -I_{xz_b} \\ 0 & I_{yy_b} & 0 \\ -I_{zx_b} & 0 & I_{zz_b} \end{bmatrix} \begin{Bmatrix} M_{x_b} + (I_{yy_b} - I_{zz_b})qr + I_{xz_b}pq \\ M_{y_b} + (I_{zz_b} - I_{xx_b})pr + I_{xz_b}(r^2 - p^2) \\ M_{z_b} + (I_{xx_b} - I_{yy_b})pq - I_{xz_b}qr \end{Bmatrix} \\
 \begin{Bmatrix} \dot{x}_f \\ \dot{y}_f \\ \dot{z}_f \end{Bmatrix} &= \begin{bmatrix} C_\theta C_\psi & S_\phi S_\theta C_\psi - C_\phi S_\psi & C_\phi S_\theta C_\psi + S_\phi S_\psi \\ C_\theta S_\psi & S_\phi S_\theta S_\psi - C_\phi C_\psi & C_\phi S_\theta S_\psi + S_\phi C_\psi \\ -S_\theta & S_\phi C_\theta & C_\phi C_\theta \end{bmatrix} \begin{Bmatrix} u \\ v \\ w \end{Bmatrix} + \begin{Bmatrix} V_{wx_f} \\ V_{wy_f} \\ V_{wz_f} \end{Bmatrix} \\
 \begin{Bmatrix} \dot{\phi} \\ \dot{\theta} \\ \dot{\psi} \end{Bmatrix} &= \begin{bmatrix} 1 & S_\phi S_\theta / C_\theta & C_\phi S_\theta / C_\theta \\ 0 & C_\phi & -S_\phi \\ 0 & S_\phi / C_\theta & C_\phi / C_\theta \end{bmatrix} \begin{Bmatrix} p \\ q \\ r \end{Bmatrix}
 \end{aligned} \tag{3.1}$$

Since the equations of motion have units, it is convenient to nondimensionalize them for analysis. This technique requires a series of coefficients which convey the forces, moments, and rates of the aircraft in a dimensionless form. Table 3.1 shows the definitions of some of the

common and relevant coefficients used in this thesis. For a complete list one can visit any of a number of texts [57-59].

Table 3.1 Normalized forces, moments, and rates of flight

Coefficient	Symbol	Definition	Coefficient	Symbol	Definition
Axial Force Coefficient	C_X	$\frac{F_{x_b}}{\frac{1}{2}\rho V_0^2 S}$	Rolling Moment Coefficient	C_ℓ	$\frac{M_{x_b}}{\frac{1}{2}\rho V_0^2 S b}$
Side Force Coefficient	C_Y	$\frac{F_{y_b}}{\frac{1}{2}\rho V_0^2 S}$	Pitching Moment Coefficient	C_m	$\frac{M_{y_b}}{\frac{1}{2}\rho V_0^2 S c}$
Vertical Force Coefficient	C_Z	$\frac{F_{z_b}}{\frac{1}{2}\rho V_0^2 S}$	Yawing Moment Coefficient	C_n	$\frac{M_{z_b}}{\frac{1}{2}\rho V_0^2 S b}$
Lift Coefficient	C_L	$\frac{L}{\frac{1}{2}\rho V_0^2 S}$	Dimensionless Roll Rate	\bar{p}	$\frac{pb}{2V_0}$
Drag Coefficient	C_D	$\frac{D}{\frac{1}{2}\rho V_0^2 S}$	Sideslip Angle	β	$\frac{v^*}{V_0}$

* This is approximately true for deflections of small angles.

It should be noted that Equation 3.1 is defined in the body frame whereas lift or drag forces occur in what is called the “wind frame” where the axes are aligned with the oncoming wind not the aircraft. In the body frame we define axial, horizontal, and vertical forces acting on the aircraft, therefore equations are needed to combine those forces into lift and drag. These are given by Equations 3.2 and 3.3, which require that both the angle of attack (α) and sideslip angle (β) of the aircraft, be known.

$$C_L = C_Z \cos \alpha - C_X \sin \alpha \quad 3.2$$

$$C_D = C_X \cos \alpha \cos \beta + C_Y \sin \beta + C_Z \sin \alpha \cos \beta \quad 3.3$$

After nondimensionalization the equations of motion can be linearized and separated into equations for the lateral and longitudinal motion of the aircraft. The linearization process is accomplished by expanding each normalized variable into a Taylor series about a defined trim condition. The separation into lateral and longitudinal motion helps to decouple the equations by grouping the equations affecting the pitch (axial and vertical) motion of the aircraft and those which affect the roll and yaw (horizontal) of the aircraft. The complete decoupling and linearization process can be seen elsewhere [57-59]. Equation 3.4 shows the partial result of this procedure. What is shown in Equation 3.4 is the portion of the lateral set of equations of motion which is the most important to this thesis.

$$\begin{aligned}
& \begin{bmatrix} 1 & 0 & 0 \\ 0 & 1 & -I_{xz_b}/I_{xx_b} \\ 0 & -I_{xz_b}/I_{zz_b} & 1 \end{bmatrix} \begin{Bmatrix} \Delta\hat{\beta} \\ \Delta\hat{p} \\ \Delta\hat{r} \end{Bmatrix} \\
& = \begin{bmatrix} \frac{\rho S b}{4W/g} C_{Y,\beta} & \frac{\rho S b}{4W/g} C_{Y,\bar{p}} & \left(\frac{\rho S b}{4W/g} C_{Y,\bar{r}} - 1 \right) \\ \frac{\rho S b^3}{8I_{xx_b}} C_{\ell,\beta} & \frac{\rho S b^3}{8I_{xx_b}} C_{\ell,\bar{p}} & \frac{\rho S b^3}{8I_{xx_b}} C_{\ell,\bar{r}} \\ \frac{\rho S b^3}{8I_{xx_b}} C_{n,\beta} & \frac{\rho S b^3}{8I_{xx_b}} C_{n,\bar{p}} & \frac{\rho S b^3}{8I_{xx_b}} C_{n,\bar{r}} \end{bmatrix} \begin{Bmatrix} \Delta\beta \\ \Delta\bar{p} \\ \Delta\bar{r} \end{Bmatrix} \\
& + \begin{bmatrix} \frac{\rho S b}{4W/g} C_{Y,\delta_a} & \frac{\rho S b}{4W/g} C_{Y,\delta_r} \\ \frac{\rho S b^3}{8I_{xx_b}} C_{\ell,\delta_a} & \frac{\rho S b^3}{8I_{xx_b}} C_{\ell,\delta_r} \\ \frac{\rho S b^3}{8I_{xx_b}} C_{n,\delta_a} & \frac{\rho S b^3}{8I_{xx_b}} C_{n,\delta_r} \end{bmatrix} \begin{Bmatrix} \delta_a \\ \delta_r \end{Bmatrix}
\end{aligned} \tag{3.4}$$

Terms like $C_{\ell,\beta}$ in Equation 3.4 are the partial derivatives that result from the Taylor series expansion of the normalized coefficients. These terms are called stability derivatives because, for example, the $C_{\ell,\beta}$ term is the partial derivative of the rolling moment coefficient with respect to sideslip angle. Therefore, when looking at a static stability analysis, these terms describe the stability characteristics of the aircraft. For the example given before, if $C_{\ell,\beta} < 0$ the aircraft will be stable in roll, and if $C_{\ell,\beta} > 0$ the aircraft will naturally roll out of control once any deviation from level flight occurs. For more information on how the different stability derivatives affect the stability characteristics of the aircraft see Etkin [57], Phillips [58], or Stevens and Lewis [59].

All of the above coefficients and stability derivatives need to be determined prior to flight, and are also required for autopilot programming. There are two ways to determine these coefficients and their derivatives. One classic way is by instrumenting a wind tunnel model to measure the forces resulting from recreating the flight conditions with either full size or scaled models. The downside of this method is that it is both expensive and time consuming. It also requires either a large wind tunnel or an accurately scaled model. Also, in order to measure the rate dependent terms, i.e. $C_{\ell,\bar{p}}$, $C_{\ell,\bar{r}}$, a special setup is required to dynamically measure the forces and moments.

Another method to determine the coefficients and derivatives is by creating a computer model to run an aerodynamic simulation. This method has gained immense popularity due to its low cost and fast turnaround time. There are several programs that will calculate the aerodynamic and stability characteristics of an aircraft. A few examples of these types of programs are DATCOM [60], Tornado [61], and Athena Vortex Lattice (AVL) [62]. DATCOM is a program developed by the United States Air Force (USAF) and is an acronym for ‘‘Data Compendium.’’ It uses the definition of the aircraft’s configuration to empirically determine its characteristics from a data base of information on how different configurations affect stability

characteristics. Tornado and AVL both use a vortex lattice algorithm to calculate the aircraft's aerodynamic properties and stability derivatives. Tornado is a MATLAB based program written by Redhammer Consulting Ltd. in conjunction with universities. AVL, however, is a standalone program written by Mark Drela of Massachusetts Institute of Technology (MIT) which does not require any external compiler. AVL is the program used for the modeling and analysis of the aircraft in this thesis.

3.1 Piccolo II Autopilot Systems

The University of Kentucky's UAV lab has autonomous flight capability with the use of Cloud Cap Technologies Piccolo II autopilot systems [63]. These autopilots are an industry standard for autonomous flight control systems. They provide a robust control system which supports a wide variety of aircraft configurations. The control laws are based on simplified aerodynamic and kinematic models of aircraft, and use smooth gain scheduling to control the aircraft [64].



Image courtesy of Cloud Cap Technology

Figure 3.3 Cloud Cap Technology Piccolo II autopilot [63]

Most of the Piccolo autopilot system's control laws use inner and outer loop control architectures. In this scheme the outer loop reads the output of the inner loop controller, and then provides a command to the inner loop controller. For example the bank angle controller has an outer loop which controls the bank angle by sending commands to an inner loop controlling the roll rate [64]. This basic inner and outer loop bank angle control setup is illustrated by the block diagram in Figure 3.4. In the illustration the bank angle (ϕ) is fed back from the outer loop's output and compared to the bank angle signal (ϕ_c). The bank angle controller adjusts the bank angle and after any wind disturbances (W), and this signal (u_a) is sent to the actuators resulting in an aileron deflection (δ_a). The roll rate (p) is then read by the gyro and fed into the rate controller. The roll rate is then adjusted by the controller until the desired bank angle is achieved.

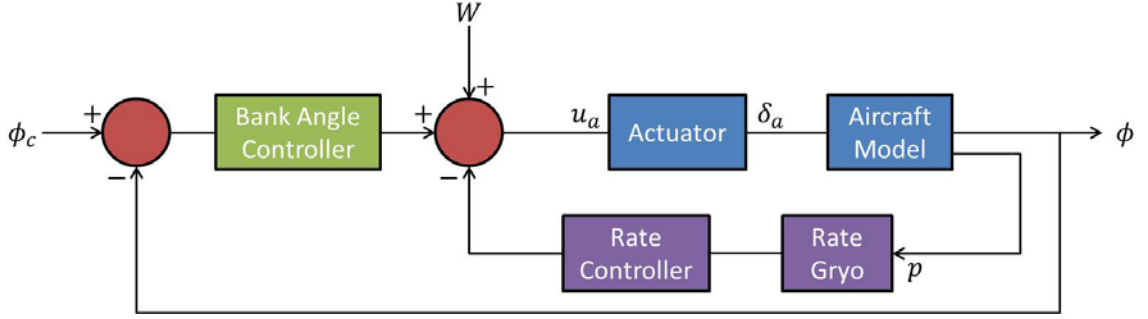


Figure 3.4 Block diagram of autopilot bank angle control loops

The aircraft model block in Figure 3.4 is where the stability derivatives and the coefficients governing the aircraft's properties come into play in the autopilot system. The outputs from the AVL analysis are used to build this simplified aircraft model [64]. Some of the most important terms in this model are the control effectiveness terms, which are calculated based on terms output from the AVL model as well as other physical properties of the aircraft. The purpose of these terms is to provide the autopilot with information on how far to deflect the control surfaces of the aircraft.

Of these parameters the aileron effectiveness is particularly important to this thesis, because it is the term which correlates a change in dimensionless roll rate ($\delta\bar{p}$) to a change in aileron deflection (δ_a):

$$a_{eff} \equiv \frac{\delta\bar{p}}{\delta_a}. \quad 3.5$$

This aileron effectiveness term is derived from the differential equation governing pure rolling motion of the aircraft. To get pure rolling motion one starts with the second equation in the set given by Equation 3.4, note that all terms are dimensionless, and the hat terms are dimensionless rate terms:

$$\begin{aligned} \Delta\hat{\bar{p}} - \frac{I_{xz_b}}{I_{xx_b}} \Delta\hat{\bar{r}} = & \frac{\rho S b^3}{8 I_{xx_b}} C_{\ell, \beta} \Delta\beta + \frac{\rho S b^3}{8 I_{xx_b}} C_{\ell, \bar{p}} \Delta\bar{p} + \frac{\rho S b^3}{8 I_{xx_b}} C_{\ell, \bar{r}} \Delta\bar{r} + \frac{\rho S b^3}{8 I_{xx_b}} C_{\ell, \delta_a} \Delta\delta_a \\ & + \frac{\rho S b^3}{8 I_{xx_b}} C_{\ell, \delta_r} \Delta\delta_r, \end{aligned} \quad 3.6$$

and apply the assumption that $\Delta\beta = \Delta\bar{r} = \Delta\delta_r = 0$. By setting all changes in sideslip (β), yaw rate (\bar{r}), and rudder deflection (δ_r) to zero, it is assumed that the rate of change in roll rate ($\hat{\bar{p}}$) is a result of the current roll rate (\bar{p}) and aileron deflection (δ_a). Then after substituting $\bar{p} = \Delta\bar{p}$ (roll rate for the change in roll rate), the ODE in Equation 3.6 becomes Equation 3.7:

$$\frac{d\bar{p}}{d\tau_y} - R_{\ell, \bar{p}} \bar{p} = R_{\ell, \delta_a} \Delta\delta_a, \quad 3.7$$

where

$$\bar{p} \equiv \frac{pb}{2V_0}, \quad \tau_y \equiv \frac{2V_0t}{b}, \quad R_{\ell,\bar{p}} \equiv \frac{\rho S b^3}{8I_{xxb}} C_{\ell,\bar{p}}, \quad R_{\ell,\delta_a} \equiv \frac{\rho S b^3}{8I_{xxb}} C_{\ell,\delta_a}. \quad 3.8$$

The above ODE has the solution:

$$\begin{aligned} \bar{p} &= \frac{R_{\ell,\delta_a} \Delta\delta_a}{-R_{\ell,\bar{p}}} [1 - \exp(-\sigma_r t)], \\ \sigma_r &\equiv -\frac{\rho S b^2 V_0}{4I_{xxb}} C_{\ell,\bar{p}}. \end{aligned} \quad 3.9$$

Since $C_{\ell,\bar{p}}$ is always negative, the exponent in the solution is always negative. Therefore, \bar{p} will always approach a steady state value. Due to the size of σ_r (known as the roll damping rate) this decay will happen rapidly. Hence, Equation 3.9 can be reduced to:

$$\bar{p} = \frac{C_{\ell,\delta_a} \Delta\delta_a}{-C_{\ell,\bar{p}}}, \quad 3.10$$

thus leaving the definition of aileron effectiveness as the ratio two of the aircraft's properties: aileron power (C_{ℓ,δ_a}), and the negative of the aircraft's roll damping ($C_{\ell,\bar{p}}$). After dropping the increment notation in Equation 3.10:

$$\frac{\delta\bar{p}}{\delta_a} \equiv \frac{C_{\ell,\delta_a}}{-C_{\ell,\bar{p}}}. \quad 3.11$$

It should be noted that the above analysis only holds if $\Delta\delta_a$ remains constant. However, using this equation to determine the roll rates for aircraft in flight will provide an acceptable approximation if small aileron deflections are considered. If the aileron deflections become large, then the response of the aircraft will become higher order, which has been seen during flight testing [45], thus showing that this first order ODE approximation will not hold for large deflections.

As mentioned previously, in order to obtain the coefficients used in Equation 3.11 either an aerodynamic simulation or a wind tunnel model is required. The Piccolo II autopilot utilizes the computer program AVL to obtain these stability derivatives. The Piccolo specifically requires a form of analysis known as an α -sweep which implies varying the angle of attack (α) and performing the aerodynamic analysis at each α . The required stability derivatives and aerodynamic coefficients are then output and stored into a look-up file which the Piccolo uses to determine the aerodynamic characteristics of the aircraft.

When considering a deployable wing UAV with inflatable wings and wing shaping for flight control, the first modeling challenge arises when attempting to model the wing shaping control surface. This challenge originates from the way the wing shaping is performed versus how control surfaces are defined within AVL. By the nature of wing shaping of a deformable wing, there is no distinct hinge line to model on the wing which precludes modeling the case in

AVL. This directly correlates to a problem in programming the autopilot as well, since the Piccolo requires the aileron effectiveness term defined in Equation 3.11. As seen above, this term uses the change in rolling moment due to control surface deflection. If a control surface cannot be defined in the model this derivative cannot be obtained. The process used in this thesis to model an aircraft with wing shaping was developed to address these challenges and is described in Chapter 5.

The second challenge in the aircraft modeling process comes from the aerodynamic shape of the inflatable wing airfoil. The bumps on the surface of the airfoil inhibit the vortex lattice solver in AVL from being able to calculate a solution. Therefore, another means must be used to determine the necessary aerodynamic coefficients for the autopilot to reference. In this case a wind tunnel model was created and tested to determine these coefficients. The results of this comprehensive study on the aerodynamics of the bumpy inflatable airfoil over a wide range of flight conditions are discussed in Chapter 4.

Copyright © Michael Andrew Thamann 2012

Chapter 4 Determination of Aerodynamic Coefficients of Inflatable Airfoils

The presence of bumps on the inflatable wing airfoil geometry does not allow for aerodynamic simulations to be performed using the vortex lattice algorithm used by AVL. In some cases a smooth skin has been added to the inflatable surface, effectively creating a smooth airfoil shape which can be modeled without any problems. For the cases when a skin is not added, wind tunnel tests were performed to determine the aerodynamic properties of the airfoil. A comparison between the smooth and bumpy shape of the airfoil allowed for performance curves to be created, allowing for simulations to be run using the smooth airfoil shape, then corrected for the bumpy airfoil properties. This will allow for a more rapid autopilot integration process into UAVs with inflatable wings.

The airfoil shape being studied in this thesis is in the inflatable wings currently in use at the University of Kentucky's UAV lab. The shape is based on a regular NACA 4-digit series airfoil, the NACA 4318. The airfoil is then modeled using a MATLAB code that adds the bumps on the surface created by the baffles in the inflatable wing. The NACA 4318 airfoil is thicker and has less camber than the previously tested inflatable airfoil, the Eppler 398. Table 4.1 highlights the differences between the base shapes of these airfoils and Figure 4.1 gives a side by side comparison of both their smooth and bumpy profiles.

Table 4.1 Comparison of Eppler 398 airfoil to NACA 4318 airfoil (dimensions in percent chord)

	Eppler 398	NACA 4318
Max Camber (%c)	5.3	4
Location (%c)	46.8	31.5
Max Thickness (%c)	14.2	18
Location (%c)	29.6	29.1

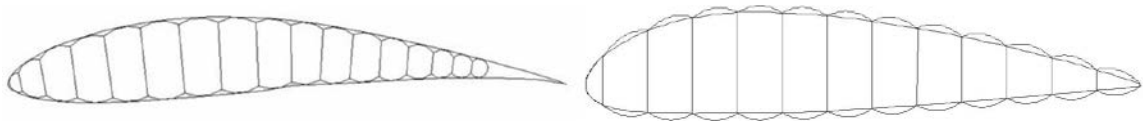


Figure 4.1 *Left)* Eppler 398 airfoil smooth and bumpy shape, *right)* NACA 4318 airfoil smooth and bumpy shape

When considering wind tunnel speeds to test the airfoil, the Reynolds number (Re) range must be determined. The Reynolds number is a dimensionless number that quantifies the ratio between inertial and viscous forces in a fluid. It is calculated by dividing the product of the aircraft's velocity and characteristic length by the kinematic viscosity of the fluid (seen in Equation 4.1). When studying airfoils, the characteristic length used to calculate Re becomes the airfoil chord length, so it can be seen that this term is effected by both the size and speed of the aircraft.

$$\text{Re} \equiv \frac{\rho U_{\infty} c}{\mu} \equiv \frac{U_{\infty} c}{\nu} \quad 4.1$$

Different aircraft will fly in different Re regimes, so the intended use of the aircraft will determine the Re ranges that should be tested. For example, a commercial airliner will fly in the range of $Re = \mathcal{O}(10^7 - 10^9)$, UAVs typically in $Re = \mathcal{O}(10^5 - 10^6)$, and NASA's Mars glider concept in $Re = \mathcal{O}(10^4)$. The wind tunnel testing in this thesis will cover the range $Re = 25,000 - 500,000$ which will encompass the Re predicted for the Mars glider through the Re range of a typical small UAV.

Table 4.2 Test matrix

Re	α sweep
25k	$-7^\circ - 15^\circ$
50k	$-7^\circ - 15^\circ$
100k	$-7^\circ - 15^\circ$
150k	$-7^\circ - 15^\circ$
200k	$-7^\circ - 25^\circ$
250k	$-7^\circ - 25^\circ$
300k	$-7^\circ - 25^\circ$
500k	$-7^\circ - 25^\circ$

In the each of the test runs listed in the test matrix of Table 4.2 the angle of attack, α , was varied in two stages. During the linear portion of the lift curve slope, until $\alpha \approx 9^\circ$, α was incremented by $\Delta\alpha \approx 2^\circ$. Then the increments were shrunk to $\Delta\alpha \approx 1^\circ$ to try and better capture the stall angle and stall pattern. Using the test matrix above 15 measurements per Re at low-Re cases and 25 at the higher Re. With the two different airfoil shapes and three repetitions for statistics, this comes to a total of approximately 960 data points.

4.1 Experimental Methodology

In the wind tunnel tests the pressure distribution over the airfoil was measured. As air passes over an airfoil, the air accelerates over the top surface of the airfoil, creating a region of low pressure on this surface. The air on the bottom surface of the airfoil is moving slower than the air on the top generating a higher pressure region, thus creating a pressure differential across the airfoil. Hence, it is common terminology to refer to the top surface of an airfoil as the suction side because of low pressure sucking up on the airfoil surface, and the bottom surface as the pressure side because of the higher pressure region pushing upward on this surface. This concept is illustrated by Figure 4.2. By integrating over the surface of the airfoil, this difference of pressure can be used to calculate the lift and pressure drag of the airfoil. The equation for calculating the lift coefficient from the pressure distribution is given by Equation 4.2 [65]. It is important to note that the lift coefficient in Equation 4.2 uses C_l , which is the lift coefficient of the airfoil, not C_L the lift coefficient of the wing or C_p the rolling moment coefficient. In this thesis the drag coefficient was determined using the momentum deficit method discussed later.

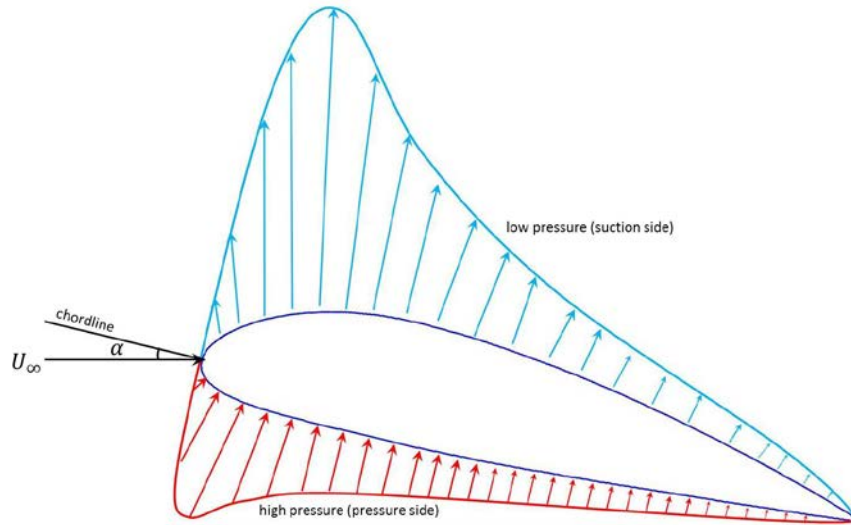


Figure 4.2 Typical pressure distribution over an airfoil

$$C_l = \frac{1}{c} \int \frac{\Delta p}{q} \cos(\alpha) dx + \frac{1}{c} \int \frac{\Delta p}{q} \sin(\alpha) dy \quad 4.2$$

$$C_l = \int C_p \cos(\alpha) dx + \int C_p \sin(\alpha) dy$$

Another standard way to measure the aerodynamic forces is by using a force balance. Here, the pressure distribution was used for lift calculations rather than a force balance for two reasons. The first is that there was not a force balance system readily available for use in this experiment. The second reason is because the pressure measurements provide insight into the fluid interaction with the surface of the airfoils. The regions in between the bumps were of particular interest, so by placing pressure taps on the tops of the bumps and in the valleys between them we could gain insight into what the bumps do to the flow.

Although we do gain more information about the airfoil, measuring the pressure distribution of the airfoil presents several inherent difficulties. The first challenge to overcome was that in order to instrument the airfoil, pressure taps had to be built into the model. This adds complexity and cost to the airfoil model being tested and also limits the available methods of construction. The details of the airfoil model are discussed in Section 4.2.1. Other difficulties arose when selecting pressure transducers, as well as how to perform the measurements. First the transducers had to be able to measure in a range that allowed sufficient resolution and accuracy at lower Re yet be able to measure the pressures that occur at higher Re. The next hurdle was to determine if manual pressure scanning should be used or if a pressure scanner should be built. These factors are discussed in Section 4.2.3. The last difficulty with measuring the pressure distribution over the airfoil surface is that the C_d calculated from the measurements only gives the pressure drag and lacks the drag that is created by the skin friction. Therefore, to get the full value of C_d another method must be used.

In order to calculate the full value of C_d , the momentum deficit method was used. When a uniform velocity profile passes over an object, momentum is transferred to the object

through pressure and viscous effects, creating a wake aft of the object corresponding to a loss of momentum, or a momentum deficit. The velocity of the disturbed air in the wake is thus slower than the air outside of the wake which maintains the original velocity from before the fluid came in contact with the object. This phenomenon is illustrated in Figure 4.3. It is possible to integrate this loss in velocity and calculate the resulting C_d of the object shown by Equation 4.3 [65]. The second form of Equation 4.3 is convenient for the implementation of a Pitot tube rake, as discussed in Section 4.2.2, because Pitot tubes measure dynamic pressure. Using a Pitot tube rake also requires pressure measurements as discussed in Section 4.2.3.

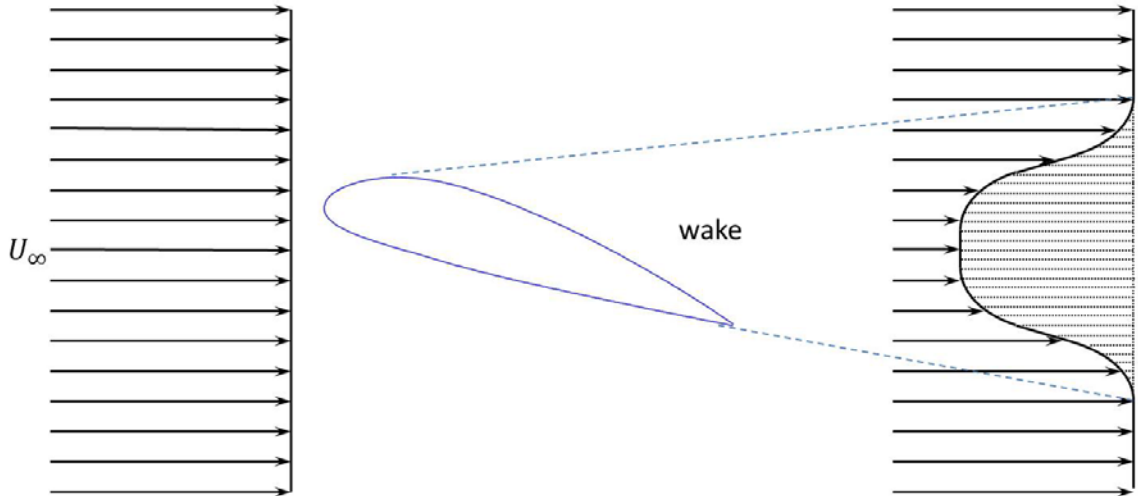


Figure 4.3 Typical velocity profile aft of an object

$$C_d = \frac{2}{c} \int \left(\frac{U}{U_\infty} - \frac{U^2}{U_\infty^2} \right) dy$$

$$C_d = \frac{2}{c} \int \left(\sqrt{\frac{q}{q_\infty}} - \frac{q}{q_\infty} \right) dy \quad 4.3$$

4.2 Experimental Setup

The general experimental setup is illustrated in Figure 4.4. The instrumented airfoil model was placed in the forward portion of the University of Kentucky's low speed wind tunnel's test section. Aft of the airfoil section was the instrumented Pitot tube rake to measure the velocity profile in the wake of the airfoil. The pressure taps in the airfoil and the Pitot tubes in the rake were connected to their own pressure scanner and data acquisition system (DAQ) which was connected to a laptop running programs to collect the resulting data. These sets of data were recorded into text files which could be read by a MATLAB program written to calculate the aerodynamic coefficients.

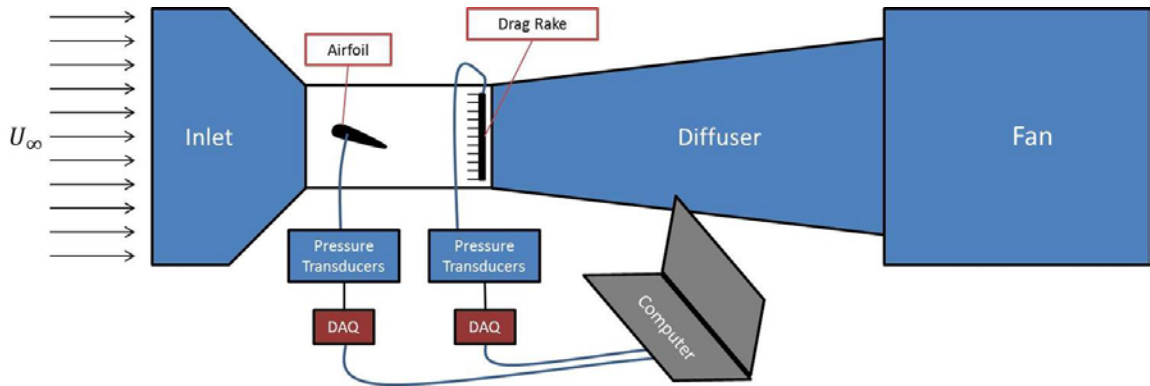


Figure 4.4 Block diagram of experimental set up



Figure 4.5 University of Kentucky low speed wind tunnel

The wind tunnel being used for these experiments is an Engineering Laboratory Design model 406(B). This is an open circuit wind tunnel with a $2' \times 2' \times 4'$ ($0.61m \times 0.61m \times 1.22m$) test section and a 40 Hp ($29.828kW$) motor giving it a speed range of up to $\sim 150 \text{ fps}$ ($\sim 45 \text{ m/s}$). This wind tunnel provided a wide range of testable Re . The details of the other portions of the experiment are given in the following sections.

4.2.1 Airfoil Models

There were two airfoil models used in this experiment, each with the same chord length and span. The first model was of the smooth NACA 4318 shape, and the second was the inflatable NACA 4318. The smooth airfoil was used to validate the testing procedure since it could be compared to previously published data. Since the wind tunnel walls had a fixed dimension of $24''$ ($0.61m$) the model span had to be sized so that it could be placed inside the tunnel which created the potential for the appearance of 3D effects on the airfoil surface. In order to ensure 2D airfoil results from the wind tunnel tests, all 3D effects must be eliminated,

and to do this the model must simulate an infinite span. Traditionally this is done by having the model span the entire width of tunnel. If the model does not span the width of the tunnel tip vortices will form which are the source of the 3D effects, unless these vortices are properly mitigated.

The chord length of the model was sized so that the desired Re range could be achieved with the available wind tunnel speeds. With the $U_{\infty,max} \approx 150fps$ ($45 m/s$) and using Equation 4.1 with a desired $Re_{max} \approx 500,000$, the airfoil chord length was calculated to be $\sim 6.8"$ ($0.17m$). The final chord length was set to $8"$ ($0.2m$) to allow the max Re to occur at less than the tunnel's top speed to help prevent damaging the wind tunnel, and also gave more internal area for routing the pressure lines. The final span was then set to $22.5"$ ($0.57 m$) to allow for tunnel clearance and it was decided that end plates would be added to negate the 3D effects of the finite geometry. Figure 4.6 shows the model's geometry as well as its placement in the wind tunnel.

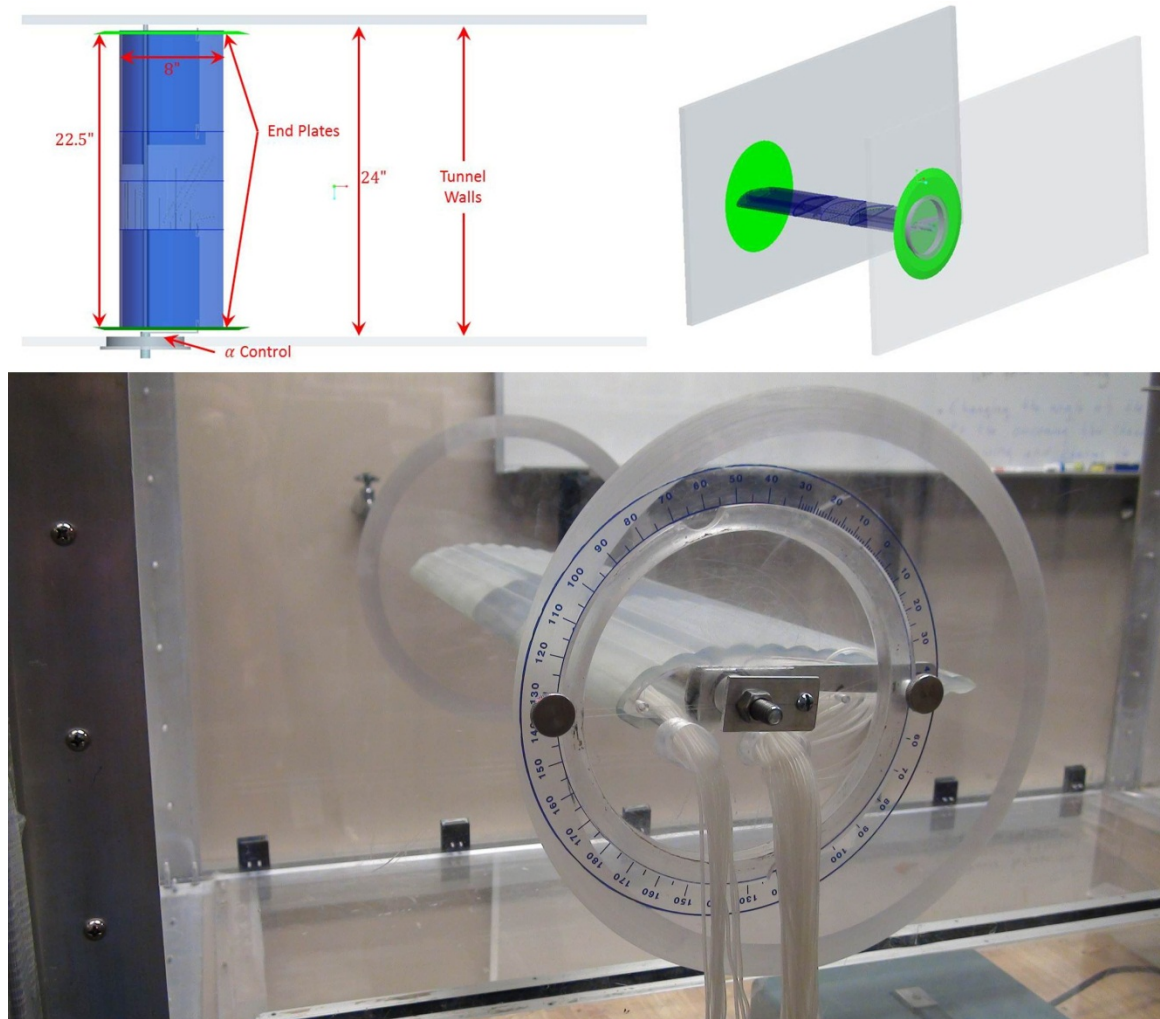


Figure 4.6 Model dimensions and wind tunnel clearances

Once the model had been sized, its construction method was determined. Due to the complexity of this measurement technique very few construction methods were viable. In order to measure the pressure on the surface of the airfoil pressure lines were built into the model. Adding these lines to an existing part is extremely difficult especially when considering the accuracy needed to reduce errors in the readings. Therefore, only construction techniques allowing for internally integrated features were considered. This limited the decision to direct metal laser sintering (DMLS), 3D printing, and stereo lithography (SLA). In each of these techniques the part is built up in layers of material which allows for internal geometry to be built into the part. In DMLS a fine metal powder is spread in thin layers and melted using a laser, and similarly SLA uses an ultra violet (UV) laser to cure a UV-hardening resin in layers. 3D printing melts plastic through a nozzle and builds the part in layers. Table 4.3 lists the benefits and drawbacks of the three techniques. Ultimately SLA was chosen as the desired construction technique.

Table 4.3 Construction technique pros and cons

Method	Pros	Cons
DMLS	<ul style="list-style-type: none"> - Excellent Precision - Great surface finish - Limited geometric constraints 	<ul style="list-style-type: none"> - Expensive - Post machining is extensive to achieve desired surface finish and also costly - Technology not available at UK
3D Printing	<ul style="list-style-type: none"> - Inexpensive - Technology available at UK 	<ul style="list-style-type: none"> - Poor surface finish - Extensive manual post processing to achieve desired surface finish - Geometric constraints for the part
SLA	<ul style="list-style-type: none"> - Technology available at UK - Better surface finish than 3D printing - Only moderate post processing required - Less costly than DMLS - Limited geometric constraints 	<ul style="list-style-type: none"> - More expensive than 3D printing - Required post processing is manual

To build a part using SLA first a detailed solid model of the part was created, and these models were generated using the computer aided drafting (CAD) package ProEngineer Wildfire 4 (ProE). The wind tunnel models would need to be built in three separate sections due to restrictions on the size of the SLA machine, and to reduce the build time and reduce the cost of the models. Thus the overall solid model was split into three sections: two hollow outer sections, and one semi-solid middle section containing the pressure taps and lines. The center section was considered to be the test section of the model. Figure 4.7 shows an example of the test section solid model built in ProE, and Figure 4.8 shows the finished SLA parts. The post processing mentioned in Table 4.3 included joining the three sections, inserting the tubing to connect the pressure transducers, adding a support rod (also used for mounting), and sanding the model smooth.

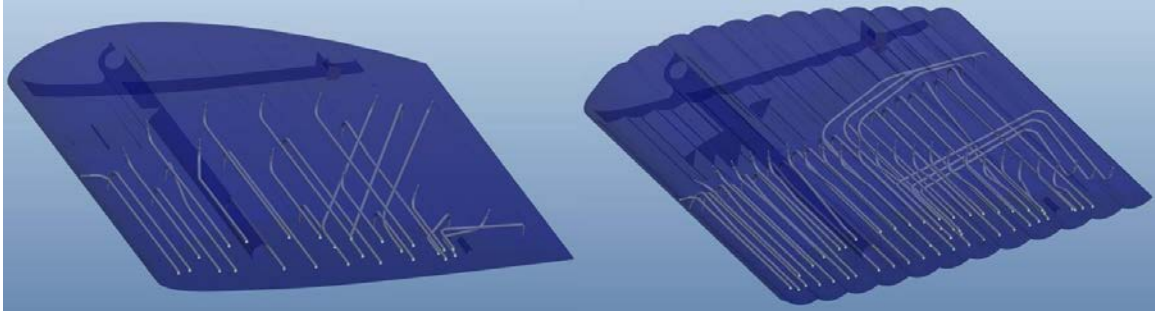


Figure 4.7 Airfoil wing section ProE models *left*) smooth profile with 25 taps, *right*) bumpy profile with 49 taps

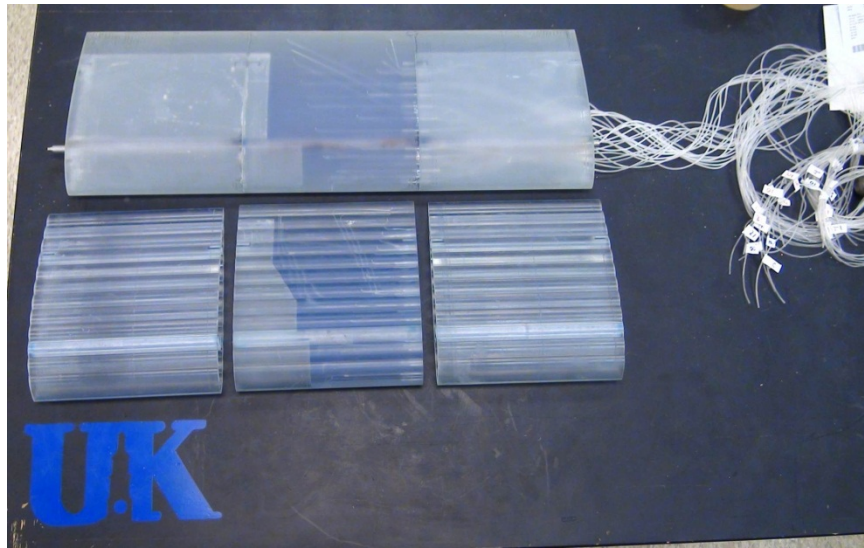


Figure 4.8 Finished SLA wing sections with fully assembled model

The pressure taps built into the airfoil were designed to minimize the potential for errors in the pressure measurements. The design for these taps used the guidelines provided in Tavoularis [66]. The taps should have a circular cross section with the ratio of tap depth (ℓ) to tap diameter (d) $5 \leq \ell/d \leq 15$, and be oriented perpendicular to the surface to within 15° . Figure 4.9 illustrates the geometry of the pressure taps and the lines that the tubing to the transducers will connect to. As seen in Figure 4.9 the $\ell/d = 5$, which fell into the appropriate range for minimizing errors but allowed for the best use of limited space in the model. Figure 4.9 also shows that each airfoil model has an array of pressure taps on both the top and bottom surfaces. The smooth airfoil has a total of 25 taps: 1 leading edge tap, 12 top surface taps, and 12 bottom surface taps. This number of taps was selected guided by another successful airfoil model from a previous project with an identical chord length. The bumpy airfoil had 49 taps: 1 leading edge tap, 24 top surface taps, and 24 bottom surface taps. The 24 taps on both the top and bottom surfaces are split up into 12 taps on the top of each bump, and 12 in the valleys between the bumps. Table 4.4 summarizes the specifications of the taps for each airfoil.

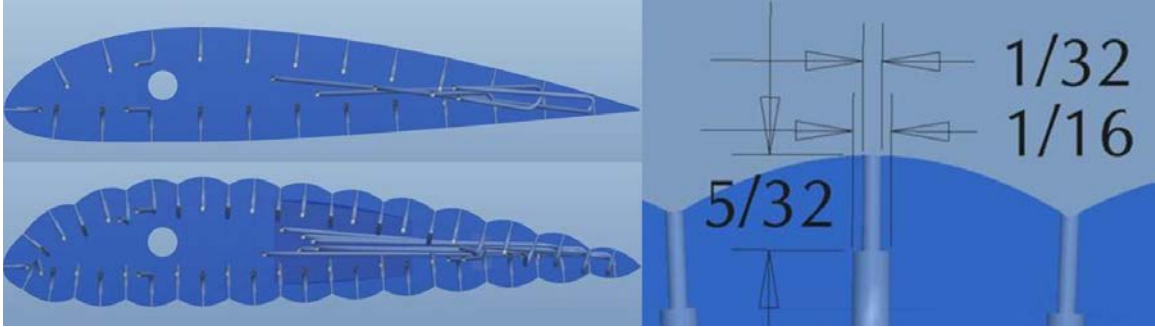


Figure 4.9 *Top left*) side view of smooth airfoil, *bot left*) Side view of bumpy airfoil, *right*) pressure tap geometry (dimensions in inches)

Table 4.4 Pressure tap specifications for the smooth and bumpy airfoils

	Smooth	Bumpy
Cross section	Circular	
ℓ	5/32" (3.96875 mm)	
d	1/32" (0.79375 mm)	
Number of taps	25	49
Top surface taps	12	24
Bottom surface taps	12	24

Each array of taps was raked at an angle from the centerline. This was done for two reasons: 1) it allowed better use of the internal space for routing the pressure lines, and 2) it minimized the possibilities of disturbances from forward taps affecting aft taps. These rakes also allowed for the ability to measure any 3D effects occurring on the model. This was done by using two different rake angles, and then alternating which rake the tap occurs on. This can be seen in the left picture of Figure 4.10. If there were strong 3D effects happening on the model, there would be a measurable difference in the pressure distribution as you moved out from the centerline. The pressure distribution for the smooth airfoil should be smooth, so if bumps in the pressure distribution were noticed, the presence of 3D effects would be noticed and need to be dealt with. The alternating tap locations were only on the smooth airfoil since the setup for both models was the same, if the effects were negated on the smooth airfoil they should be negated on the bumpy airfoil. On the bumpy airfoil the top and bottom tap arrays followed individual rakes, but these rakes were still angled as seen in the right side of Figure 4.10. Following the same rake on each surface allows for better quantification of the effect of the bumps on the surface.

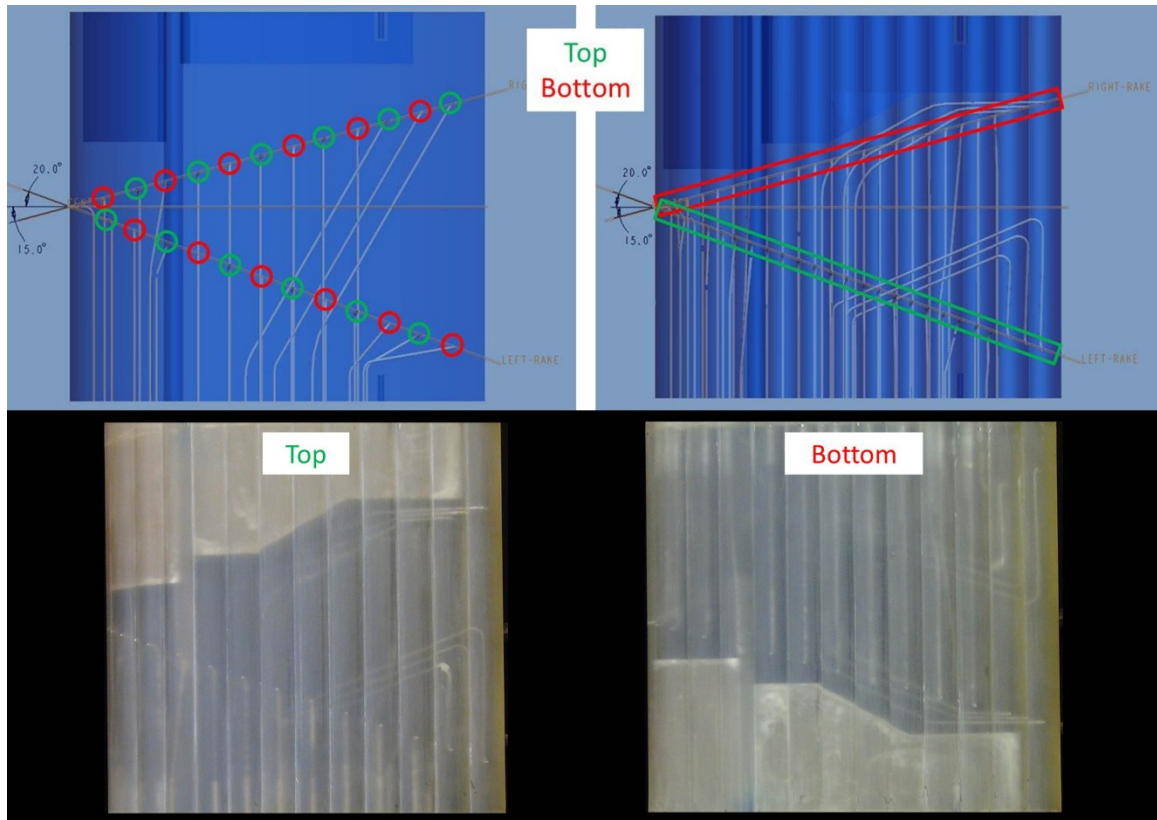


Figure 4.10 Pressure rake geometry and orientation *top left*) smooth profile, *top right*) bumpy profile, *bot*) SLA test section with internal pressure lines

As mentioned earlier, end plates were added to the model as a means to negate the potential 3D effects that occur on the model. Since the model could not span the width of the tunnel, tip vortices would form around the ends of the model causing it to behave as a finite span wing. Adding the end plates displaces these vortices so that the model will simulate an “infinite span” wing thus giving an effective 2D airfoil pressure distribution at the center of the airfoil. For the testing in this thesis circular end plates were used with chamfered edges to minimize the thickness of the boundary layer forming on the plates. The dimensions of the plates can be seen in Figure 4.11.

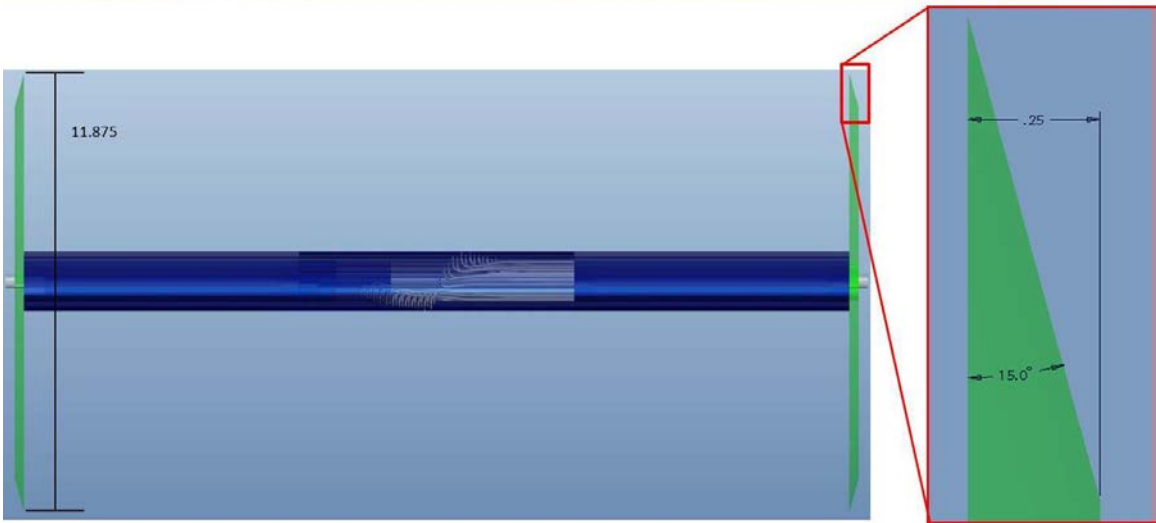
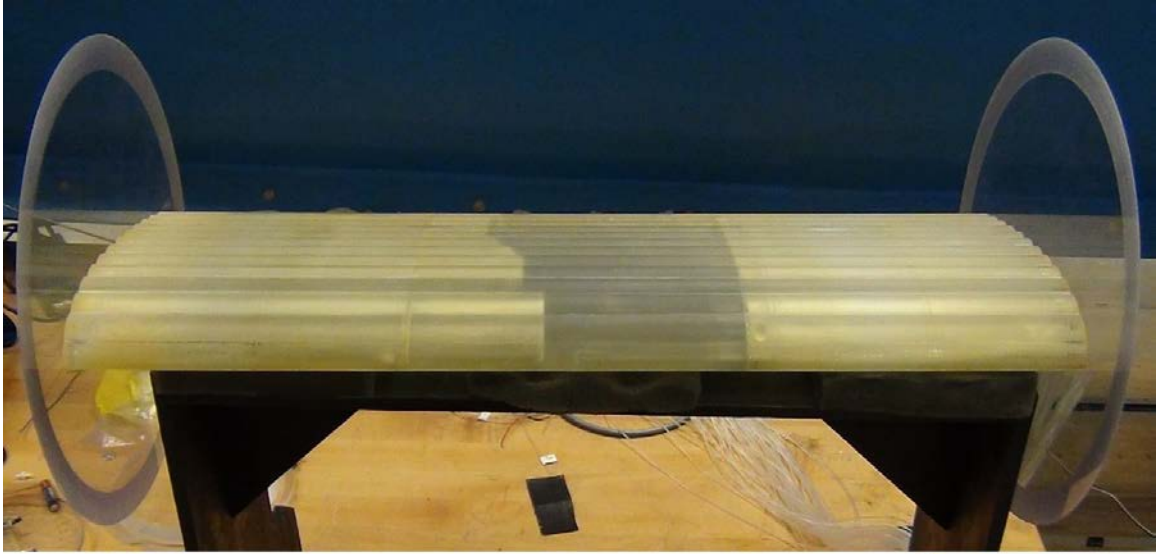


Figure 4.11 End plate geometry (dimensions in inches)

4.2.2 Drag Rake

A 16 Pitot tube wake rake system was used to measure the drag force of the airfoil. A wake rake is a series of Pitot tubes arranged such that it can measure the velocity profile downstream of the model. To get the best possible results from these measurements, the velocity profile was measured in three locations along the span of the model: the midpoint and at the edge of each top and bottom surface tap rake, as shown in Figure 4.12. The results were then averaged to calculate the C_{d} . In order to perform these measurements along the span of the model, the rake was built on a single axis traverse allowing precise movements in the span direction. Using the multiple spanwise locations to measure the wake also provided another means to identify any 3D effects in the measurements, because these effects would cause a significant change in the wake profile between the three locations. The rake was then positioned 2.5 chord lengths aft of the airfoil to allow the wake enough development length that the static pressure within the wake could be assumed constant and streamlines approximately parallel to the tunnel walls.

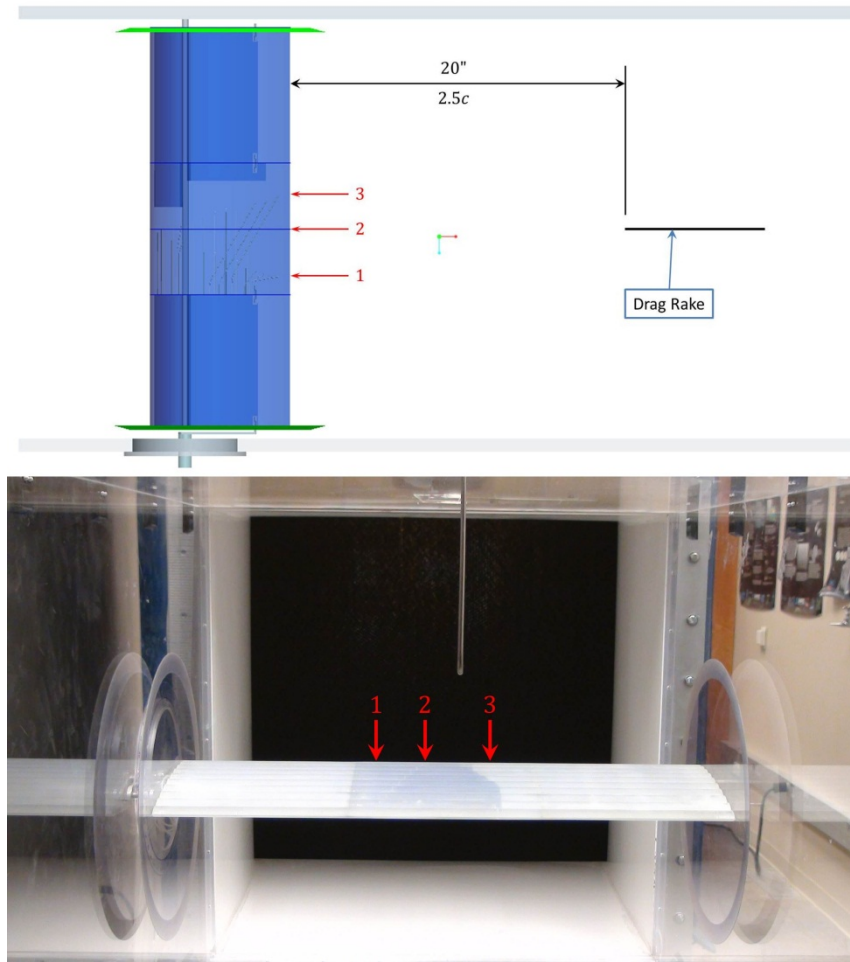


Figure 4.12 Wake measurement locations

The Pitot tubes used for the rake were designed and positioned on the rake to minimize the interruption to the flow yet still cover a wide enough spatial range to measure the entire wake and a portion of the undisturbed flow. To support the Pitot tubes a $1/4 \times 2$ ($6.35\text{mm} \times 50.8\text{mm}$) aluminum bar was suspended into the flow from the top plate of the wind tunnel test section. The tubes were then mounted to the side of the bar parallel to the flow as illustrated in Figure 4.13. To minimize interference from the support bar the tubes were required to extend a minimum of 5 times the cross sectional width of the fixture, which required a minimum tube length of 1.25" (31.75mm) be extended into the flow. Since the tube holders added width and the tubing to transmit the pressure to the transducers were exposed, it was necessary to ensure that all upstream effects of these were avoided. To do this, the length of the tubes were extended to 6" (0.15m).

The Pitot tubes were made of small diameter aluminum tubing fashioned together using JB Weld. The opening at the front of the tube used $1/32$ " (0.79mm) tubing, which was sleeved with $1/16$ " (1.59mm) tubing to add rigidity while maintaining minimal effect on the flow. Lastly, since all Pitot tubes measure total pressure only, a small Pitot-static tube was added to

the tunnel such that the static pressure directly in line with the tips of the rake's Pitot tubes could be measured by the Pitot-static tube's static pressure ports. This Pitot-static tube then provided the reference pressure for both the airfoil model as well as the drag rake. All of these features are illustrated in Figure 4.13 and Figure 4.14.

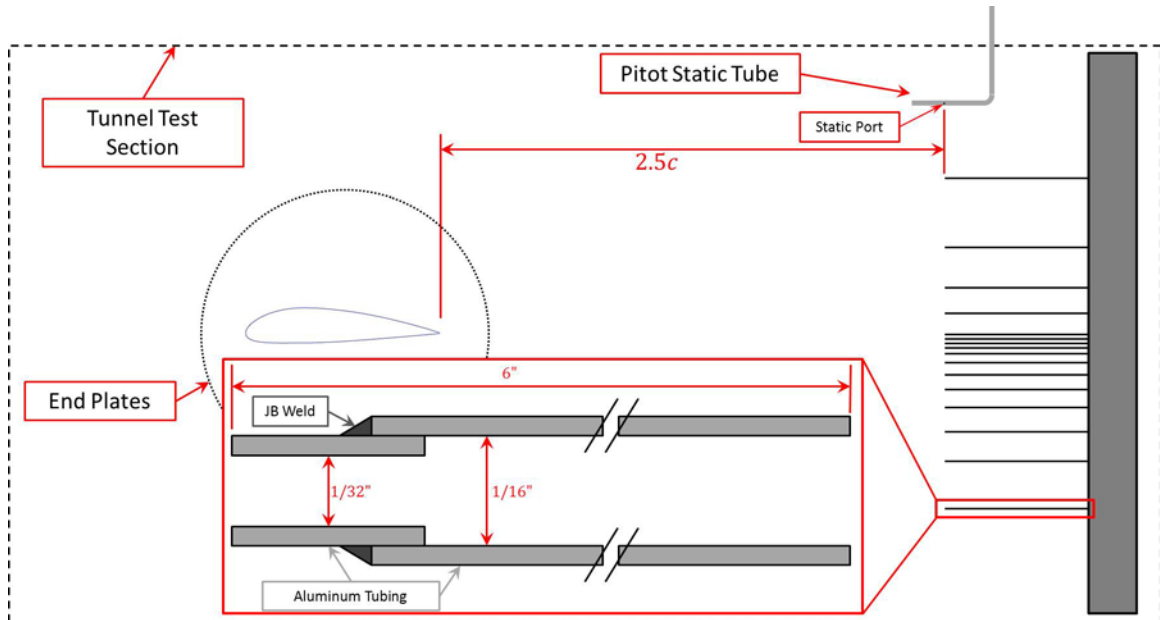


Figure 4.13 Drag rake and Pitot tube configuration

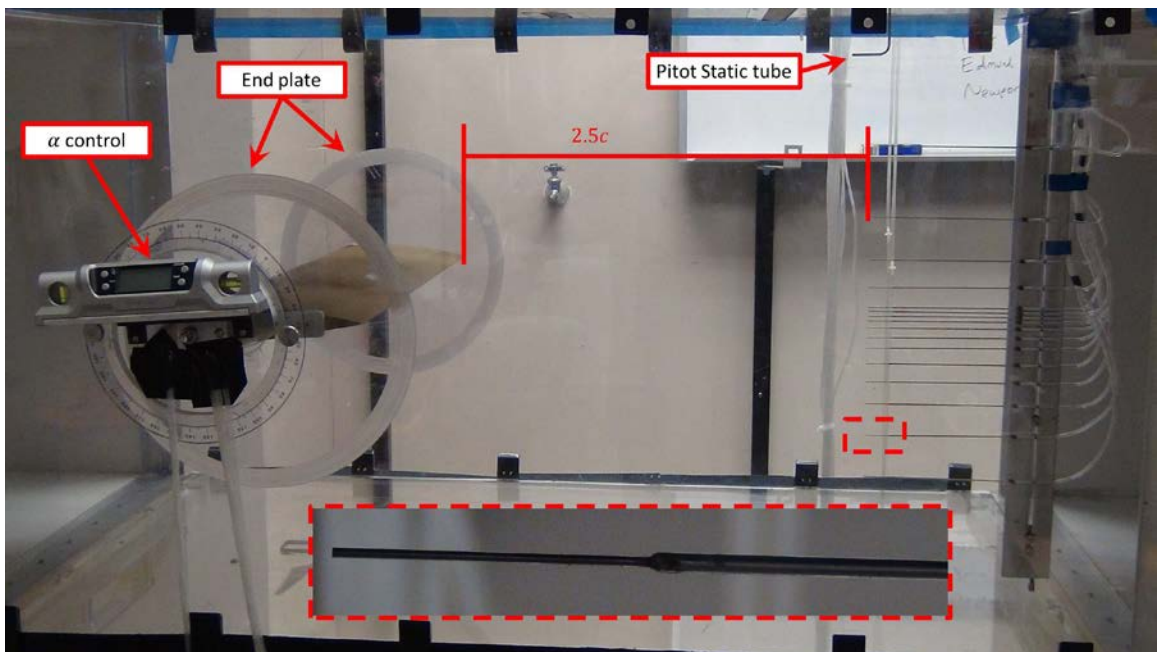


Figure 4.14 Wind tunnel test section setup

In this rake there are 16 fixed tubes positioned on the support bar. In some wind tunnel tests that use the momentum deficit method, a 2-axis traverse is used so that a single Pitot tube is run through the entire velocity profile so that measurements are made at many vertical

stations, and at some span wise stations. In these cases the system is usually automated. Even so, the process is prohibitively time consuming. For example, taking only 20 seconds of data at 20 vertical locations in the flow would take a total of 6.67 minutes per span location, and with 3 span locations this would take 20 minutes for each α . Without an automated traverse system, manually performing is not a practical option.

For the testing in this thesis, stationary Pitot tubes were used for two reasons: 1) the stationary setup gave a more instantaneous view of what is happening in the wake, and 2) it significantly reduced testing time. It allowed for the ability to take 45 seconds of data at each of the span locations for a total of 2.25 minutes per α . This also allowed for more data to be included in the averaging, giving better statistical convergence and improving the estimation of the mean values. In order to measure the small velocity drops in the wake, highly sensitive pressure transducers are needed. This thesis used a 16-channel pressure scanner equipped with sufficiently sensitive transducers to measure the small velocity fluctuations in the wake (details of the scanner are found in Section 4.2.3). Therefore, 16 Pitot tubes were used in the rake.

The tubes then had to be arranged in a configuration which best captured the wake of the airfoil, which was determined using a series of preliminary tests. The top and bottom tubes in the array (as seen in Figure 4.13) were placed so that they would remain in the undisturbed flow. These two points gave the uniform velocity reference from which to integrate the velocity losses, U_∞ in Equation 4.3. It can also be seen that there is a tight group of tubes just below the centerline of the tunnel. This was done to capture the small wake changes at small α . This cluster was placed below the centerline at a location determined during preliminary testing to correspond to the mean wake centerline because even at $\alpha = 0^\circ$ the downwash created by the airfoil displaces the wake downward, and as you increase α the wake translates downward. Because of this fact more tubes were concentrated below the airfoil. The tubes in the upper half of the rake primarily capture the widening of the wake as the airfoil approaches stall due to flow separation. The spacing for the remaining tubes was incrementally increased outward from the center grouping. Table 4.5 shows the spacing used for the tubes in the rake.

Table 4.5 Pitot-tube locations from top of the test section

Tube #	Location
1	5.5 in (13.97 mm)
2	8.38 in (21.27 mm)
3	10.06 in (25.56 mm)
4	11.13 in (28.26 mm)
5	12 in (30.48 mm)
6	12.19 in (30.96 mm)
7	12.38 in (31.43 mm)
8	12.56 in (31.91 mm)
9	12.81 in (32.54 mm)
10	13.19 in (33.5 mm)
11	13.69 in (34.77 mm)
12	14.31 in (36.35 mm)
13	15.06 in (38.26 mm)
14	16.06 in (40.8 mm)
15	17.31 in (43.97 mm)
16	19.25 in (48.9 mm)

4.2.3 Pressure Measurement

Since there are 49 pressure taps on the bumpy airfoil model it was decided that a pressure scanner needed to be developed to measure the surface pressures simultaneously. A 50 channel pressure scanner was then built using $\pm 0.3 \text{ psi}$ ($\pm 2 \text{ kPa}$) transducers made by Freescale Semiconductor (MPXV7002DP). These transducers were relatively inexpensive, readily available, and maintained sufficient sensitivity and accuracy to reliably measure the pressures during the test. The transducers have an output accuracy of $\pm 2.5\%$ full scale span (FSS). Then in order to read the 50 output signals, two National Instruments NI-9205 DAQs, each with 32-channels, were used giving a total of 64 available channels. These DAQs have 16 bit resolution and a sample rate of up to 250 kHz. During the $Re = 500,000$ test the pressures at some locations on the airfoil were too low for the transducers to read. In these cases the transducers were replaced with $\pm 1 \text{ psi}$ ($\pm 6.895 \text{ kPa}$) transducers from Honeywell (SSCDRRN001PDAA5), which have total error band of $\pm 2\%$ FSS. During all tests the airfoil pressures were sampled at 1000 Hz for 45 seconds and then time averaged, and repeated 3 times. The properties were then calculated for the three runs and averaged to produce the results for this thesis.

A 16-channel pressure scanner was used for the wake pressure measurements. This Scanner used $0 - 4 \text{ inH}_2\text{O}$ ($0 - .995 \text{ kPa}$) transducers from All Sensors (4INCH-D-CGRADE-MV), with an accuracy of $\pm 1\%$ FSS. These transducers output signal amplitude was on the

order of millivolts, so to better measure the signal it was amplified using $100 \times$ amplifier from Texas Instruments (INA131BP). These amplifiers have a maximum of $\pm 0.024\%$ error in the gain value. Therefore, the resulting maximum possible error of the system was $\pm 0.040096 \text{ inH}_2\text{O}$ ($\pm 0.009987 \text{ kPa}$). These voltage outputs were read by a Measurement computing USB-1608G DAQ with 16 bit resolution and a sample rate of 250 kHz . During the testing total pressure measured at each Pitot tube was sampled for 45 seconds at a rate of 2000 Hz and then time averaged at the three spanwise locations. The higher sample rate was used because the transducers were susceptible to noise due to their sensitivity, so the increased sampling rate added more points to average out any possible noise. The drag results were calculated for each span location and averaged to produce the results for this thesis.

Before each run of the experiment, a zero measurement was taken and recorded. This zero was performed with the wind tunnel off in ambient conditions. This zero measurement was then subtracted from the pressure measurements for each run. This removed the potential for zero drift between each run.

4.3 Results

4.3.1 Smooth Airfoil Results

During the course of the experiment, not all of the results were ideal. Of all the available data, the pressure distribution results for the $Re = 25k$ case were the most susceptible to errors. At this Re , on the majority of the airfoil, and in the drag rake the pressures being measured were near or below the accuracy of the transducers, especially at low angles of attack when the airfoil does not produce much lift. An example pressure distribution from this case is shown in Figure 4.15 along with a more typical pressure distribution measured at a higher Re . Figure 4.15 shows the pressure distributions recorded during each of the three repetitions at the given α . It can be seen from this figure that there was a large amount of experimental scatter in the pressure during the lowest Re tests, but at the other Re the pressures were much more consistent due to the higher static pressures being measured.

The difference between the minimum and maximum C_p for the $Re = 25k$ was $\Delta C_p \approx 1.5$. At this Re this represents a pressure range of approximately $\Delta P \approx 4 \text{ Pa}$ (0.001 psi). This pressure range was only $0.1\% \text{ FSS}$, which is smaller than the accuracy of the transducers, which was $2.5\% \text{ FSS}$. Conversely, in the $Re = 250k$ case, the C_p range increased to $\Delta C_p \approx 2.5$, which translated to $\Delta P \approx 700 \text{ Pa}$ (0.102 psi) or $18\% \text{ FSS}$. Although, the irregularities in the $Re = 25k$ pressure distribution, shown in Figure 4.15, could be indications of small detachment and recirculation regions due to a low energy boundary layer, this cannot be confirmed without further testing. Therefore, it should be noted that although the $Re = 25k$ data is still included in the results, it will be left out of the discussion due to the potential for errors. This should be considered when using the data for $Re = 25k$.

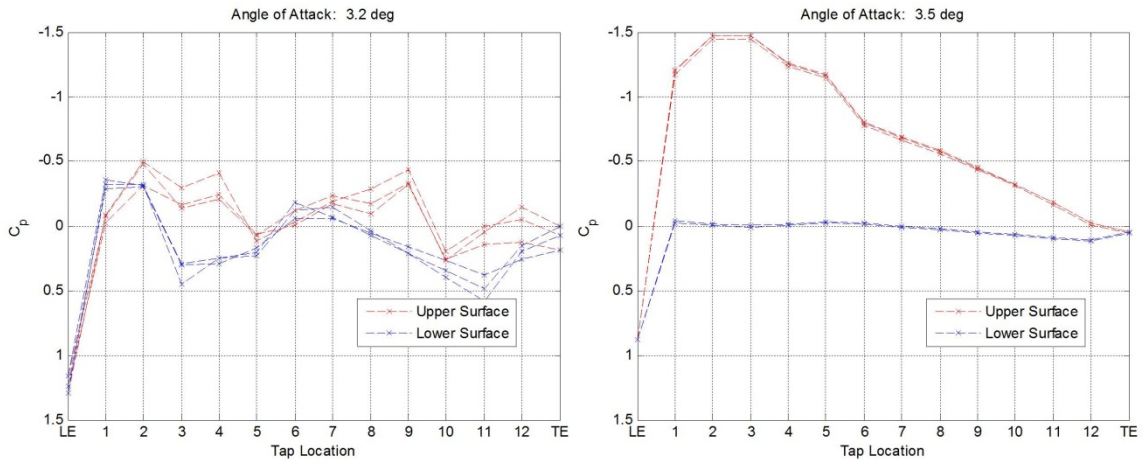


Figure 4.15 *Left*) worst case data: $Re = 25k, \alpha = 3.2^\circ$, *right*) typical data: $Re = 250k, \alpha = 3.5^\circ$

The test setup was validated by comparing the results from the smooth airfoil to the data from the published by NACA in a technical report [67]. The initial results from these comparisons indicated that the drag rake position allowed sufficient length for the transverse pressure gradients in the wake to decay since the drag polars showed good agreement with the published results. However, they also indicated that the 25 taps on the smooth airfoil did not provide sufficient resolution around the leading edge of the model. This was made apparent by a reduction in the lift curve slope as well as reduced maximum lift as shown in Figure 4.16. The lack of resolution also changed the zero lift angle of attack. Blockage was first thought to be the origin of the problem. However, once blockage corrections (Barlow, Rae, and Pope [65]) were applied, they were found to have negligible effect on the results.

The problem was resolved by implementing a cubic interpolation scheme to interpolate between the data points of the leading edge and first three taps on both the top and bottom surfaces of the airfoil, as shown in the plots of the pressure coefficient (C_p) distributions in Figure 4.16. A polynomial interpolation scheme was used for simplicity, using cubic interpolation as it was the lowest order polynomial which would capture the multiple inflection points needed. The result of this interpolation is also shown in Figure 4.16. After the interpolation good agreement was realized in the lift curve slope with this Re case so it was applied to the other cases with similar results without further modification. However, there was still some disagreement in the stall behavior of the model near the maximum lift coefficient, but this is believed to be due a combination of Re effects and a difference in surface roughness between SLA model and the polished steel used in the NACA report.

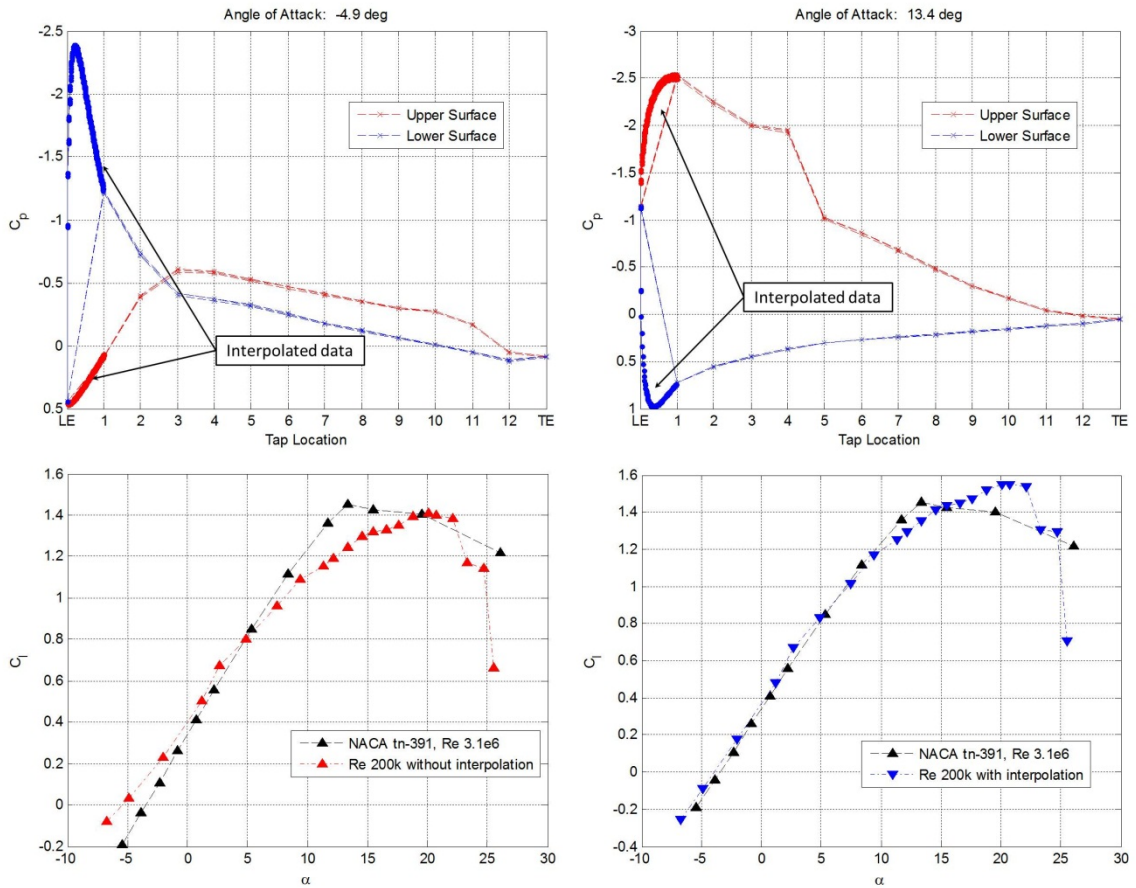


Figure 4.16 *Top Left*) low α C_p distribution with interpolation, *top right*) high α C_p distribution with interpolation, *bot left*) lift curve without interpolation, and *bot right*) lift curve with interpolation.

Once this post processing was added to the measured pressure distributions, the smooth airfoil testing regime was started as described in Table 4.2. Figure 4.17 shows a summary of the results of the smooth airfoil testing. The detailed results can be seen in Appendix A.

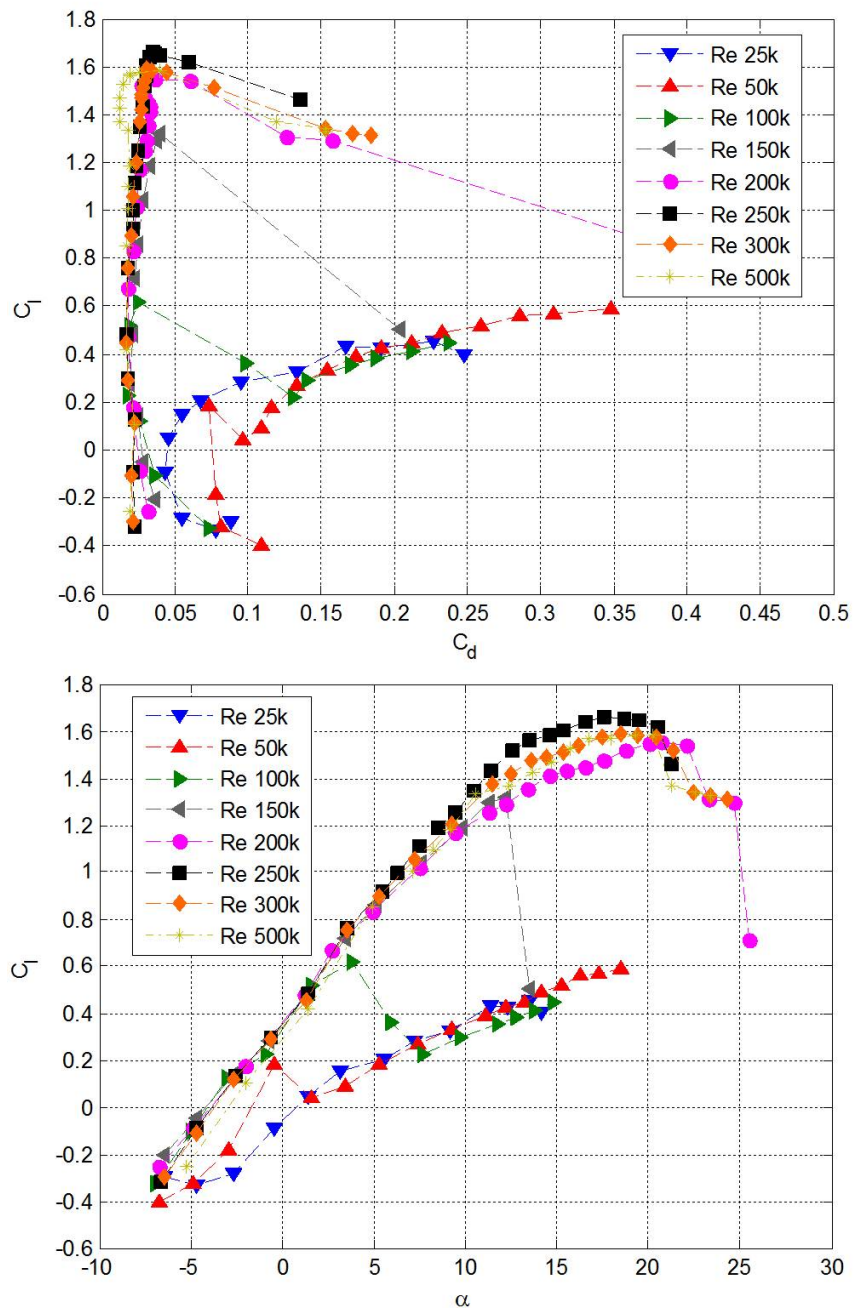


Figure 4.17 *Top*) drag polars and *bot*) lift curves for the smooth NACA 4318 airfoil

It can be seen in Figure 4.17 that there is a strong Re dependence in the smooth airfoil aerodynamic coefficients. It should be noted that as the Re is increased from $Re = 50k$ to $Re = 150k$ there is a drastic increase in airfoil performance. The drag polars rapidly collapse (starting at $Re = 100k$) and the maximum lift coefficient increases significantly between each Re case. Starting with $Re = 200k$ the lift curves begin to collapse and the Re effects begin to be reduced. It is also interesting to note that at the $Re \leq 150k$ the stall pattern is a sudden severe drop off of lift whereas for $Re > 150k$ it is much more gradual.

To verify these trends the same test cases were simulated in a computer program called XFOIL [25, 26]. This program is also written by Mark Drela and has gained popularity in UAV design because of its simplicity and accuracy. XFOIL is also used during the modeling process for the Piccolo autopilot system. XFOIL is a low Reynolds number aerodynamics calculator used to predict the aerodynamic characteristics of 2D airfoils. The airfoil shapes are imported as a series of points, which break the airfoil down into a collection of “panels.” The flow is solved on each of these panels to accurately and quickly calculate the pressure distribution and aerodynamic properties, and also predicts transition to turbulence and flow separation. Turbulence transition is predicted using an e^N calculation method where the eigenvalues of the Orr-Sommerfeld equation are solved on each panel and when they have grown to e^N times the original value the flow is considered to have transitioned to turbulence.

Figure 4.18 shows the results of this simulated test regime with the value of N set to be 9, which is a standard procedure. It can be observed that both the XFOIL simulations and the smooth airfoil test results demonstrate the same trends in Re dependence, which added confidence to our experimental results. The biggest discrepancy can be found in the $Re = 100k$ and $150k$ run cases. This is most likely due to the simplified XFOIL flow model not fully capturing transition of significance of the viscous effects going from low- Re to higher Re . at low- Re the viscous effects of the fluid are much more significant than at higher Re .

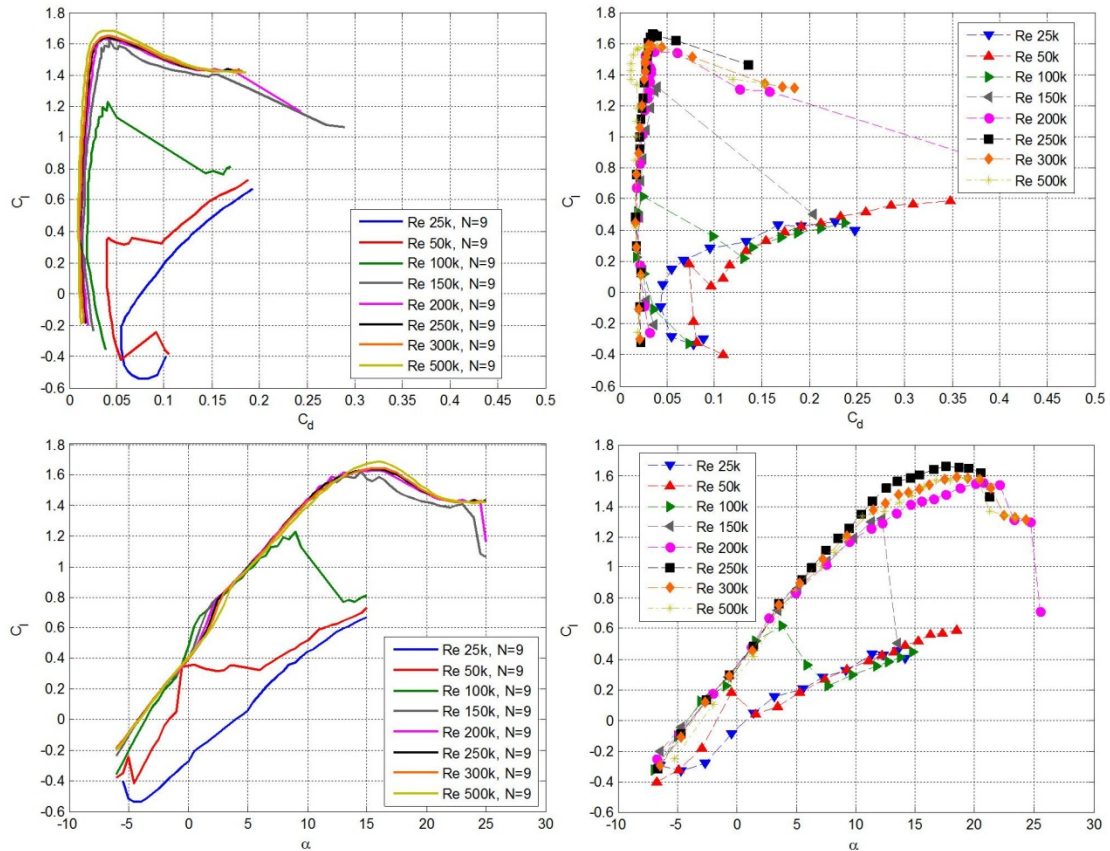


Figure 4.18 *Top left)* drag polars from XFOIL, *top right)* drag polars from experiment, *bot left)* lift curves from XFOIL, and *bot right)* lift curves from experiment.

4.3.2 Bumpy Airfoil Results

After all of the smooth airfoil testing was completed, the bumpy airfoil was tested to compare its aerodynamic properties to those of the smooth airfoil. The first point of interest in the data was the modification made to the pressure distribution due to the presence of the bumps. An example measured pressure distribution is shown in Figure 4.19. It can be seen that bumps have a significant effect on the pressure distribution of the airfoil. Because of the bumps, local surface pressure oscillations form – indicated by the peaks and the valleys of the pressure distribution. These pressure oscillations are due to the formation of localized separation, reattachment, and recirculation regions between the bumps. As α is increased it is easily seen where the flow has detached from the airfoil’s surface because, the C_p values form a smooth curve instead of indicating the presence of the bumps (shown in the low α plot of Figure 4.19). The detachment of the flow from the airfoil surface removes the local separation and reattachment zones, hence creating a smooth pressure across the entire detached region of the surface.

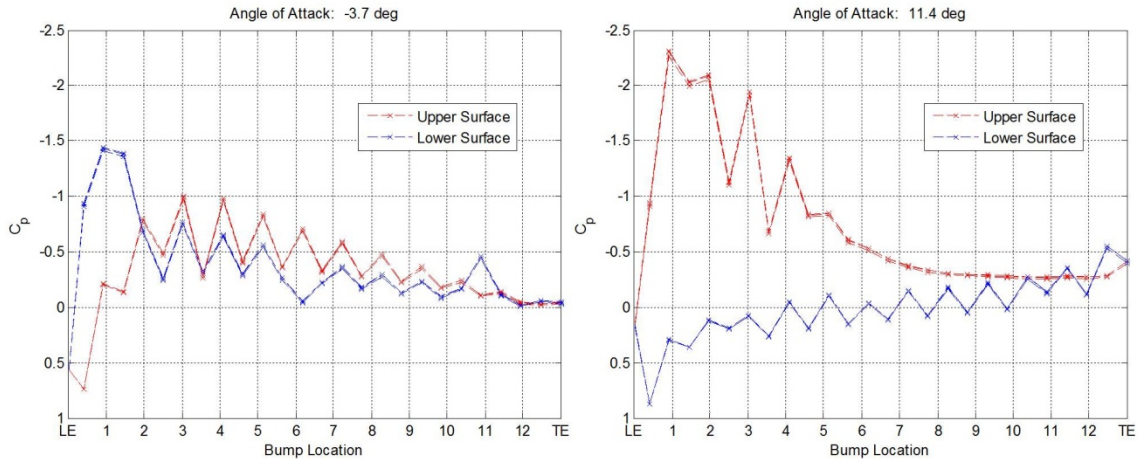


Figure 4.19 *Left*) low α pressure distribution, *right*) high α pressure distribution $Re = 250k$

Once these initial observations were made, the aerodynamic properties were calculated to quantify the effect of the bumps on the airfoil. Figure 4.20 and Figure 4.21 summarize the results of these calculations. As in the smooth airfoil case, the $Re = 25k$ case is subject to potential errors because of the low pressures being measured, so it will be excluded from discussion though it is presented in the results.

The delay in flow separation observed in previous work gave confidence that the $2.5c$ distance between the trailing edge and the drag rake would provide enough distance for the wake to develop. The delay in separation meant the wake should be “smaller” than that of the smooth airfoil at the same angle of attack. Given that the smooth airfoil’s wake results matched the published results with good agreement, and that its wider wake was more likely to not be fully developed, it was felt that the rake measurement location did not need to be adjusted for the bumpy airfoil testing.

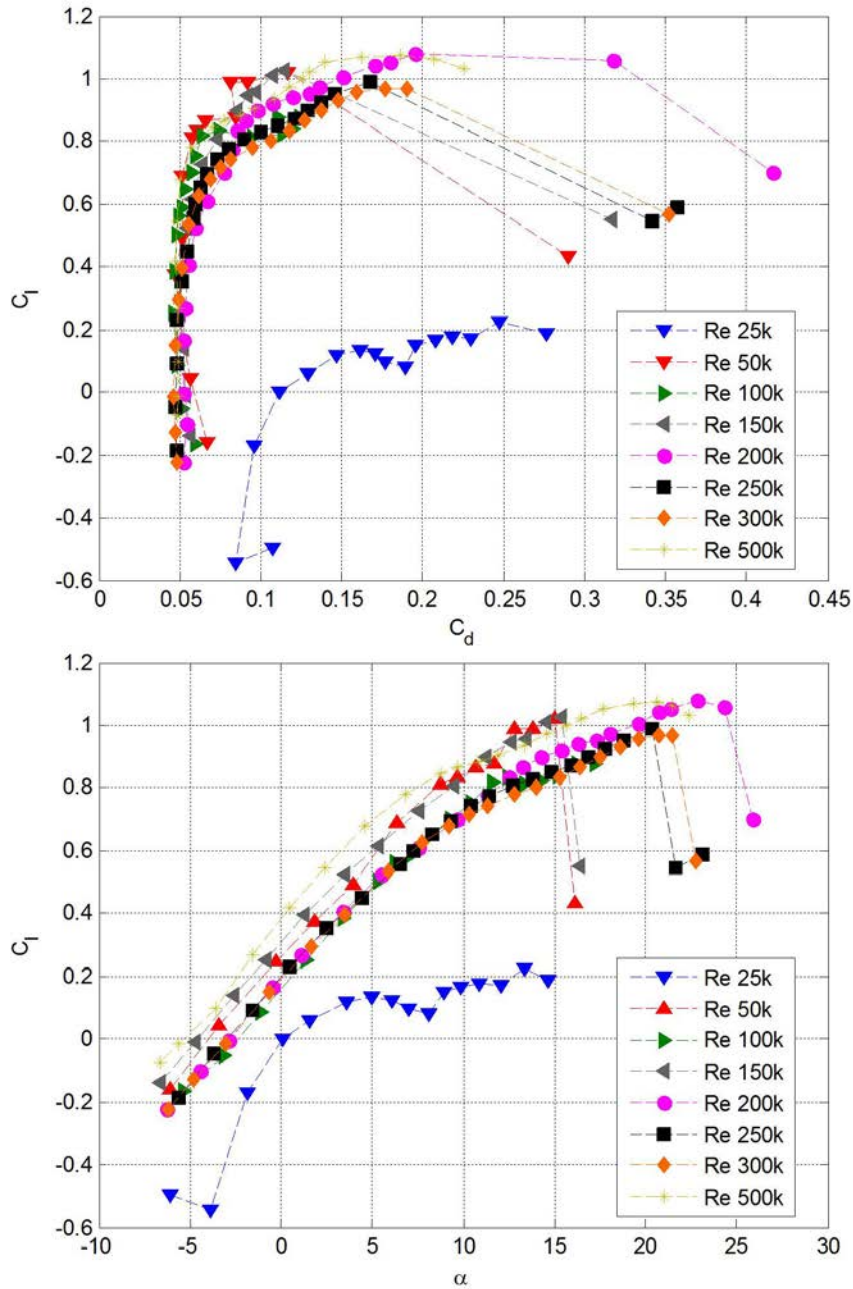


Figure 4.20 *Top*) drag polars and *bot*) lift curves for the bumpy NACA 4318 airfoil

From these results it appears that at $Re = 50k - 150k$ the presence of the bumps delays stall and increases the maximum lift (except in the $Re = 150k$ case where max lift is decreased). It can also be noticed that in all cases the lift curve slope was reduced from that of the smooth airfoil's lift curve slopes. The $Re = 50k$ case also indicates a reduction induced drag. All other cases demonstrated approximately double the drag of the smooth airfoil at the same Re.

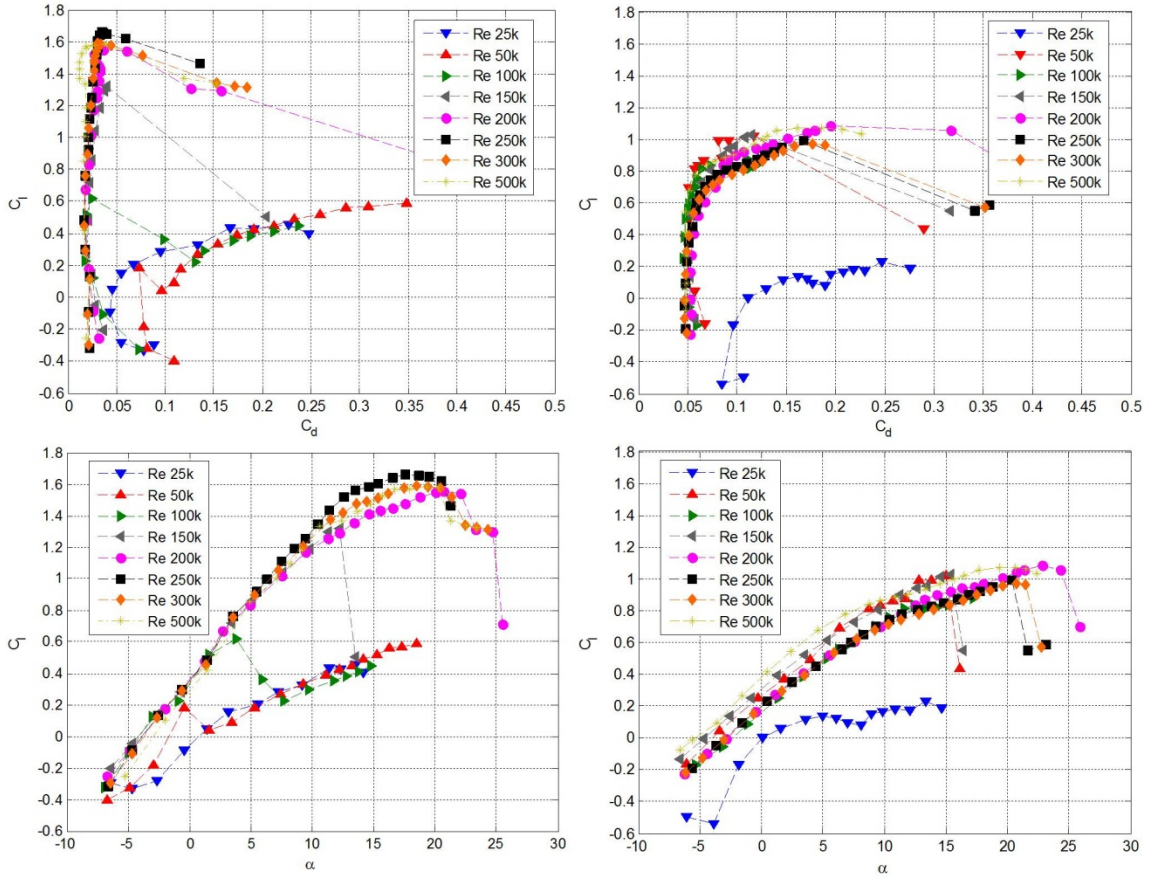


Figure 4.21 *Left*) smooth airfoil drag polars and lift curves, *right*) bumpy airfoil drag polars and lift curves

Another important characteristic used to compare airfoils is the ratio of lift to drag, L/D . This characteristic measures the efficiency of the airfoil's lift production. This ratio is plotted for both airfoils in Figure 4.22 (note the scale difference). This graph shows that for most of the Re examined the L/D for the smooth airfoil is much higher than that of the bumpy airfoil. However, in the lowest Re regime it can be seen that the bumpy airfoil's L/D ratio is improved from that of the smooth airfoil. The $(L/D)_{max}$ even stays fairly constant throughout the remaining order of magnitude difference in Re ($(L/D)_{max}$ only varies $\sim 4\%$). This L/D benefit at low Re indicates that the bumps on this airfoil improve its performance, optimizing it for the Mars flight regime for which was originally intended. As Re increases, there is a significant degradation in L/D from that of the smooth airfoil, indicating the potential need for an additional external smooth skin for drag reduction on the bumpy inflatable.

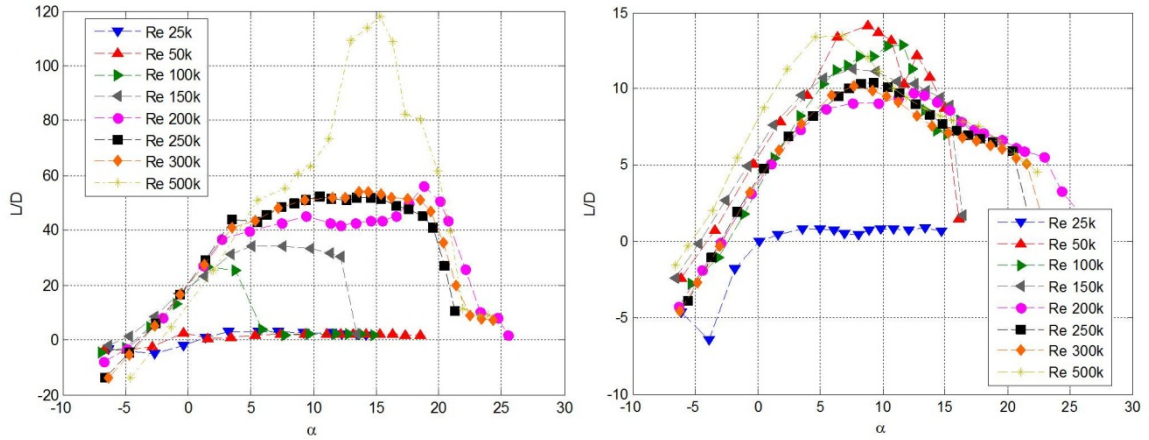


Figure 4.22 Left) smooth airfoil L/D vs α , right) bumpy airfoil L/D vs α

4.3.3 Smooth to Bumpy Airfoil Correction

To determine the appropriate corrections for autopilot programming, the smooth and bumpy airfoil properties were directly compared. Figure 4.23 through Figure 4.36 compare the lift curves and drag polars for the measured Re.

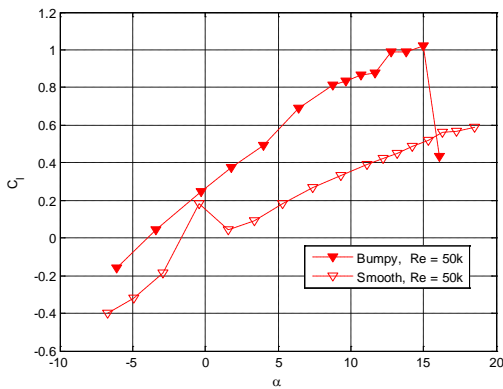


Figure 4.23 Lift curve comparison, Re = 50k

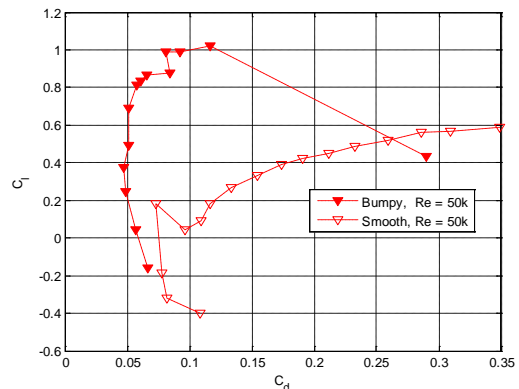


Figure 4.24 Drag polar comparison, Re = 50k

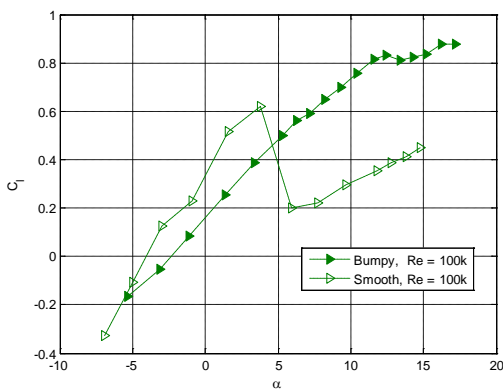


Figure 4.25 Lift curve comparison, Re = 100k

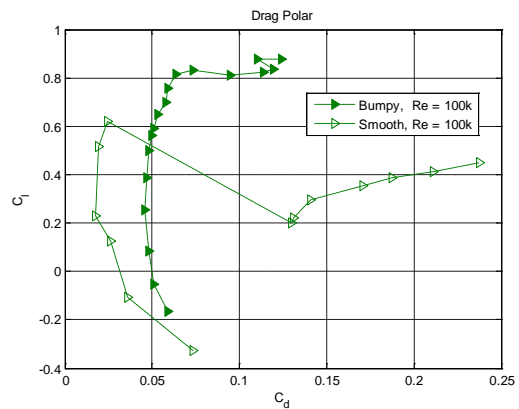


Figure 4.26 Drag polar comparison, Re = 100k

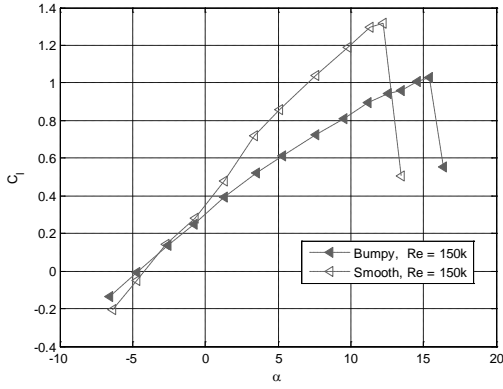


Figure 4.27 Lift curve comparison, $Re = 150k$

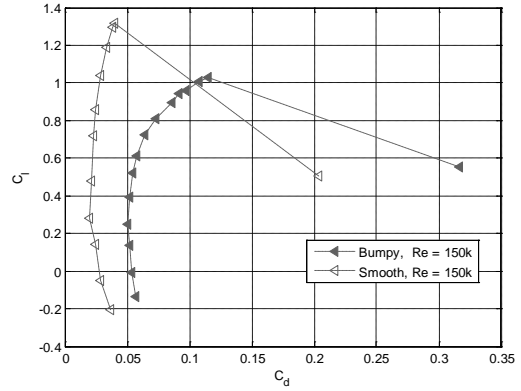


Figure 4.28 Drag polar comparison, $Re = 150k$

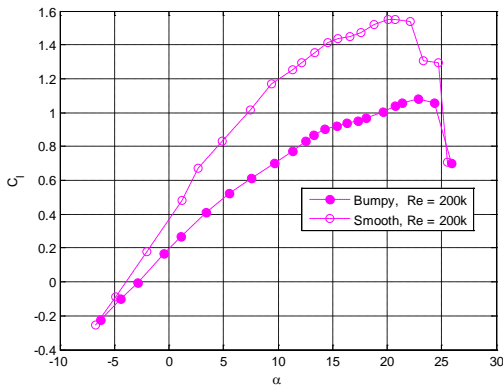


Figure 4.29 Lift curve comparison, $Re = 200k$

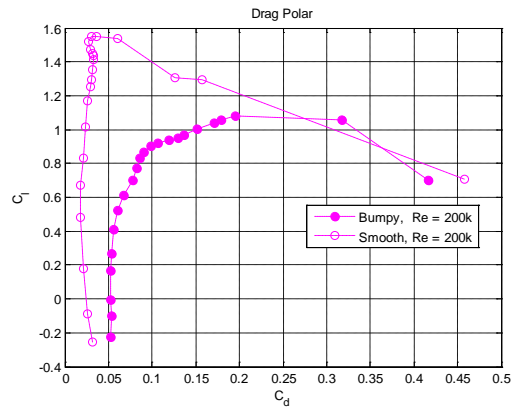


Figure 4.30 Drag polar comparison, $Re = 200k$

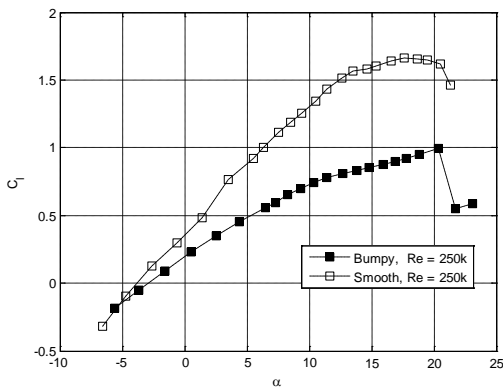


Figure 4.31 Lift curve comparison, $Re = 250k$

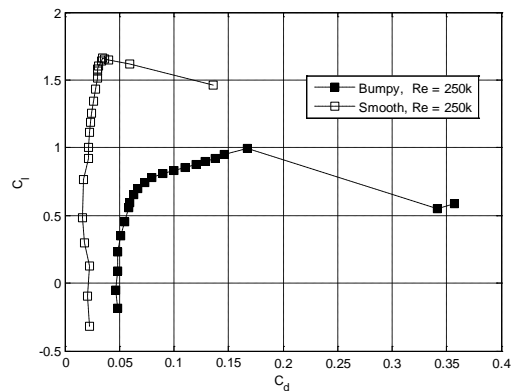


Figure 4.32 Drag polar comparison, $Re = 250k$

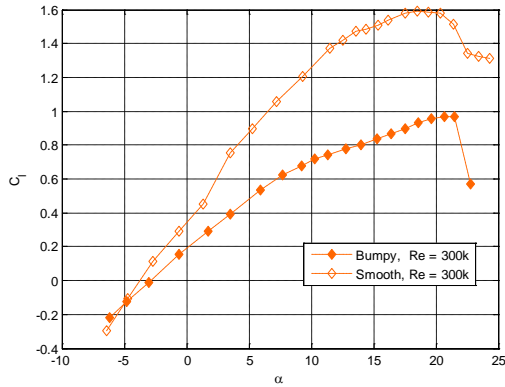


Figure 4.33 Lift curve comparison, $Re = 300k$

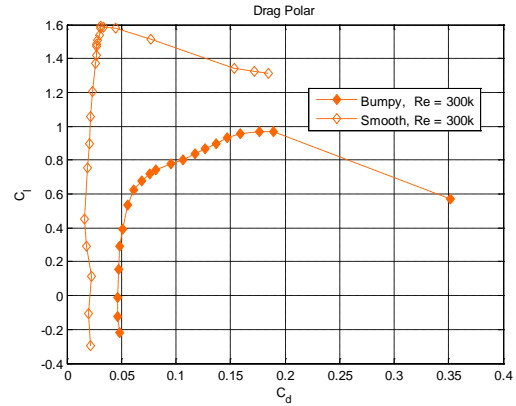


Figure 4.34 Drag polar comparison, $Re = 300k$

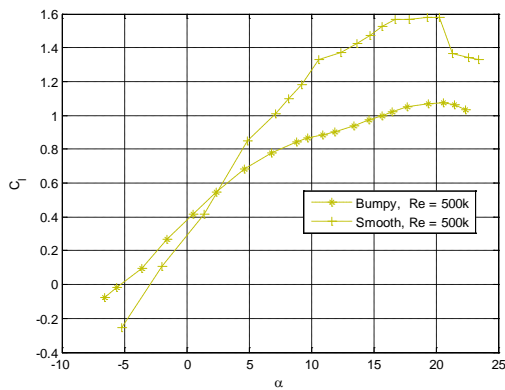


Figure 4.35 Lift curve comparison, $Re = 500k$

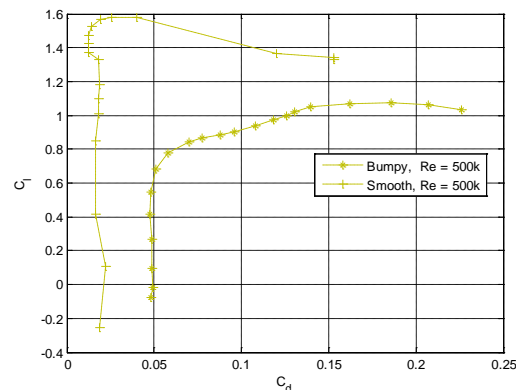


Figure 4.36 Drag polar comparison, $Re = 500k$

The key features of the lift curve for the bumpy airfoil across all measured Re have been tabulated in Table 4.6. From this table it can be seen that these features remain quite constant throughout the test regime, with the most variation coming from the zero lift angle of attack. This had a total variation of approximately $\pm 40\%$ representing a total variation of only 3° across an order of magnitude change in Re . Thus this amount of change was deemed to be due to experimental error. Table 4.6 shows that the zero lift angle of attack has the most variance at $Re = 150k$ and $Re = 500k$. If these two outliers are removed from the data set, the variance halves, and it becomes nearly constant. The lift curve slope and maximum lift coefficient varied less than $\pm 10\%$ and the stall angle varied less than $\pm 20\%$.

Table 4.6 Effects of the bumps on the lift curve at varying Re

	$\alpha_{C_l=0}$	$C_{l,\alpha}$	$C_{l,max}$	α_{stall}
Re = 50k	-3.96°	0.0618/°	1.02	15°
Re = 100k	-2.33°	0.0622/°	0.88	17.2°
Re = 150k	-4.58°	0.0622/°	1.03	15.4°
Re = 200k	-2.81°	0.0622/°	1.08	22.9°
Re = 250k	-2.98°	0.0568/°	0.99	20.4°
Re = 300k	-2.80°	0.0622/°	0.97	20.7°
Re = 500k	-5.33°	0.0664/°	1.07	20.6°
Variation (%)	±42.36	±7.69	±9.94	±20.92
Average	-3.54°	0.0625/°	1.01	18.89°

It can be seen in Table 4.6 that lift curve remains sufficiently Re independent to build a simple model from these curves. This model can be used to replace that of the smooth airfoil which is required in the AVL model discussed in Chapter 3 and as implemented in Chapter 5. This lift curve can be built using the average values given in Table 4.6 except for the stall angle. This yields the linear function:

$$C_l = 0.0625\alpha + 0.2218. \quad 4.4$$

This lift curve will approximate the actual lift curve as straight line from the zero lift angle to the maximum lift coefficient as shown in Figure 4.37. This will not effectively capture the stall pattern of the airfoil or the appropriate stall angle, but this fact is negligible because the analysis performed by AVL is linear and is conducted in the linear region of the lift curve. Using linear least squares, the coefficient of determination for the model was $r^2 = 0.8767$, if only used for lift coefficients up to $C_l \approx 0.7$. Note that the applicable 3D corrections should be applied to this lift curve when using it for an aircraft.

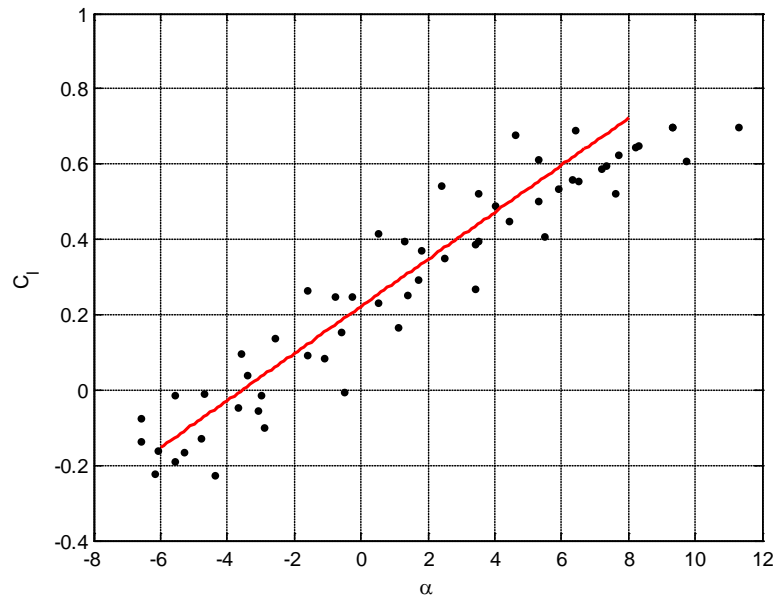


Figure 4.37 Approximated lift curve for use with the autopilot system with experimental data

The next approximation needed for the autopilot is the drag polar. To do this, the portion of the drag polar associated with the linear region of the lift curve ($C_l < \sim 0.7$) was examined for each Re , and was fit with a quadratic model of the form:

$$C_d = kC_l^2 + aC_l + C_{d,0}. \quad 4.5$$

The regression values for each Re are shown in Table 4.7.

Table 4.7 Effects of the bumps on the drag polar

	k	a	$C_{d,0}$	r^2
$Re = 50k$	0.0594	-0.0478	0.0580	0.9483
$Re = 100k$	0.0632	-0.0358	0.0506	0.9794
$Re = 150k$	0.0492	-0.0218	0.0531	0.9760
$Re = 200k$	0.0668	-0.0105	0.0503	0.9837
$Re = 250k$	0.0404	-0.0010	0.0467	0.9913
$Re = 300k$	0.0402	-0.0020	0.0462	0.9903
$Re = 500k$	0.0280	-0.0127	0.0485	0.7572
Variation (%)	± 39.11		± 11.68	
Model	0.0496	-0.0188	0.0505	0.3467

As in the case with the lift curve, the drag polar was quite consistent across the entire range of flight regimes, allowing for the use of averages to build the model. The total variation in the induced drag coefficient (k) in the regression was approximately $\pm 40\%$ which is high, but

this was caused by the $Re = 500k$ value. The low quality fit in the $Re = 500k$ case was caused by a slight deviation in some data points in the measured polar. $C_{d,0}$ remained quite constant, only varying by approximately $\pm 10\%$. The variation in the a parameter was not calculated since it is not contained in the actual drag polar equation:

$$C_d = C_{d,0} + kC_l^2, \quad 4.6$$

and only serves the purpose of improving the curve fit. The resulting equation for this approximation is:

$$C_d = 0.0496C_l^2 - 0.0188C_l + 0.0505. \quad 4.7$$

Again, as in the case with the lift curve, this approximation does not adequately capture the nonlinear region of the lift curve near stall. However, this model does provide a sufficiently accurate model for the linear region of the lift curve indicated by Figure 4.38 showing the drag polar model with the experimental data. Again using linear least squares, the resulting coefficient of determination is relatively low at $r^2 = 0.3467$, but this due to a relatively large amount of scatter toward the bounds of the curve, where the most nonlinearities begin to occur in the data.

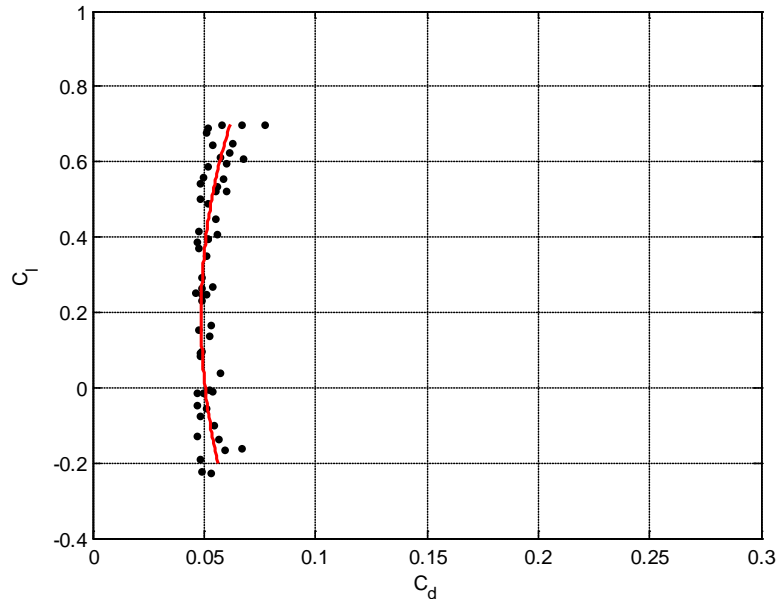


Figure 4.38 Approximated drag polar for use in the autopilot system with experimental data

4.3.4 Lift Hysteresis

An important characteristic to be considered in aircraft design is stall recovery. Once the flow completely separates from the airfoil surface at lower Re there is delay in reattachment. For example, if an airfoil stalls at $\alpha = 15^\circ$ the flow may not reattach until the angle of attack is reduced back to $\alpha = 8^\circ$. In this area of delayed reattachment, the lift coefficient will remain at the post stall lift coefficient creating what is commonly referred to as

the lift hysteresis loop. This hysteresis loop can be captured during wind tunnel testing by raising the angle of attack up to and past the stall angle, taking lift measurements as the angle of attack is increasing. Then once the airfoil has completely stalled and the flow is no longer attached, begin slowly reducing the angle of attack and continue to take the lift measurements while the angle of attack is decreasing. In this experimental setup stall, complete separation, and reattachment were indicated by a real time plot of the wake profile. As the flow separated the wake took a deep curve shape across all but the first and last Pitot tubes in the wake rake, thus identifying stall. This is illustrated in Figure 4.39. It can be seen that as the angle of attack approaches stall the wake widens and post stall the wake spans most if not all the tube positions. Then once stall was realized, the angle of attack was increased to approximately 45° , then reduced back to near where stall had occurred. From that angle of attack the lift hysteresis measurements were started.

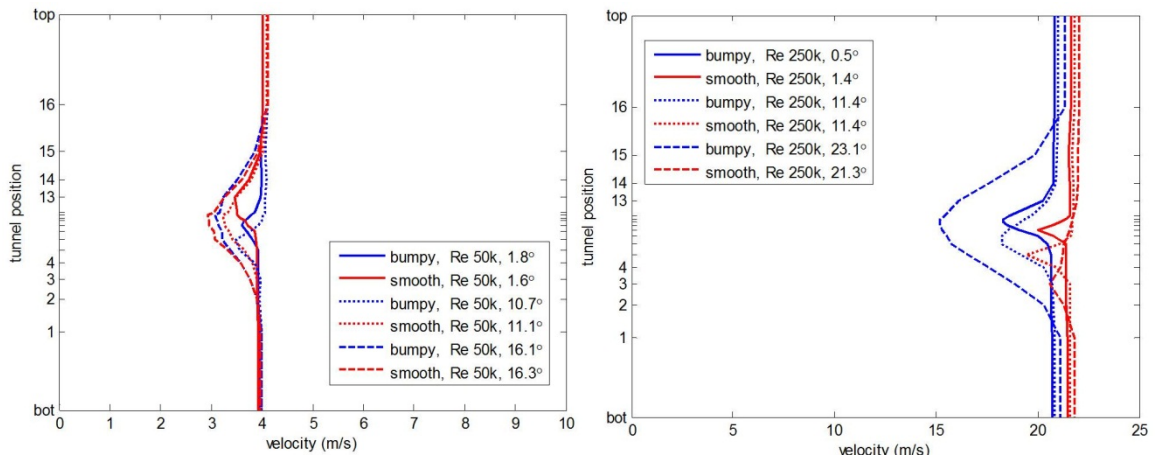


Figure 4.39 Wake shapes at various α for *left*) $Re = 50k$ and *right*) $Re = 250k$

These techniques for identifying stall and measuring the lift hysteresis were used at each Re for both the smooth and bumpy airfoil. Figure 4.40 shows these lift hysteresis results for the smooth airfoil at two of the tested Re . The lift hysteresis for the bumpy airfoil was studied as well, and the results of these tests are shown in Figure 4.41. The remaining test results can be found in Appendix A and Appendix B.

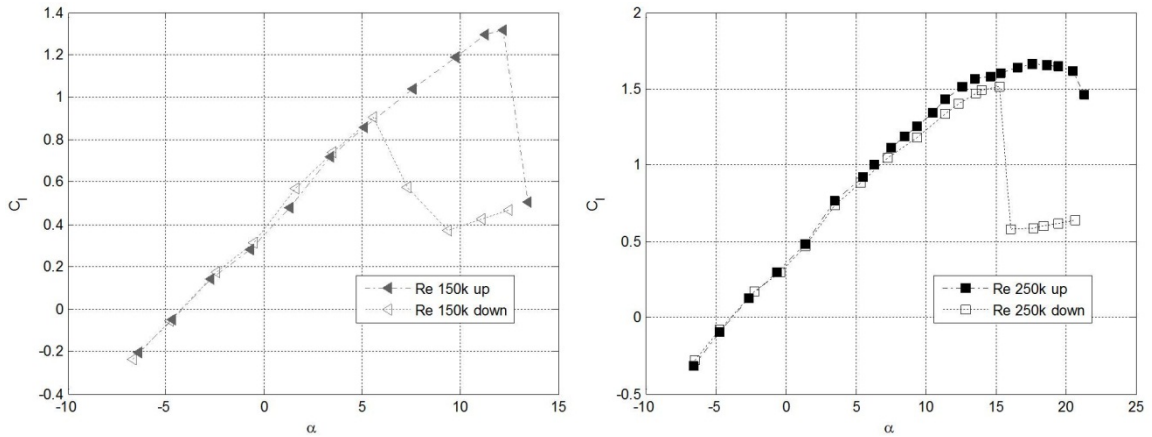


Figure 4.40 Smooth airfoil lift hysteresis for *left*) $Re = 150k$, and *right*) $Re = 250k$

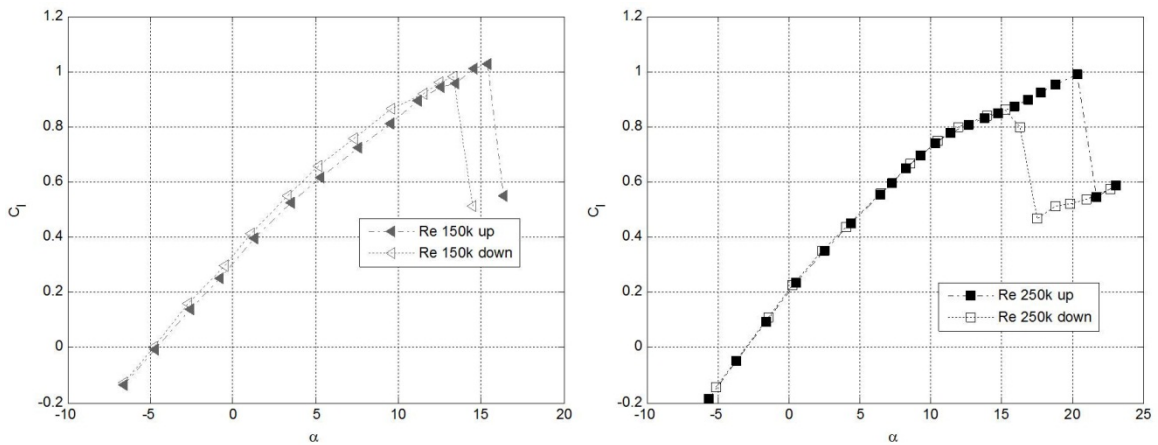


Figure 4.41 Bumpy airfoil lift hysteresis for *left*) $Re = 150k$, and *right*) $Re = 250k$

It can be seen from Figure 4.40 that, for smooth airfoils, as the airspeed increases this phenomenon becomes less prevalent. This means that at lower flight speeds it is more difficult to recover from incidents of stall. However, Figure 4.41 shows the opposite trend for the bumpy airfoil.

According to Figure 4.41, the bumps not only delay stall at lower Re as discussed earlier, but they also help the flow reattach post stall. This is indicated by directly comparing the left hand plots of both Figure 4.40 and Figure 4.41. Then as the flight speed was increased the right hand plots of the two figures indicate nearly identical stall angles as well as reattachment patterns. This means that in lower Re flight regimes the bumpy airfoil will also produce stall recovery benefits, as well as the lift and drag benefits mentioned previously, while at higher Re regimes it will behave like the smooth airfoil post stall. Table 4.8 summarizes the separation and reattachment behavior of both the smooth and bumpy airfoils.

Table 4.8 Summary of separation and reattachment angles of attack from lift hysteresis results

Re	Smooth			Bumpy		
	Separate	Reattach	$\Delta\alpha$	Separate	Reattach	$\Delta\alpha$
50k	N/A		N/A	15°	9.9°	5.1°
100k	N/A		N/A	17.2°	12.6°	4.6°
150k	12.2°	5.6°	6.6°	15.4°	13.3°	2.1°
200k	22.1°	7.6°	14.5°	24.3°	14.6°	9.7°
250k	20.5°	15.3°	5.2°	20.4°	15.3°	5.1°
300k	20.4°	17.5°	2.9°	21.5°	16°	5.5°
500k	N/A		N/A	N/A		N/A

4.3.5 Laminar Separation Bubble

The results of the smooth airfoil pressure distribution measurements not only validated the testing procedure, but also confirmed the presence of a laminar separation bubble on the upper surface of the airfoil. This can be seen as a “bump” in the pressure distribution over the upper surface of the airfoil as highlighted in Figure 4.42.

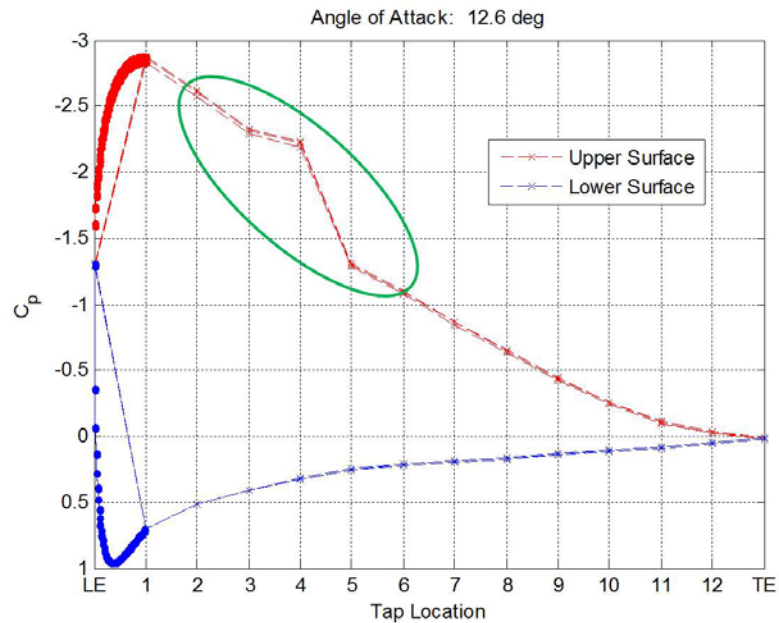


Figure 4.42 Indication of the laminar separation bubble $Re = 250k$

This phenomenon is common in low Re aerodynamics, and it occurs because the flow will separate from the surface of the airfoil then reattach later causing a small recirculation region. These laminar separation bubbles increase the drag on the airfoil, and are often mitigated by introducing disturbance to the flow forward of the bubble’s location. This disturbance will trip the boundary layer, effectively forcing it to become turbulent. Forcing this transition to turbulence adds energy to the boundary layer giving it the momentum it needs to

remain attached to the surface. It has been hypothesized that presence of the bumps on the surface of the inflatable airfoil will perform this same function, and reduce the drag at lower Re [9, 10]. It is illustrated in Figure 4.43 (originally from McMasters and Henderson [10]) that there exists a critical Re (at approximately $Re = 70k$) where a smooth airfoils demonstrate a dramatic improvement in aerodynamic performance [9]. It is important to note that rough airfoils do not and this performance jump effectively separates the airfoils into two performance classes [9]. The resulting data collected from the wind tunnel experiment illustrates this same sudden jump in performance for the smooth airfoils near $Re = 70k$ and the relatively constant performance of the rough airfoil.

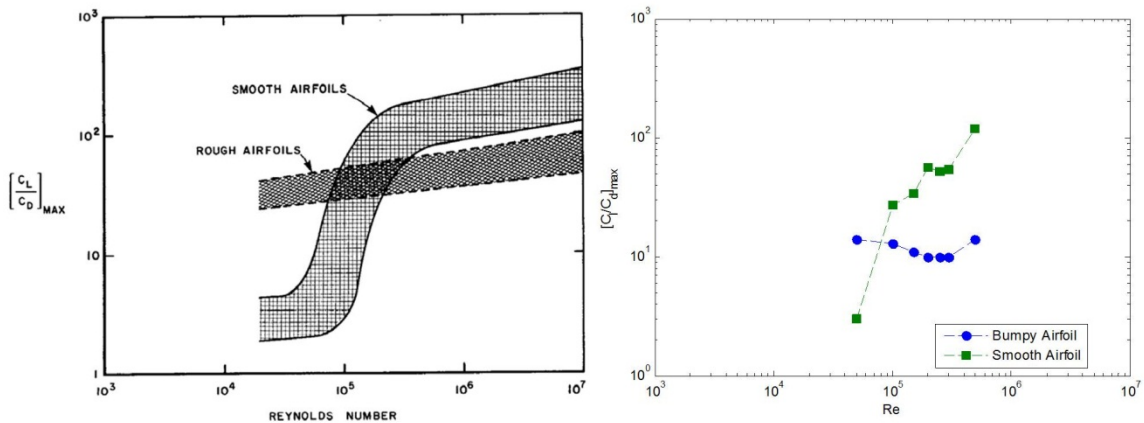


Figure 4.43 Left) Low-Re airfoil performance [9, 10, 17], right) demonstrated airfoil performance

The effect on aerodynamic performance is illustrated by Figure 4.43, showing that at low Re, $Re = 50k$, the bumpy airfoil does experience a drastic improvement in the lift to drag ratio over the smooth airfoil. Then, as predicted by Lissamen [9] and McMasters and Henderson [10], once $Re = 100k$ the smooth airfoil begins to have the higher lift to drag ratio. Between these two tests the critical $Re = 70k$ point in flight regime was crossed lowering the significance of the viscous effects on the airfoil surface, and causing the rough surface to hinder airfoil performance. This is demonstrated by the resulting $(L/D)_{max}$ of the smooth airfoil being an order of magnitude higher than that of the bumpy airfoil as Re was increased (shown in Figure 4.43).

It can be seen in Figure 4.44 that the presence of the bumps does in fact remove the separation bubble which appeared in the smooth airfoil case (Figure 4.42). Figure 4.44 compares a pressure distribution of the bumpy and smooth airfoils at approximately the same α and at the same Re. It can be seen from the comparison that the flow around the bumpy airfoil remains attached until it separates from the airfoil aft of the 8th bump. This is shown by the bumpy profile of the pressure distribution until the 8th bump where it becomes smooth. In this same case the smooth airfoil pressure distribution reflects the presence of a separation bubble that reattaches just forward of the same chord location as the bumpy airfoil separates.

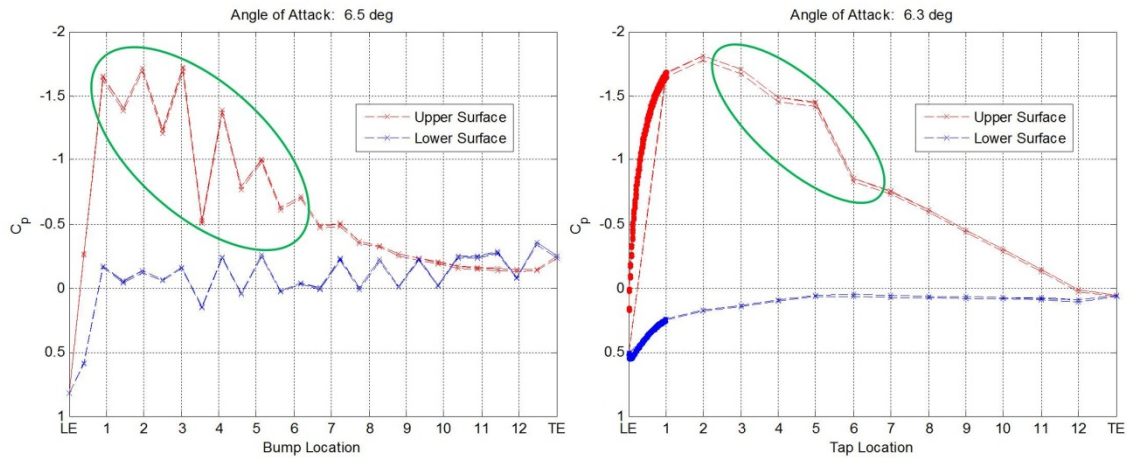


Figure 4.44 *Left*) Bumpy pressure distribution, *right*) smooth pressure distribution $Re = 250k$

Copyright © Michael Andrew Thamann 2012

Chapter 5 Autopilot Programming for Wing Shaping

5.1 Modeling of Standard Wing

There are two pieces of information needed about an aircraft to calculate the aileron effectiveness: aileron power, C_{ℓ, δ_a} , and roll damping, $C_{\ell, \dot{p}}$. Both of these terms are calculated by the AVL [62] analysis of the aircraft. AVL automatically deflects the aileron control surfaces defined in the model to calculate the change in C_{ℓ} , giving the resulting C_{ℓ, δ_a} . The roll damping term is a property of the aircraft and is calculated with the control surfaces un-deflected. These terms can then be output along with all the other stability derivatives from the AVL analysis and used to calculate the aileron effectiveness.

For conventional aircraft (those with ailerons, rudders, and elevators) the Piccolo autopilot's built-in simulator will automatically calculate the aileron effectiveness as well as other necessary aerodynamic characteristics needed to control the aircraft. As a first step, to verify that the calculation of aileron effectiveness described in Chapter 3 is the same as used by the Piccolo simulator, an analysis was performed to manually calculate the aileron effectiveness and compare it to the value automatically produced by the Piccolo simulator. This analysis was done on a model for a Hobbico® NexSTAR™, a common off the shelf kit RC aircraft, which has been used and successfully flown with a Piccolo II autopilot system by the University of Kentucky UAV Lab and the RECUV Lab at the University of Colorado Boulder. Figure 5.1 shows the AVL model and the actual NexSTAR™ and Table 5.1 shows the results of the comparison.



Figure 5.1 AVL model of a standard Hobbico® NexSTAR™ compared to the autonomous NexSTAR™

Table 5.1 a_{eff} calculation comparison

Manual Calculation	C_{ℓ, δ_a}	0.2774
	$C_{\ell, \bar{p}}$	-0.4584
	a_{eff}	0.6051
Simulator a_{eff}		0.6052

The results shown in Table 5.1 indicate that this approach for calculating the aileron effectiveness was valid. Therefore, this same approach was followed to calculate the aileron effectiveness for the warping wing.

5.2 Modeling Wing Shaping

Next the modeling process was completed for the wing shaping test bed aircraft developed in Doepke [45]. This aircraft is built around the Hobbico® NexSTAR™ platform and accepts a wing with wing shaping control surfaces. The aircraft had been flown manually several times prior to the integration of the autopilot to ensure the ability of the warping surfaces to control the aircraft. These flights were performed with an ArduPilot system onboard to collect data about the aircraft during the flights. Information on the ArduPilot system and the data from these manual flights can be seen elsewhere [45]. The specifications of the warping wing are given in Table 5.2, and the aircraft is shown in Figure 5.2.



Figure 5.2 Twisting wing used in this study, $\delta_a = -15^\circ$

Table 5.2 Specifications of the twisting wing

Wing		Airfoil	USA-35B
		Span	73"
		Chord	10.5"
		Wing Area	766.5 in ²
Control Surfaces	Flap	Chord	2.5"
		Span (per semi-span)	15.3125"
		Total Flapped Area	321.5625 in ²
		Starting Location (From Root)	2.1875"
	Wing Shaping	Chord	10.5"
		Span (per semi-span)	12"
		Total Twisting Area	252"
		Starting Location (From Root)	24.5 in ²

Modeling the wing shaping testbed aircraft (Figure 5.2) presented some challenges. Since the wing is changing shape to produce control authority, defining it as a control surface in an AVL model becomes difficult because AVL requires that a hinge line be defined in the model for the control surface to appear. This creates two distinct problems: 1) the a_{eff} term requires the control surface be defined to calculate C_{ℓ, δ_a} , and 2) in order to test the flight model in the simulator, a control surface must be defined.

The first problem was dealt with by modeling the wing in its deflected configuration. This is exhibited in Figure 5.3 and can be compared to Figure 5.2. Note that in Figure 5.2 the aircraft is resting in a cradle causing the nose to be elevated. This is effectively pitching the plane approximately 10° and creating a simulated difference in twist angle from what is shown in Figure 5.3. By modeling the twisted wing, the analysis calculates the resulting aerodynamic imbalance created by the twisting of the warping sections which produces the resulting rolling moment coefficient.

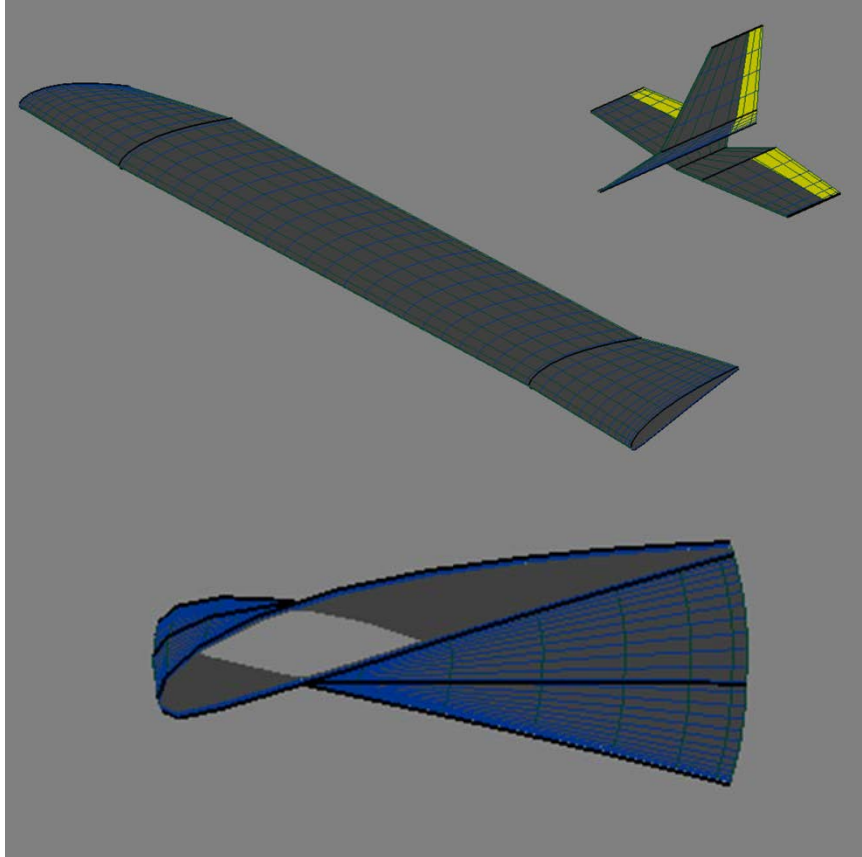


Figure 5.3 AVL model of the twisting wing, $\delta_\alpha = -15^\circ$

Various δ_α were modeled and the resulting C_ℓ was calculated and plotted in Figure 5.4. The resulting change in C_ℓ with respect to δ_α (in radians) was then determined and this gives you the required C_{ℓ, δ_α} for use in Equation 3.11. The $C_{\ell, \bar{p}}$ term in Equation 3.11 is a property of the aircraft and is calculated with $\delta_\alpha = 0^\circ$ but does not change with δ_α . The resulting aileron effectiveness calculated from this model was calculated to be $a_{eff} = 0.3063$, which would be the value used during flight testing. A summary of the values of the aileron effectiveness terms is given in Table 5.3.

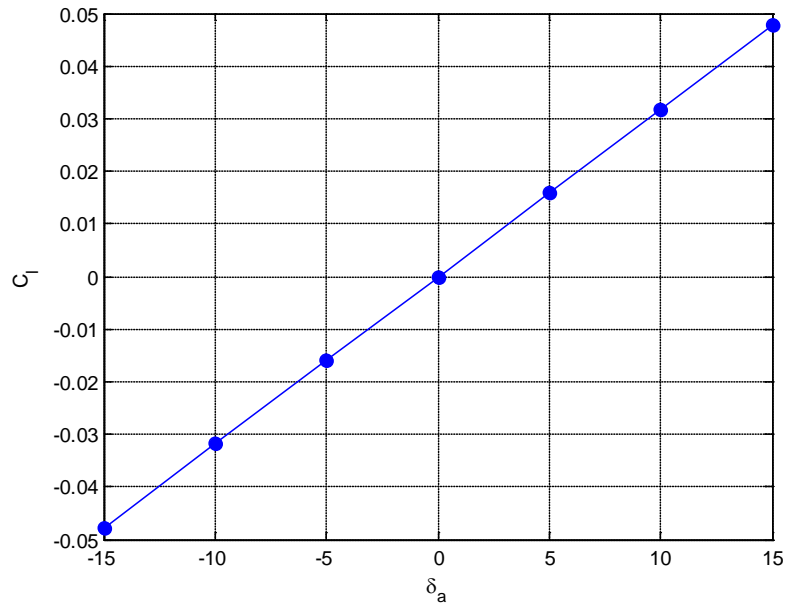


Figure 5.4 C_l vs δ_a in degrees

Table 5.3 Summary of aileron effectiveness calculation for wing shaping

C_{l,δ_a}	0.1809
$C_{l,\bar{p}}$	-0.5908
a_{eff}	0.3062

The second problem was then addressed by modifying the control surfaces of the model. In order to do this, the twisting motion of the actual warping wing was simulated by defining a hinge line from the trailing edge of the section's root to the leading edge of the section's tip as shown in Figure 5.5. This effectively created a triangular shaped "aileron" which the simulator could deflect in order to control the aircraft model. This model lacks the deflection at the leading edge caused by the rotation of the tip airfoil about the quarter chord, but since this deflection is small compared the deflection at the trailing edge it should be closely representative of the real wing shaping control response. This model gave a predicted value of $a_{eff} = 0.346098$. From testing in simulations, a difference in a_{eff} of 0.1 only causes a slight change in the frequency of rolling oscillations produced from the controller correcting the aircraft's bank angle. Therefore, the difference in a_{eff} from the wing shaping model to the simulator model was determined to be acceptable for use in simulations. Table 5.4 shows the a_{eff} calculated for the different wings discussed in Sections 5.1 and 5.2.

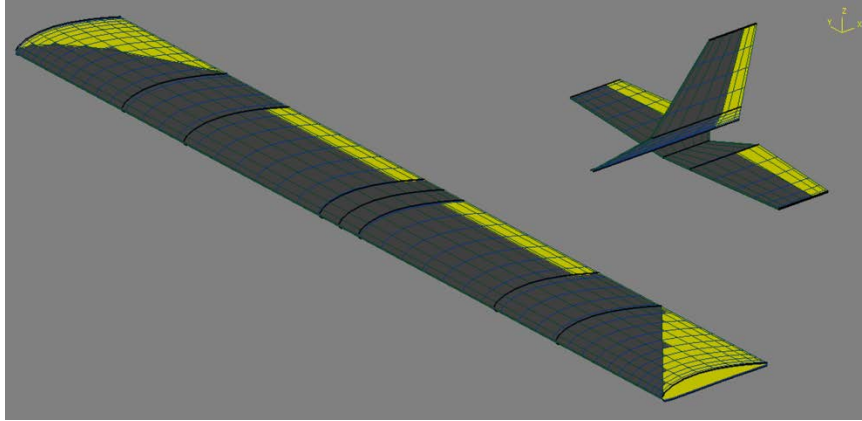


Figure 5.5 AVL model used for the Piccolo flight simulator

Table 5.4 Summary of aileron effectiveness from various wing configurations

Configuration	a_{eff}
Standard NexSTAR™ Wing	0.6052
Warping Wing	0.3062
Simulator Warping Wing	0.3451

5.3 Performance of Model in Simulations

Prior to flight testing, simulations were run to test both the aerodynamic model and the physical aircraft systems prior to flight. In the first of these simulations the computer feeds air data (velocity, altitude, etc.) as well as gyro and accelerometer data to a simulated autopilot which responds to this data accordingly. These are referred to as software in the loop (SiL) simulations. The purpose of the SiL simulations is to test the aerodynamic properties of the aircraft before risking the aircraft during flight testing. Figure 5.6 illustrates a SiL setup and Figure 5.7 shows a screen capture from one of these simulations. The flight plan shown in Figure 5.7 was designed to replicate the proposed flight test mission profile discussed later.

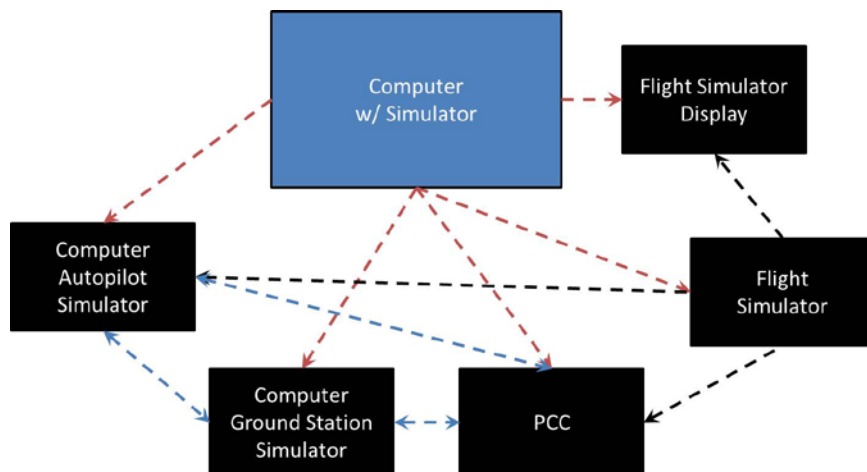


Figure 5.6 Block diagram of SiL set up

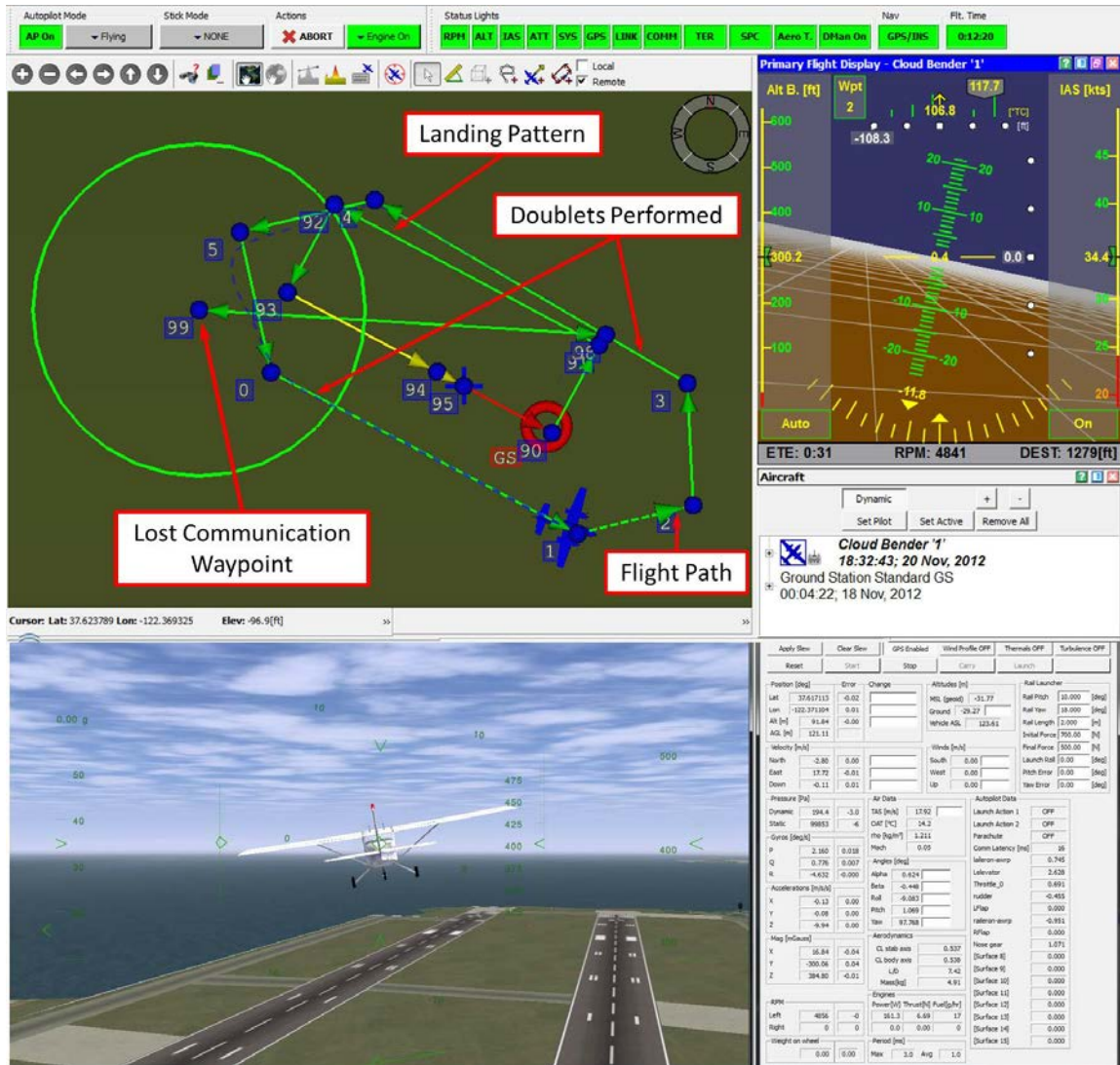


Figure 5.7 Screen capture from SiL. *Top*) Piccolo Command Center (PCC), *Bot Left*) Simulator display, *Bot Right*) Piccolo flight simulator

To test the response of the aircraft (in simulations or in flight) the suggested technique is to command doublets to the aircraft. A doublet is where a control surface deflection is commanded in one direction immediately followed by an equal command in the opposite direction; for example, commanding $\delta_a = 10^\circ$ immediately followed by a command of $\delta_a = -10^\circ$. With a Piccolo autopilot this process can be done automatically through a doublet command feature built into the Piccolo Command Center (PCC). Then, while these commands are being executed, the response of the aircraft is measured, recorded, and the data is then compiled and output into a text file. For the case of testing the aileron effectiveness, during the commanded aileron deflection the resulting roll rate p is measured. These doublets were commanded on the long straight legs of the proposed flight path (shown in Figure 5.7) and results of these doublets are shown in Figure 5.8 and Figure 5.9.

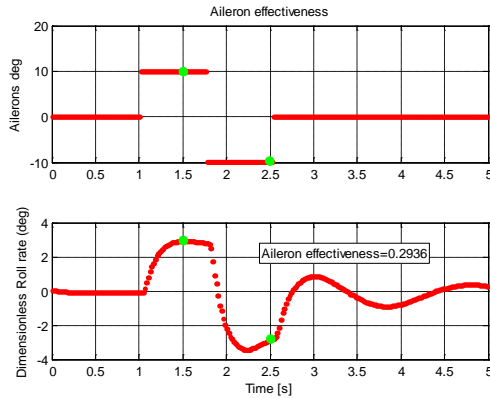


Figure 5.8 Analysis of first SiL doublet

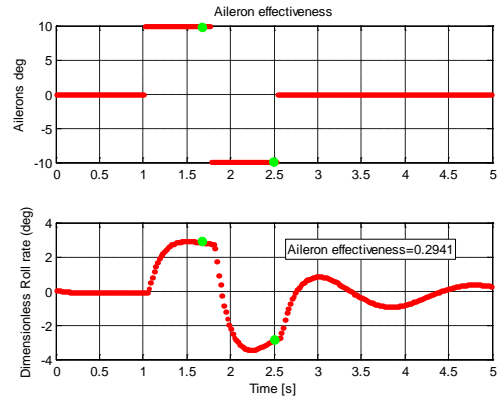


Figure 5.9 Analysis of second SiL doublet

The doublets from simulations, as well as from later flight tests, were analyzed using a MATLAB tool provided by Could Cap Technology. This tool reads the doublet output file created by the PCC and plots the necessary data as shown in Figure 5.8 from the model shown in Figure 5.5. Then the user selects the four points on the plots which are highlighted in green. These points correspond to the two control surface inputs (given by the top plot) and the resulting steady state roll rate found in the bottom plot. From this data the tool can calculate the $\delta\bar{p}$ and δa needed from the definition of aileron effectiveness given by Equation 3.5 and output the resulting a_{eff} , as shown in the bottom plot of Figure 5.8. For this case the $a_{eff} = 0.2941$. This tool allowed for rapid analysis of the doublets and verification of the predicted aileron effectiveness. Table 5.5 shows the results from the two simulation doublets. The $\Delta\delta_{a,max} \approx 0.05$ showed the predicted values for a_{eff} should be acceptable initial flight values.

Table 5.5 Summary of model performance during simulations

Case	a_{eff}
AVL Prediction	0.3451
Simulated Doublets	0.2936
	0.2941
Simulation Average	0.2939

After the SiL simulations, hardware in the loop (HiL) simulations were performed to validate the aircraft's physical systems prior to flight testing. The HiLs are similar to SiLs except that the simulated air data is given directly to the integrated autopilot and the actual autopilot is commanding the control surface movements instead of a computer a simulation. It is during these HiL simulations that the servos are programed to ensure proper orientation during control surface movements for flight. Figure 5.10 illustrates the basic set up of a HiL simulation and Figure 5.11 shows the wing shaping aircraft in the HiL setup.

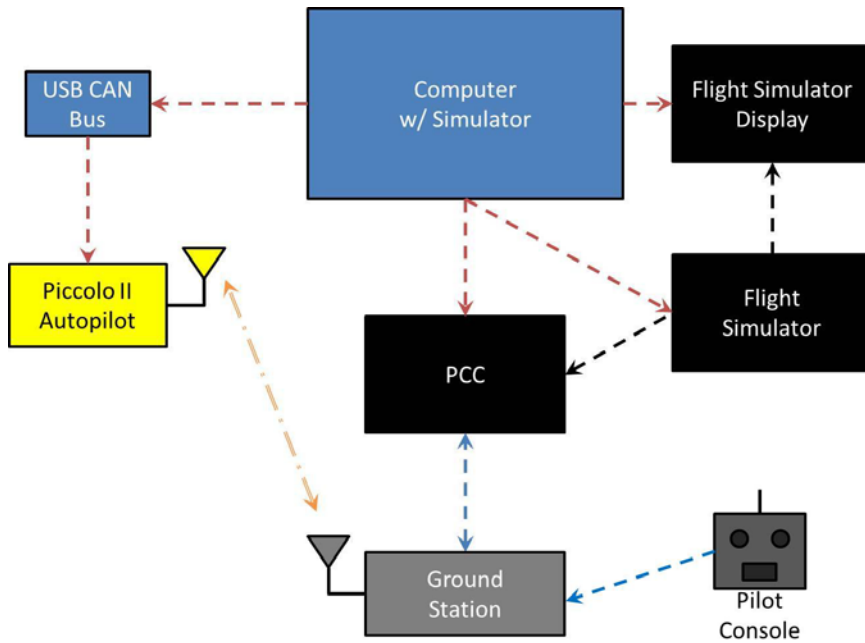


Figure 5.10 Block diagram of the HiL set up

In the HiL simulations several complete flight plans were executed to validate the control surface movements during the entire flight regime. These simulated flight profiles included all phases of the proposed test mission profile including take off, cruise, doublets, and landing. Figure 5.11 shows the aircraft performing during one of the phases of the simulated mission. Several simulated flights were completed to verify that the wing shaping aircraft would execute all phases of the flight test mission profile.

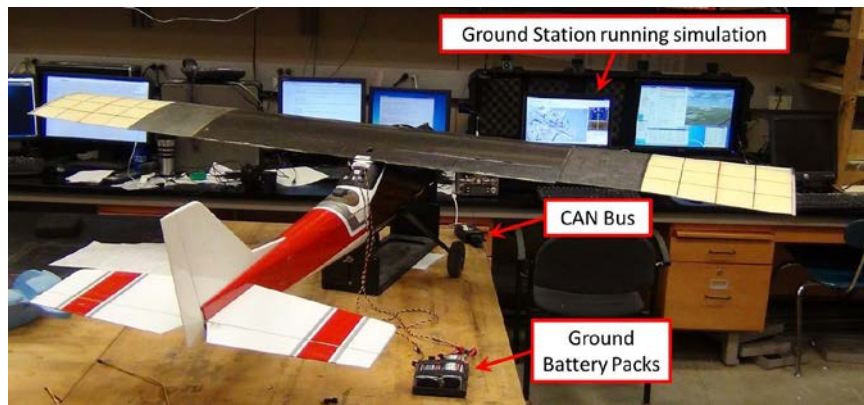


Figure 5.11 Wing warping aircraft during HiL simulation

5.4 Flight Performance of Autonomous Wing Shaping

After the model and physical systems of the aircraft were tested via simulations, the flight testing phases outlined in Table 5.6 were begun. The first stages of the flight test regime were to fly the platform under manual control (radio control) to verify the wing would fly and was able to control the aircraft. The flight mission profile was programmed into the autopilot along with a landing plan and a lost communication waypoint for safety purposes. These flight

plans are shown in Figure 5.12. This mission profile was used for all flight tests. Once all preflight checks were completed at the test flight location for both the autopilot ground station and aircraft the takeoff call was made.

Table 5.6 Flight test process

Testing Phase		Complete?
Manual Flight Testing		
	Flights Completed?	Y / N
	Aircraft Controllable?	Y / N
Autonomous Flight Testing		
	Autopilot Integrated	Y / N
	Flight Simulations	
	SiL	Y / N
	Doublets Performed	Y / N
	HiL	Y / N
Field Flight Tests		
	Pre Flight Checks	Y / N
	Manual Takeoff	Y / N
	Autonomous Switch Over	Y / N
	Waypoints Tracked	Y / N
	Doublets Performed	Y / N
	Landing	Y / N

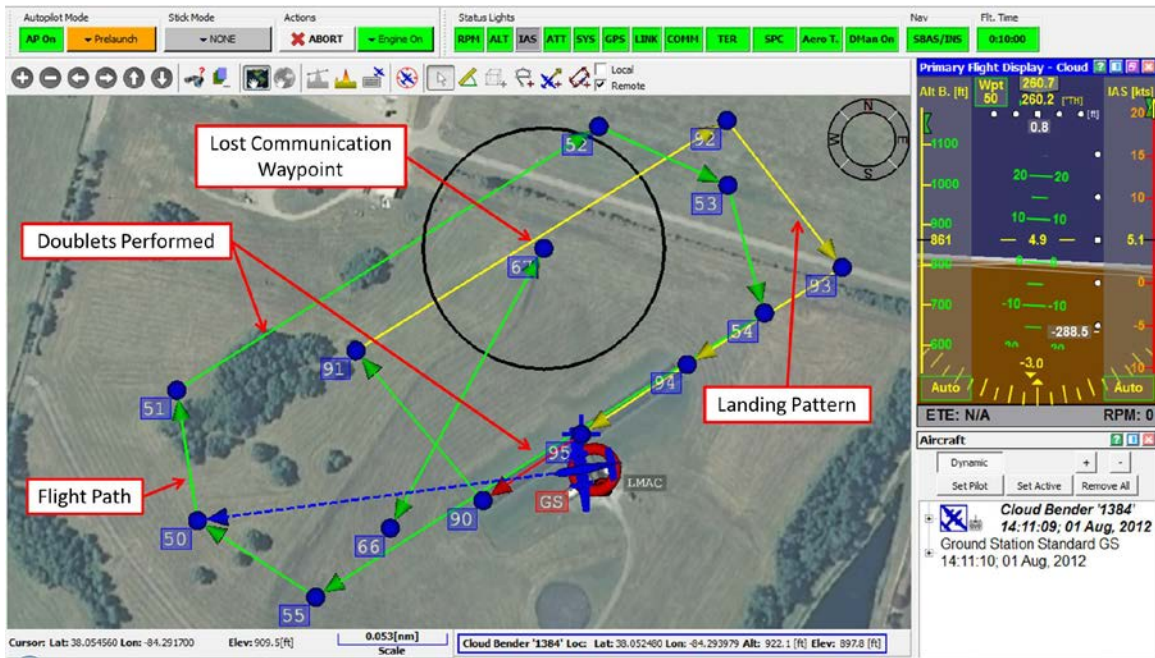


Figure 5.12 Mission plan for light testing of the wing shaping aircraft

For all flight tests the wing shaping test bed aircraft was taxied and taken off under manual control. Figure 5.13 shows the aircraft being prepared for takeoff. It was not until the aircraft had reached a safe altitude that the autopilot was given control of the aircraft. Once at altitude the aircraft was commanded into the programmed flight path (shown in Figure 5.12) to observe the aircraft's ability to track waypoints. After observation of successful tracking, the doublet test phase was initiated. As seen in Figure 5.12 these doublets occurred on the long straight legs of the flight path, similar to in the simulations.

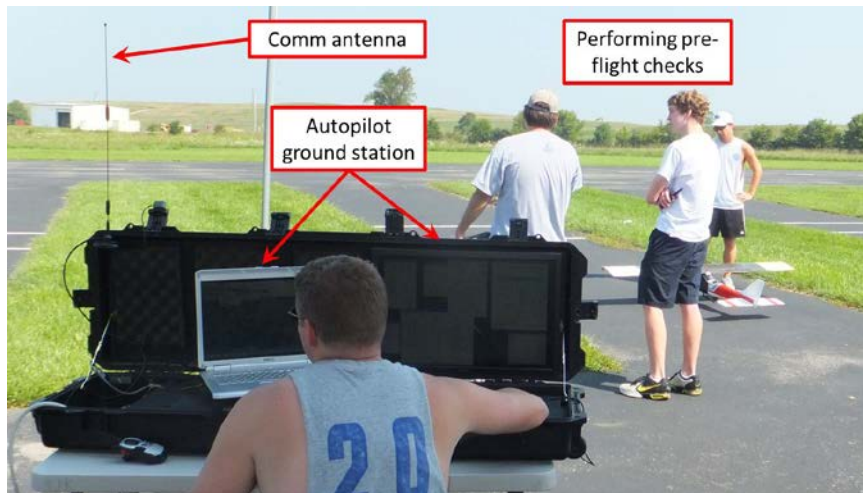


Figure 5.13 Warping wing preparing for take off

During the autonomous flight testing phase a total of two complete test flight missions were completed each lasting approximately 5 minutes. In both missions the aircraft successfully tracked the programmed flight path while compensating for wind. The aircraft did display errors

in tracking the exact path shown in Figure 5.14 and Figure 5.15 but these errors were determined to be a result of wind gusts and a need for tuning other gains in the controller not related to the aileron effectiveness. In Figure 5.14 the green portion of the plots indicate the aircraft was under autonomous control, showing almost the entire flight was flown under autonomous control. The major deviations from the flight path originated from the execution of the doublets and after completing each doublet the aircraft was able to autonomously return to its programmed course. It was also discovered after both test flights the aircraft was flying with the propulsion system being approximately 250 watts under-powered (max power calculated was $\sim 500W$ when the expected power was $\sim 750W$). It is believed that once this problem is corrected the aircraft will have increased excess power, and thus improved acceleration. This should allow it to track better than what was displayed, and be able to perform an autonomous landing.

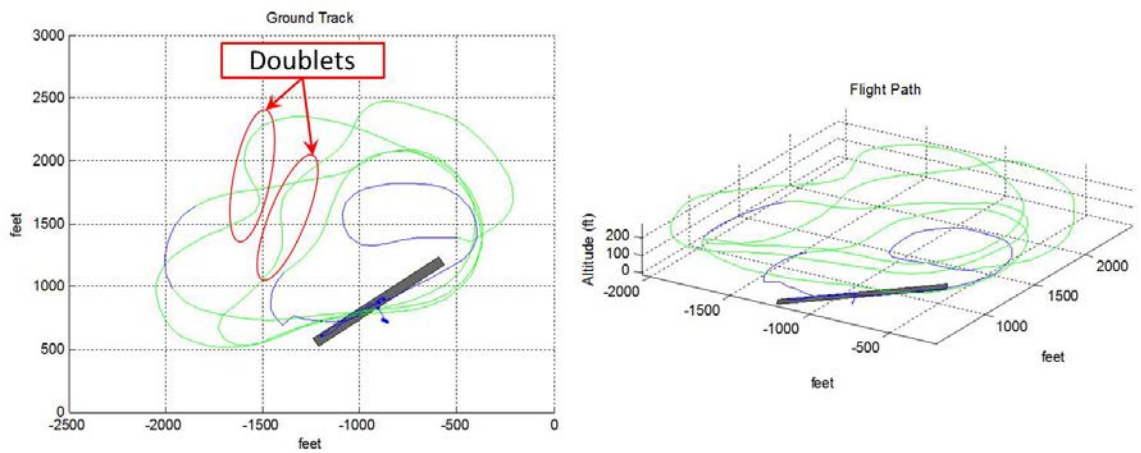


Figure 5.14 Ground track and flight path from one autonomous test flight (green indicates autonomous control)



Figure 5.15 Wing warping aircraft in flight under autonomous control

The doublets performed during the flight plans exhibited in Figure 5.14 were analyzed to calculate the actual aileron effectiveness of the aircraft in the same manner as described in Section 5.3. During the two flights that were performed a total of four doublets were executed. The analyses of these flight doublets are shown in Figure 5.16 through Figure 5.19. Table 5.7 shows the calculated a_{eff} results from all four flight doublets as well as the predicted value from the AVL model.

Table 5.7 Summary of model performance during flight

Case	a_{eff}	Δa_{eff}
AVL Prediction	0.3062	
Flight Doublets	0.2765	0.0298
	0.3182	0.0119
	0.3613	0.0550
	0.3696	0.0633
Flight Average	0.3314	0.0251

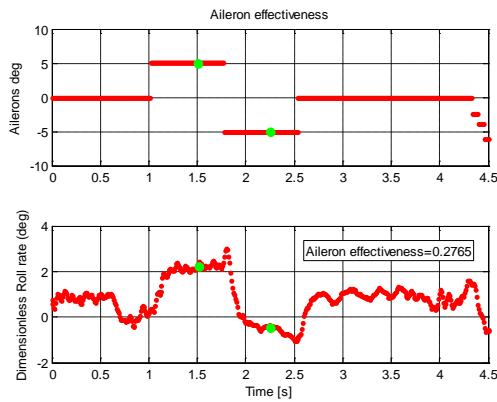


Figure 5.16 Analysis of first in-flight doublet, manual control taken at ~4.25 s

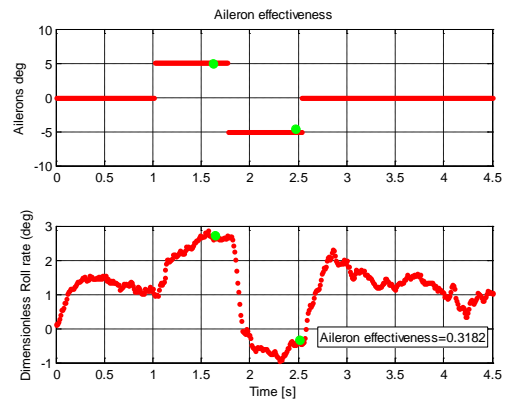


Figure 5.17 Analysis of second in-flight doublet

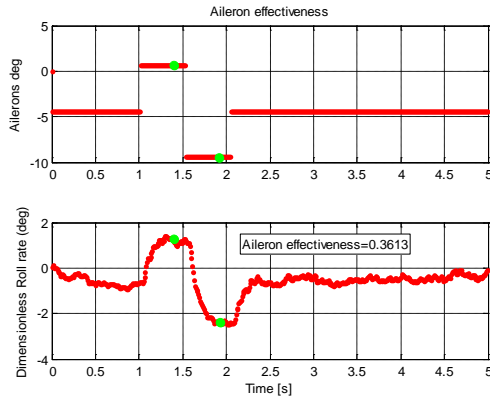


Figure 5.18 Analysis of third in-flight doublet

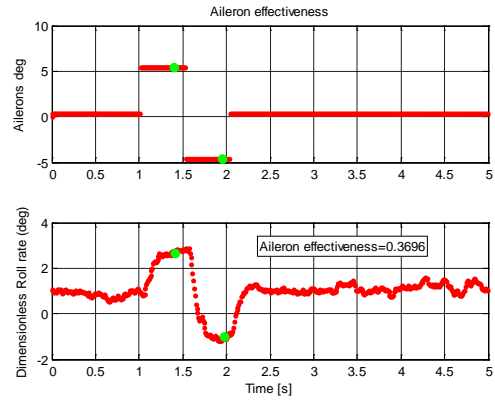


Figure 5.19 Analysis of fourth in-flight doublet

It can be seen in Table 5.7 that the maximum Δa_{eff} from the predicted value was 0.0633, and that the average a_{eff} from the in-flight doublets differed by only 0.0251. As discussed in Section 5.2, if the a_{eff} is changed by 0.1 the resulting effect on the flight controller is a slight change in the frequency of oscillations as the controller corrects the bank angle. Since the maximum difference in a_{eff} from the predicted value was less than 0.1, this means that there would only be a marginal effect in the performance of the aircraft. Therefore, it can be determined that the method outlined in Section 5.2 is valid for predicting the aileron effectiveness of an aircraft which uses wing shaping for flight control. This provides the ability to successfully program a Piccolo II autopilot for autonomous flight control of an aircraft which uses wing shaping.

Chapter 6 Summary, Conclusions, and Future Work

6.1 Summary and Conclusions

With the drastic increase in UAV usage in the last 15 years, new needs and uses for these aircraft have begun to arise. One of these needs includes the deployable UAV. These aircraft can be packed into small containers, transported to, and deployed from forward locations in short amounts of time to immediately satisfy a desired task. Inflatable wing UAVs provide a unique solution for this role because of their high packability and the potential for wing shaping for flight control. To better understand this potential the equations of motion for aircraft are shown, and are used to derive aileron effectiveness, a key parameter for autonomous flight. In this thesis several objectives were addressed:

- Wind tunnel tests were conducted to determine the aerodynamic characteristics of the bumpy inflatable wing airfoil shape and its baseline smooth airfoil shape.
- Lift and drag curves were developed for the bumpy inflatable wing profile for use in autopilot modeling.
- A modeling process was developed for calculation of the aileron effectiveness for a warping wing aircraft.
- Successful autonomous flight tests were performed of a warping wing demonstrator aircraft using the predicted aileron effectiveness calculated from the model.

The wind tunnel experiment was designed to test the effect of the bumpy inflatable wing's airfoil shape on its aerodynamic performance compared to that of the smooth baseline shape. To accomplish this development of a wake rake apparatus, SLA airfoil models, and a 50-channel pressure scanner were necessary. Each SLA airfoil model (one of the smooth NACA 4318 shape and one of the bumpy 4318 shape) contained built in pressure taps to measure the pressure distribution over the airfoil from which the lift was calculated, and the drag was calculated from the wake rake. The aerodynamic properties of each airfoil were then measured for $Re = 25k - 500k$ and the effects of the bumps on the lift curve and drag polar were determined.

At $Re = 25k$ the pressures did not have sufficient magnitude to confidently calculate the lift and drag. However, at $Re = 50k$ and $100k$ the bumpy airfoil had both improved maximum lift, and delayed stall. In all other cases the maximum lift was decreased for the inflatable profile, although stall was delayed. Also, in all cases the bumpy airfoil demonstrated a reduced lift curve slope. The $Re = 50k$ case indicated a reduction in total drag and a significant increase in L/D relative to the smooth airfoil case across all α . In all other cases the inflatable wing profile demonstrated approximately double the drag of the smooth airfoil at the same Re indicating a regime where smooth airfoils should be used, or external skins be added to create a smooth surface. These results indicate the bumpy airfoil does improve aerodynamic performance at the lowest Re and the lift hysteresis results show that it also improves flow reattachment post stall, as well as delays the initial separation. From the measured wind tunnel data, a lift curve and drag polar were generated which can be used to create aircraft models for

autopilot integration. Smooth airfoils are required for the modeling (because of the type of analysis used) so these generated curves can be used to replace the smooth airfoil data produced by the model's aerodynamic simulations.

Next a modeling process was developed to predict the aileron effectiveness term used within a commercial autopilot system. This technique was verified using the model of an aircraft with autonomous flight hours to validate its accuracy. The modeling procedure was applied to a wing shaping demonstrator aircraft. The aileron effectiveness was calculated for the warping wing using the modeling procedure and used to program the autopilot integrated into the wing warping demonstrator aircraft. In order to perform simulations to verify the functionality prior to flight testing, a separate model had to be created, which provided proof of concept during simulations. The vehicle was then flight tested under autonomous control with the predicted aileron effectiveness from the wing shaping model after RC tests were performed verify control authority and stability of the aircraft. The wing shaping demonstrator proved capable of successfully tracking waypoints under autonomous control. In-flight doublets were performed during the flight tests and analyzed to verify the actual aileron effectiveness for comparison against model predictions. The actual effectiveness was measured to be $a_{eff} = 0.3314$ matching the predicted $a_{eff} = 0.3062$ within 8%, proving that the modeling method used is a viable method for autopilot programming of UAVs using wing shaping for flight control.

6.2 Future Work

6.2.1 Wind Tunnel Testing

The wind tunnel testing could be replicated using a force balance, negating any effects due to lack of resolution in the pressure distribution. There was also the potential to automate the entire process with the inclusion of more precise angle of attack control. Recreating the $Re = 25k$ case with a model of smaller chord length would also be beneficial, because this would allow for higher velocities, and thus higher pressure differences. Also particle image velocimetry (PIV) could be incorporated to measure the airfoil circulation. Recreating the testing conditions of this thesis in the new tests would provide further validation of the results presented herein, and provide further information which could be used to validate future CFD results.

Another interesting experiment would be to measure the effect of adding the bumpiness to an arbitrary geometry. Comparisons of the aerodynamic characteristics of these arbitrary bumpy and smooth shapes could be used to develop correction factors which could transform the smooth geometry aerodynamics into the corresponding bumpy aerodynamics. Then bumpy correction factors could be incorporated into the modeling programs used for commercial autopilots, improving the capability to integrate commercial autopilots into deployable UAVs that utilize inflatable wings. If implemented properly, these corrections for the addition of arbitrary shapes to a smooth airfoil surface could be used for simple flow trips as well as complicated shapes such as the bumpy inflatable wing geometries. This would

incorporate the improved low-Re aerodynamics of the rough airfoils into the small deployable UAVs.

6.2.2 Wing Shaping & Autopilot Programming

The next natural step with this research would be to build an inflatable wing UAV and incorporate a Piccolo II autopilot. This would allow for testing the experimentally-determined lift curve and drag polar for the inflatable airfoil. The next step in the wing shaping would be to increase the warping portion of the span to a fully warping wing. Once that has been determined to be feasible wing shaping could then be incorporated into the inflatable wing. This would be the true culmination of the modeling discussed herein. Then flight testing could be carried out to test the full flight envelope of the warping inflatable wings.

However, the modeling process developed in this thesis has broader application than just warping inflatable wings. This modeling approach could be used to add autonomous control for any form of flexible wing UAV. The modeling approach could also be modified to calculate the effects of adding washout by symmetrically deflecting the warping sections. Then the autopilot could be programmed to optimize the wing shape based on varying flight conditions like speed and angle of attack. Or it could be programmed to autonomously add the necessary amount of washout to prevent wing-tip stall during high bank angle turns and increase the UAV flight envelope.

Copyright © Michael Andrew Thamann 2012

Appendix A Smooth Airfoil Results

For completeness, the following are all the results from the wind tunnel testing of the smooth airfoil.

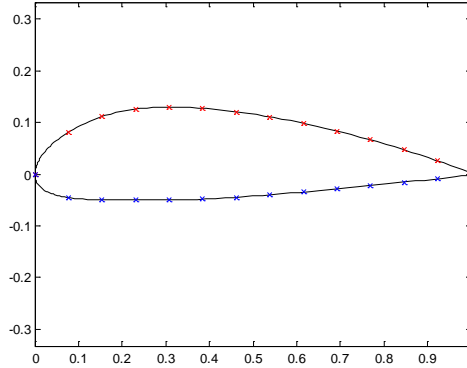


Figure A.1 Smooth airfoil tap profile

A.1 $Re = 25,000$

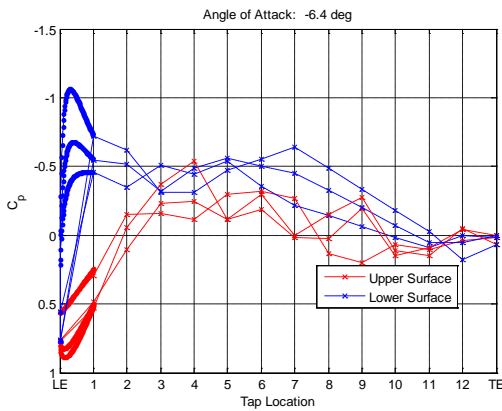


Figure A.2 C_p distribution $Re = 25k$,
 $\alpha = -6.4^\circ$

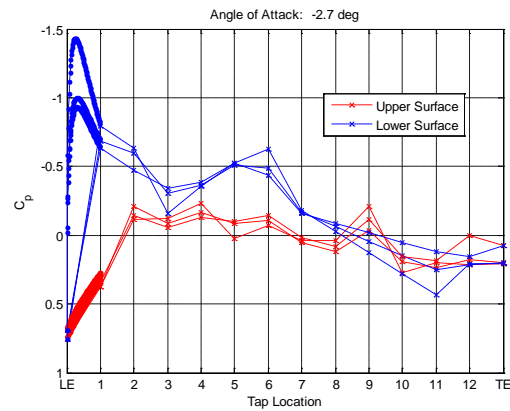


Figure A.4 C_p distribution, $Re = 25k$,
 $\alpha = -2.7^\circ$

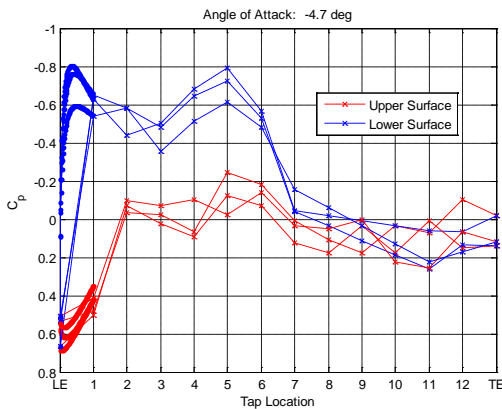


Figure A.3 C_p distribution $Re = 25k$,
 $\alpha = -4.7^\circ$

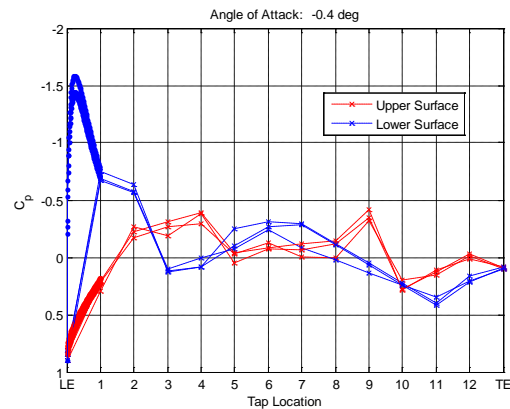


Figure A.5 C_p distribution, $Re = 25k$,
 $\alpha = -0.4^\circ$

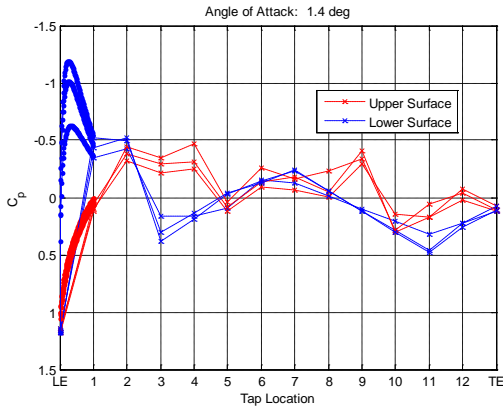


Figure A.6 C_p distribution, $Re = 25k$, $\alpha = 1.4^\circ$

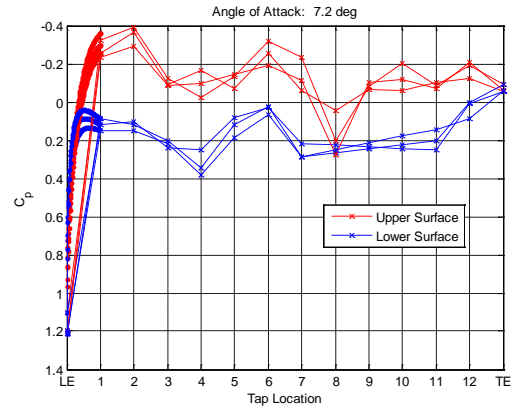


Figure A.9 C_p distribution, $Re = 25k$, $\alpha = 7.2^\circ$

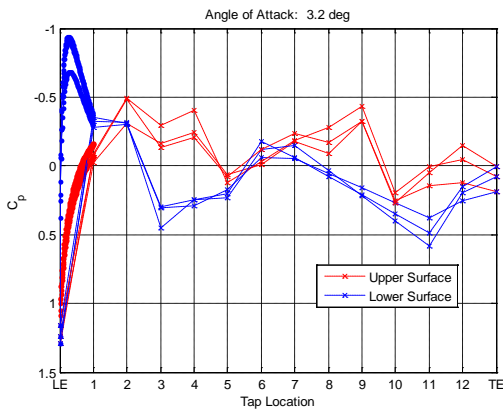


Figure A.7 C_p distribution, $Re = 25k$, $\alpha = 3.2^\circ$

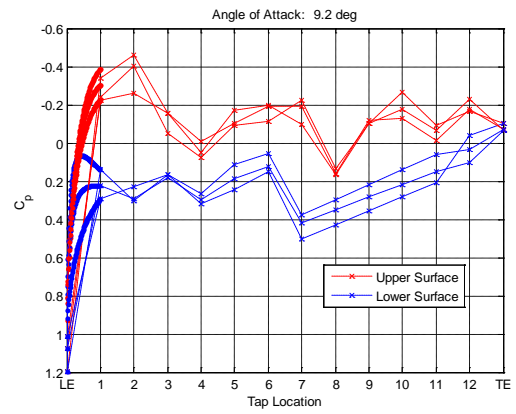


Figure A.10 C_p distribution, $Re = 25k$, $\alpha = 9.2^\circ$

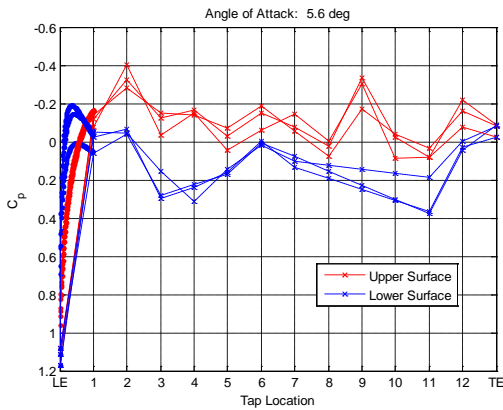


Figure A.8 C_p distribution, $Re = 25k$, $\alpha = 5.6^\circ$

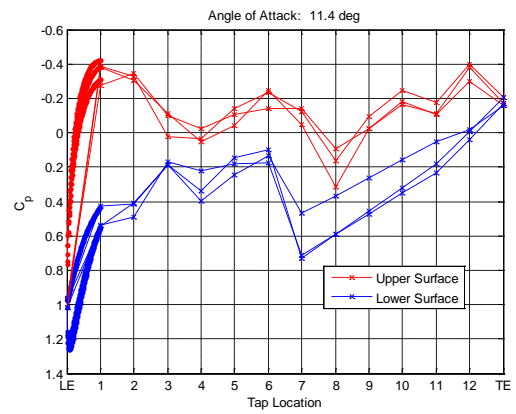


Figure A.11 C_p distribution, $Re = 25k$, $\alpha = 11.4^\circ$

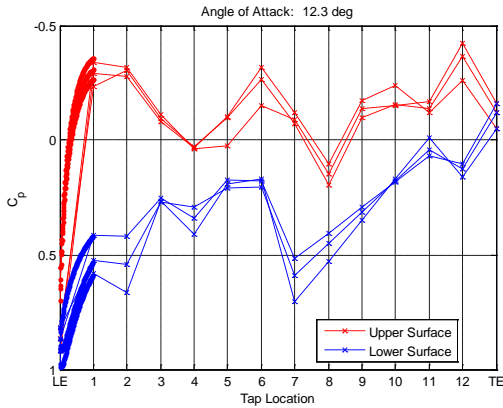


Figure A.12 C_p distribution, $Re = 25k$, $\alpha = 12.3^\circ$

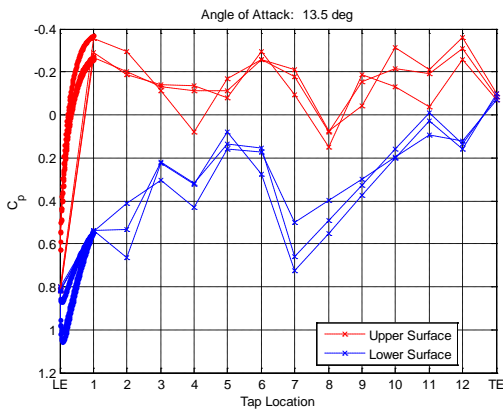


Figure A.13 C_p distribution, $Re = 25k$, $\alpha = 13.5^\circ$

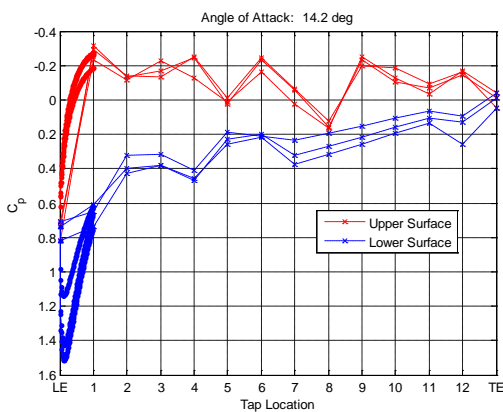


Figure A.14 C_p distribution, $Re = 25k$, $\alpha = 14.2^\circ$

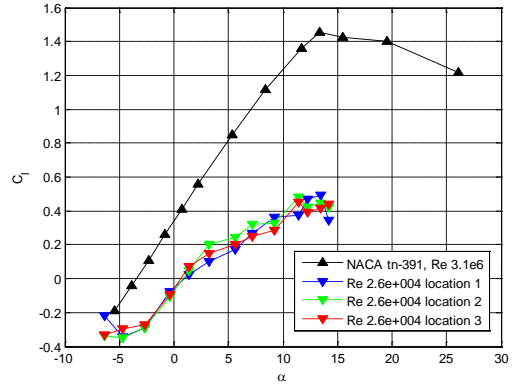


Figure A.15 $Re = 25k$ pre-averaged lift curves from 3 run locations

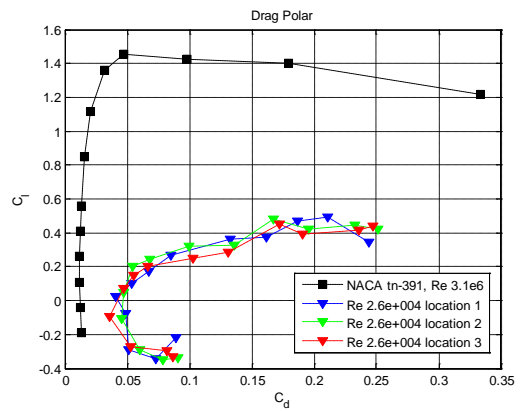


Figure A.16 $Re = 25k$ pre-averaged drag polars from 3 run locations

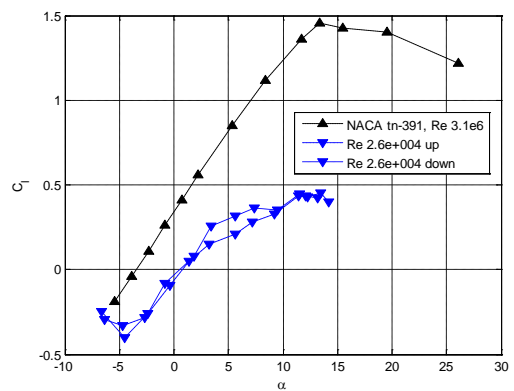


Figure A.17 $Re = 25k$ averaged lift curve with lift hysteresis

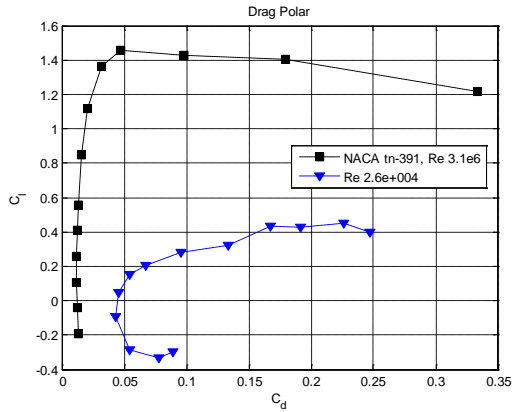


Figure A.18 $Re = 50k$ averaged drag polar

A.2 $Re = 50,000$

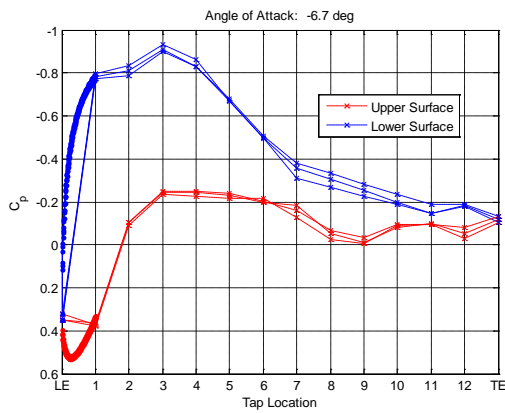


Figure A.19 C_p distribution, $Re = 50k$, $\alpha = -6.7^\circ$

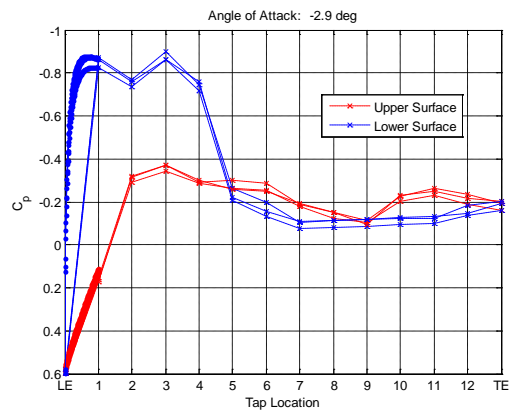


Figure A.21 C_p distribution, $Re = 50k$, $\alpha = -2.9^\circ$

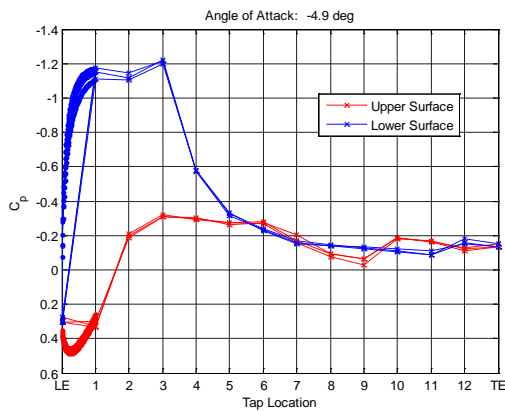


Figure A.20 C_p distribution, $Re = 50k$, $\alpha = -4.9^\circ$

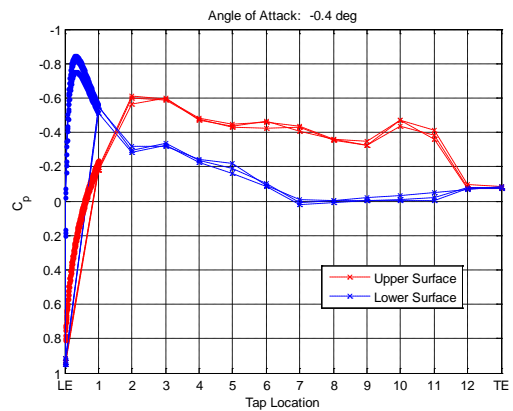


Figure A.22 C_p distribution, $Re = 50k$, $\alpha = -0.4^\circ$

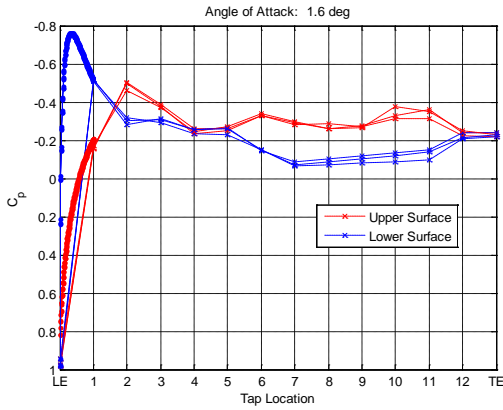


Figure A.23 C_p distribution, $Re = 50k$, $\alpha = 1.6^\circ$

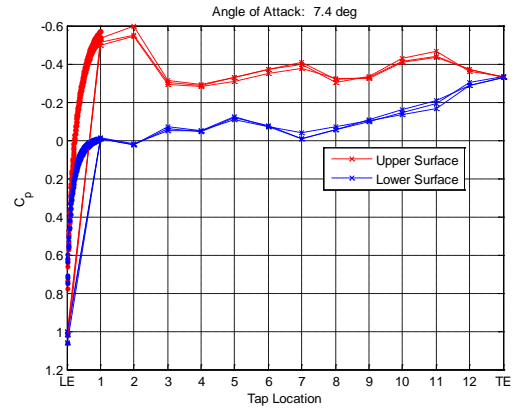


Figure A.26 C_p distribution, $Re = 50k$, $\alpha = 7.4^\circ$

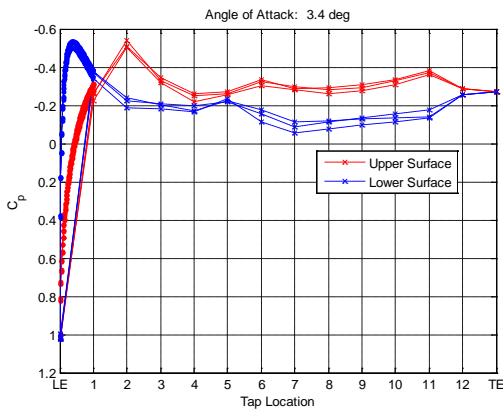


Figure A.24 C_p distribution, $Re = 50k$, $\alpha = 3.4^\circ$

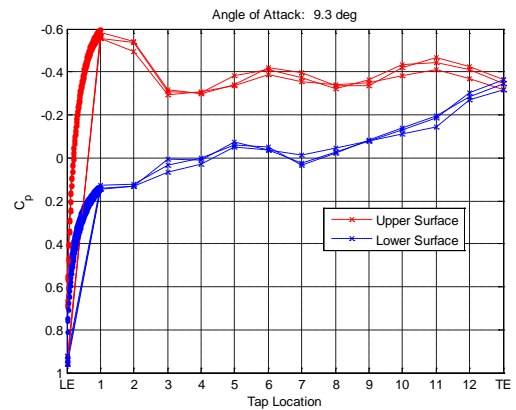


Figure A.27 C_p distribution, $Re = 50k$, $\alpha = 9.3^\circ$

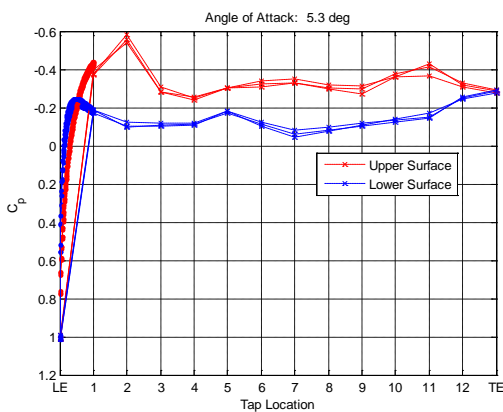


Figure A.25 C_p distribution, $Re = 50k$, $\alpha = 5.3^\circ$

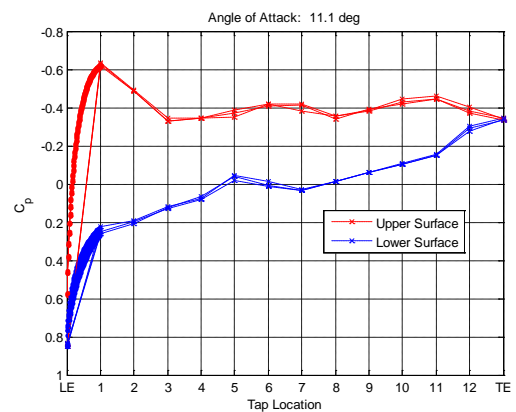


Figure A.28 C_p distribution, $Re = 50k$, $\alpha = 11.1^\circ$

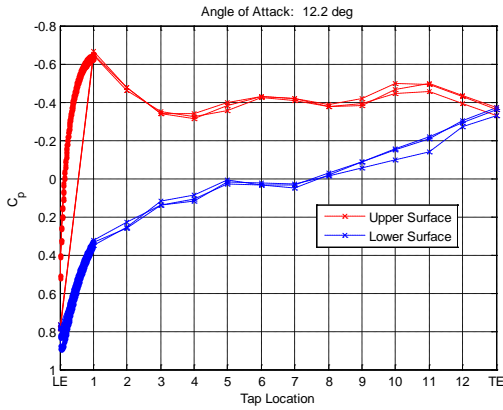


Figure A.29 C_p distribution, $Re = 50k$, $\alpha = 12.2^\circ$

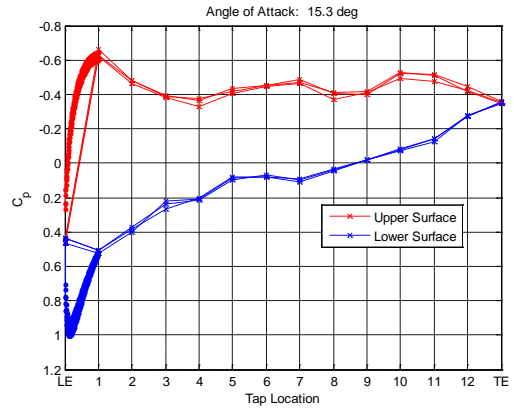


Figure A.32 C_p distribution, $Re = 50k$, $\alpha = 15.3^\circ$

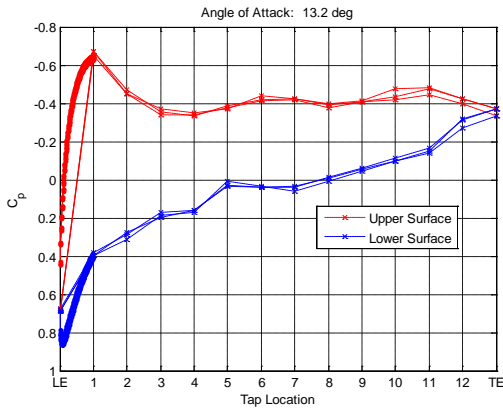


Figure A.30 C_p distribution, $Re = 50k$, $\alpha = 13.2^\circ$

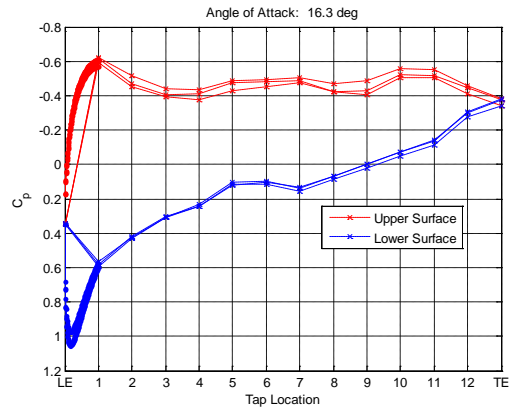


Figure A.33 C_p distribution, $Re = 50k$, $\alpha = 16.3^\circ$

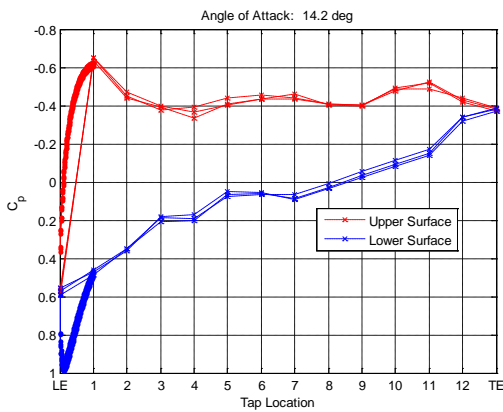


Figure A.31 C_p distribution, $Re = 50k$, $\alpha = 14.2^\circ$

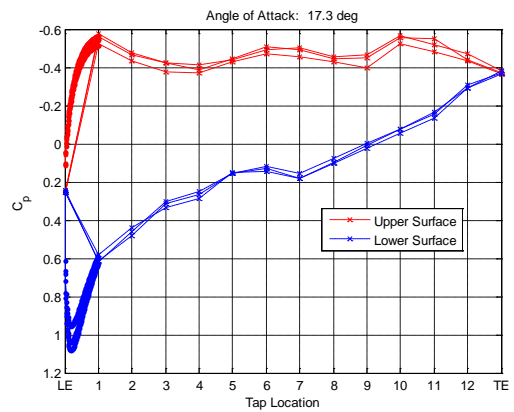


Figure A.34 C_p distribution, $Re = 50k$, $\alpha = 17.3^\circ$

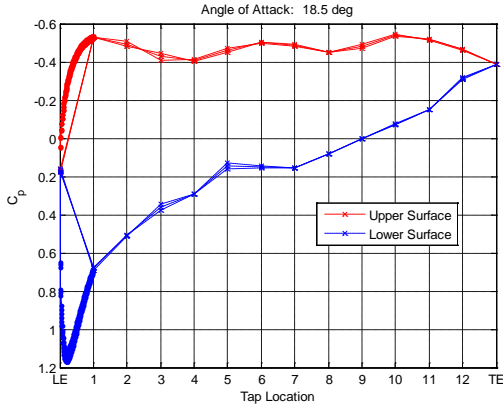


Figure A.35 C_p distribution, $Re = 50k$, $\alpha = 18.5^\circ$

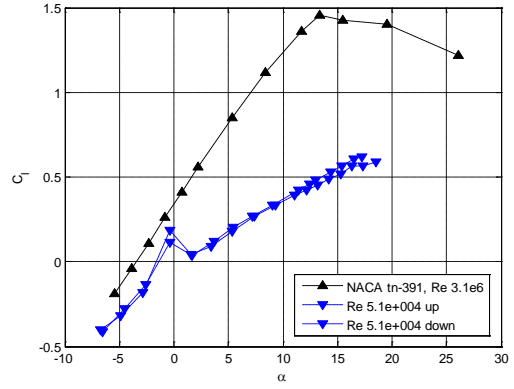


Figure A.38 $Re = 50k$ averaged lift curve with lift hysteresis

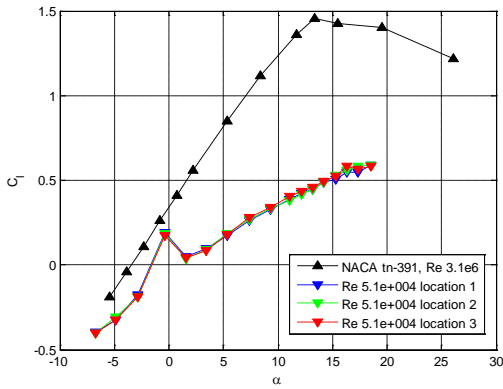


Figure A.36 $Re = 50k$ pre-averaged lift curves from 3 run locations

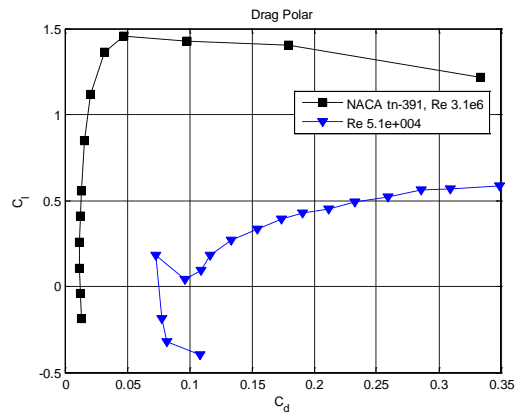


Figure A.39 $Re = 50k$ averaged drag polar

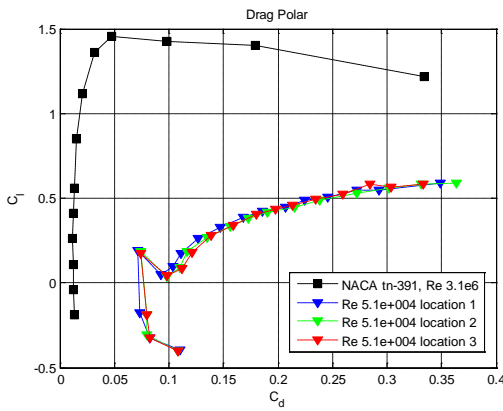


Figure A.37 $Re = 50k$ pre-averaged drag polars from 3 run locations

A.3 Re = 100,000

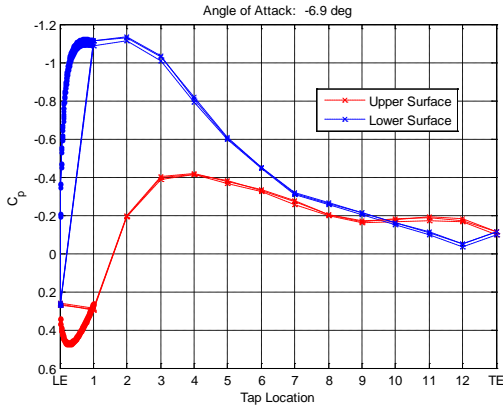


Figure A.40 C_p distribution, $Re = 100k$, $\alpha = -6.9^\circ$

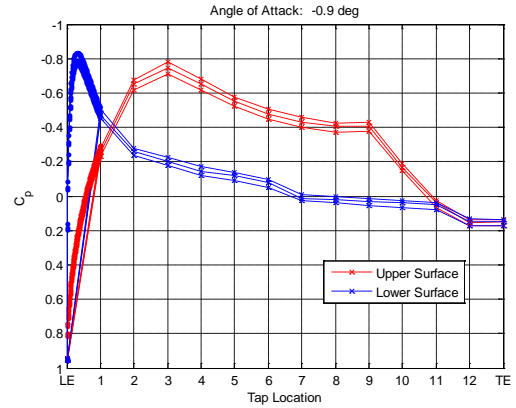


Figure A.43 C_p distribution, $Re = 100k$, $\alpha = -0.9^\circ$

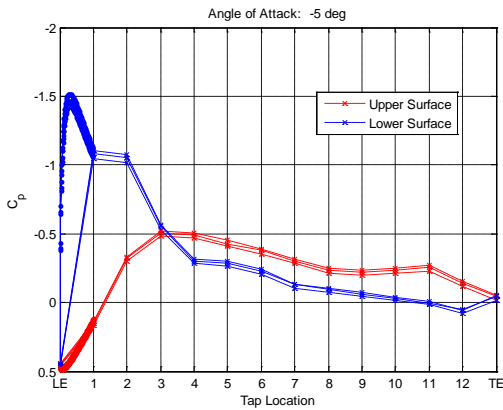


Figure A.41 C_p distribution, $Re = 100k$, $\alpha = -5^\circ$

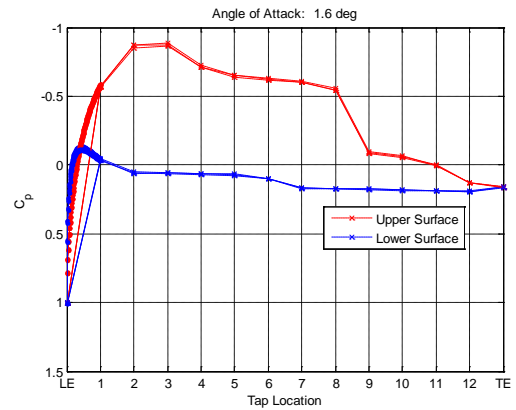


Figure A.44 C_p distribution, $Re = 100k$, $\alpha = 1.6^\circ$

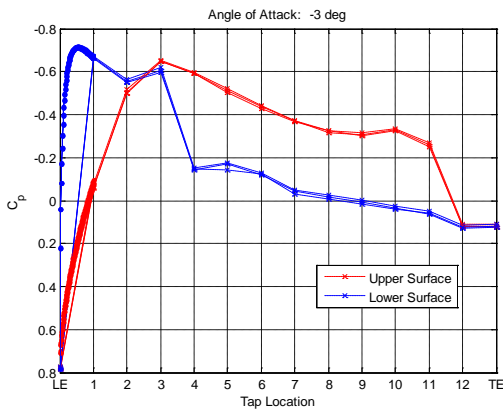


Figure A.42 C_p distribution, $Re = 100k$, $\alpha = -3^\circ$

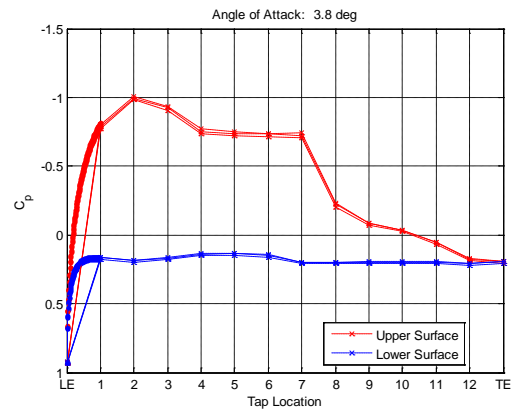


Figure A.45 C_p distribution, $Re = 100k$, $\alpha = 3.8^\circ$

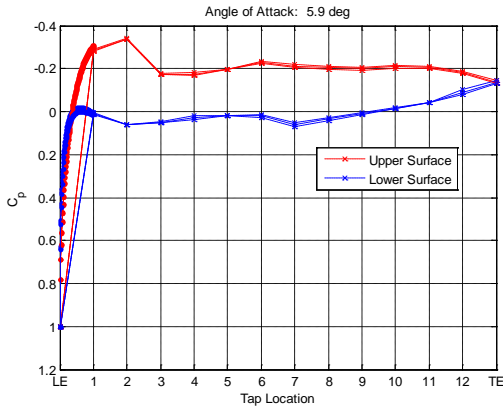


Figure A.46 C_p distribution, $Re = 100k$,
 $\alpha = 5.9^\circ$

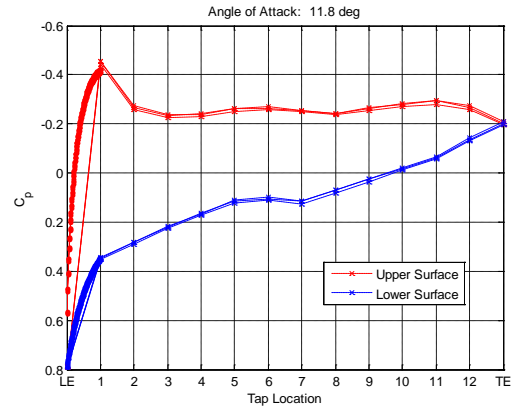


Figure A.49 C_p distribution, $Re = 100k$,
 $\alpha = 11.8^\circ$

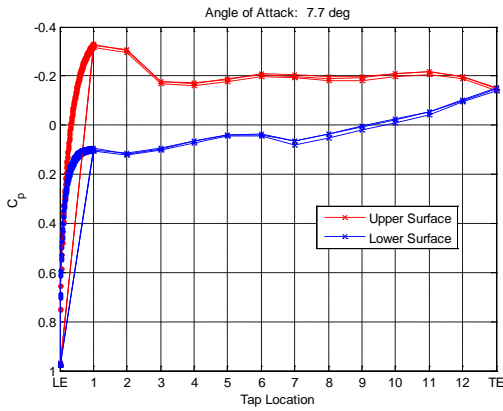


Figure A.47 C_p distribution, $Re = 100k$,
 $\alpha = 7.7^\circ$

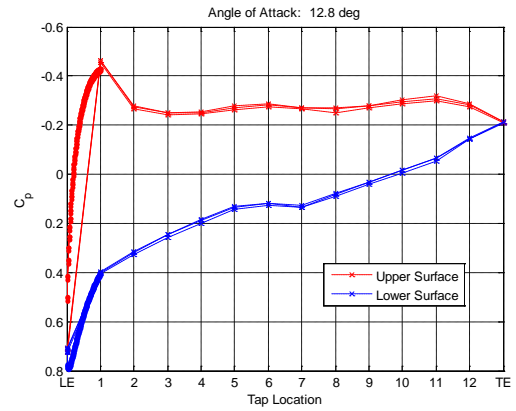


Figure A.50 C_p distribution, $Re = 100k$,
 $\alpha = 12.8^\circ$

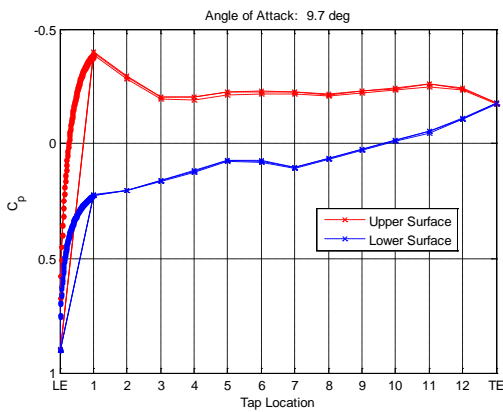


Figure A.48 C_p distribution, $Re = 100k$,
 $\alpha = 9.7^\circ$

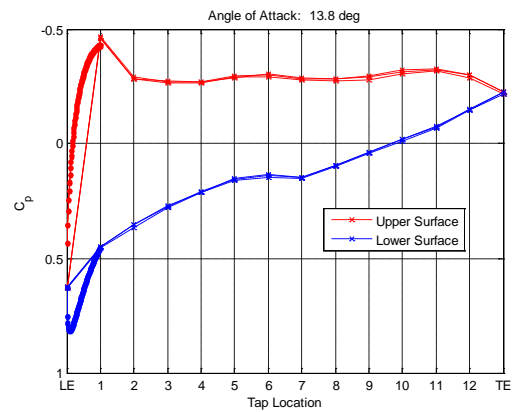


Figure A.51 C_p distribution, $Re = 100k$,
 $\alpha = 13.8^\circ$

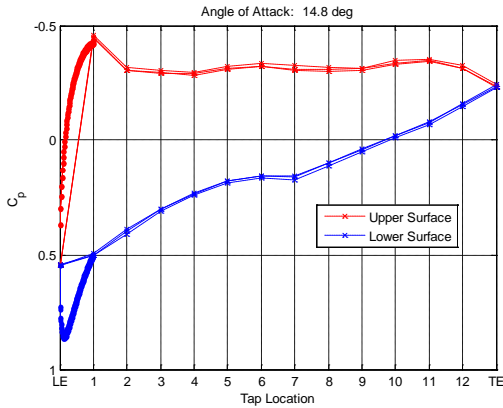


Figure A.52 C_p distribution, $Re = 100k$, $\alpha = 14.8^\circ$

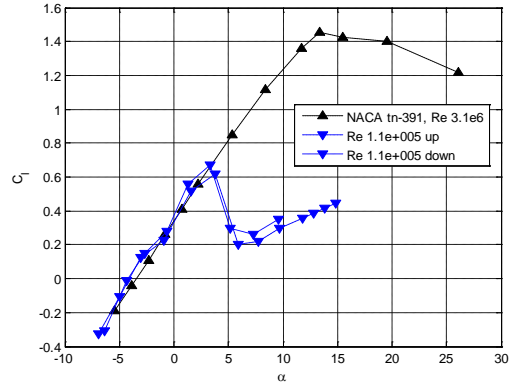


Figure A.55 $Re = 100k$ averaged lift curve with lift hysteresis

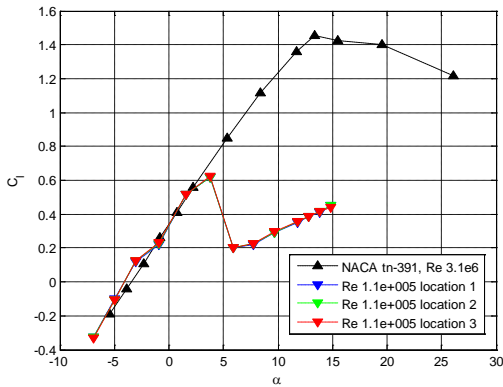


Figure A.53 $Re = 100k$ pre-averaged lift curves from 3 run locations

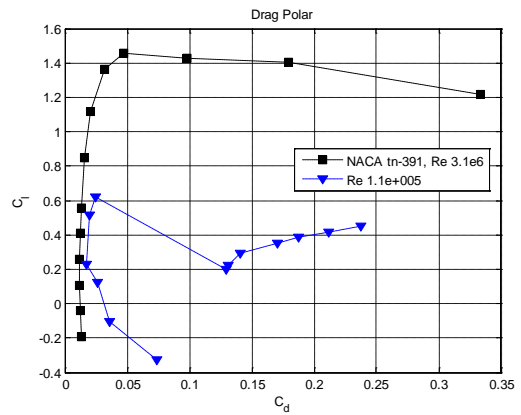


Figure A.56 $Re = 100k$ averaged drag polar

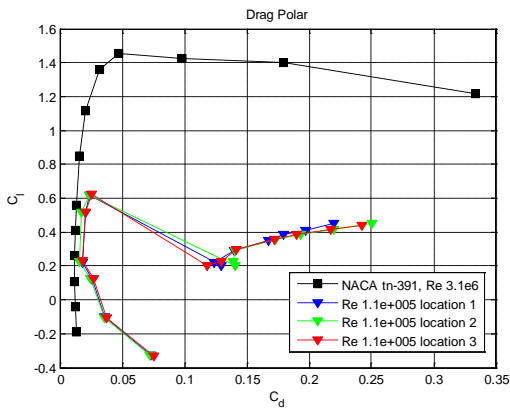


Figure A.54 $Re = 100k$ pre-averaged drag polars from 3 run locations

A.4 Re = 150,000

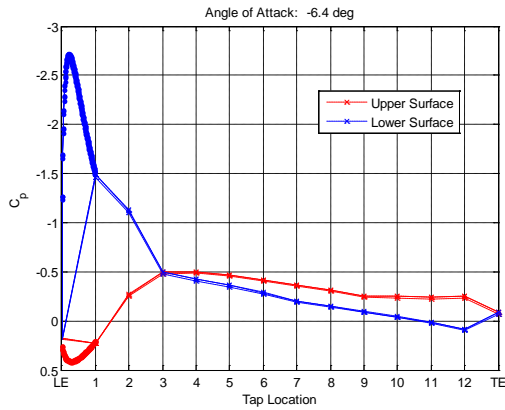


Figure A.57 C_p distribution, $Re = 150k$,
 $\alpha = -6.4^\circ$

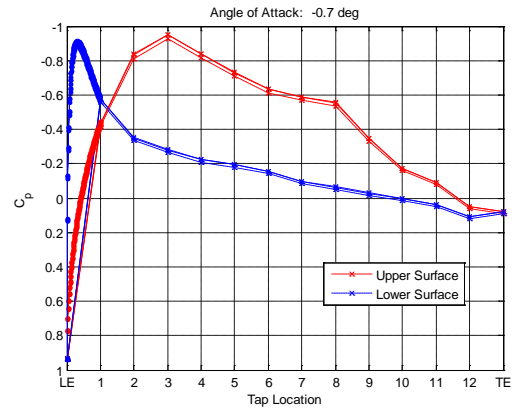


Figure A.60 C_p distribution, $Re = 150k$,
 $\alpha = -0.7^\circ$

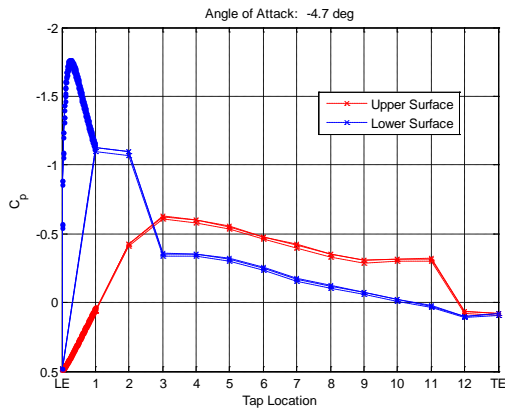


Figure A.58 C_p distribution, $Re = 150k$,
 $\alpha = -4.7^\circ$

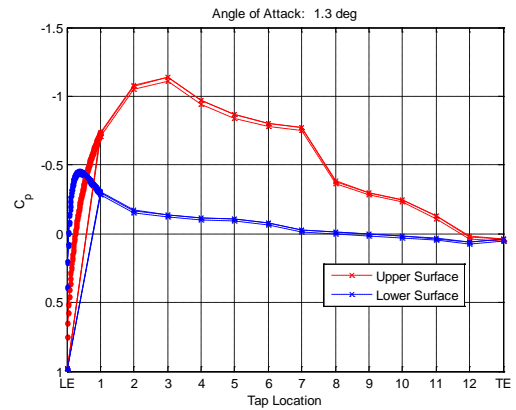


Figure A.61 C_p distribution, $Re = 150k$,
 $\alpha = 1.3^\circ$

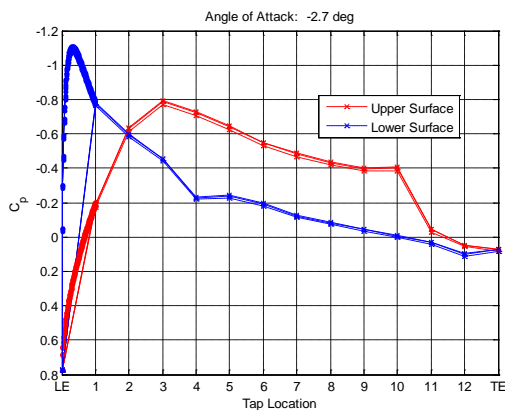


Figure A.59 C_p distribution, $Re = 150k$,
 $\alpha = -2.7^\circ$

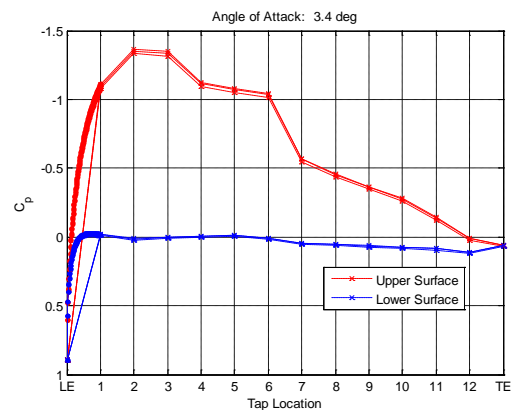


Figure A.62 C_p distribution, $Re = 150k$,
 $\alpha = 3.4^\circ$

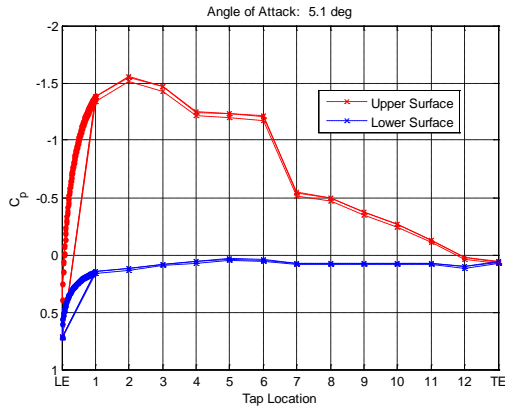


Figure A.63 C_p distribution, $Re = 150k$, $\alpha = 5.1^\circ$

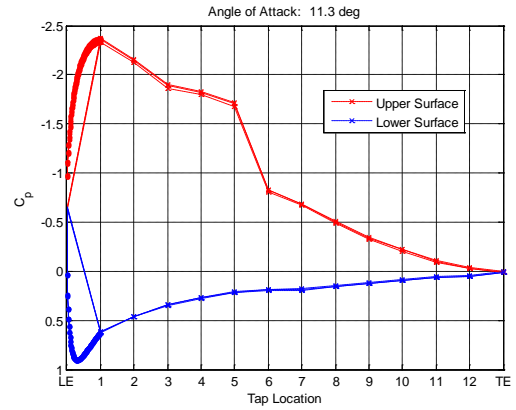


Figure A.66 C_p distribution, $Re = 150k$, $\alpha = 11.3^\circ$

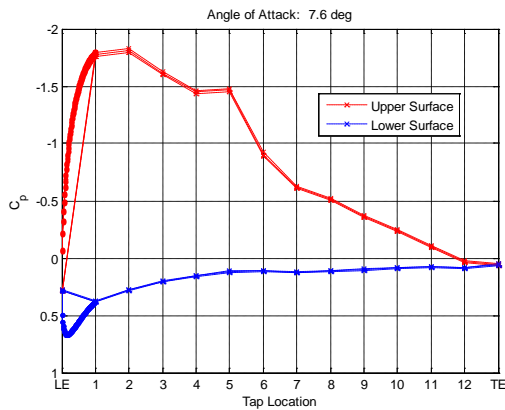


Figure A.64 C_p distribution, $Re = 150k$, $\alpha = 7.6^\circ$

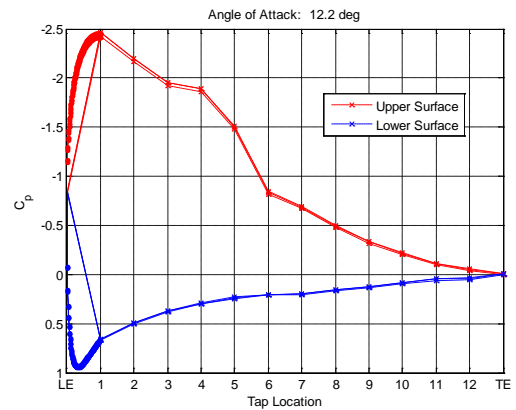


Figure A.67 C_p distribution, $Re = 150k$, $\alpha = 12.2^\circ$

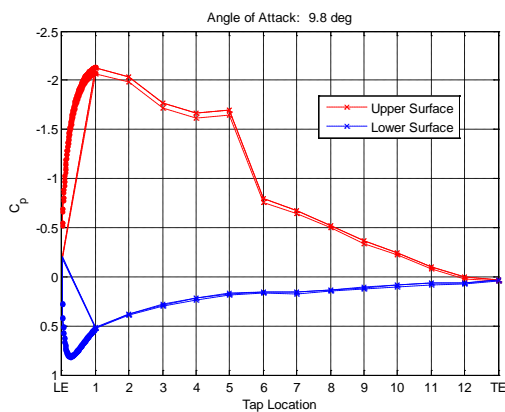


Figure A.65 C_p distribution, $Re = 150k$, $\alpha = 9.8^\circ$

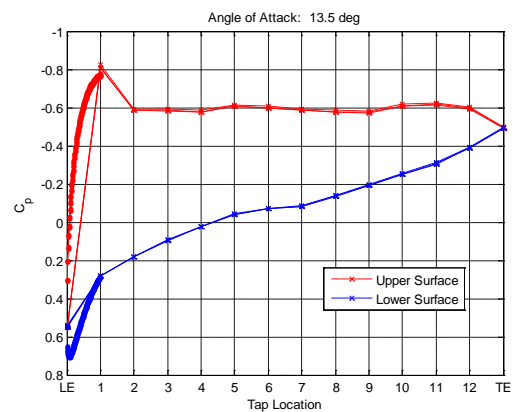


Figure A.68 C_p distribution, $Re = 150k$, $\alpha = 13.5^\circ$

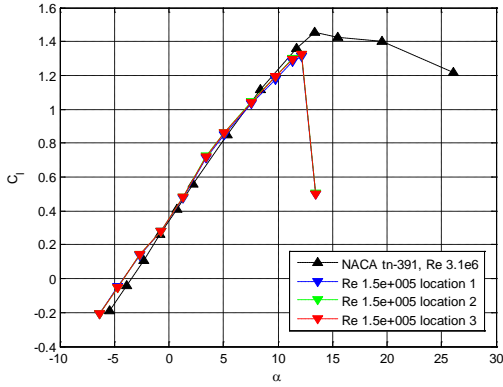


Figure A.69 $Re = 150k$ pre-averaged lift curves from 3 run locations

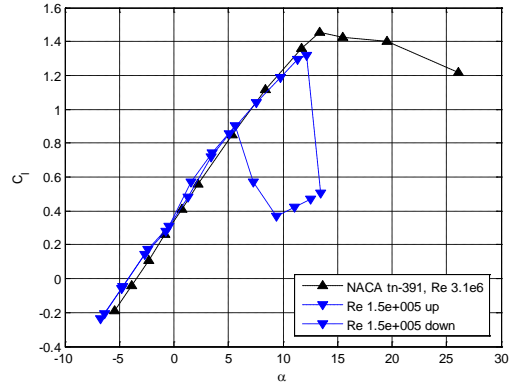


Figure A.71 $Re = 150k$ averaged lift curve with lift hysteresis

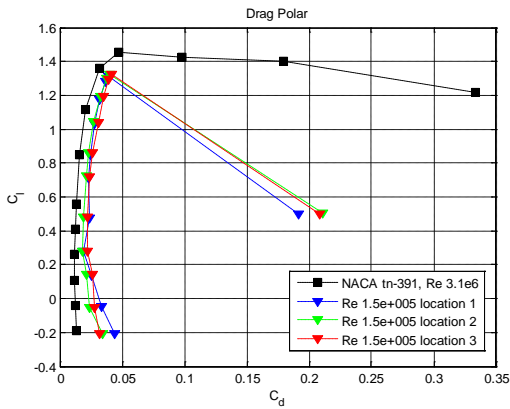


Figure A.70 $Re = 150k$ pre-averaged drag polars from 3 run locations

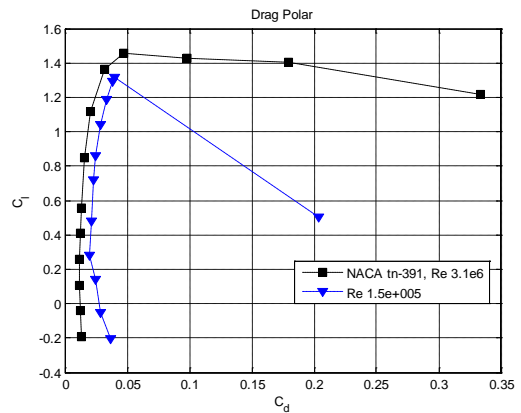


Figure A.72 $Re = 150k$ averaged drag polar

A.5 $Re = 200,000$

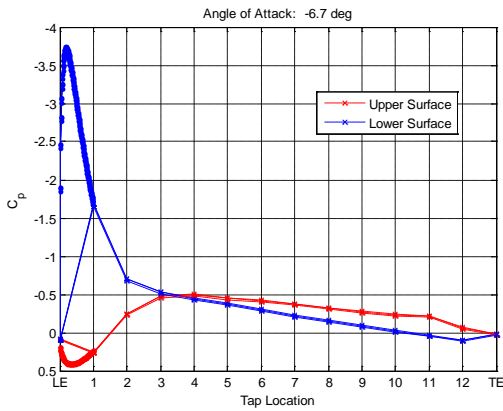


Figure A.73 C_p distribution, $Re = 200k$, $\alpha = -6.7^\circ$

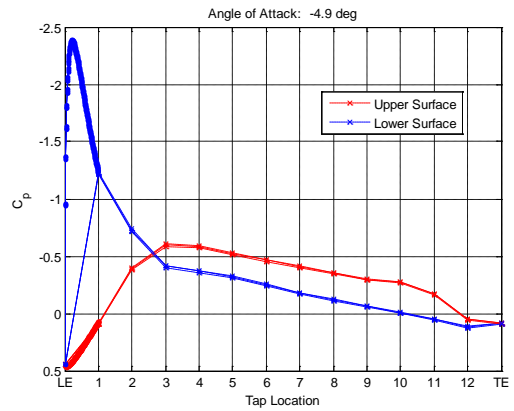


Figure A.74 C_p distribution, $Re = 200k$, $\alpha = -4.9^\circ$

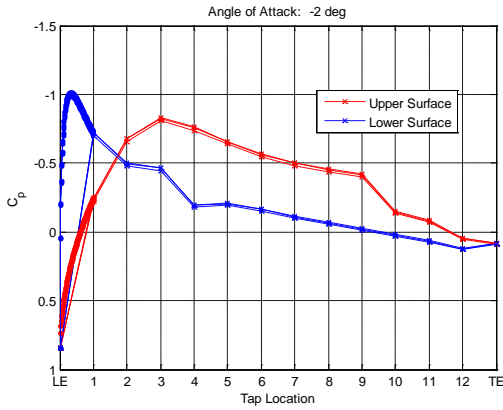


Figure A.75 C_p distribution, $Re = 200k$,
 $\alpha = -2^\circ$

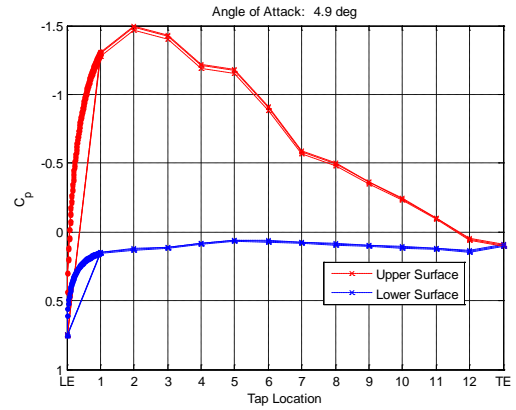


Figure A.78 C_p distribution, $Re = 200k$,
 $\alpha = 4.9^\circ$

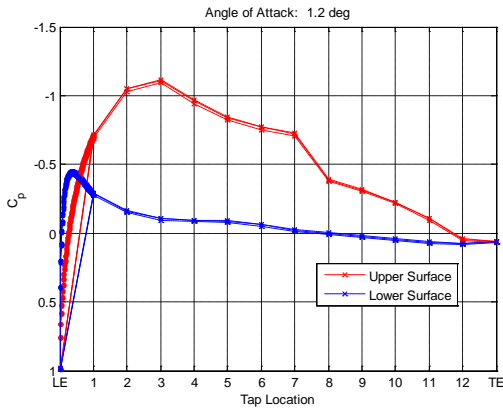


Figure A.76 C_p distribution, $Re = 200k$,
 $\alpha = 1.2^\circ$

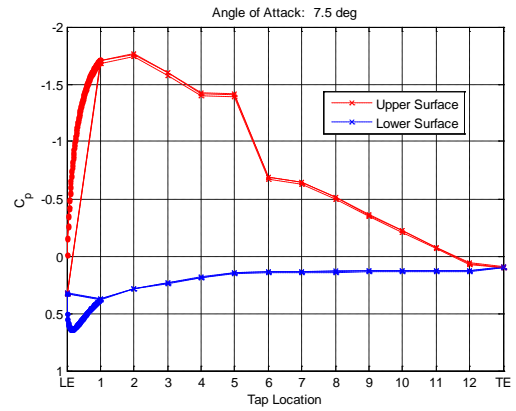


Figure A.79 C_p distribution, $Re = 200k$,
 $\alpha = 7.5^\circ$

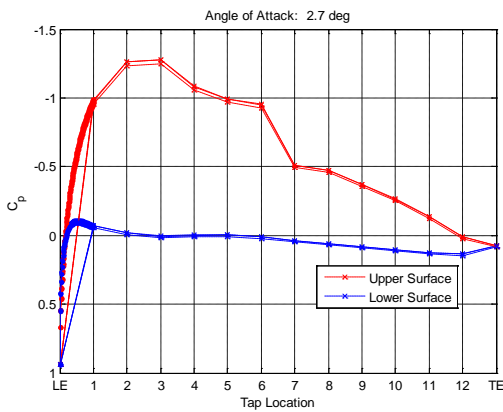


Figure A.77 C_p distribution, $Re = 200k$,
 $\alpha = 2.7^\circ$

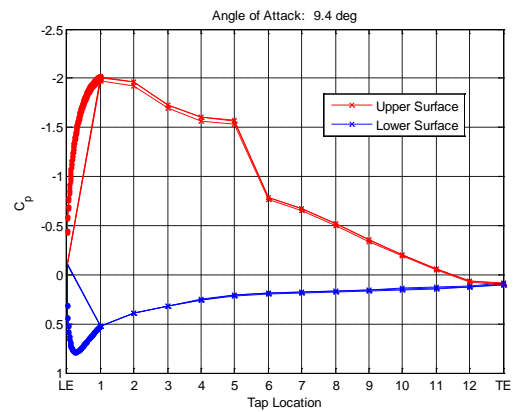


Figure A.80 C_p distribution, $Re = 200k$,
 $\alpha = 9.4^\circ$

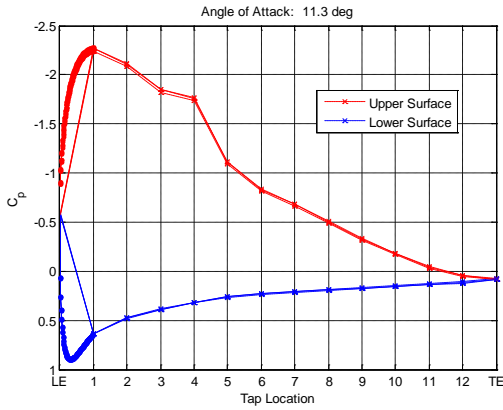


Figure A.81 C_p distribution, $Re = 200k$, $\alpha = 11.3^\circ$

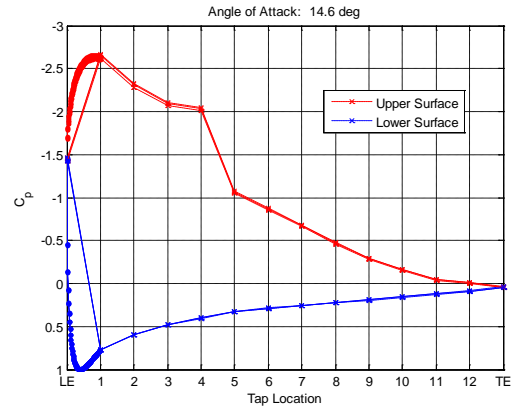


Figure A.84 C_p distribution, $Re = 200k$, $\alpha = 14.6^\circ$

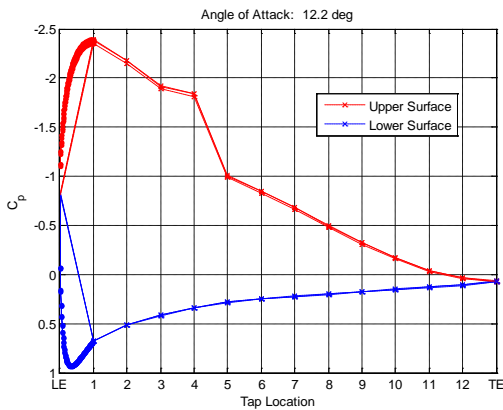


Figure A.82 C_p distribution, $Re = 200k$, $\alpha = 12.2^\circ$

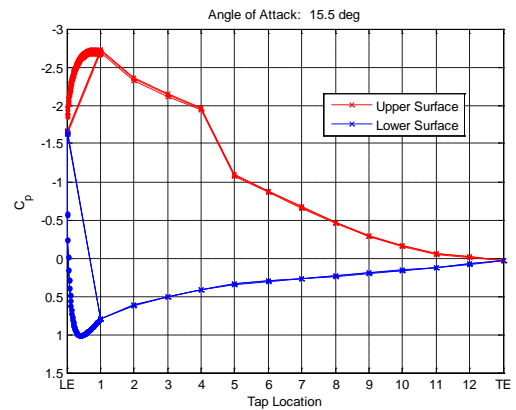


Figure A.85 C_p distribution, $Re = 200k$, $\alpha = 15.5^\circ$

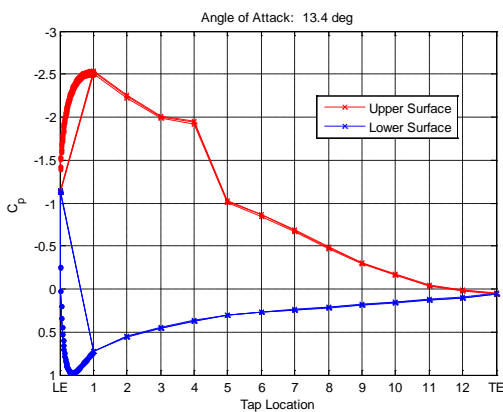


Figure A.83 C_p distribution, $Re = 200k$, $\alpha = 13.4^\circ$

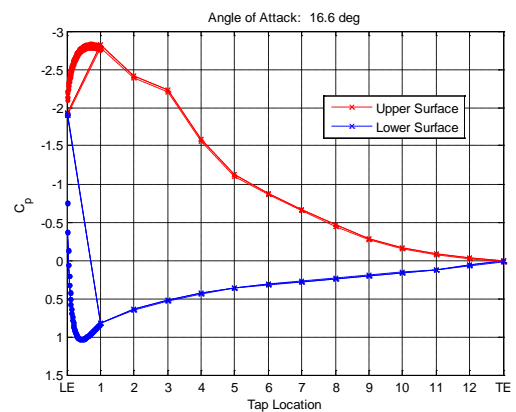


Figure A.86 C_p distribution, $Re = 200k$, $\alpha = 16.6^\circ$

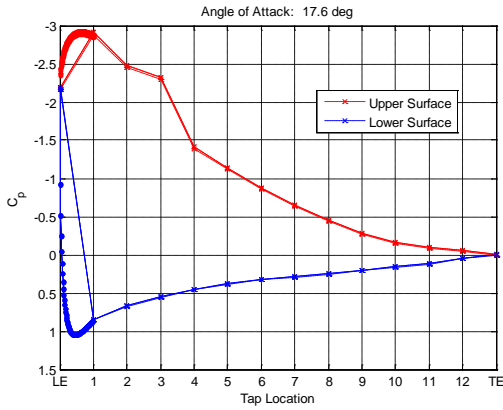


Figure A.87 C_p distribution, $Re = 200k$, $\alpha = 17.6^\circ$

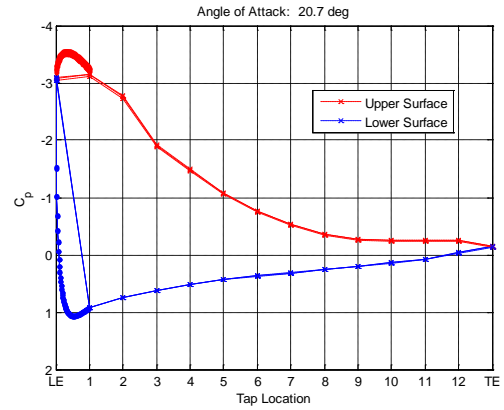


Figure A.90 C_p distribution, $Re = 200k$, $\alpha = 20.7^\circ$

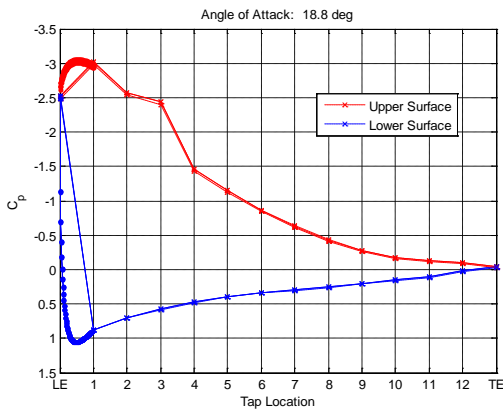


Figure A.88 C_p distribution, $Re = 200k$, $\alpha = 18.8^\circ$

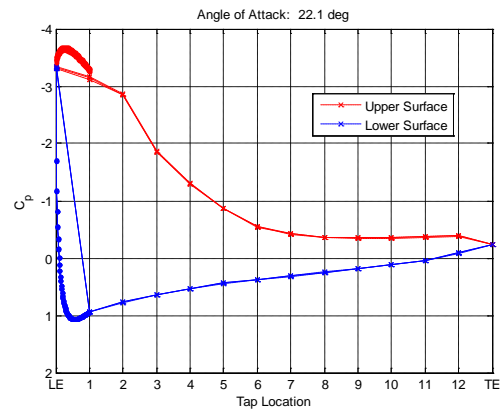


Figure A.91 C_p distribution, $Re = 200k$, $\alpha = 22.1^\circ$

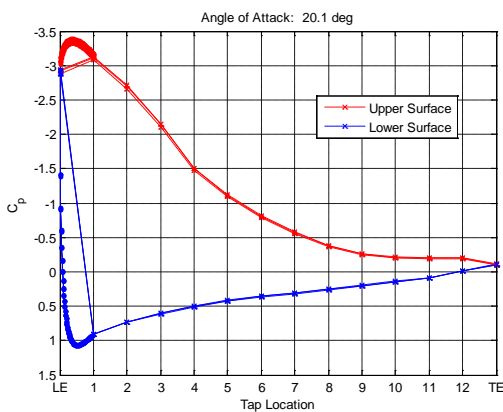


Figure A.89 C_p distribution, $Re = 200k$, $\alpha = 20.1^\circ$

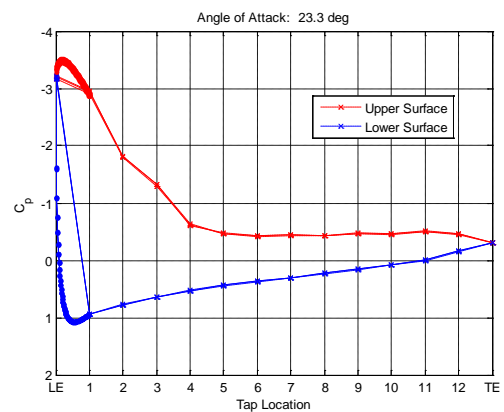


Figure A.92 C_p distribution, $Re = 200k$, $\alpha = 23.3^\circ$

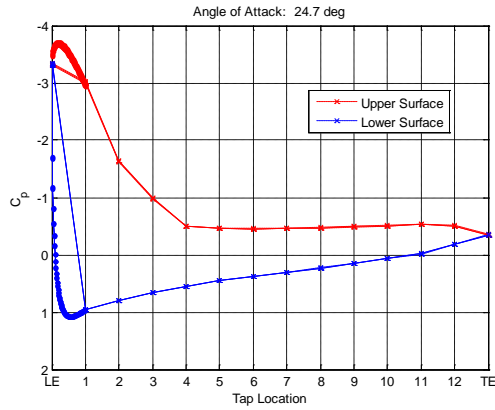


Figure A.93 C_p distribution, $Re = 200k$, $\alpha = 24.7^\circ$

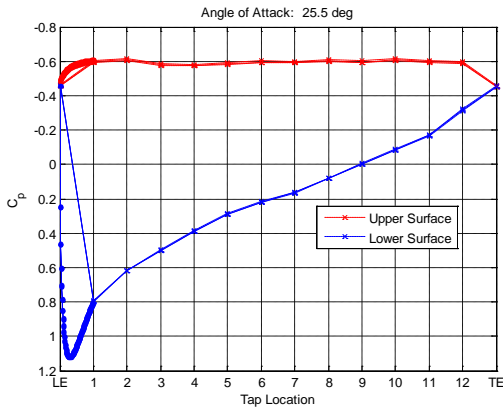


Figure A.94 C_p distribution, $Re = 200k$, $\alpha = 25.5^\circ$

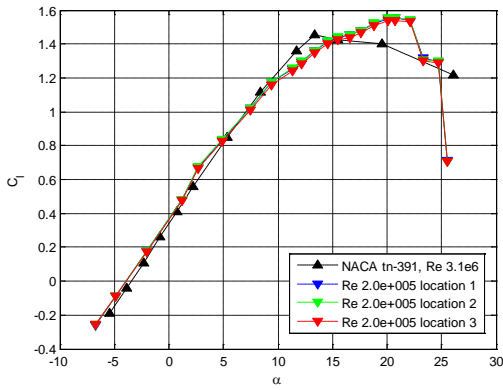


Figure A.95 $Re = 200k$ pre-averaged lift curves from 3 run locations

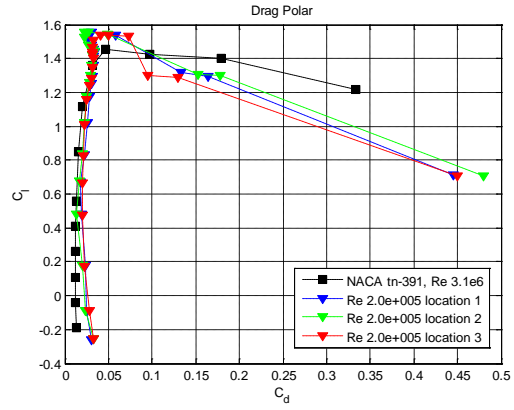


Figure A.96 $Re = 200k$ pre-averaged drag polars from 3 run locations

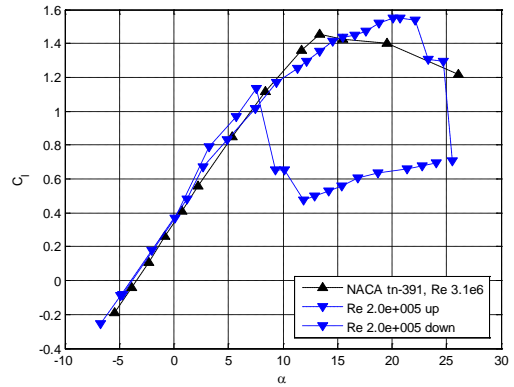


Figure A.97 $Re = 200k$ averaged lift curve with lift hysteresis

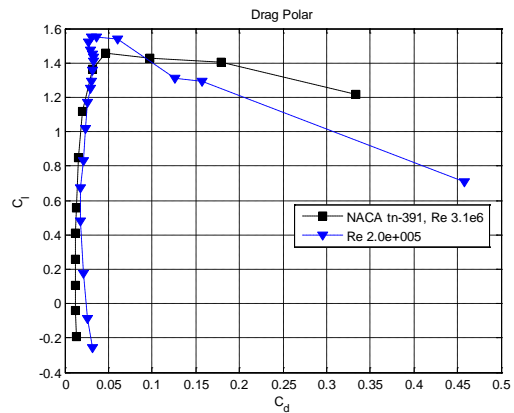


Figure A.98 $Re = 200k$ averaged drag polar

A.6 Re = 250,000

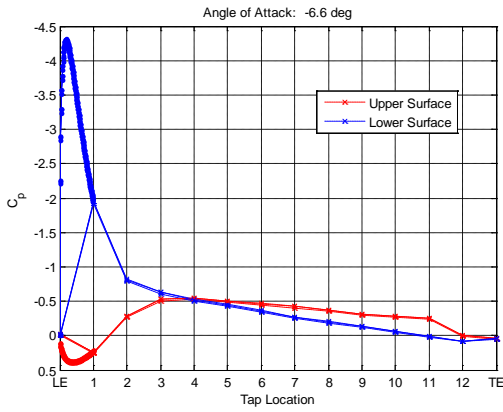


Figure A.99 C_p distribution, $Re = 250k$,
 $\alpha = -6.6^\circ$

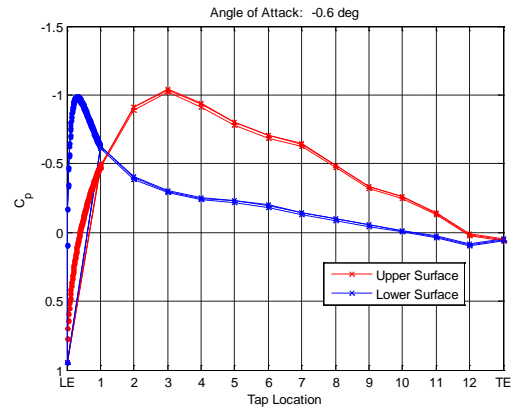


Figure A.102 C_p distribution, $Re = 250k$,
 $\alpha = -0.6^\circ$

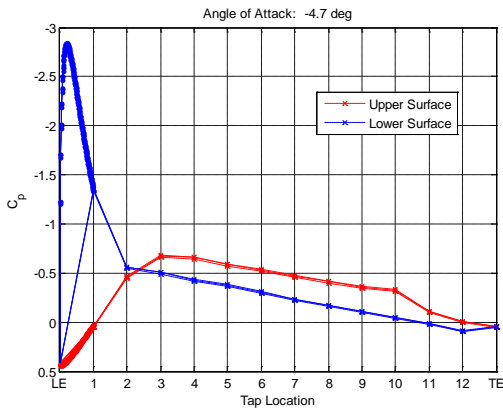


Figure A.100 C_p distribution, $Re = 250k$,
 $\alpha = -4.7^\circ$

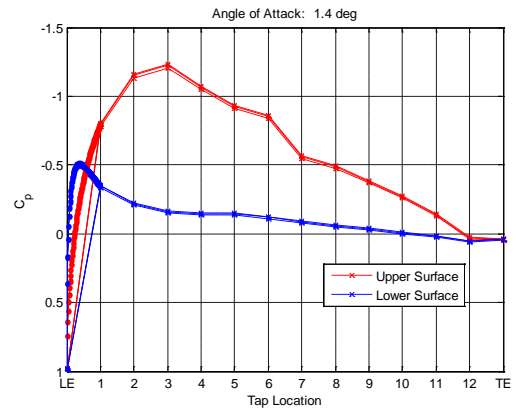


Figure A.103 C_p distribution, $Re = 250k$,
 $\alpha = 1.4^\circ$

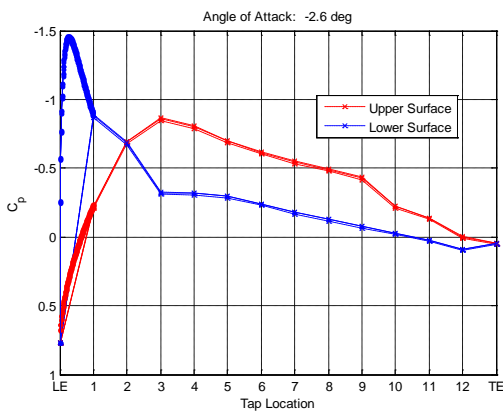


Figure A.101 C_p distribution, $Re = 250k$,
 $\alpha = -2.6^\circ$

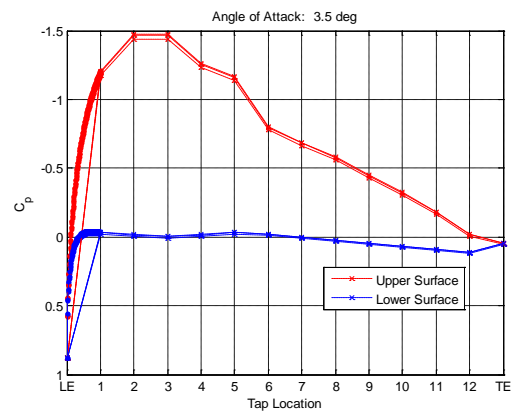


Figure A.104 C_p distribution, $Re = 250k$,
 $\alpha = 3.5^\circ$

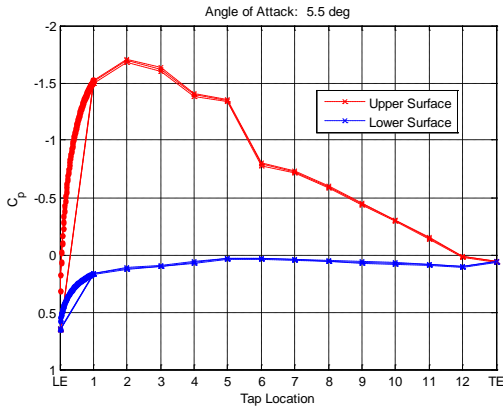


Figure A.105 C_p distribution, $Re = 250k$, $\alpha = 5.5^\circ$

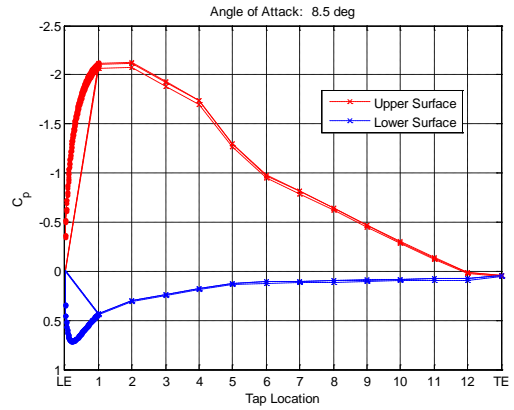


Figure A.108 C_p distribution, $Re = 250k$, $\alpha = 8.5^\circ$

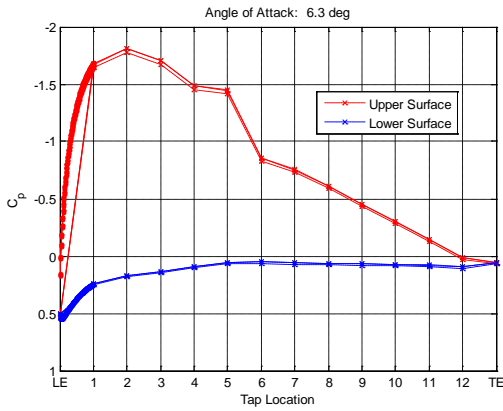


Figure A.106 C_p distribution, $Re = 250k$, $\alpha = 6.3^\circ$

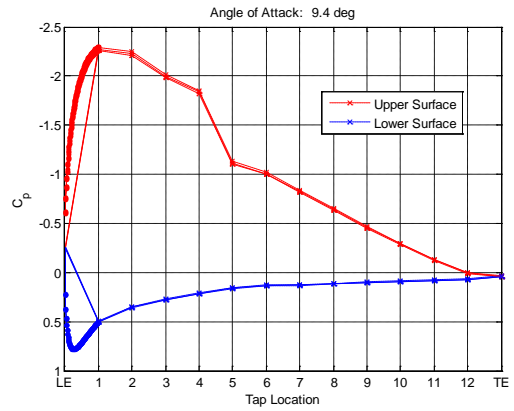


Figure A.109 C_p distribution, $Re = 250k$, $\alpha = 9.4^\circ$

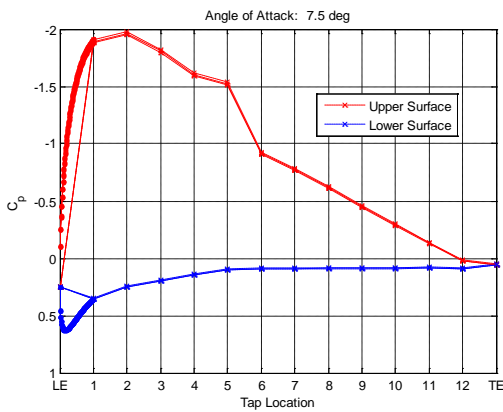


Figure A.107 C_p distribution, $Re = 250k$, $\alpha = 7.5^\circ$

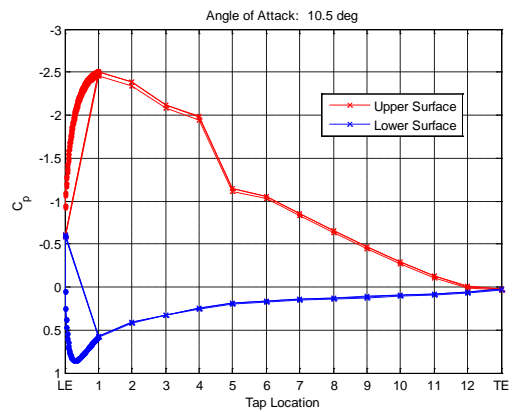


Figure A.110 C_p distribution, $Re = 250k$, $\alpha = 10.5^\circ$

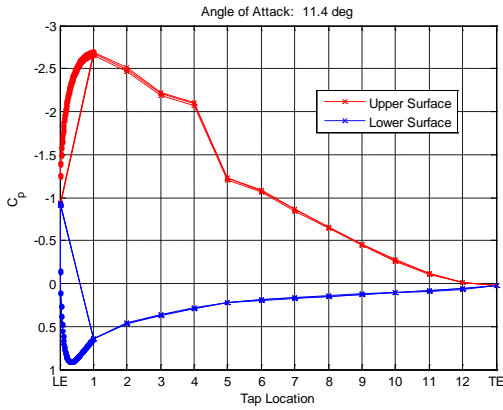


Figure A.111 C_p distribution, $Re = 250k$, $\alpha = 11.4^\circ$

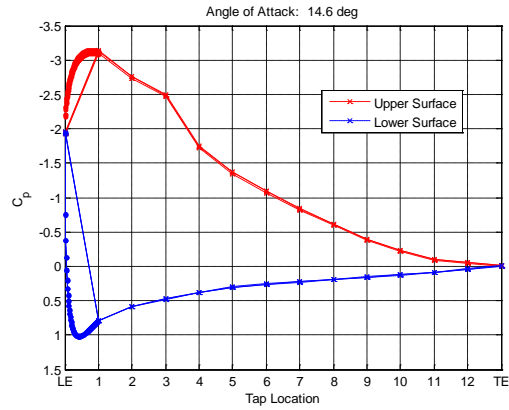


Figure A.114 C_p distribution, $Re = 250k$, $\alpha = 14.6^\circ$

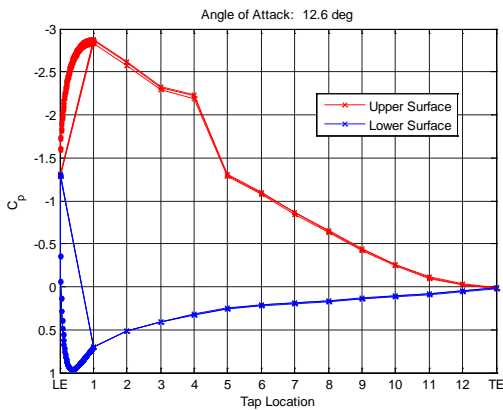


Figure A.112 C_p distribution, $Re = 250k$, $\alpha = 12.6^\circ$

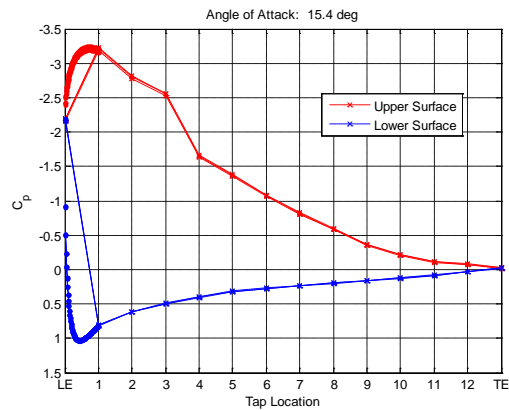


Figure A.115 C_p distribution, $Re = 250k$, $\alpha = 15.4^\circ$

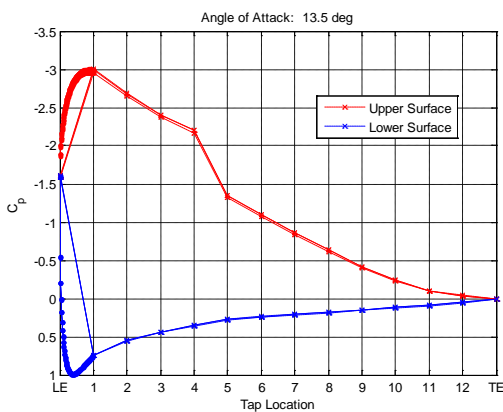


Figure A.113 C_p distribution, $Re = 250k$, $\alpha = 13.5^\circ$

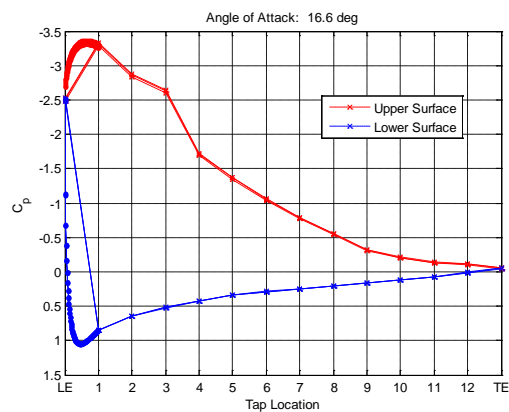


Figure A.116 C_p distribution, $Re = 250k$, $\alpha = 16.6^\circ$

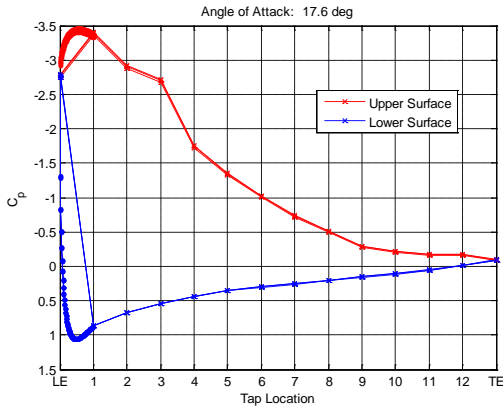


Figure A.117 C_p distribution, $Re = 250k$, $\alpha = 17.6^\circ$

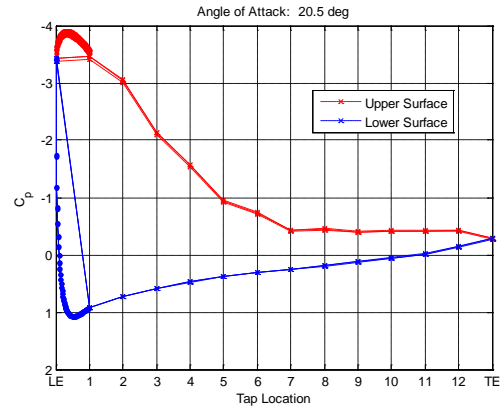


Figure A.120 C_p distribution, $Re = 250k$, $\alpha = 20.5^\circ$

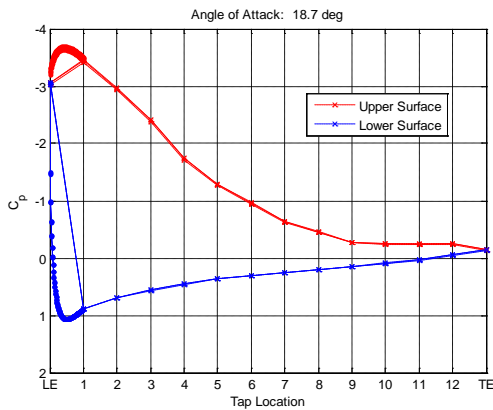


Figure A.118 C_p distribution, $Re = 250k$, $\alpha = 18.7^\circ$

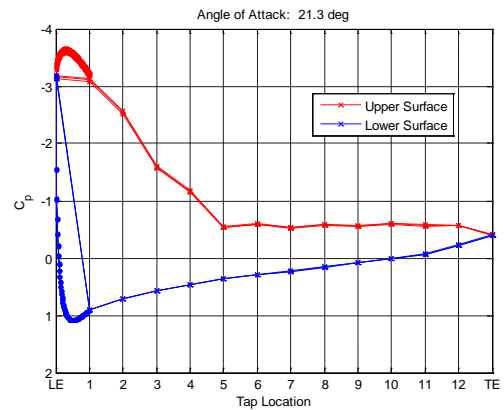


Figure A.121 C_p distribution, $Re = 250k$, $\alpha = 21.3^\circ$

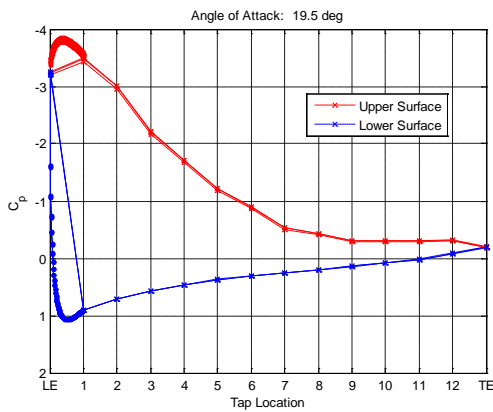


Figure A.119 C_p distribution, $Re = 250k$, $\alpha = 19.5^\circ$

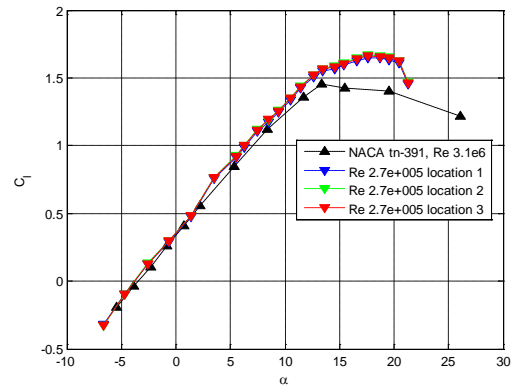


Figure A.122 $Re = 250k$ pre-averaged lift curves from 3 run locations

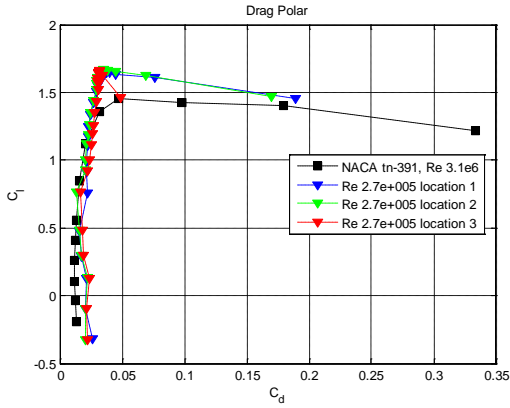


Figure A.123 $Re = 250k$ pre-averaged drag polars from 3 run locations

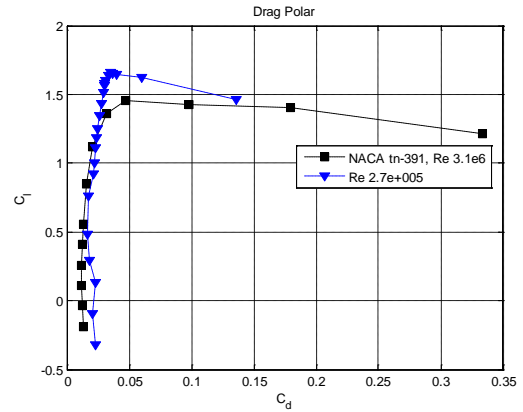


Figure A.125 $Re = 250k$ averaged drag polar

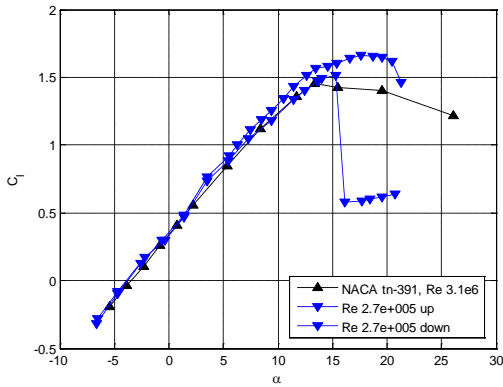


Figure A.124 $Re = 250k$ averaged lift curve with lift hysteresis

A.7 $Re = 300,000$

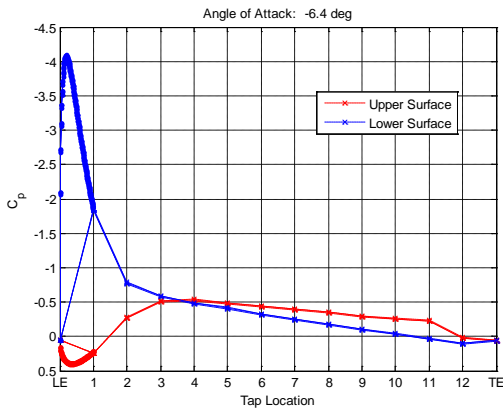


Figure A.126 C_p distribution, $Re = 300k$, $\alpha = -6.4^\circ$

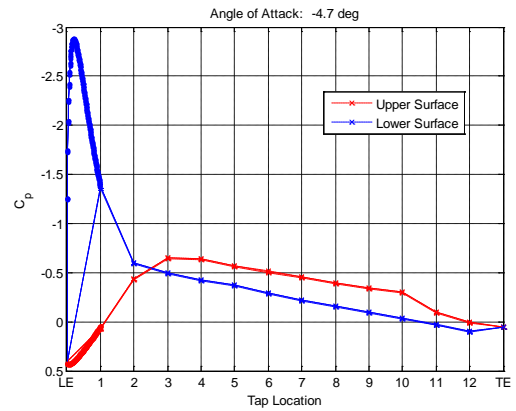


Figure A.127 C_p distribution, $Re = 300k$, $\alpha = -4.7^\circ$

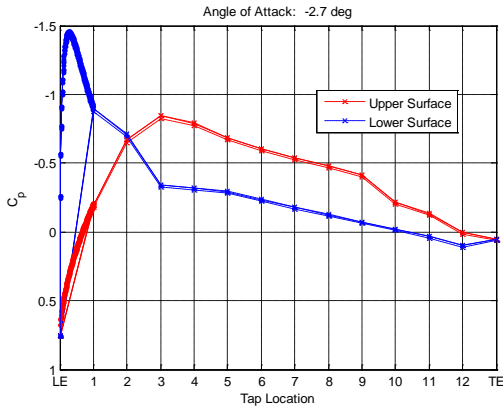


Figure A.128 C_p distribution, $Re = 300k$, $\alpha = -2.7^\circ$

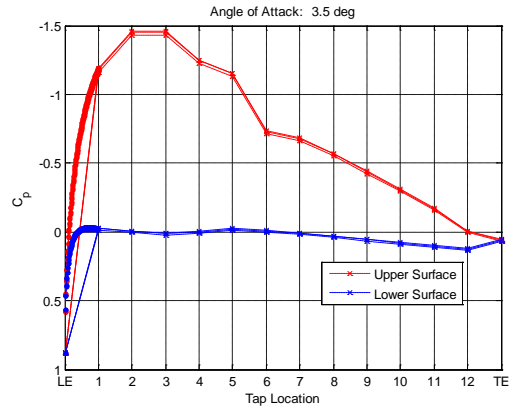


Figure A.131 C_p distribution, $Re = 300k$, $\alpha = 3.5^\circ$

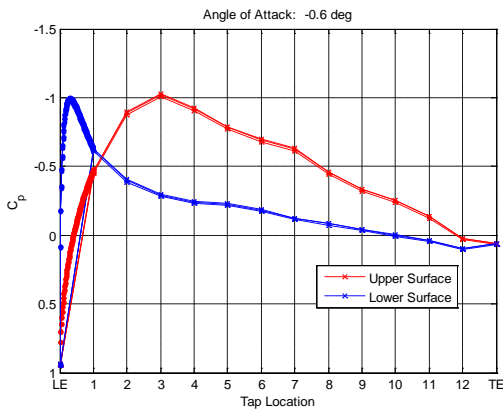


Figure A.129 C_p distribution, $Re = 300k$, $\alpha = -0.6^\circ$

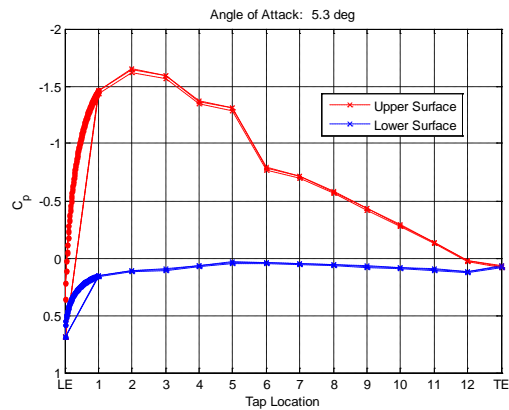


Figure A.132 C_p distribution, $Re = 300k$, $\alpha = 5.3^\circ$

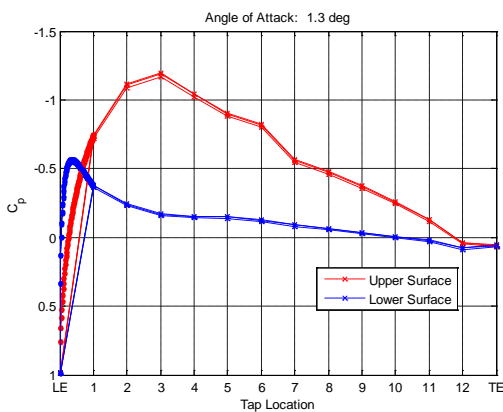


Figure A.130 C_p distribution, $Re = 300k$, $\alpha = 1.3^\circ$

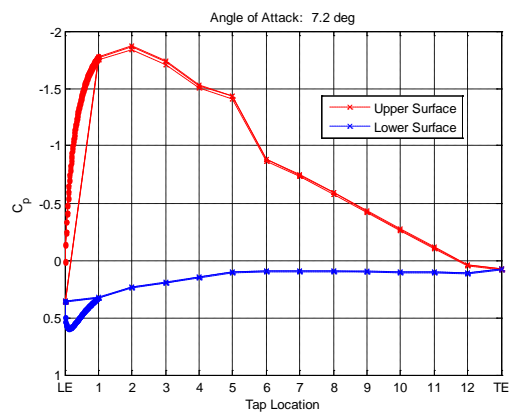


Figure A.133 C_p distribution, $Re = 300k$, $\alpha = 7.2^\circ$

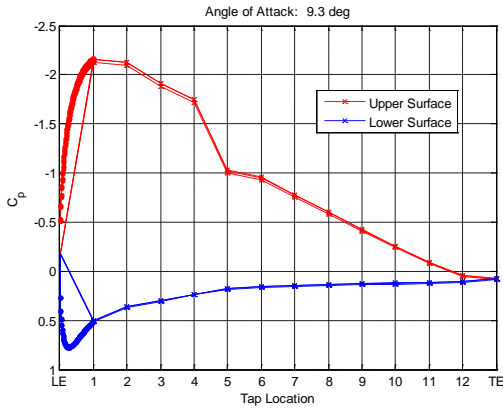


Figure A.134 C_p distribution, $Re = 300k$, $\alpha = 9.3^\circ$

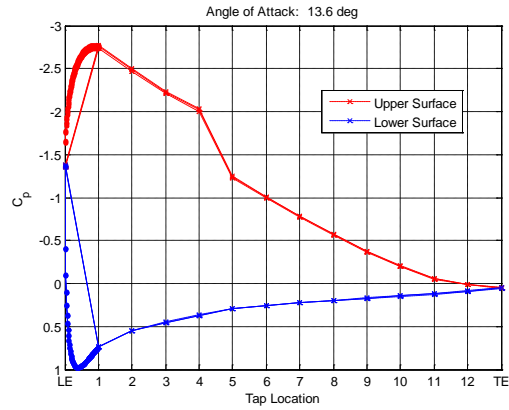


Figure A.137 C_p distribution, $Re = 300k$, $\alpha = 13.6^\circ$

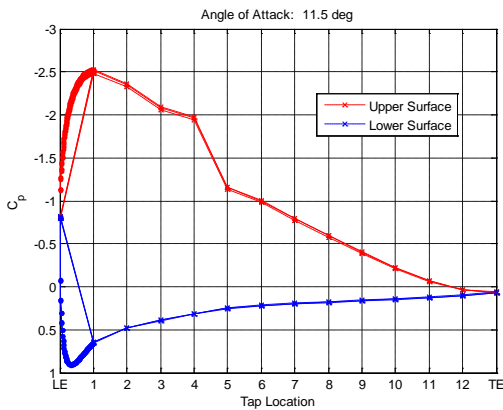


Figure A.135 C_p distribution, $Re = 300k$, $\alpha = 11.5^\circ$

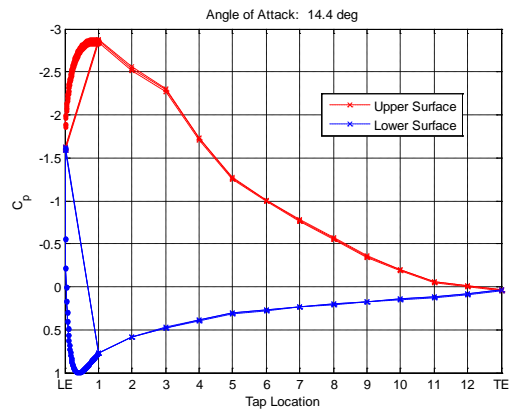


Figure A.138 C_p distribution, $Re = 300k$, $\alpha = 14.4^\circ$

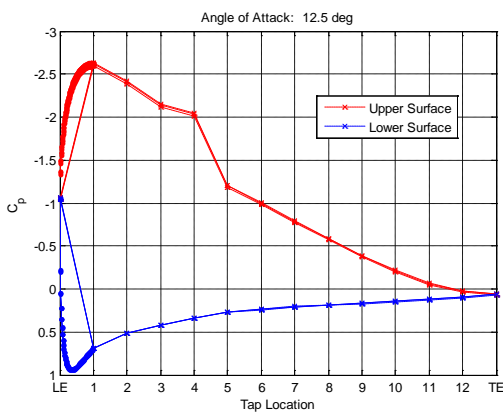


Figure A.136 C_p distribution, $Re = 300k$, $\alpha = 12.5^\circ$

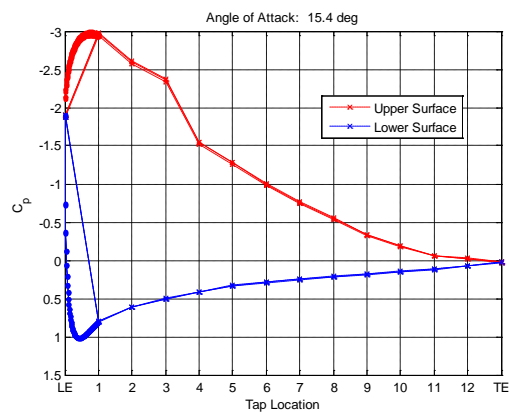


Figure A.139 C_p distribution, $Re = 300k$, $\alpha = 15.4^\circ$

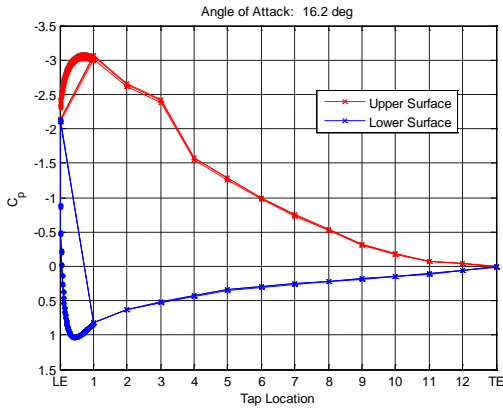


Figure A.140 C_p distribution, $Re = 300k$, $\alpha = 16.2^\circ$

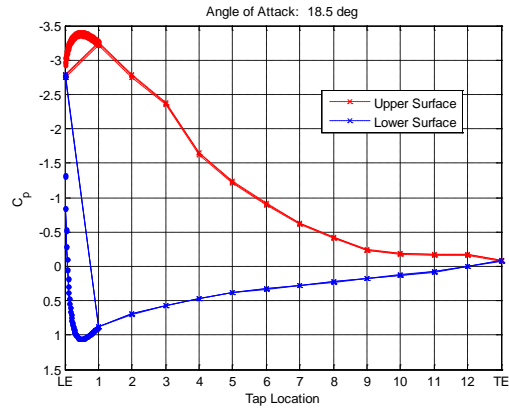


Figure A.143 C_p distribution, $Re = 300k$, $\alpha = 18.5^\circ$

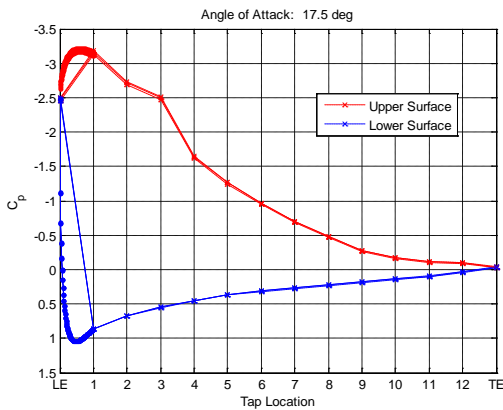


Figure A.141 C_p distribution, $Re = 300k$, $\alpha = 17.5^\circ$

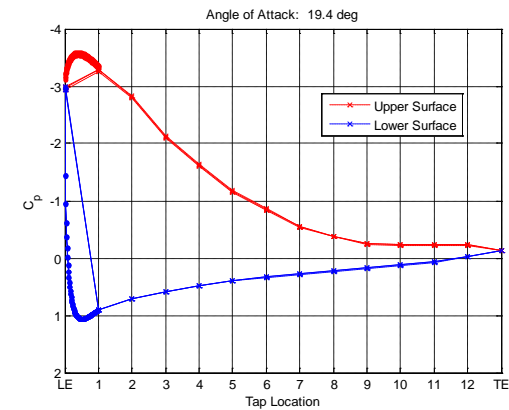


Figure A.144 C_p distribution, $Re = 300k$, $\alpha = 19.4^\circ$

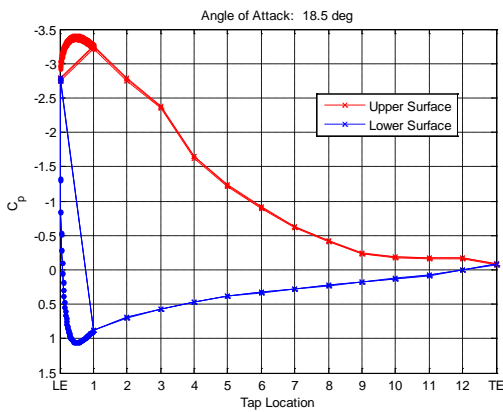


Figure A.142 C_p distribution, $Re = 300k$, $\alpha = 17.5^\circ$

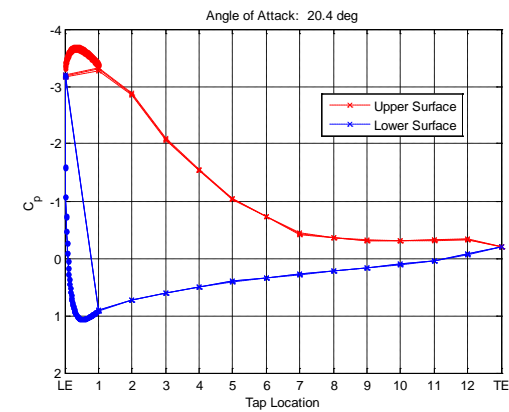


Figure A.145 C_p distribution, $Re = 300k$, $\alpha = 20.4^\circ$

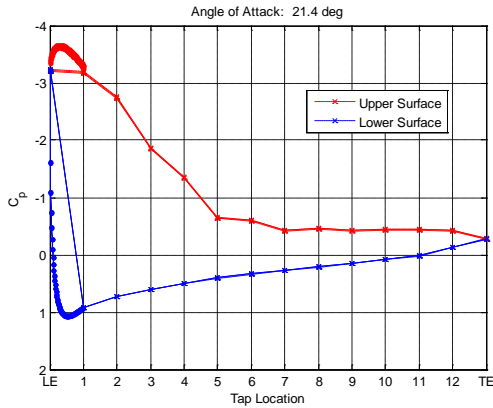


Figure A.146 C_p distribution, $Re = 300k$, $\alpha = 21.4^\circ$

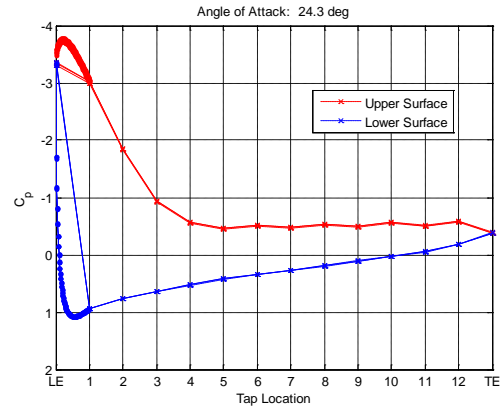


Figure A.149 C_p distribution, $Re = 300k$, $\alpha = 24.3^\circ$

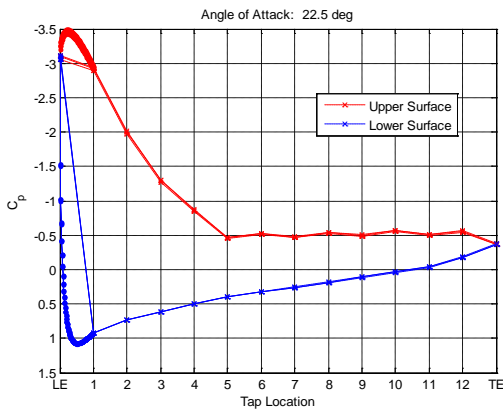


Figure A.147 C_p distribution, $Re = 300k$, $\alpha = 22.5^\circ$

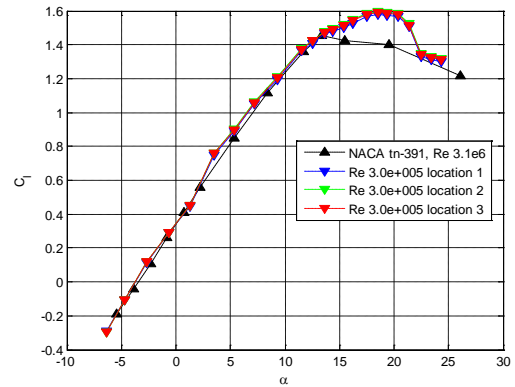


Figure A.150 $Re = 300k$ pre-averaged lift curves from 3 run locations

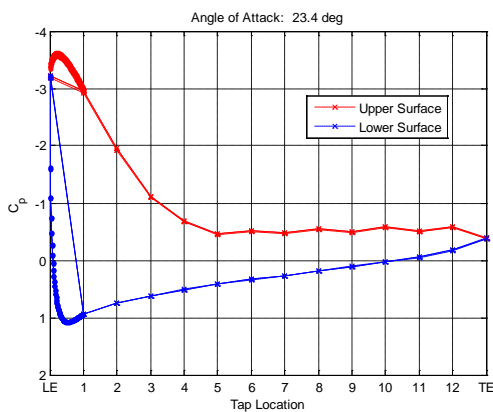


Figure A.148 C_p distribution, $Re = 300k$, $\alpha = 23.4^\circ$

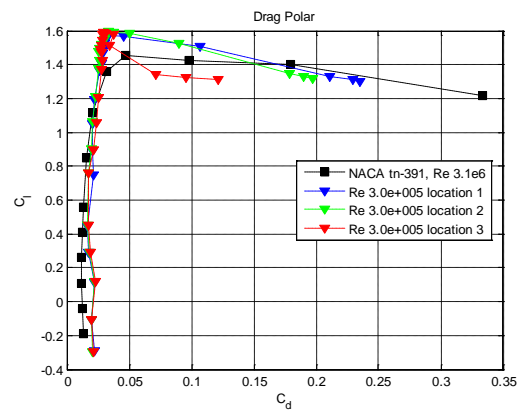


Figure A.151 $Re = 300k$ pre-averaged drag polars from 3 run locations

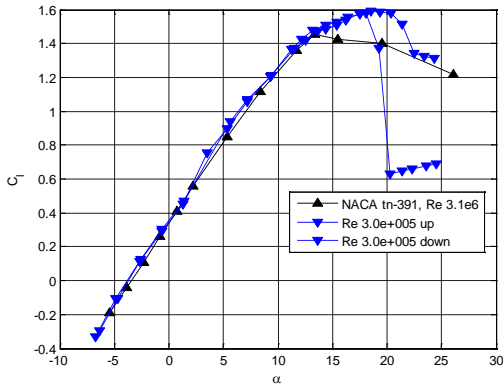


Figure A.152 $Re = 300k$ averaged lift curve with lift hysteresis

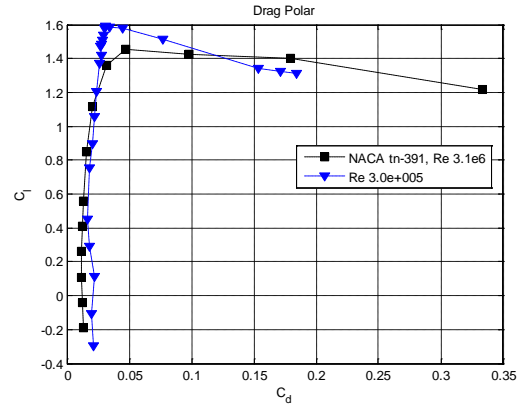


Figure A.153 $Re = 300k$ averaged drag polar

A.8 $Re = 500,000$

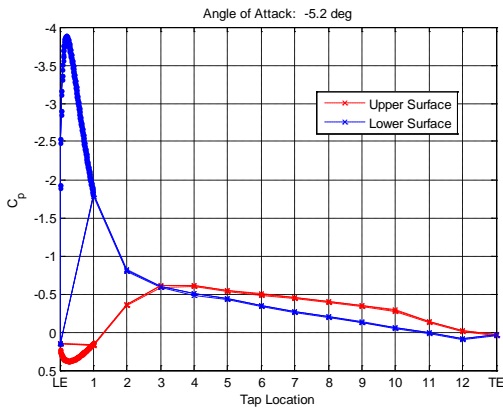


Figure A.154 C_p distribution, $Re = 500k$, $\alpha = -5.2^\circ$

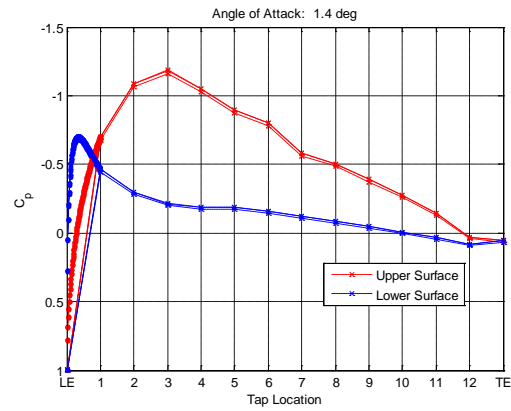


Figure A.156 C_p distribution, $Re = 500k$, $\alpha = 1.4^\circ$

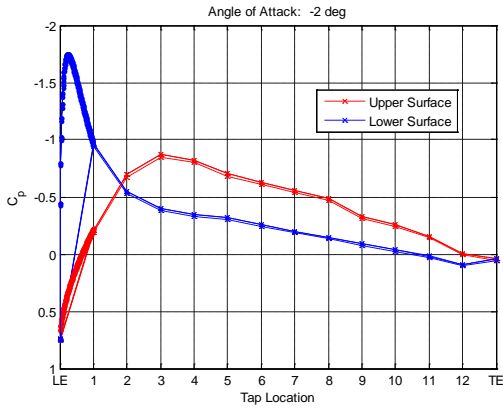


Figure A.155 C_p distribution, $Re = 500k$, $\alpha = -2^\circ$

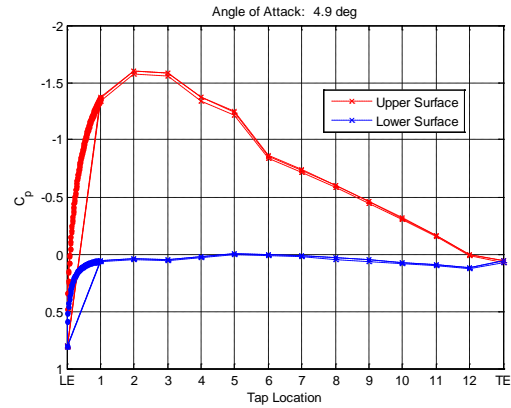


Figure A.157 C_p distribution, $Re = 500k$, $\alpha = 4.9^\circ$

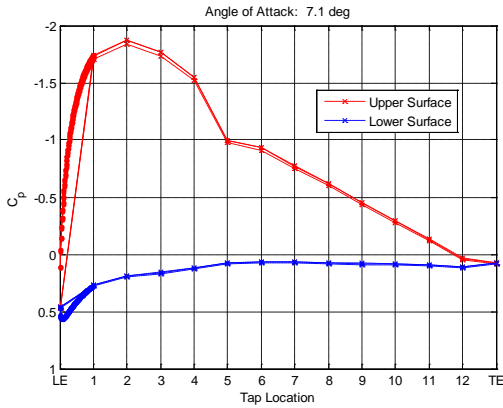


Figure A.158 C_p distribution, $Re = 500k$, $\alpha = 7.1^\circ$

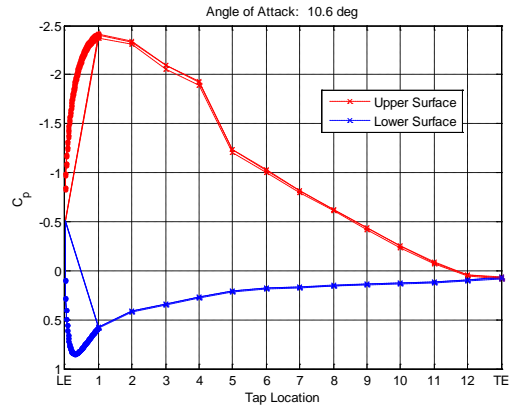


Figure A.161 C_p distribution, $Re = 500k$, $\alpha = 10.6^\circ$

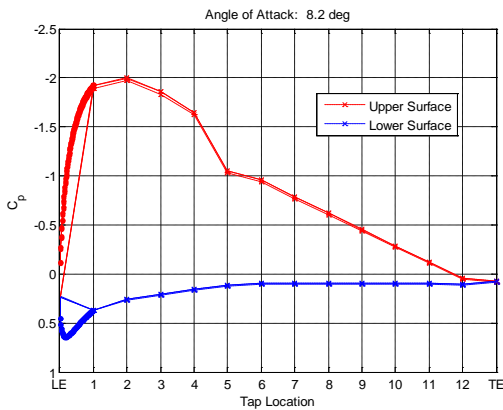


Figure A.159 C_p distribution, $Re = 500k$, $\alpha = 8.2^\circ$

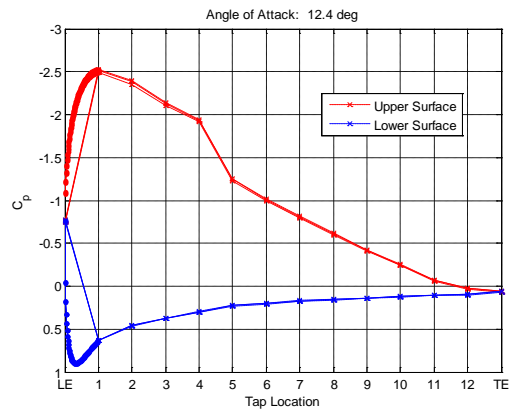


Figure A.162 C_p distribution, $Re = 500k$, $\alpha = 12.4^\circ$

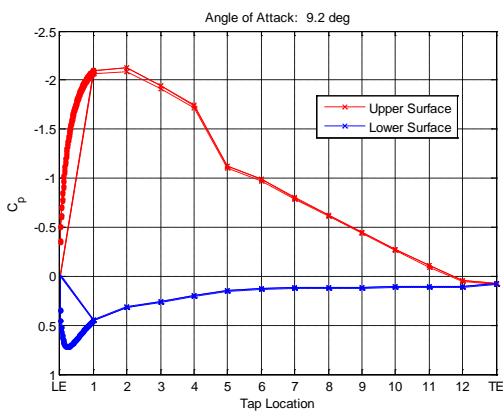


Figure A.160 C_p distribution, $Re = 500k$, $\alpha = 9.2^\circ$

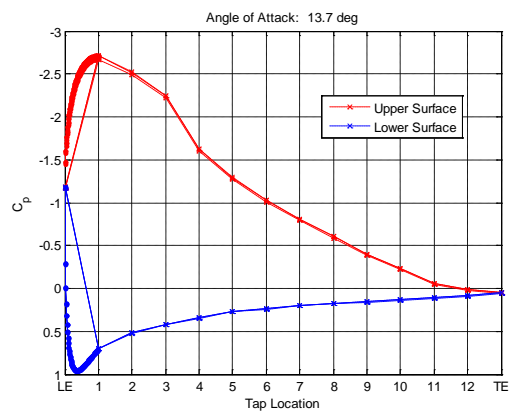


Figure A.163 C_p distribution, $Re = 500k$, $\alpha = 13.7^\circ$

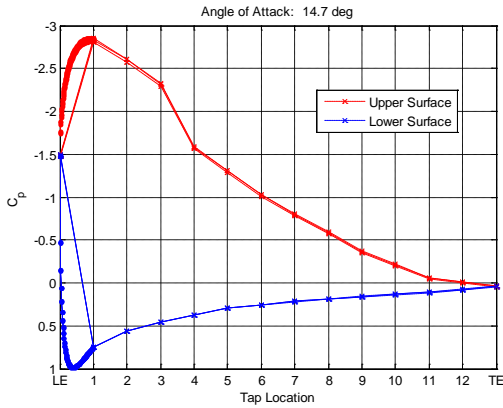


Figure A.164 C_p distribution, $Re = 500k$, $\alpha = 14.7^\circ$

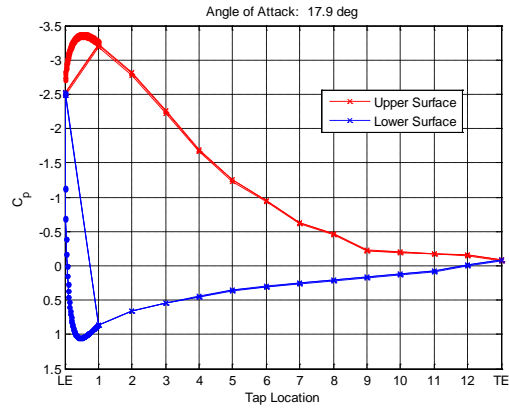


Figure A.167 C_p distribution, $Re = 500k$, $\alpha = 17.9^\circ$

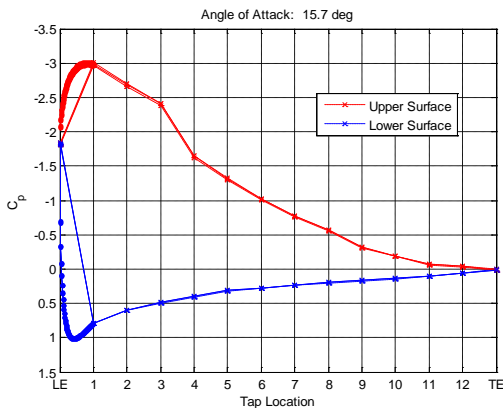


Figure A.165 C_p distribution, $Re = 500k$, $\alpha = 15.7^\circ$

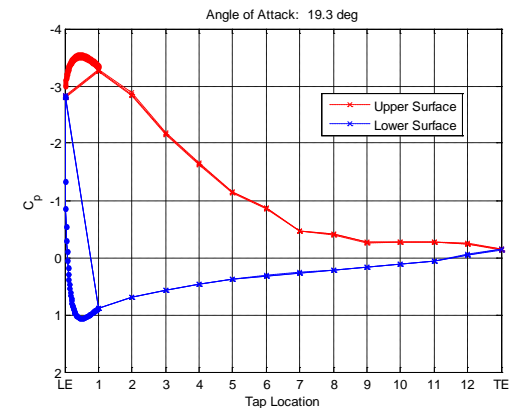


Figure A.168 C_p distribution, $Re = 500k$, $\alpha = 19.3^\circ$

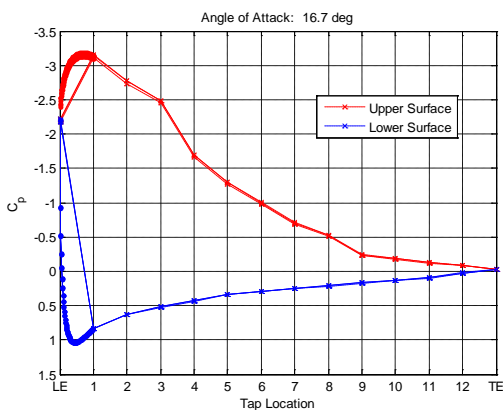


Figure A.166 C_p distribution, $Re = 500k$, $\alpha = 16.7^\circ$

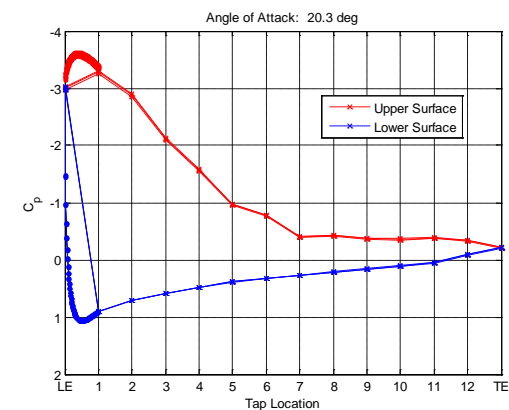


Figure A.169 C_p distribution, $Re = 500k$, $\alpha = 20.3^\circ$

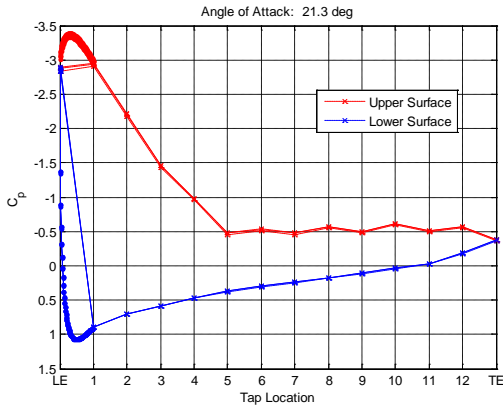


Figure A.170 C_p distribution, $Re = 500k$, $\alpha = 21.3^\circ$

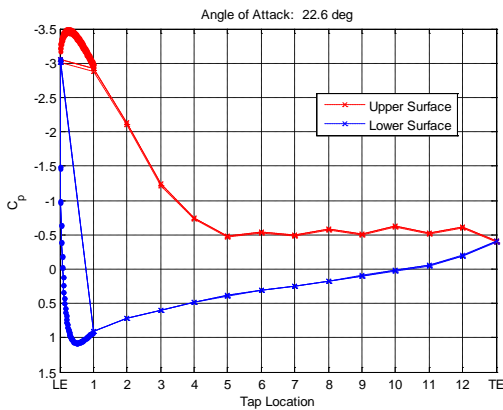


Figure A.171 C_p distribution, $Re = 500k$, $\alpha = 22.6^\circ$

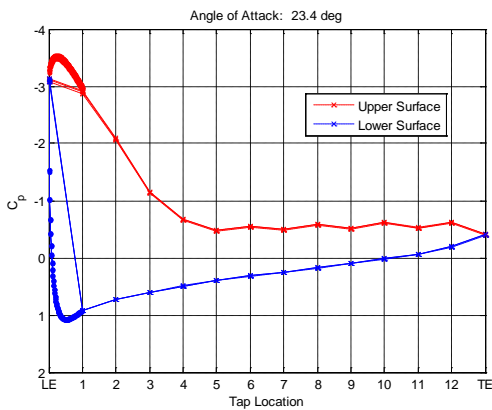


Figure A.172 C_p distribution, $Re = 500k$, $\alpha = 23.4^\circ$

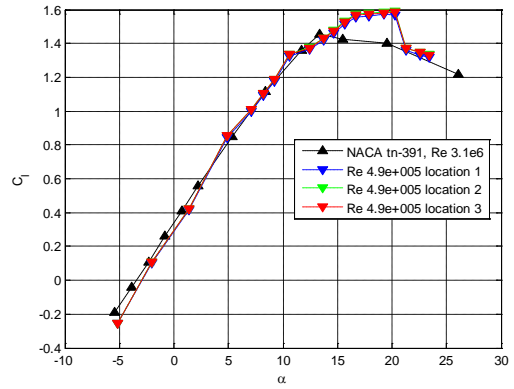


Figure A.173 $Re = 500k$ pre-averaged lift curves from 3 run locations

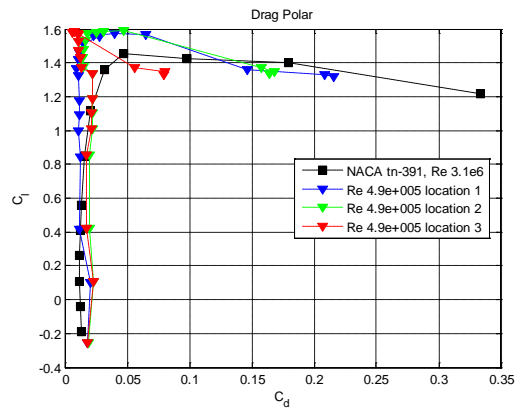


Figure A.174 $Re = 500k$ pre-averaged drag polars from 3 run locations

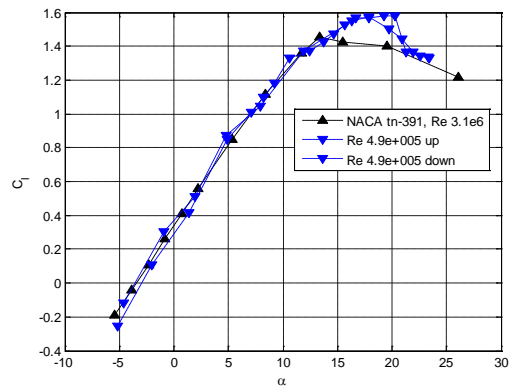


Figure A.175 $Re = 500k$ averaged lift curve with lift hysteresis

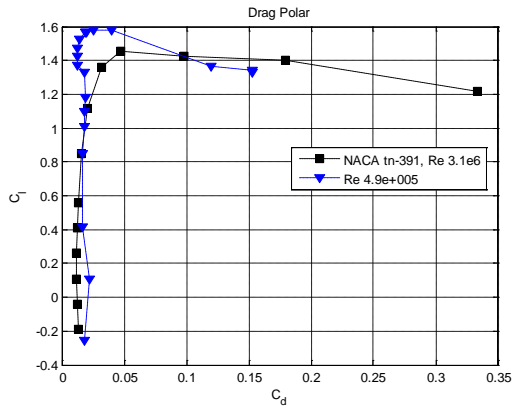


Figure A.176 $Re = 500k$ averaged drag polar

Copyright © Michael Andrew Thamann 2012

Appendix B Bumpy Airfoil Results

For completeness, the following are all the results from the wind tunnel testing of the bumpy airfoil.

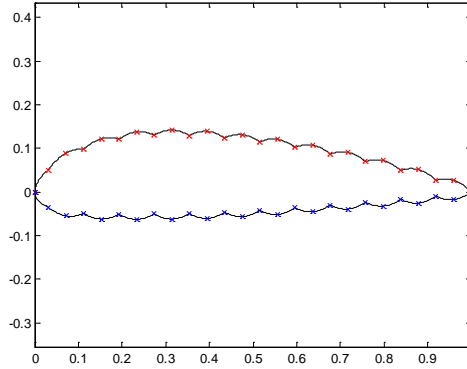


Figure B.177 Bumpy airfoil tap profile

B.1 $Re = 25,000$

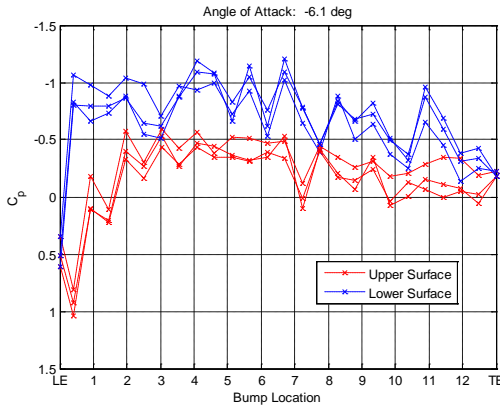


Figure B.178 C_p distribution, $Re = 25k$,
 $\alpha = -6.1^\circ$

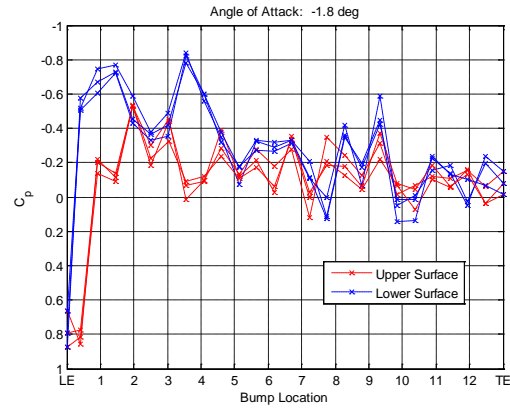


Figure B.180 C_p distribution, $Re = 25k$,
 $\alpha = -1.8^\circ$

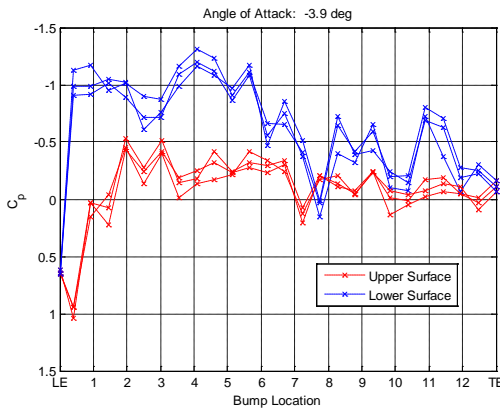


Figure B.179 C_p distribution, $Re = 25k$,
 $\alpha = -3.9^\circ$

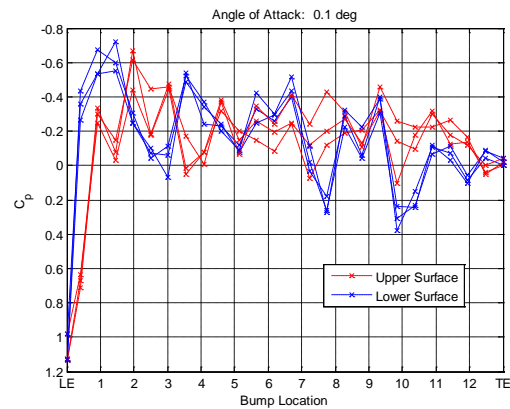


Figure B.181 C_p distribution, $Re = 25k$,
 $\alpha = 01^\circ$

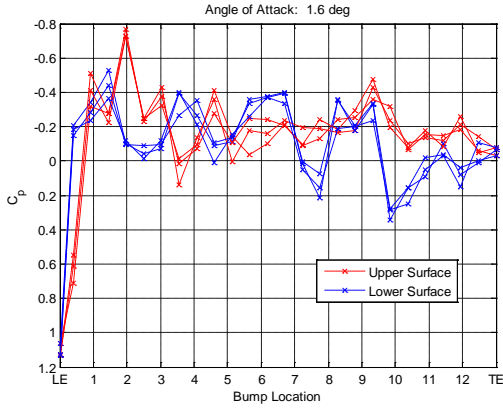


Figure B.182 C_p distribution, $Re = 25k$, $\alpha = 1.6^\circ$

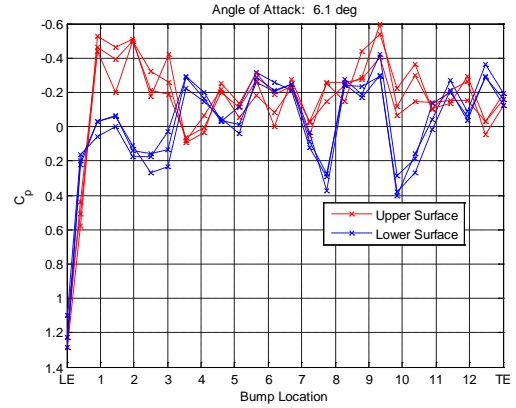


Figure B.185 C_p distribution, $Re = 25k$, $\alpha = 6.1^\circ$

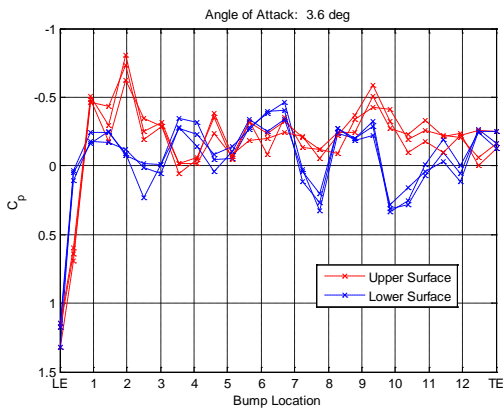


Figure B.183 C_p distribution, $Re = 25k$, $\alpha = 3.6^\circ$

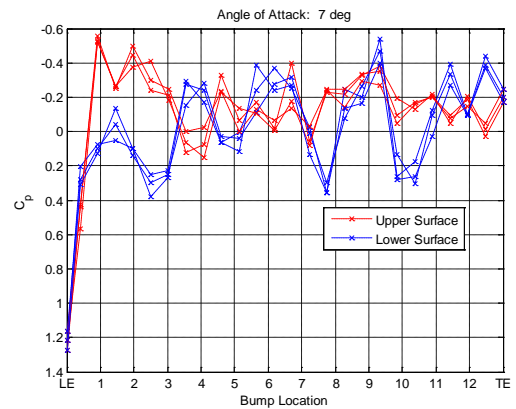


Figure B.186 C_p distribution, $Re = 25k$, $\alpha = 7^\circ$

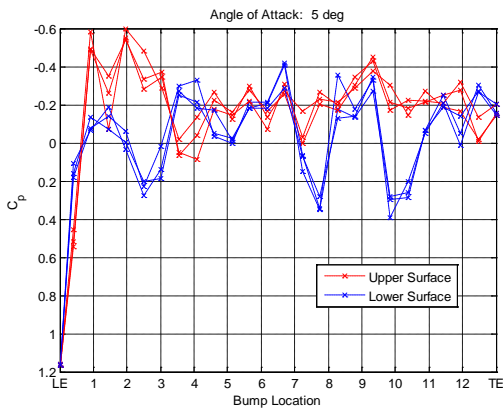


Figure B.184 C_p distribution, $Re = 25k$, $\alpha = 5^\circ$

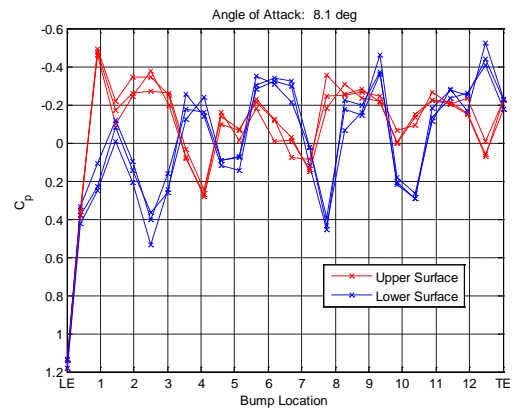


Figure B.187 C_p distribution, $Re = 25k$, $\alpha = 8.1^\circ$

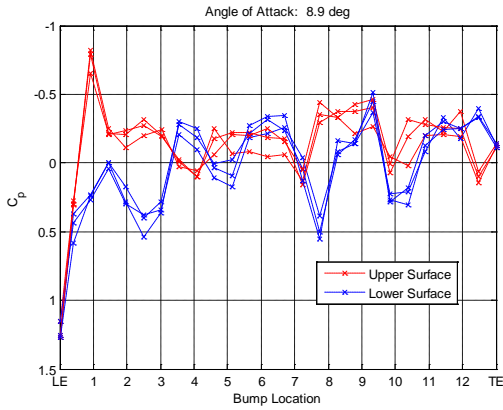


Figure B.188 C_p distribution, $Re = 25k$, $\alpha = 8.9^\circ$

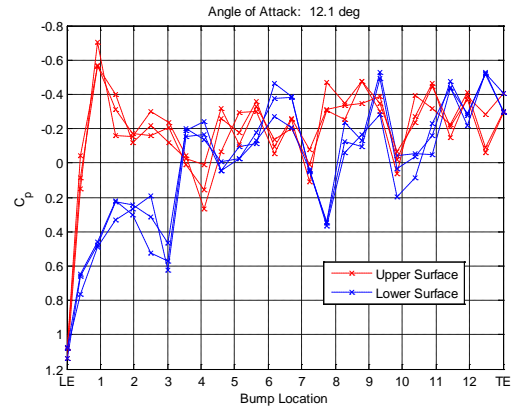


Figure B.191 C_p distribution, $Re = 25k$, $\alpha = 12.1^\circ$

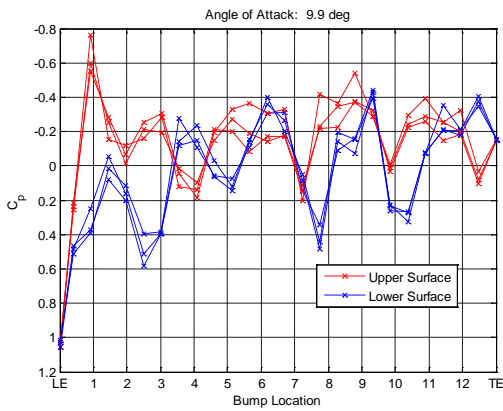


Figure B.189 C_p distribution, $Re = 25k$, $\alpha = 9.9^\circ$

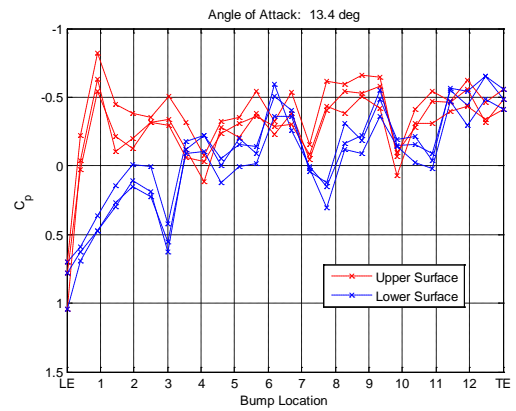


Figure B.192 C_p distribution, $Re = 25k$, $\alpha = 10.9^\circ$

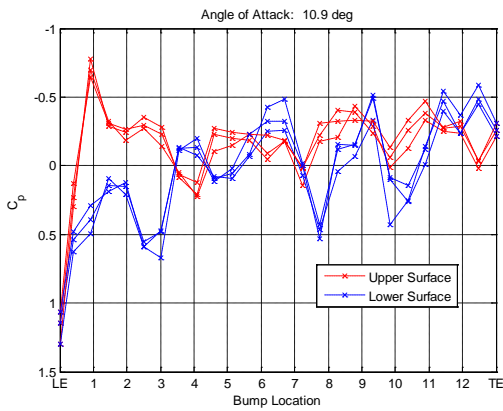


Figure B.190 C_p distribution, $Re = 25k$, $\alpha = 10.9^\circ$

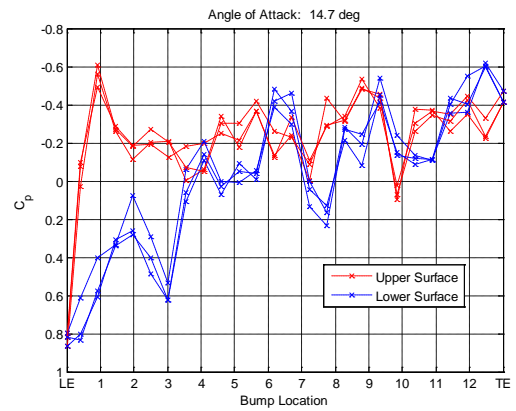


Figure B.193 C_p distribution, $Re = 25k$, $\alpha = 14.7^\circ$

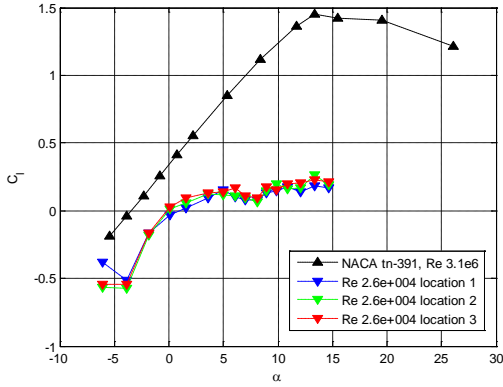


Figure B.194 $Re = 25k$ pre-averaged lift curves from 3 run locations

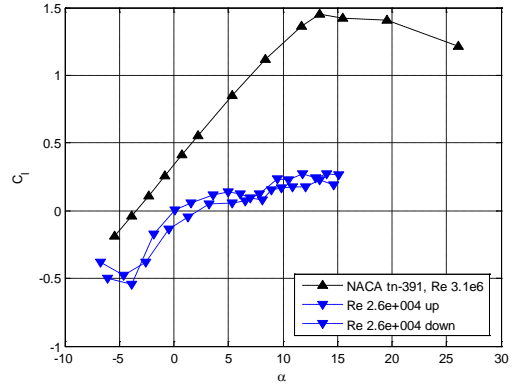


Figure B.196 $Re = 25k$ averaged lift curve with lift hysteresis

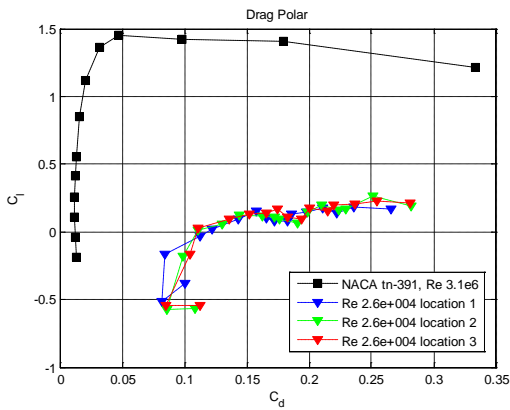


Figure B.195 $Re = 25k$ pre-averaged drag polars from 3 run locations

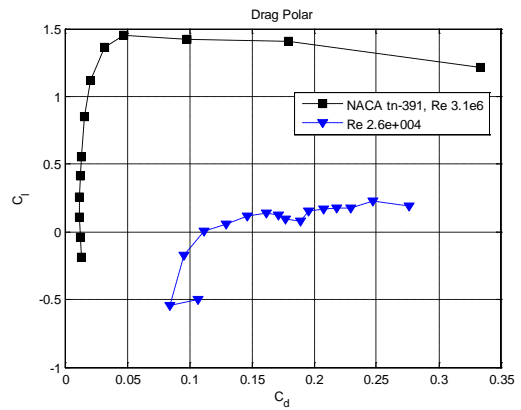


Figure B.197 $Re = 25k$ averaged drag polar

B.2 $Re = 50,000$

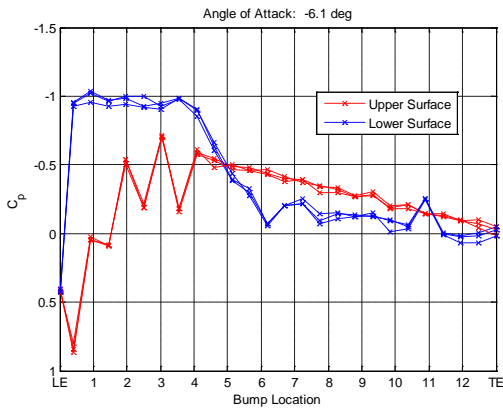


Figure B.198 C_p distribution, $Re = 50k$, $\alpha = -6.1^\circ$

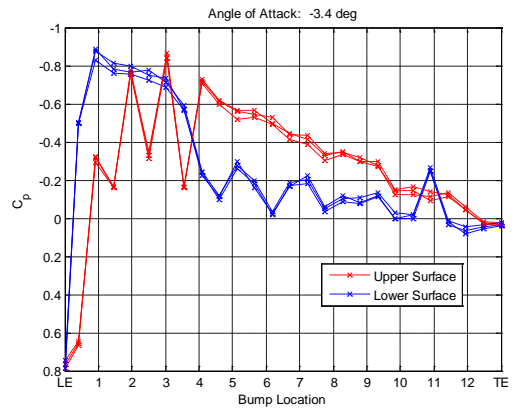


Figure B.199 C_p distribution, $Re = 50k$, $\alpha = -3.4^\circ$

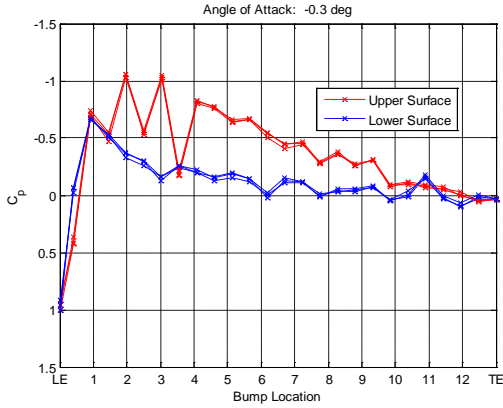


Figure B.200 C_p distribution, $Re = 50k$, $\alpha = -0.3^\circ$

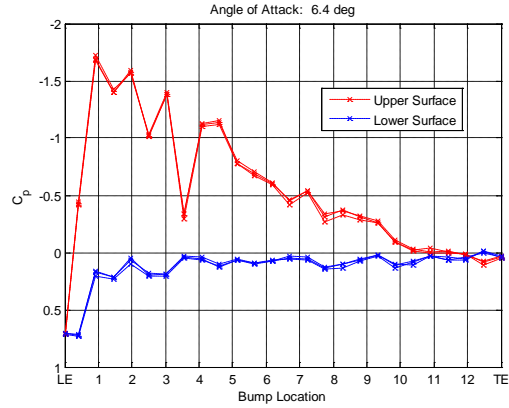


Figure B.203 C_p distribution, $Re = 50k$, $\alpha = 6.4^\circ$

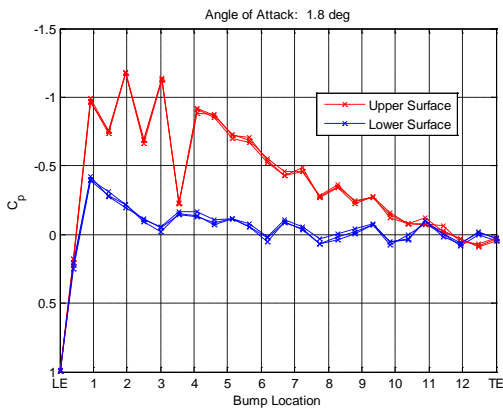


Figure B.201 C_p distribution, $Re = 50k$, $\alpha = 1.8^\circ$

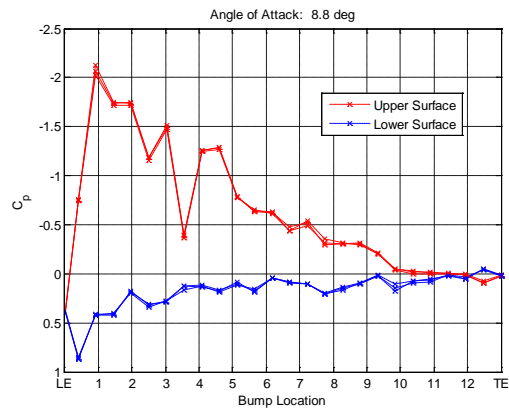


Figure B.204 C_p distribution, $Re = 50k$, $\alpha = 8.8^\circ$

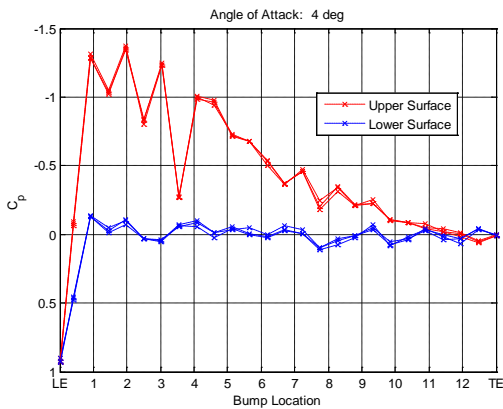


Figure B.202 C_p distribution, $Re = 50k$, $\alpha = 4^\circ$

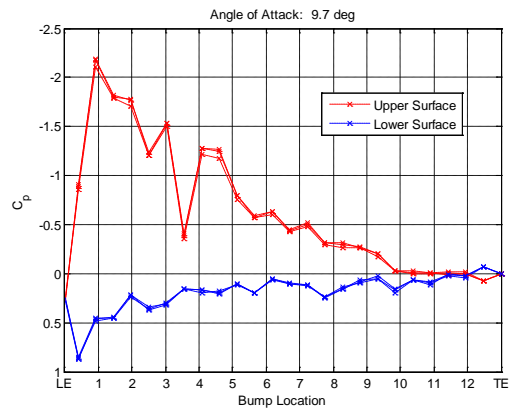


Figure B.205 C_p distribution, $Re = 50k$, $\alpha = 9.7^\circ$

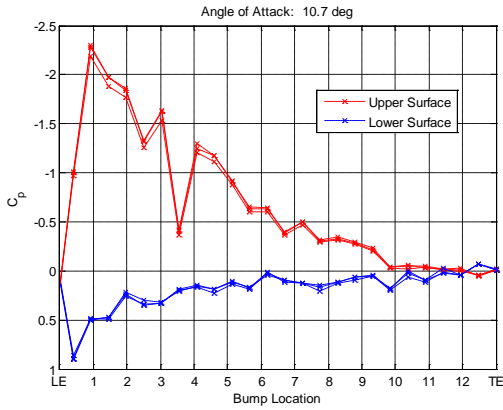


Figure B.206 C_p distribution, $Re = 50k$, $\alpha = 10.7^\circ$

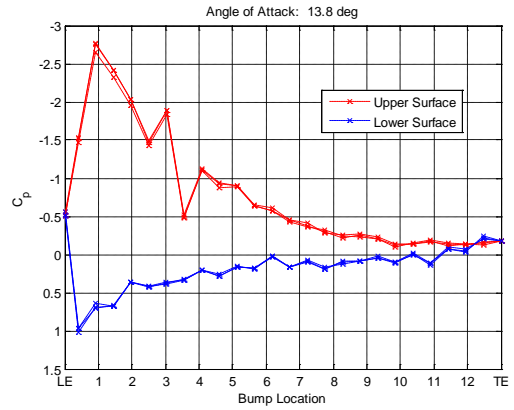


Figure B.209 C_p distribution, $Re = 50k$, $\alpha = 13.8^\circ$

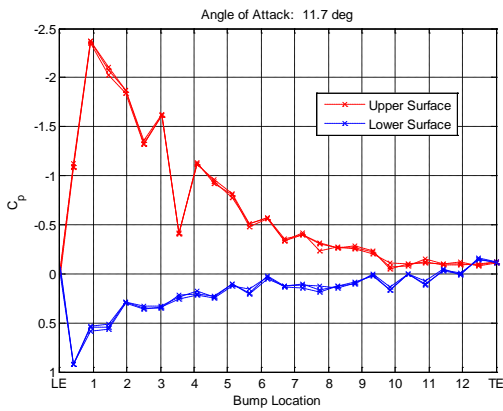


Figure B.207 C_p distribution, $Re = 50k$, $\alpha = 11.7^\circ$

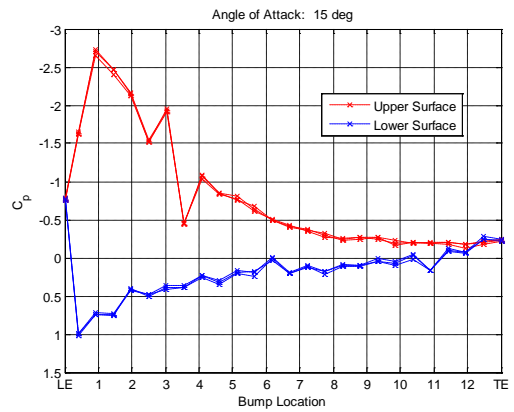


Figure B.210 C_p distribution, $Re = 50k$, $\alpha = 15^\circ$

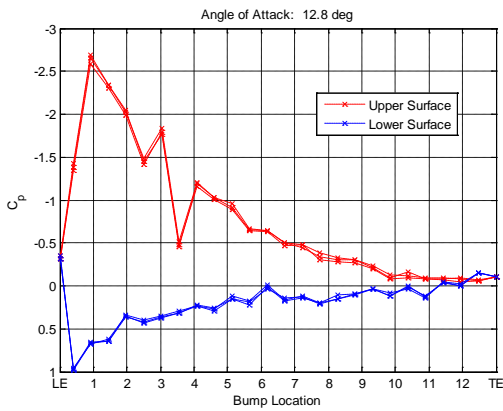


Figure B.208 C_p distribution, $Re = 50k$, $\alpha = 12.8^\circ$

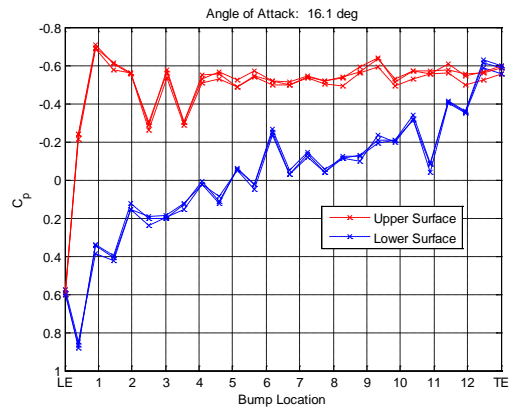


Figure B.211 C_p distribution, $Re = 50k$, $\alpha = 16.1^\circ$

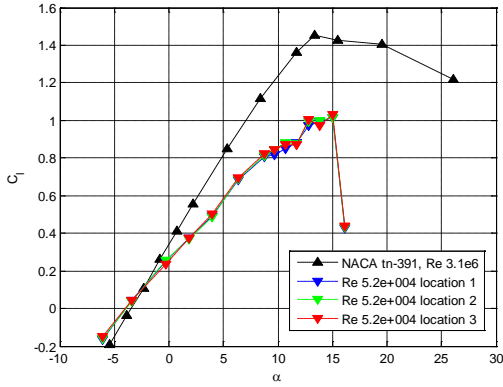


Figure B.212 $Re = 50k$ pre-averaged lift curves from 3 run locations

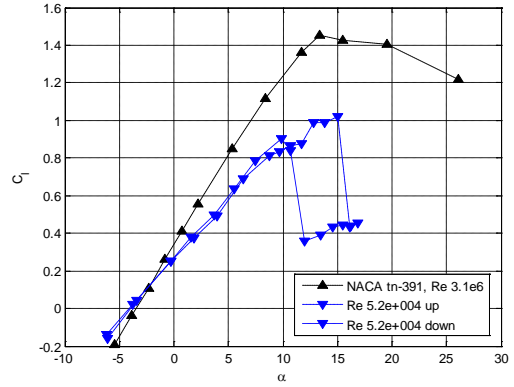


Figure B.214 $Re = 50k$ averaged lift curve with lift hysteresis

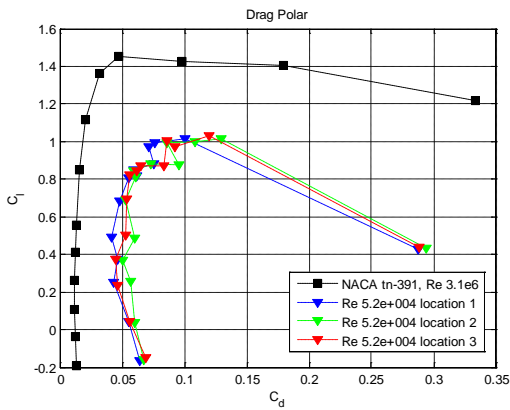


Figure B.213 $Re = 50k$ pre-averaged drag polars from 3 run locations

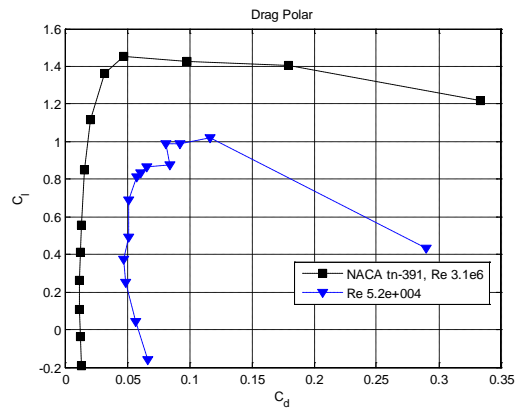


Figure B.215 $Re = 50k$ averaged drag polar

B.3 $Re = 100,000$

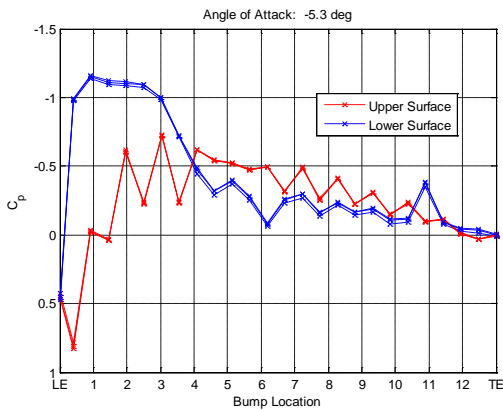


Figure B.216 C_p distribution, $Re = 100k$, $\alpha = -5.3^\circ$

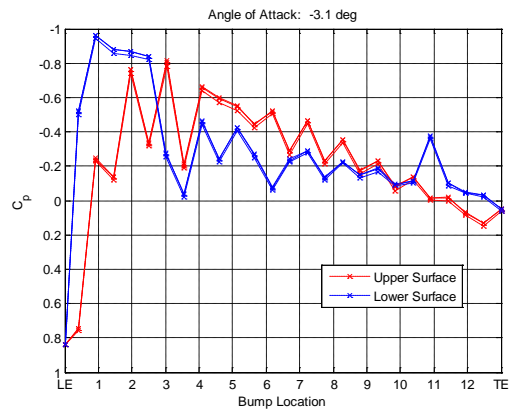


Figure B.217 C_p distribution, $Re = 100k$, $\alpha = -3.1^\circ$

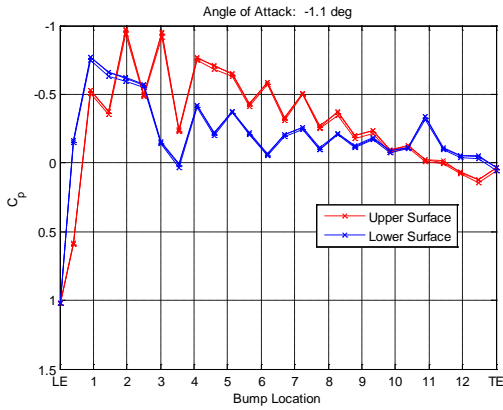


Figure B.218 C_p distribution, $Re = 100k$, $\alpha = -1.1^\circ$

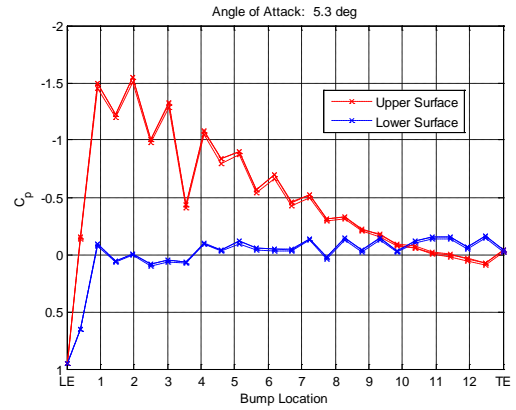


Figure B.221 C_p distribution, $Re = 100k$, $\alpha = 5.3^\circ$

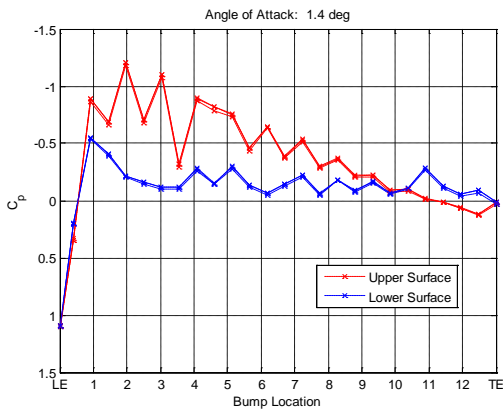


Figure B.219 C_p distribution, $Re = 100k$, $\alpha = 1.4^\circ$

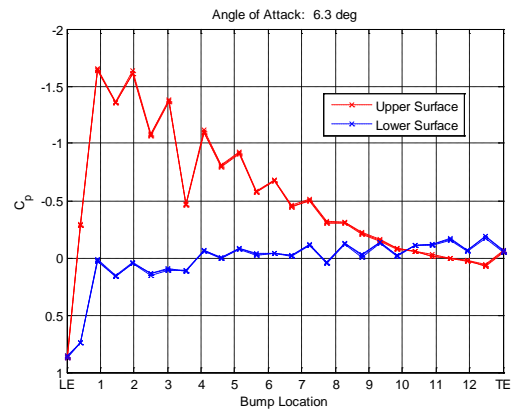


Figure B.222 C_p distribution, $Re = 100k$, $\alpha = 6.3^\circ$

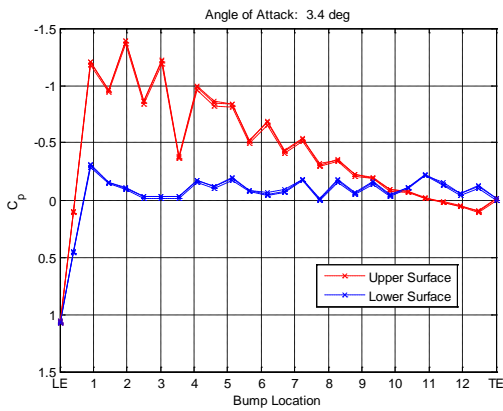


Figure B.220 C_p distribution, $Re = 100k$, $\alpha = 3.4^\circ$

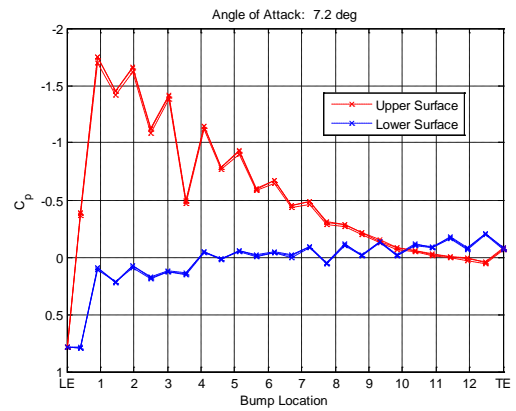


Figure B.223 C_p distribution, $Re = 100k$, $\alpha = 7.2^\circ$

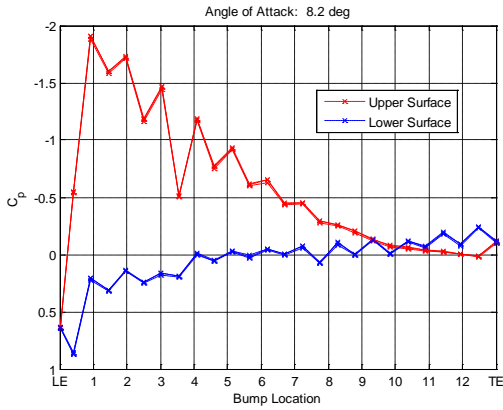


Figure B.224 C_p distribution, $Re = 100k$, $\alpha = 8.2^\circ$

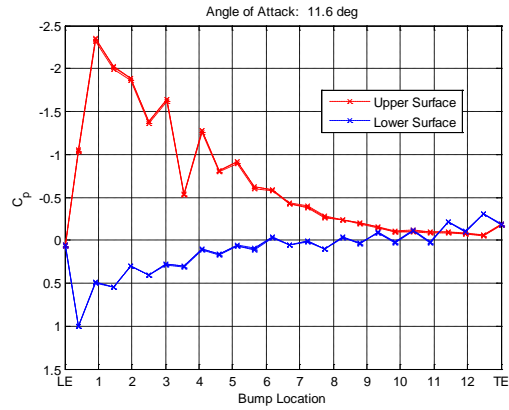


Figure B.227 C_p distribution, $Re = 100k$, $\alpha = 11.6^\circ$

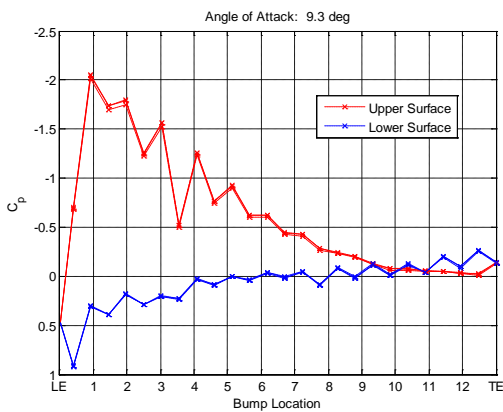


Figure B.225 C_p distribution, $Re = 100k$, $\alpha = 9.3^\circ$

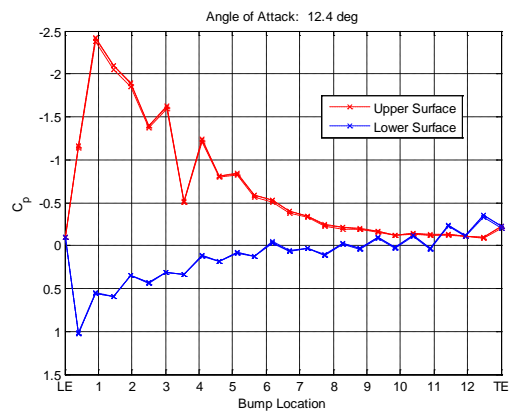


Figure B.228 C_p distribution, $Re = 100k$, $\alpha = 12.4^\circ$

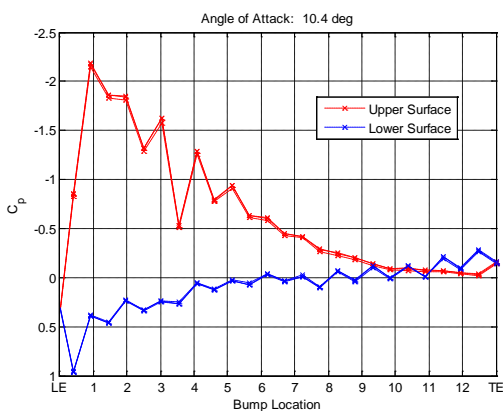


Figure B.226 C_p distribution, $Re = 100k$, $\alpha = 10.4^\circ$

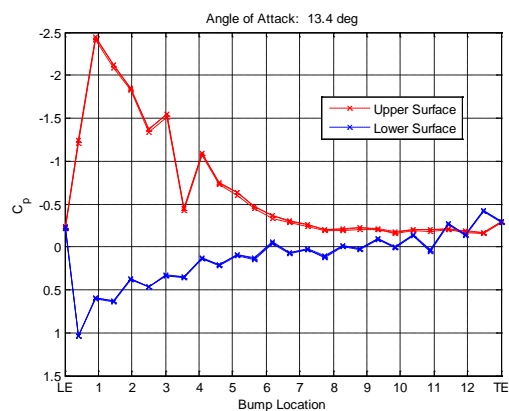


Figure B.229 C_p distribution, $Re = 100k$, $\alpha = 12.4^\circ$

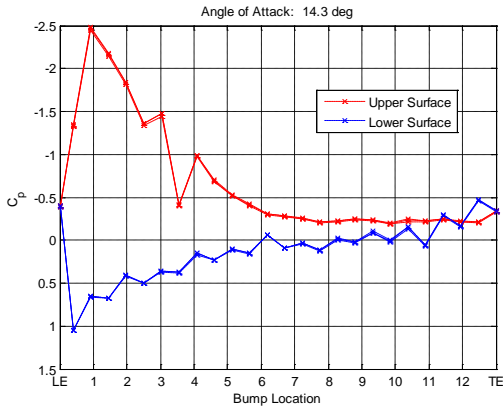


Figure B.230 C_p distribution, $Re = 100k$, $\alpha = 14.3^\circ$

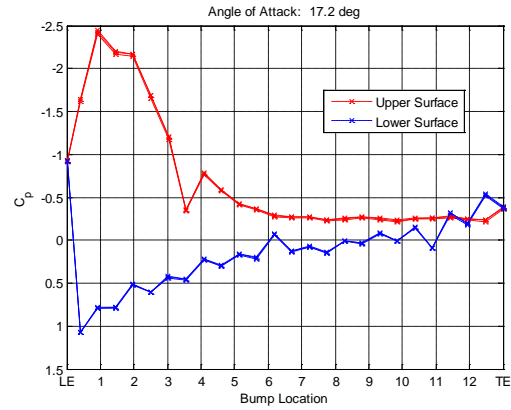


Figure B.233 C_p distribution, $Re = 100k$, $\alpha = 17.2^\circ$

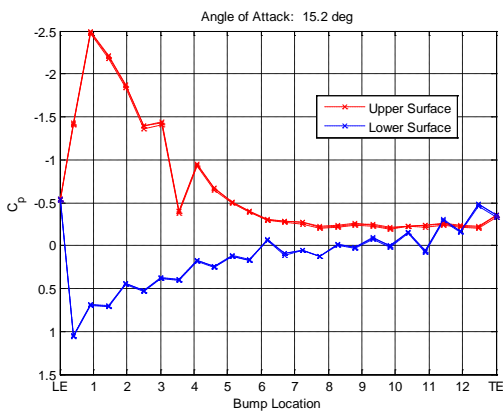


Figure B.231 C_p distribution, $Re = 100k$, $\alpha = 15.2^\circ$

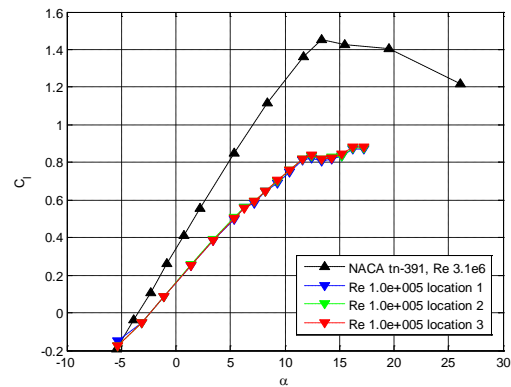


Figure B.234 $Re = 100k$ pre-averaged lift curves from 3 run locations

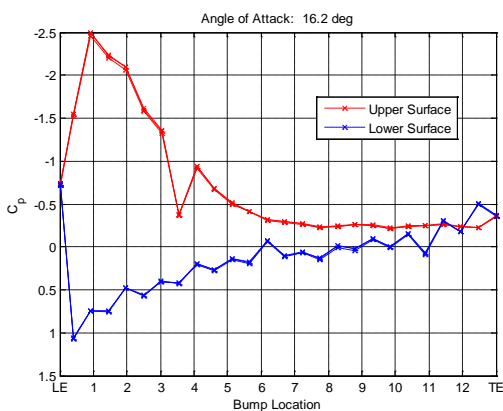


Figure B.232 C_p distribution, $Re = 100k$, $\alpha = 16.2^\circ$

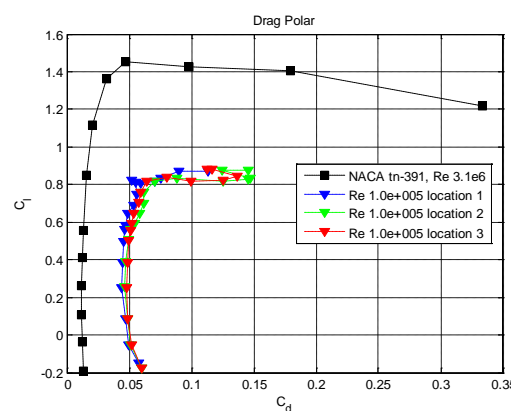


Figure B.235 $Re = 100k$ pre-averaged drag polars from 3 run locations

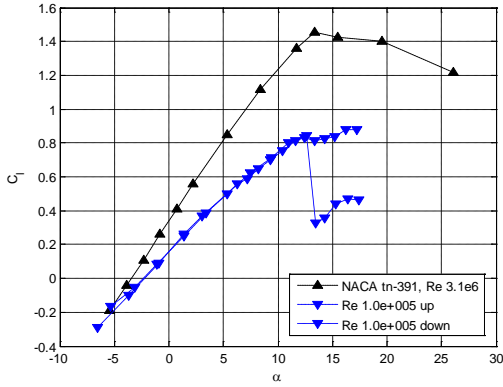


Figure B.236 $Re = 100k$ averaged lift curve with lift hysteresis

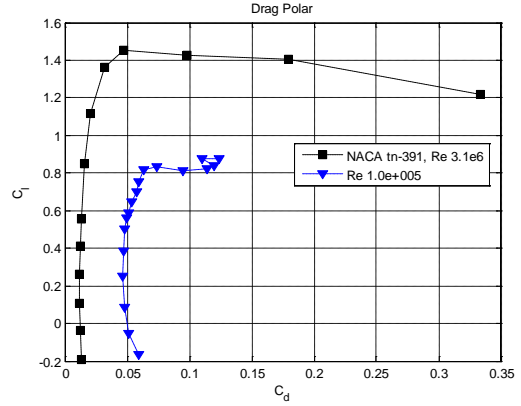


Figure B.237 $Re = 100k$ averaged drag polar

B.4 $Re = 150,000$

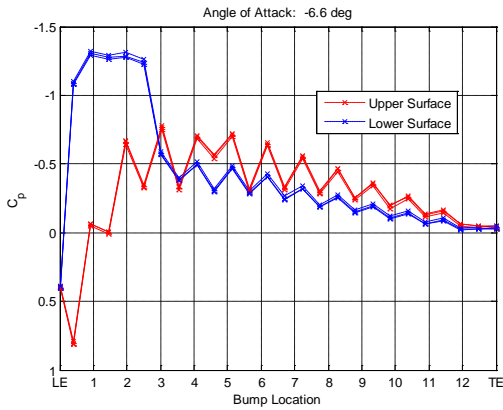


Figure B.238 C_p distribution, $Re = 150k$, $\alpha = -6.6^\circ$

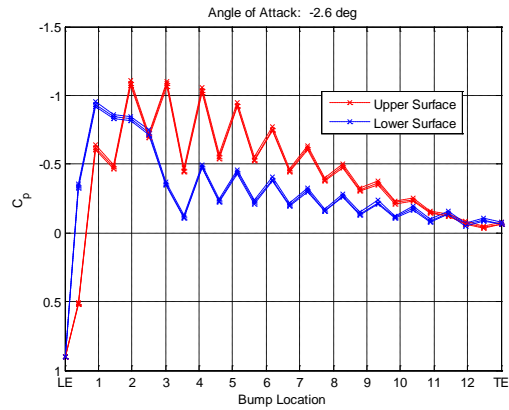


Figure B.240 C_p distribution, $Re = 150k$, $\alpha = -2.6^\circ$

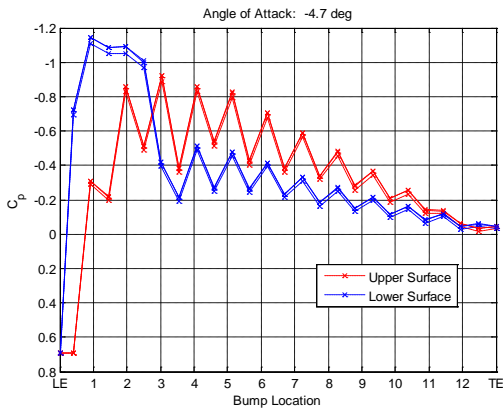


Figure B.239 C_p distribution, $Re = 150k$, $\alpha = -4.7^\circ$

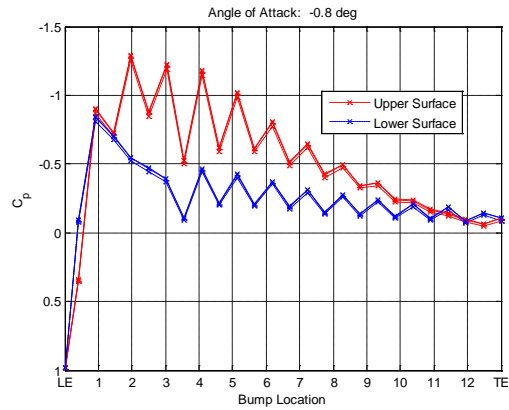


Figure B.241 C_p distribution, $Re = 150k$, $\alpha = -0.8^\circ$

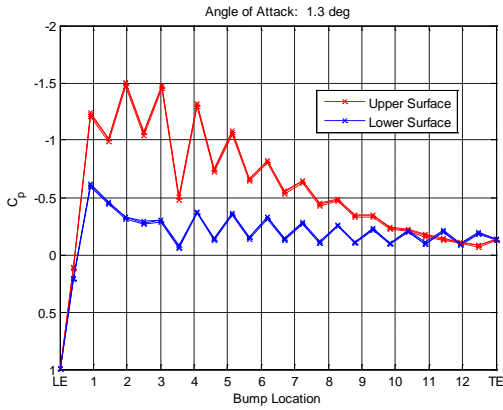


Figure B.242 C_p distribution, $Re = 150k$, $\alpha = 1.3^\circ$

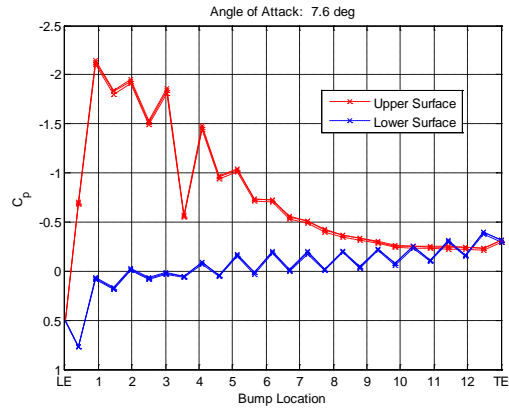


Figure B.245 C_p distribution, $Re = 150k$, $\alpha = 7.6^\circ$

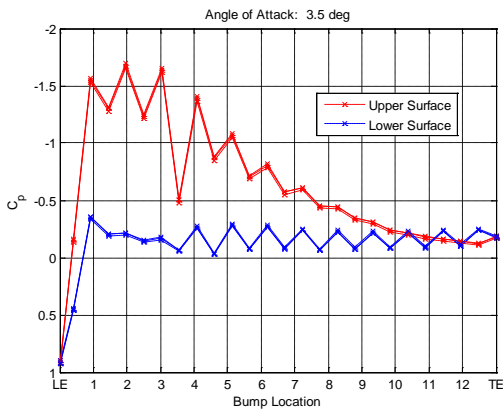


Figure B.243 C_p distribution, $Re = 150k$, $\alpha = 3.5^\circ$

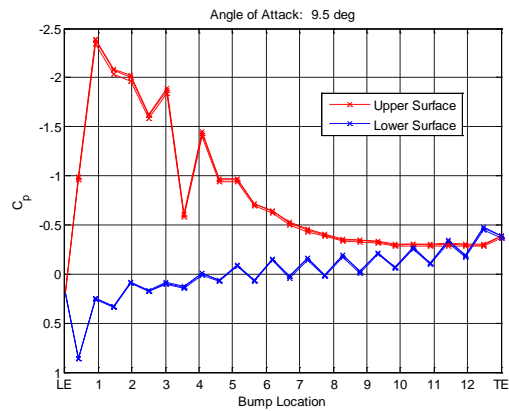


Figure B.246 C_p distribution, $Re = 150k$, $\alpha = 9.5^\circ$

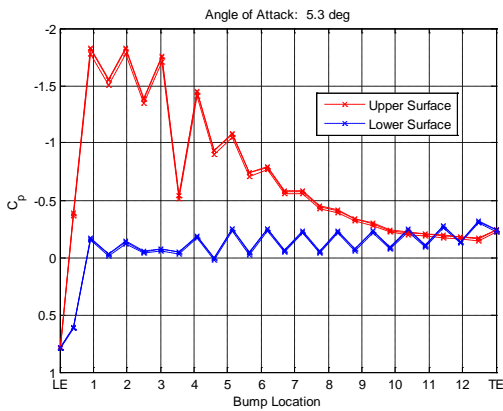


Figure B.244 C_p distribution, $Re = 150k$, $\alpha = 5.3^\circ$

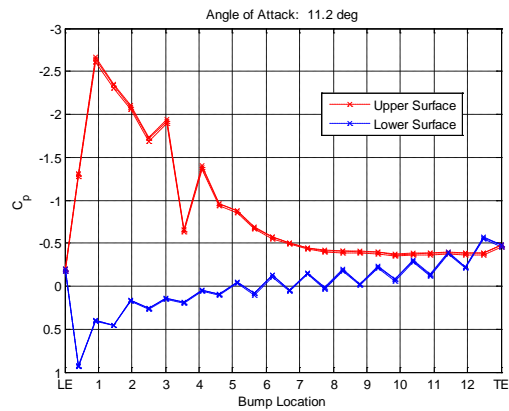


Figure B.247 C_p distribution, $Re = 150k$, $\alpha = 11.2^\circ$

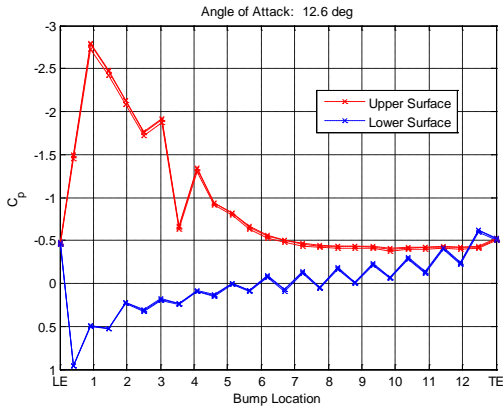


Figure B.248 C_p distribution, $Re = 150k$, $\alpha = 12.6^\circ$

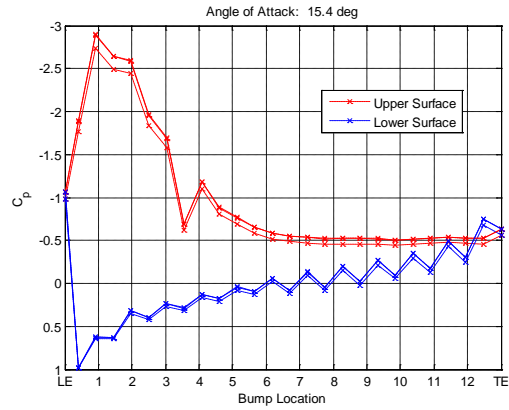


Figure B.251 C_p distribution, $Re = 150k$, $\alpha = 13.5^\circ$

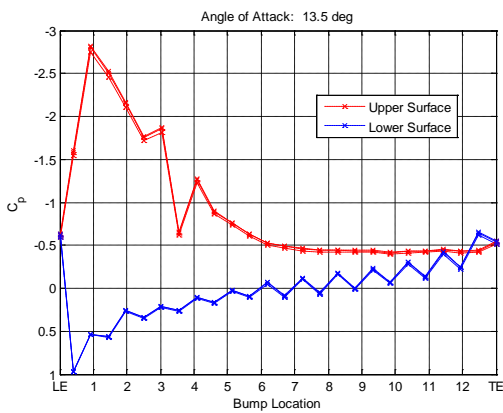


Figure B.249 C_p distribution, $Re = 150k$, $\alpha = 13.5^\circ$

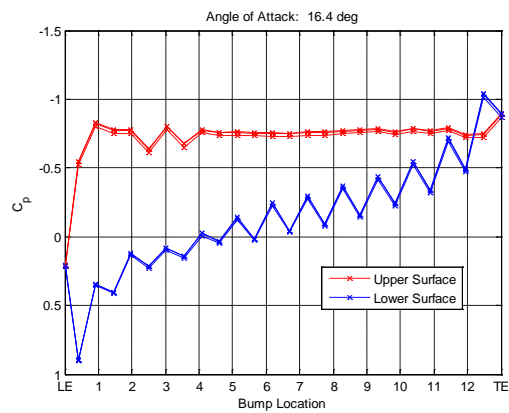


Figure B.252 C_p distribution, $Re = 150k$, $\alpha = 13.5^\circ$

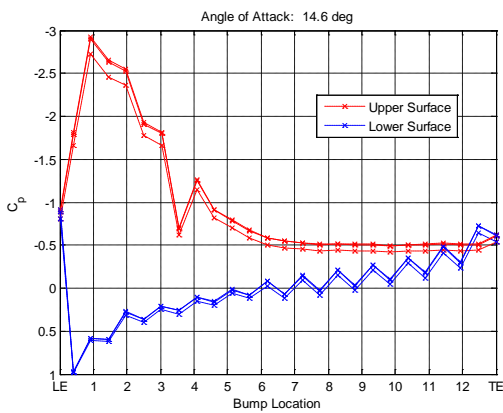


Figure B.250 C_p distribution, $Re = 150k$, $\alpha = 13.5^\circ$

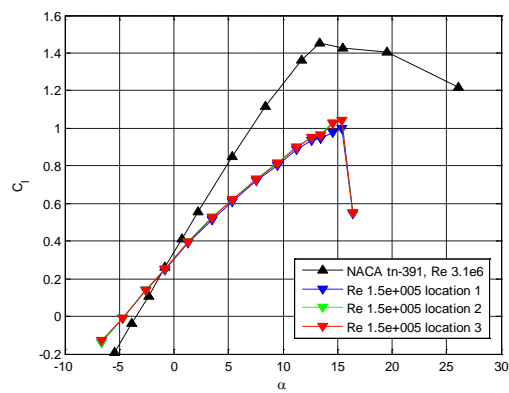


Figure B.253 $Re = 150k$ pre-averaged lift curves from 3 run locations

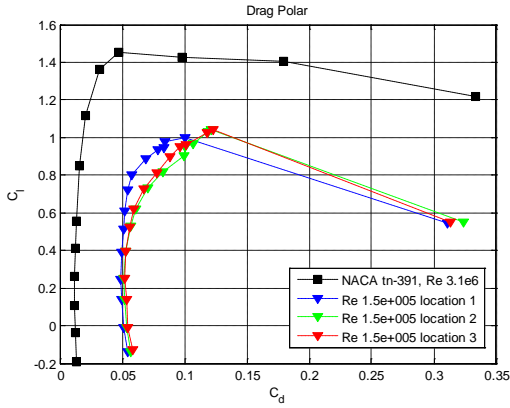


Figure B.254 $Re = 150k$ pre-averaged drag polars from 3 run locations

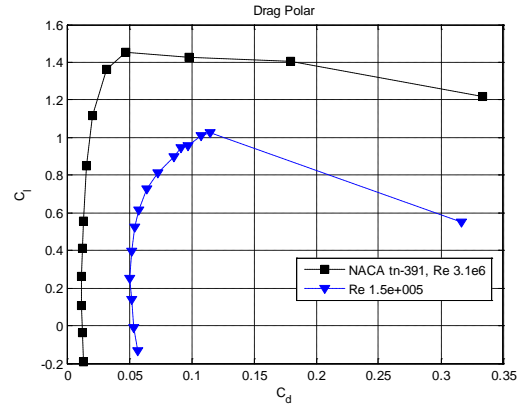


Figure B.256 $Re = 150k$ averaged drag polar

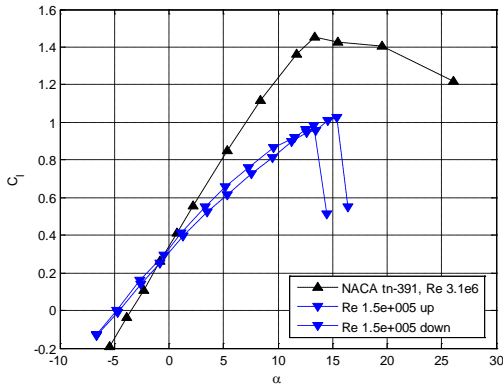


Figure B.255 $Re = 150k$ averaged lift curve with lift hysteresis

B.5 $Re = 200,000$

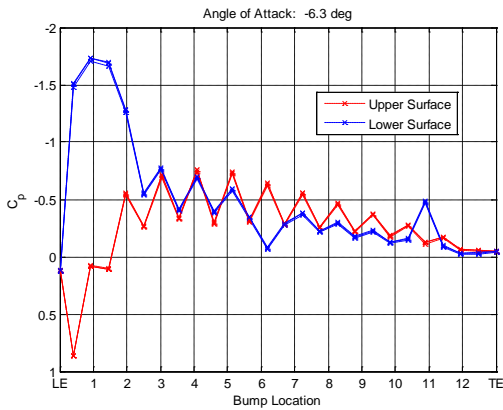


Figure B.257 C_p distribution, $Re = 200k$, $\alpha = -6.3^\circ$

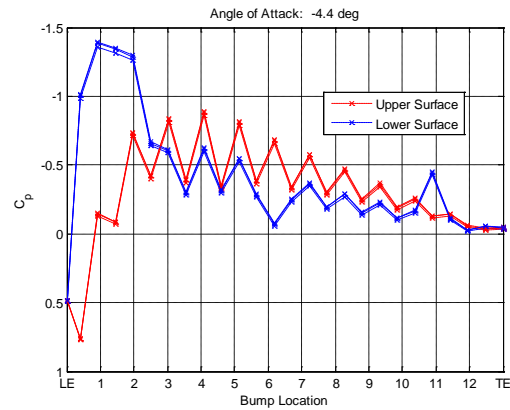


Figure B.258 C_p distribution, $Re = 200k$, $\alpha = -4.4^\circ$

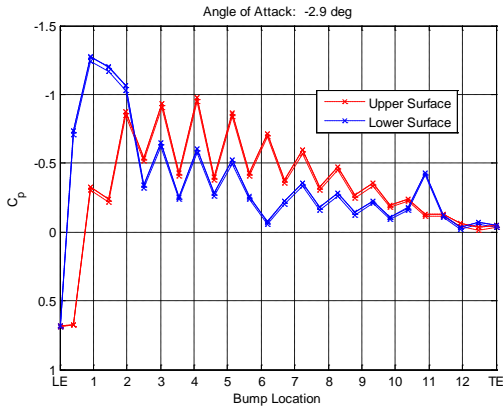


Figure B.259 C_p distribution, $Re = 200k$, $\alpha = -2.9^\circ$

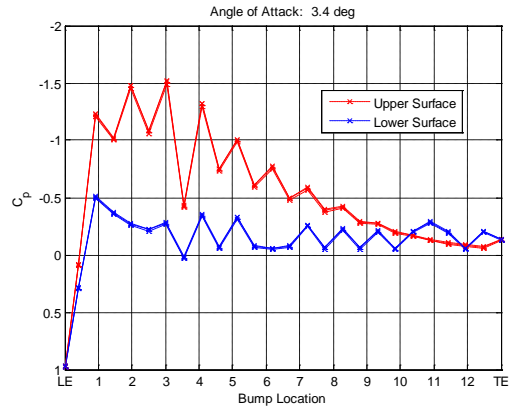


Figure B.262 C_p distribution, $Re = 200k$, $\alpha = 3.4^\circ$

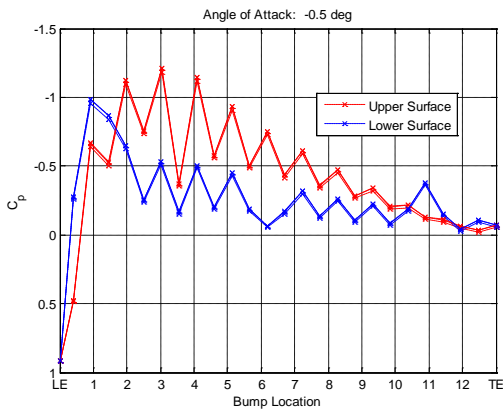


Figure B.260 C_p distribution, $Re = 200k$, $\alpha = -0.5^\circ$

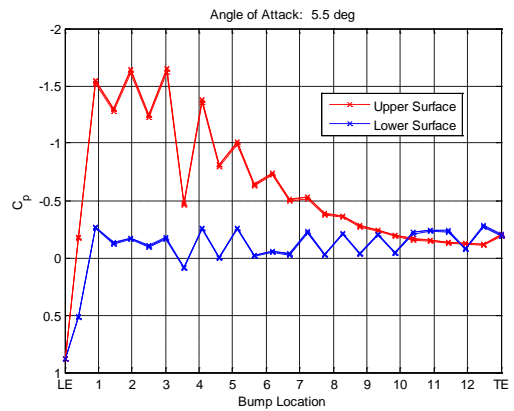


Figure B.263 C_p distribution, $Re = 200k$, $\alpha = 5.5^\circ$

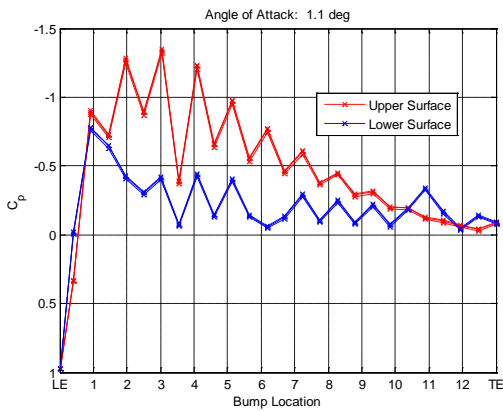


Figure B.261 C_p distribution, $Re = 200k$, $\alpha = 1.1^\circ$

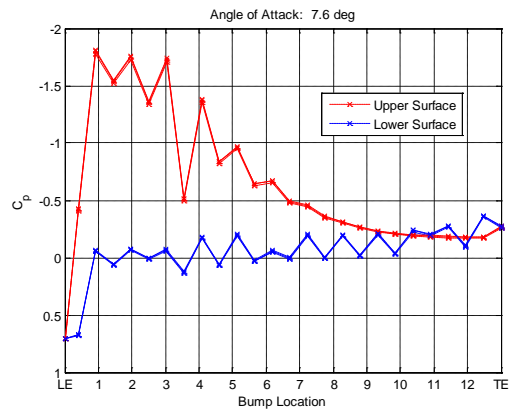


Figure B.264 C_p distribution, $Re = 200k$, $\alpha = 7.6^\circ$

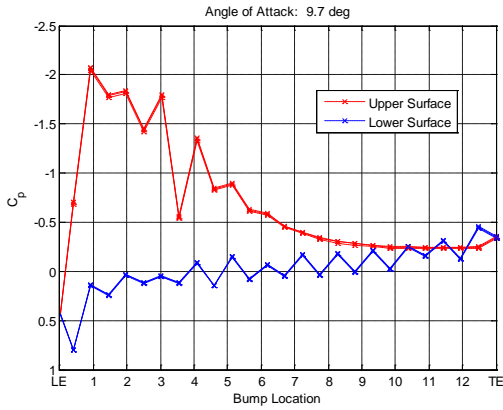


Figure B.265 C_p distribution, $Re = 200k$, $\alpha = 9.7^\circ$

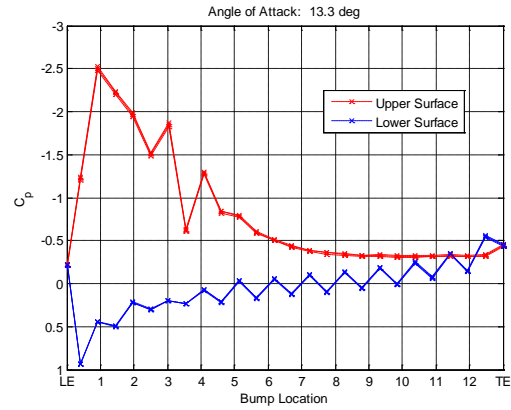


Figure B.268 C_p distribution, $Re = 200k$, $\alpha = 13.3^\circ$

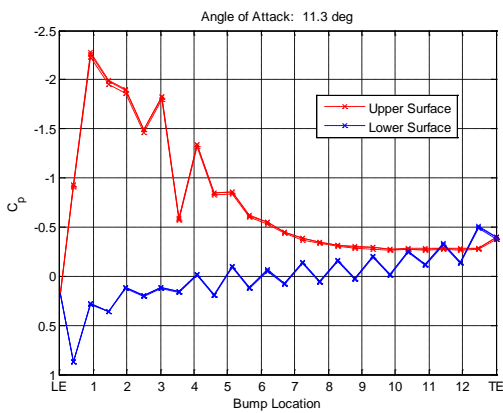


Figure B.266 C_p distribution, $Re = 200k$, $\alpha = 11.3^\circ$

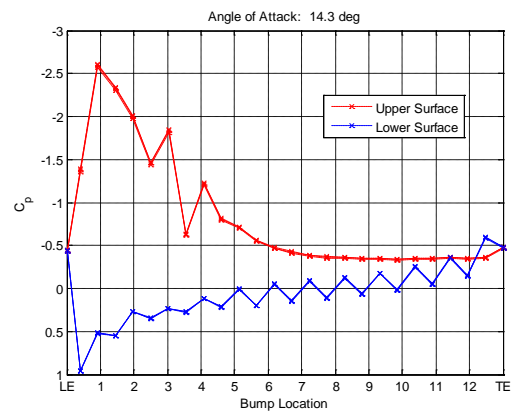


Figure B.269 C_p distribution, $Re = 200k$, $\alpha = 14.3^\circ$

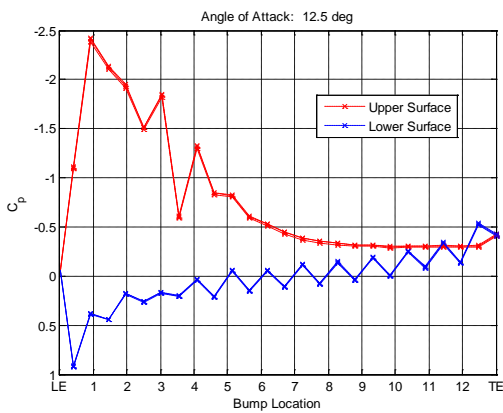


Figure B.267 C_p distribution, $Re = 200k$, $\alpha = 12.5^\circ$

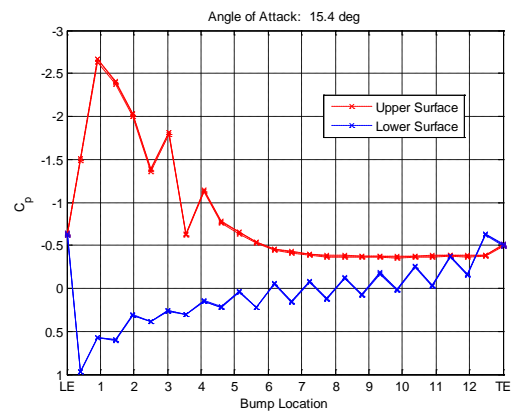


Figure B.270 C_p distribution, $Re = 200k$, $\alpha = 15.4^\circ$

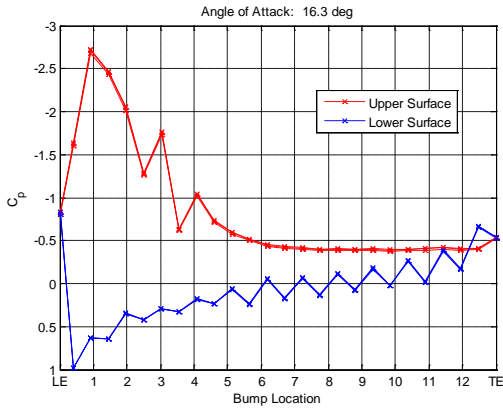


Figure B.271 C_p distribution, $Re = 200k$, $\alpha = 16.3^\circ$

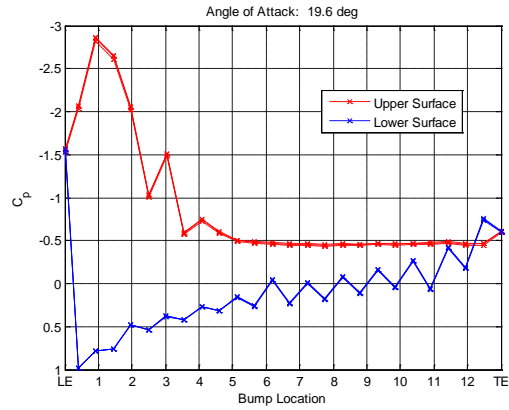


Figure B.274 C_p distribution, $Re = 200k$, $\alpha = 19.6^\circ$

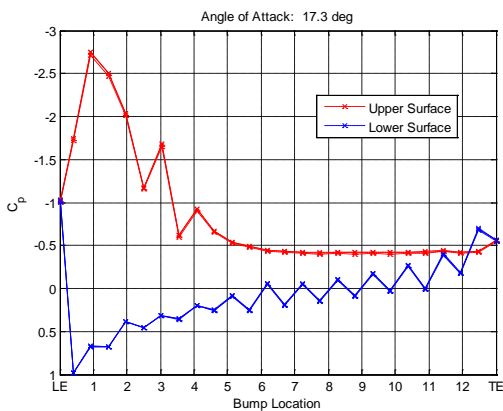


Figure B.272 C_p distribution, $Re = 200k$, $\alpha = 17.3^\circ$

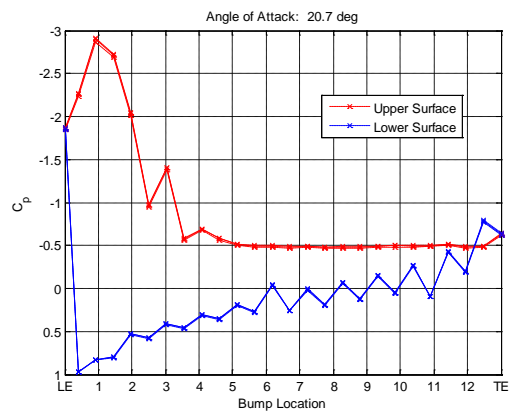


Figure B.275 C_p distribution, $Re = 200k$, $\alpha = 20.7^\circ$

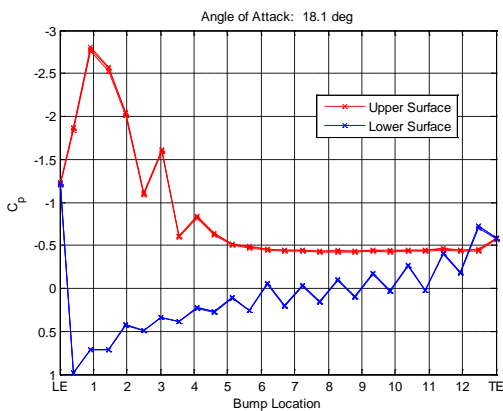


Figure B.273 C_p distribution, $Re = 200k$, $\alpha = 18.1^\circ$

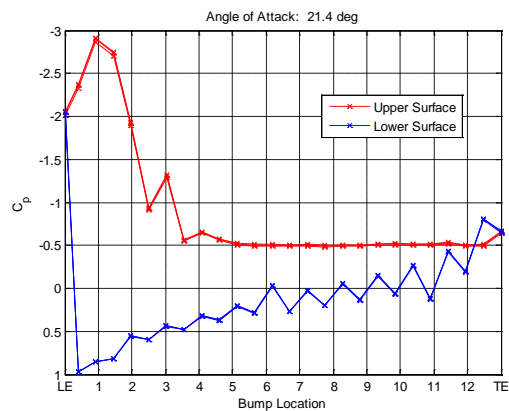


Figure B.276 C_p distribution, $Re = 200k$, $\alpha = 21.4^\circ$

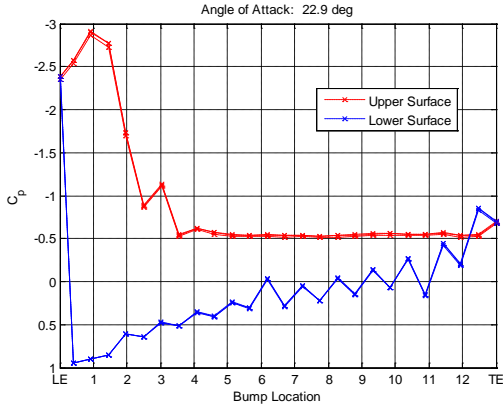


Figure B.277 C_p distribution, $Re = 200k$, $\alpha = 22.9^\circ$

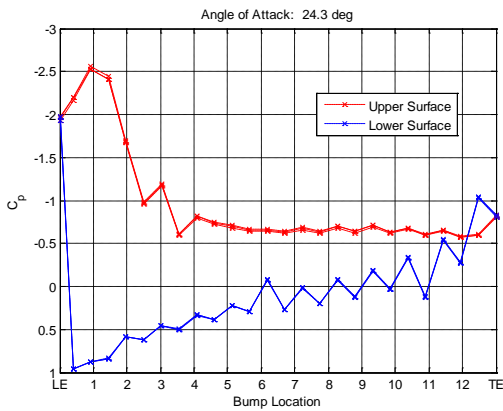


Figure B.278 C_p distribution, $Re = 200k$, $\alpha = 24.3^\circ$

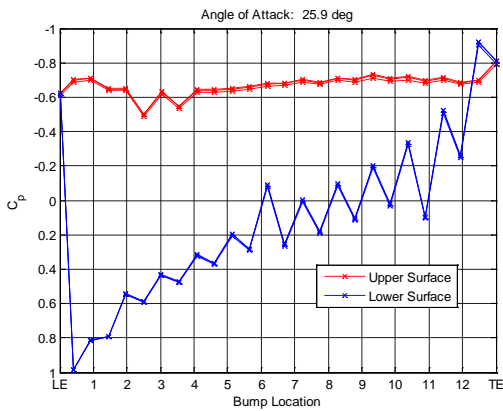


Figure B.279 C_p distribution, $Re = 200k$, $\alpha = 25.9^\circ$

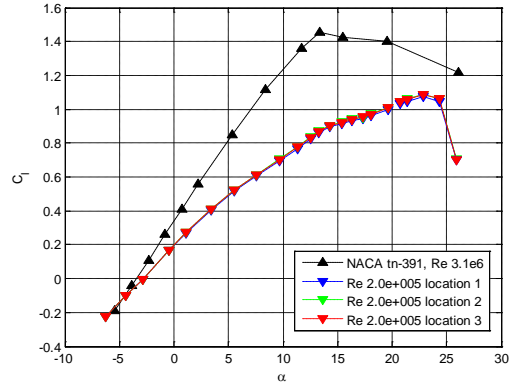


Figure B.280 $Re = 200k$ pre-averaged lift curves from 3 run locations

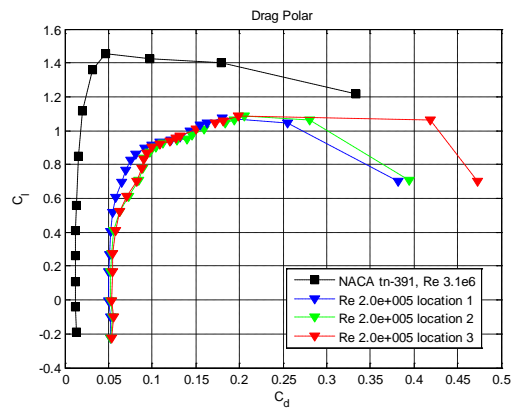


Figure B.281 $Re = 200k$ pre-averaged drag polars from 3 run locations

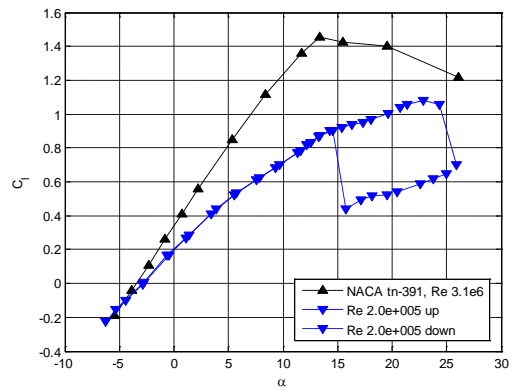


Figure B.282 $Re = 200k$ averaged lift curve with lift hysteresis

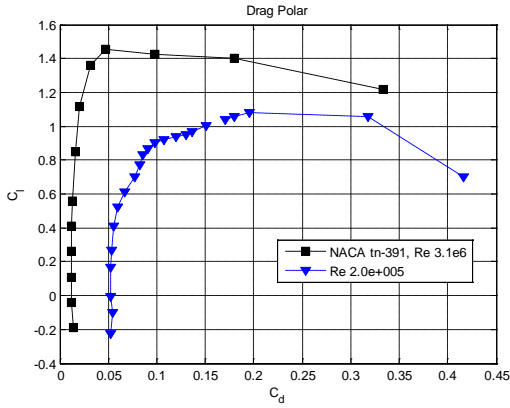


Figure B.283 $Re = 200k$ averaged drag polar

B.6 $Re = 250,000$

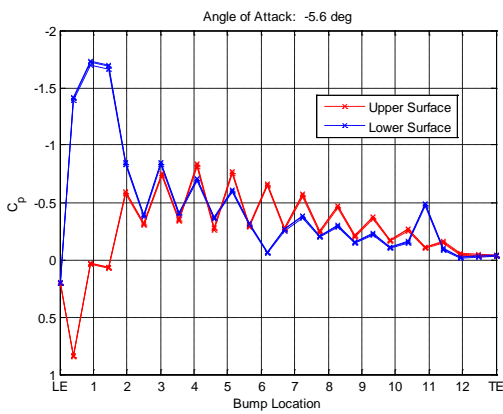


Figure B.284 C_p distribution, $Re = 250k$, $\alpha = -5.6^\circ$

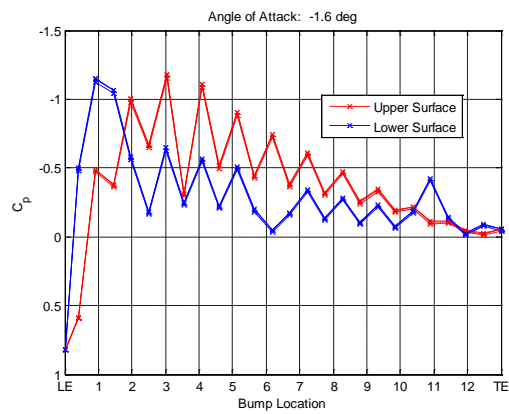


Figure B.286 C_p distribution, $Re = 250k$, $\alpha = -1.6^\circ$

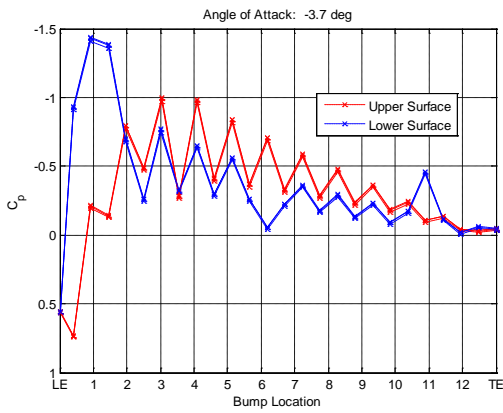


Figure B.285 C_p distribution, $Re = 250k$, $\alpha = -3.7^\circ$

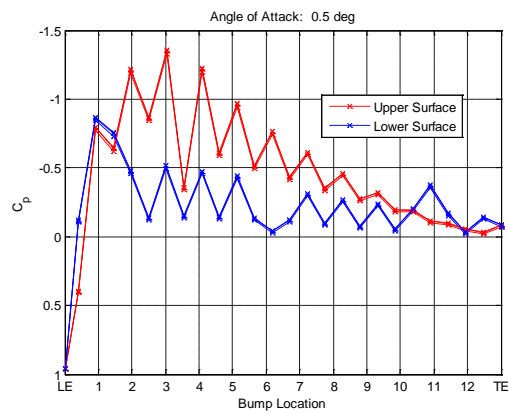


Figure B.287 C_p distribution, $Re = 250k$, $\alpha = 0.5^\circ$

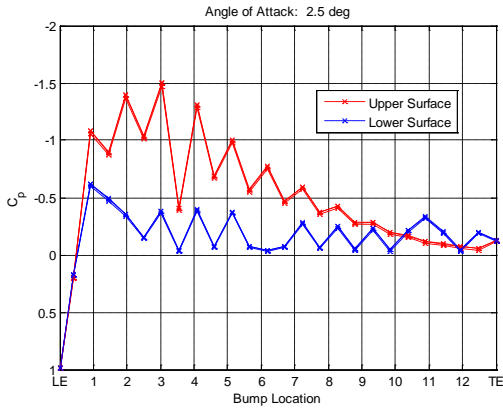


Figure B.288 C_p distribution, $Re = 250k$, $\alpha = 2.5^\circ$

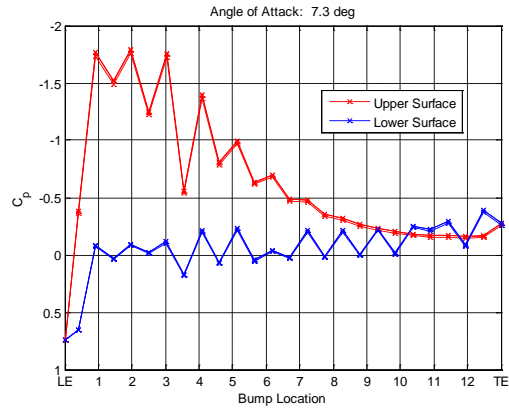


Figure B.291 C_p distribution, $Re = 250k$, $\alpha = 7.3^\circ$

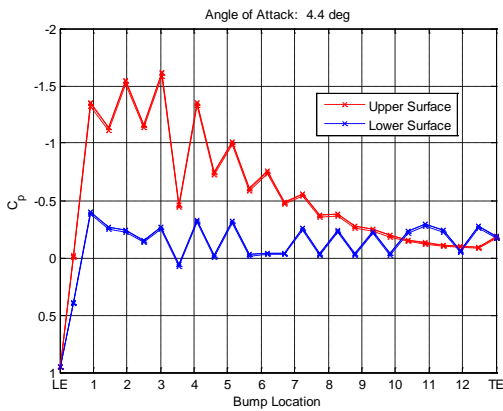


Figure B.289 C_p distribution, $Re = 250k$, $\alpha = 4.4^\circ$

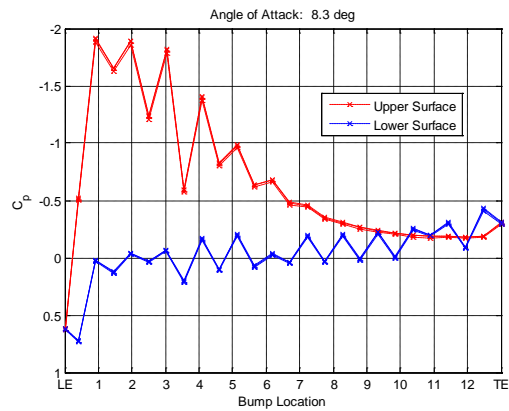


Figure B.292 C_p distribution, $Re = 250k$, $\alpha = 8.3^\circ$

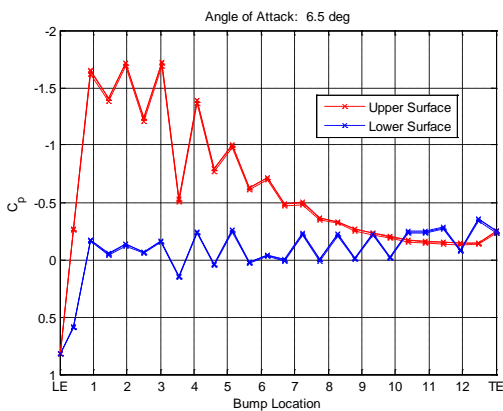


Figure B.290 C_p distribution, $Re = 250k$, $\alpha = 6.5^\circ$

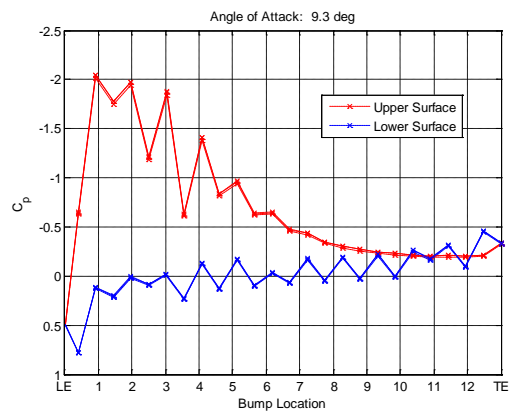


Figure B.293 C_p distribution, $Re = 250k$, $\alpha = 9.3^\circ$

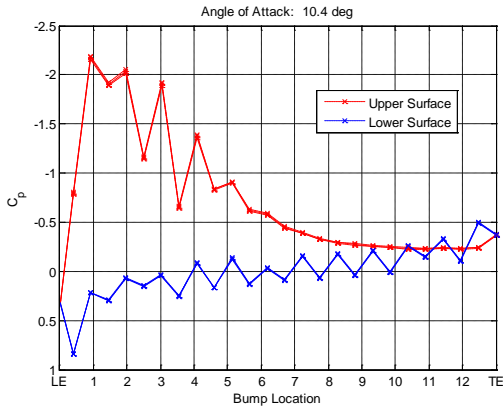


Figure B.294 C_p distribution, $Re = 250k$, $\alpha = 10.4^\circ$

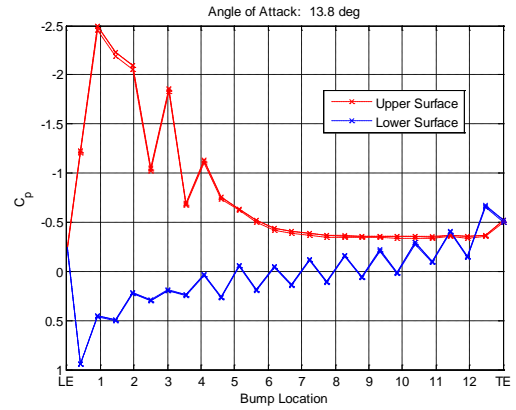


Figure B.297 C_p distribution, $Re = 250k$, $\alpha = 13.8^\circ$

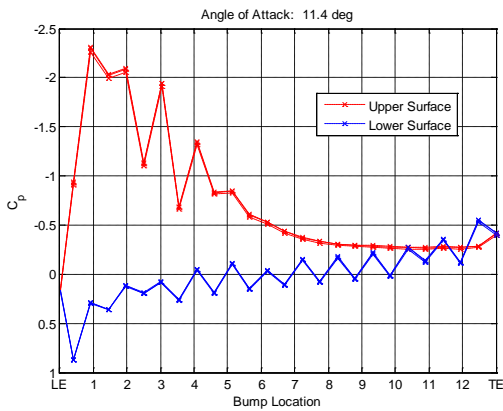


Figure B.295 C_p distribution, $Re = 250k$, $\alpha = 11.4^\circ$

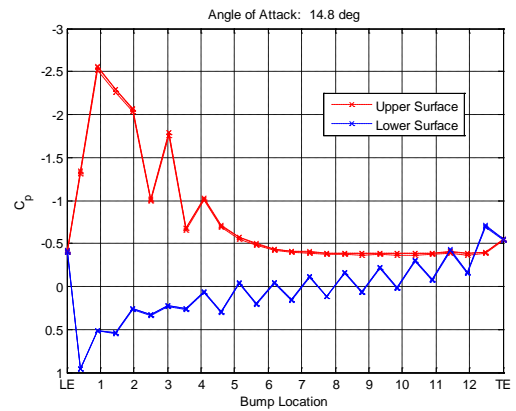


Figure B.298 C_p distribution, $Re = 250k$, $\alpha = 14.8^\circ$

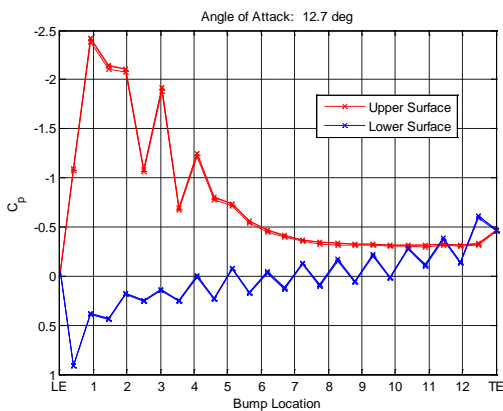


Figure B.296 C_p distribution, $Re = 250k$, $\alpha = 12.7^\circ$

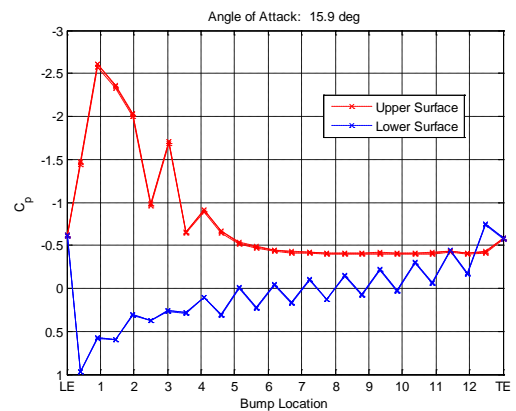


Figure B.299 C_p distribution, $Re = 250k$, $\alpha = 15.9^\circ$

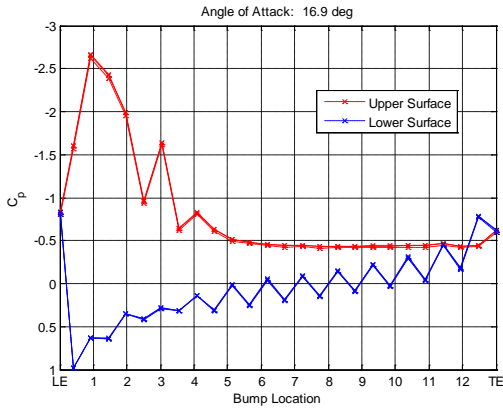


Figure B.300 C_p distribution, $Re = 250k$, $\alpha = 16.9^\circ$

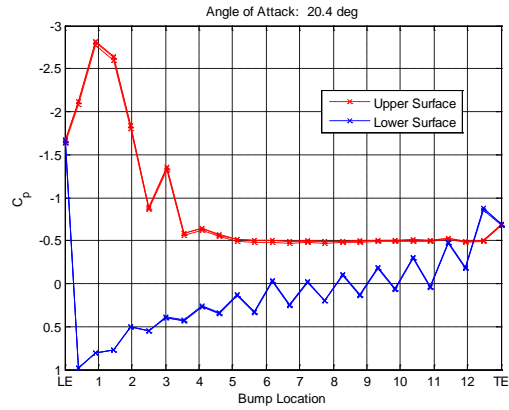


Figure B.303 C_p distribution, $Re = 250k$, $\alpha = 20.4^\circ$

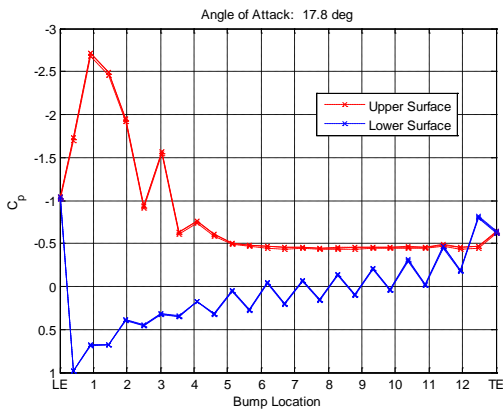


Figure B.301 C_p distribution, $Re = 250k$, $\alpha = 17.8^\circ$

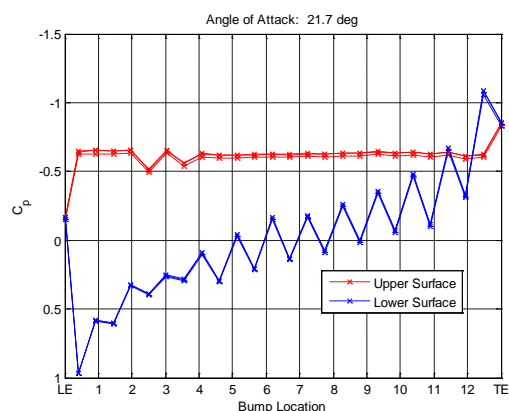


Figure B.304 C_p distribution, $Re = 250k$, $\alpha = 21.7^\circ$

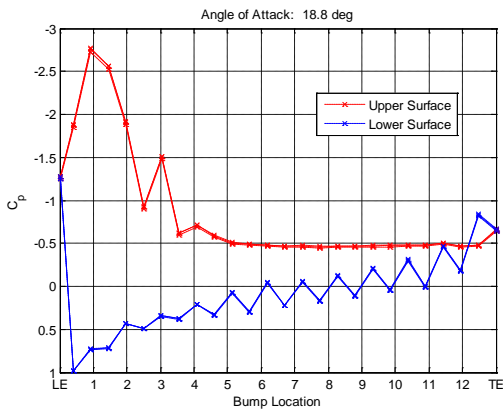


Figure B.302 C_p distribution, $Re = 250k$, $\alpha = 18.8^\circ$

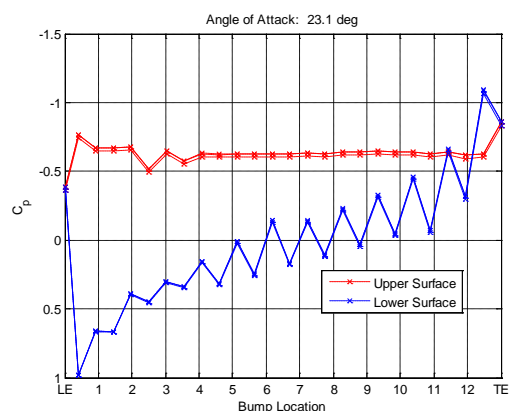


Figure B.305 C_p distribution, $Re = 250k$, $\alpha = 21.7^\circ$

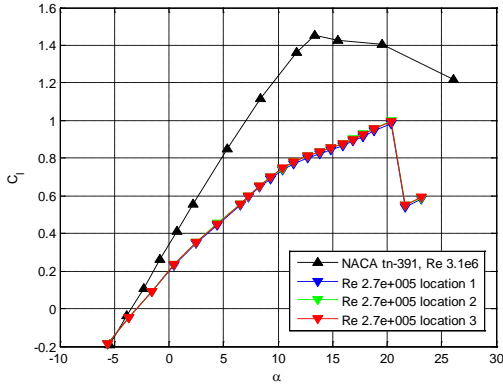


Figure B.306 $Re = 250k$ pre-averaged lift curves from 3 run locations

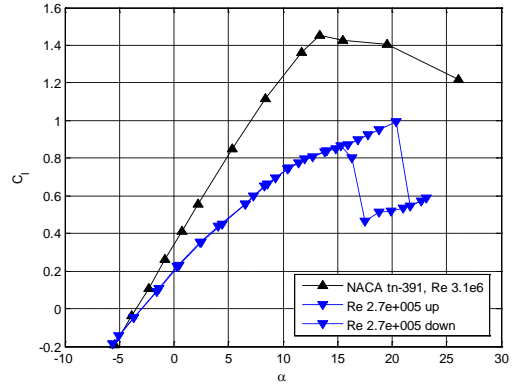


Figure B.308 $Re = 250k$ averaged lift curve with lift hysteresis

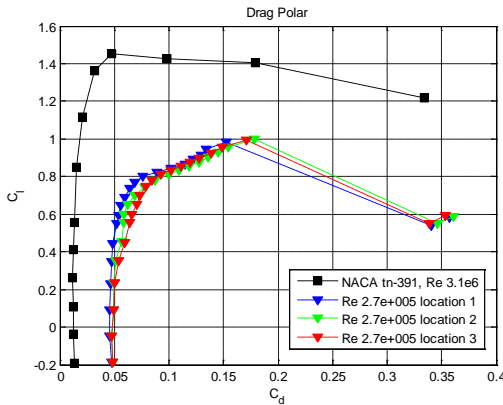


Figure B.307 $Re = 250k$ pre-averaged drag polars from 3 run locations

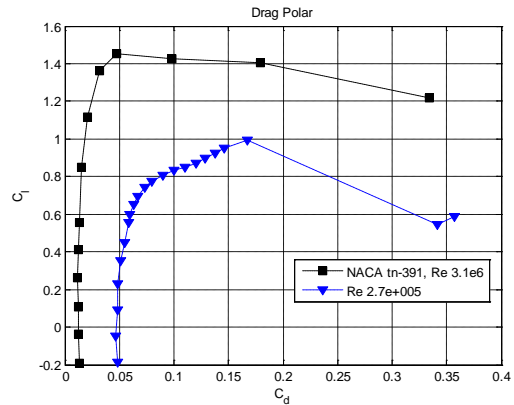


Figure B.309 $Re = 250k$ averaged drag polar

B.7 $Re = 300,000$

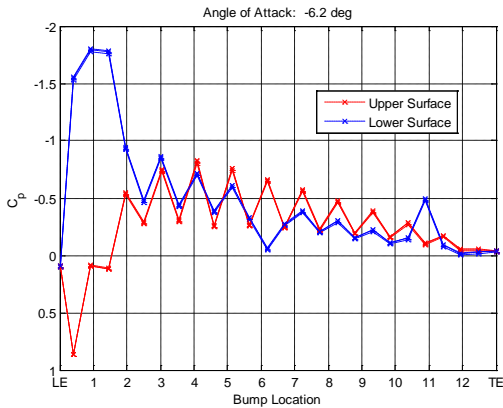


Figure B.310 C_p distribution, $Re = 300k$, $\alpha = -6.2^\circ$

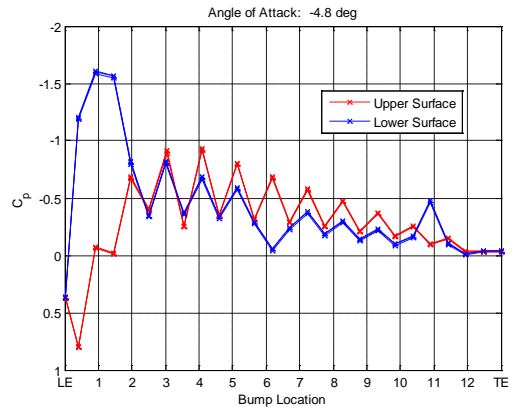


Figure B.311 C_p distribution, $Re = 300k$, $\alpha = -4.8^\circ$

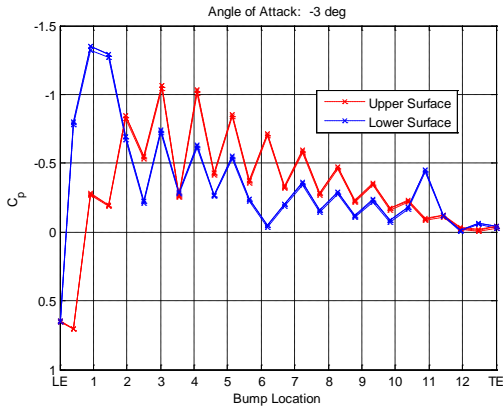


Figure B.312 C_p distribution, $Re = 300k$, $\alpha = -3^\circ$

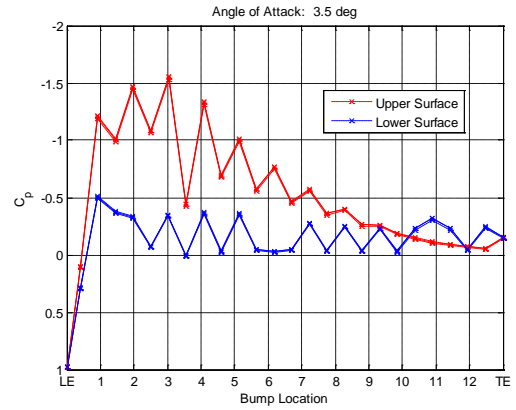


Figure B.315 C_p distribution, $Re = 300k$, $\alpha = 3.5^\circ$

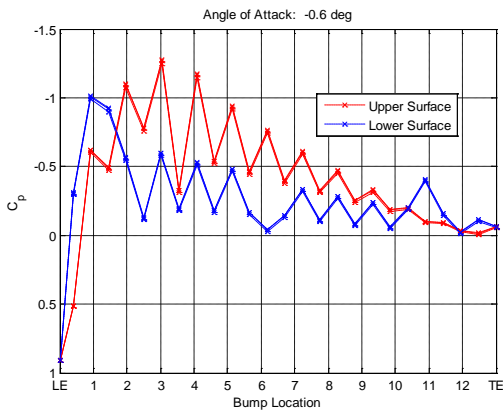


Figure B.313 C_p distribution, $Re = 300k$, $\alpha = -0.6^\circ$

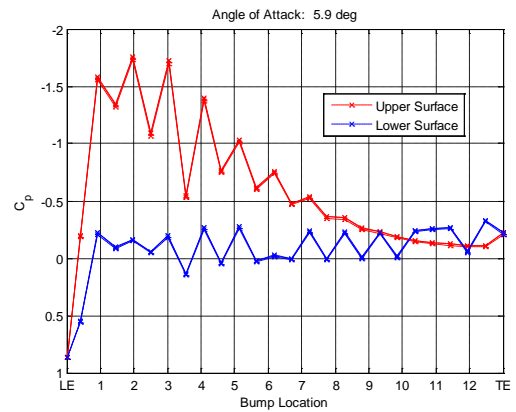


Figure B.316 C_p distribution, $Re = 300k$, $\alpha = 5.9^\circ$

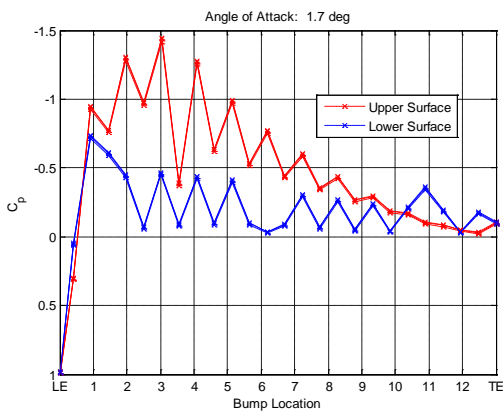


Figure B.314 C_p distribution, $Re = 300k$, $\alpha = 1.7^\circ$

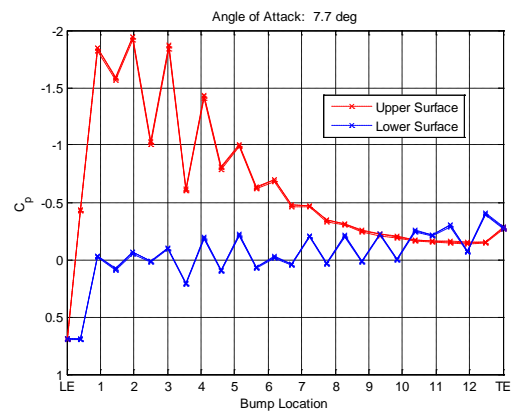


Figure B.317 C_p distribution, $Re = 300k$, $\alpha = 7.7^\circ$

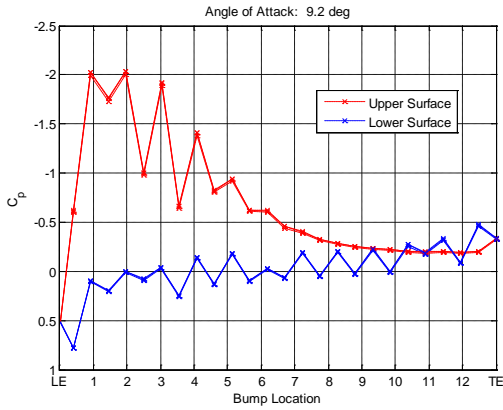


Figure B.318 C_p distribution, $Re = 300k$, $\alpha = 9.2^\circ$

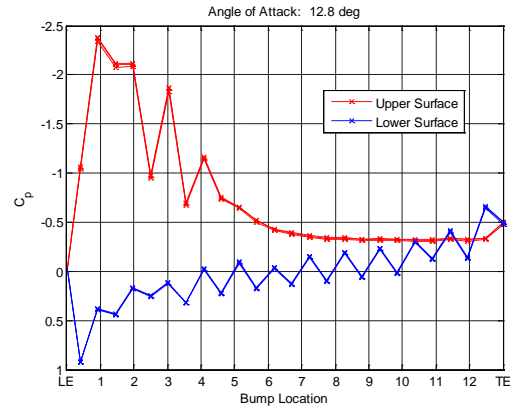


Figure B.321 C_p distribution, $Re = 300k$, $\alpha = 12.8^\circ$

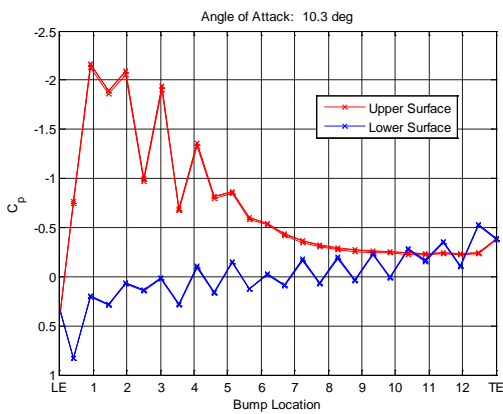


Figure B.319 C_p distribution, $Re = 300k$, $\alpha = 10.3^\circ$

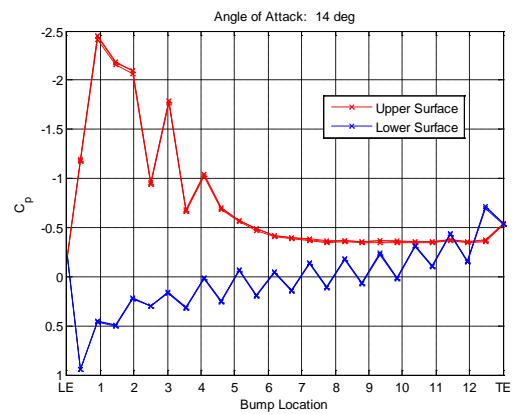


Figure B.322 C_p distribution, $Re = 300k$, $\alpha = 14^\circ$

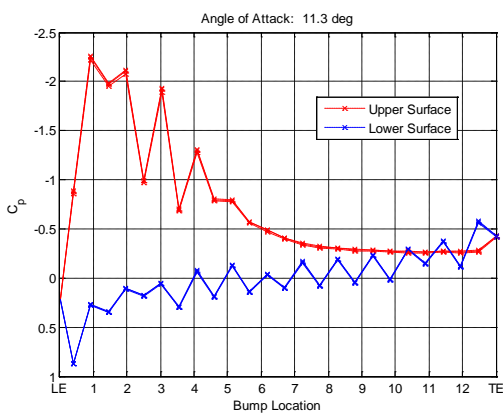


Figure B.320 C_p distribution, $Re = 300k$, $\alpha = 11.3^\circ$

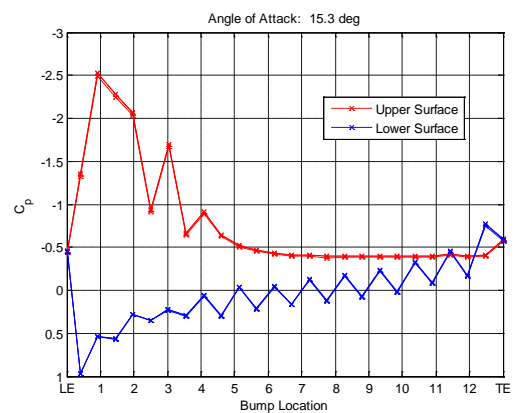


Figure B.323 C_p distribution, $Re = 300k$, $\alpha = 15.3^\circ$

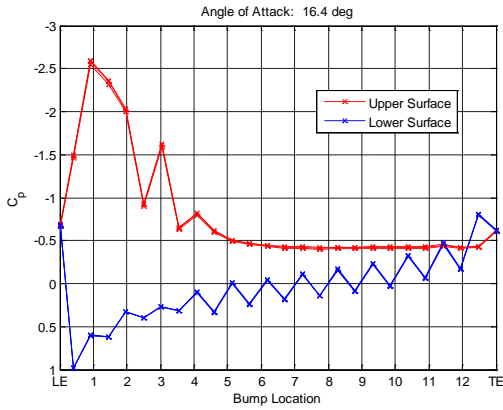


Figure B.324 C_p distribution, $Re = 300k$, $\alpha = 16.4^\circ$

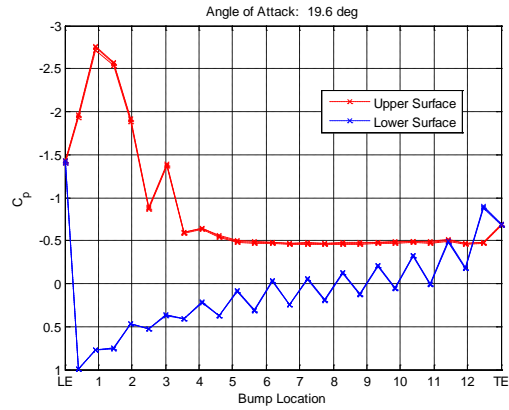


Figure B.327 C_p distribution, $Re = 300k$, $\alpha = 19.6^\circ$

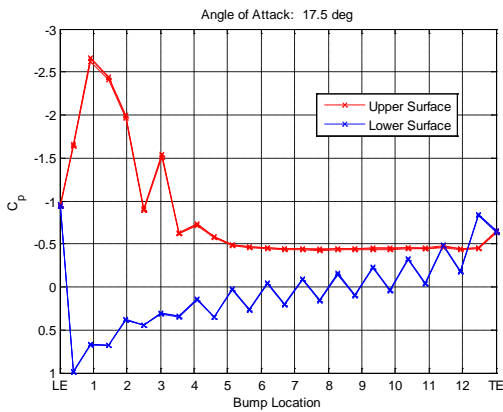


Figure B.325 C_p distribution, $Re = 300k$, $\alpha = 17.5^\circ$

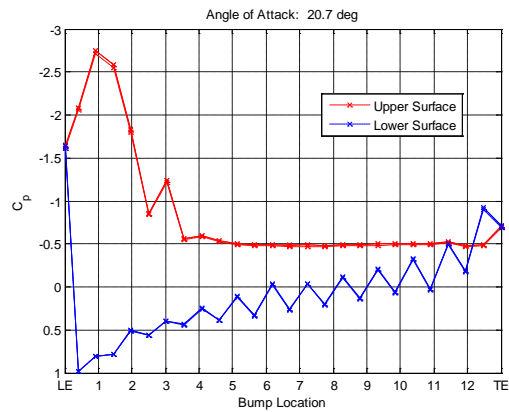


Figure B.328 C_p distribution, $Re = 300k$, $\alpha = 20.7^\circ$

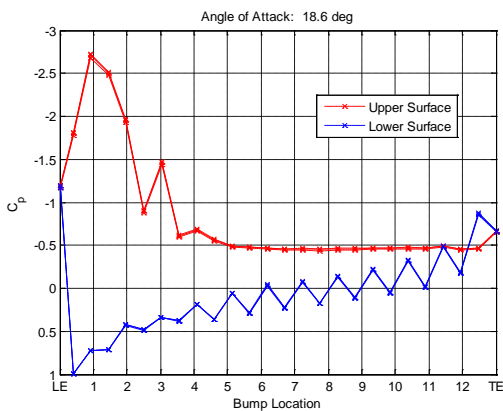


Figure B.326 C_p distribution, $Re = 300k$, $\alpha = 18.6^\circ$

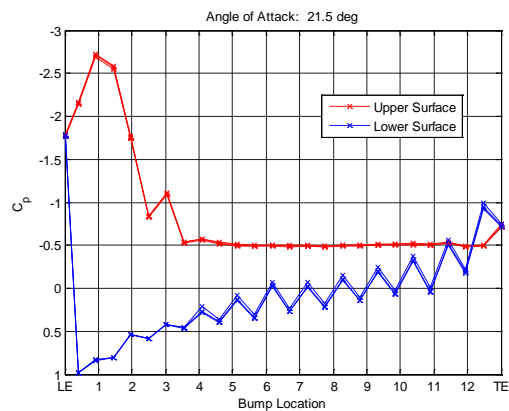


Figure B.329 C_p distribution, $Re = 300k$, $\alpha = 21.5^\circ$

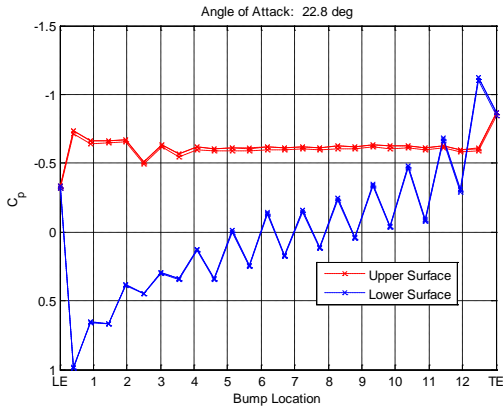


Figure B.330 C_p distribution, $Re = 300k$, $\alpha = 22.8^\circ$

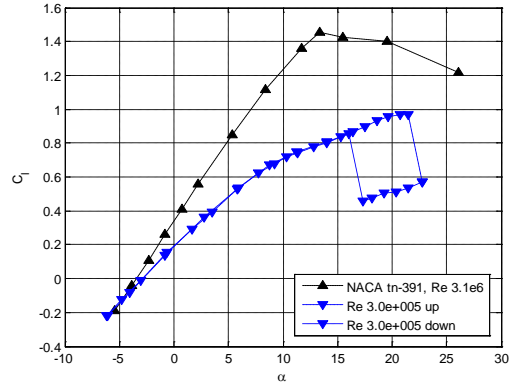


Figure B.333 $Re = 300k$ averaged lift curve with lift hysteresis

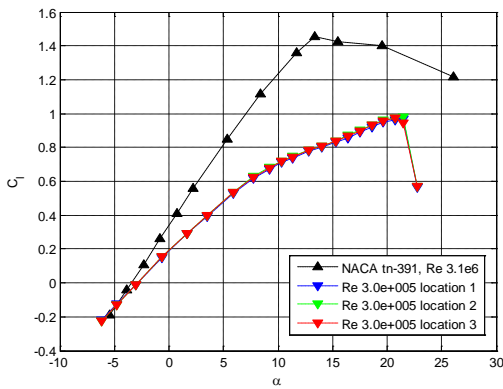


Figure B.331 $Re = 300k$ pre-averaged lift curves from 3 run locations

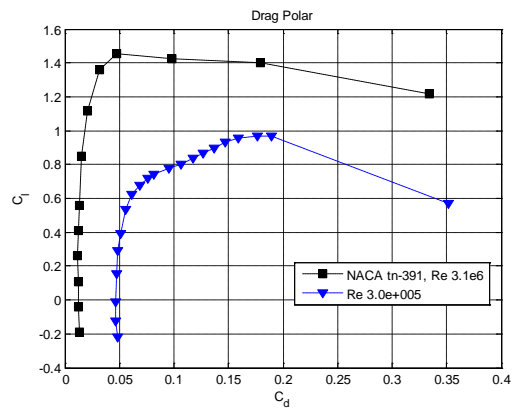


Figure B.334 $Re = 300k$ averaged drag polar

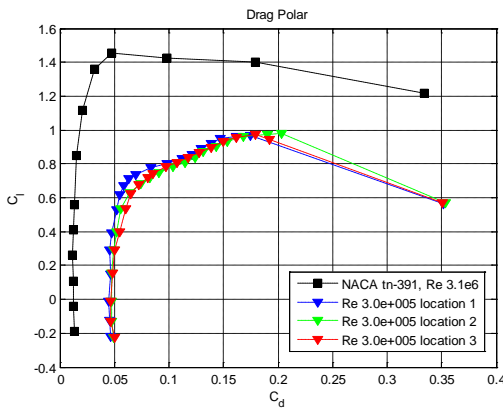


Figure B.332 $Re = 300k$ pre-averaged drag polars from 3 run locations

B.8 Re = 500,000

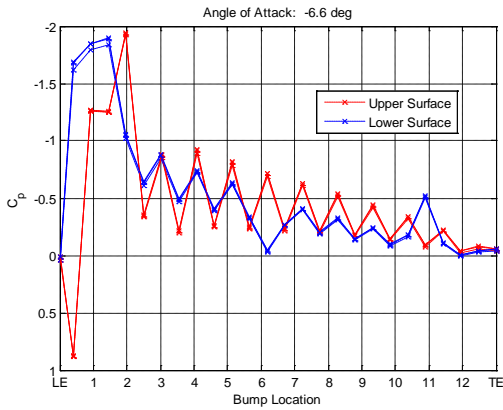


Figure B.335 C_p distribution, $Re = 500k$,
 $\alpha = -6.6^\circ$

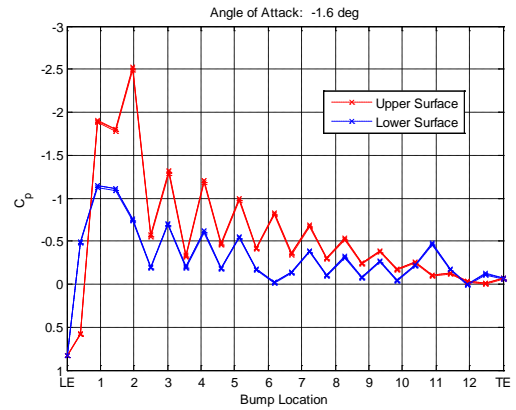


Figure B.338 C_p distribution, $Re = 500k$,
 $\alpha = -1.6^\circ$

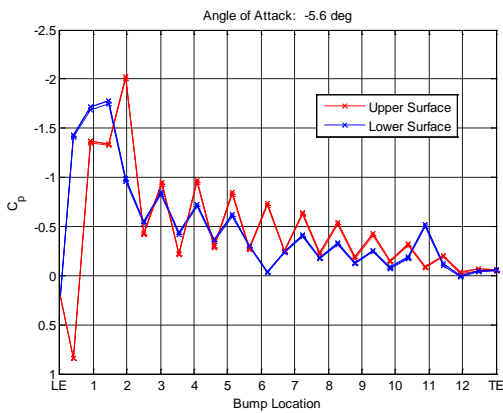


Figure B.336 C_p distribution, $Re = 500k$,
 $\alpha = -5.6^\circ$

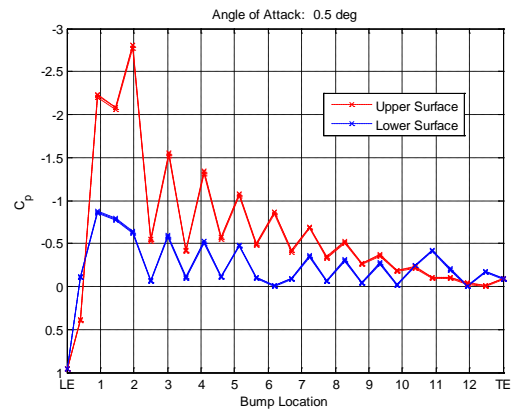


Figure B.339 C_p distribution, $Re = 500k$,
 $\alpha = 0.5^\circ$

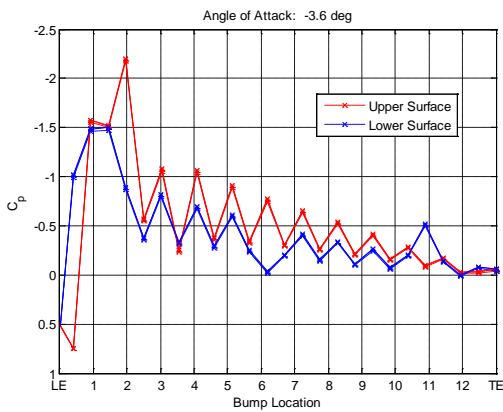


Figure B.337 C_p distribution, $Re = 500k$,
 $\alpha = -3.6^\circ$

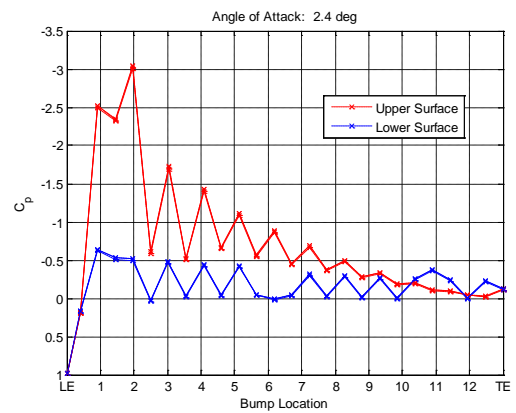


Figure B.340 C_p distribution, $Re = 500k$,
 $\alpha = 2.4^\circ$

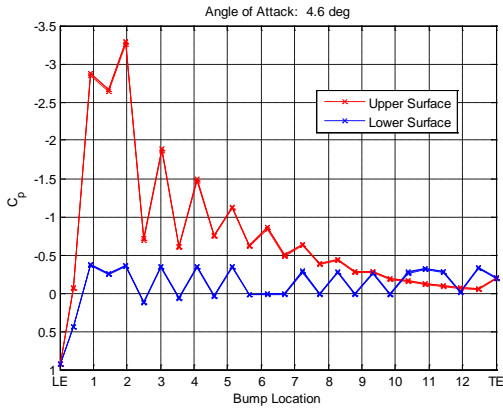


Figure B.341 C_p distribution, $Re = 500k$, $\alpha = 4.6^\circ$

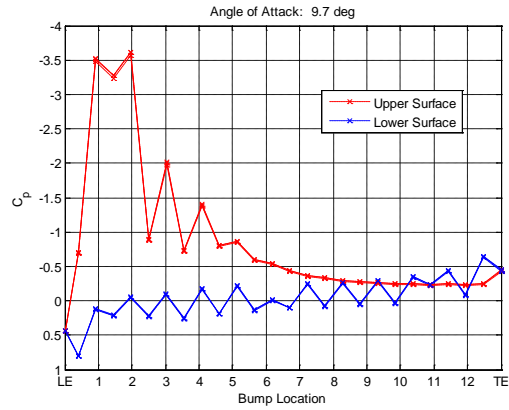


Figure B.344 C_p distribution, $Re = 500k$, $\alpha = 9.7^\circ$

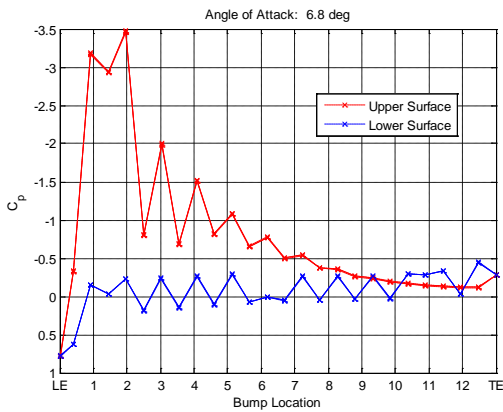


Figure B.342 C_p distribution, $Re = 500k$, $\alpha = 6.8^\circ$

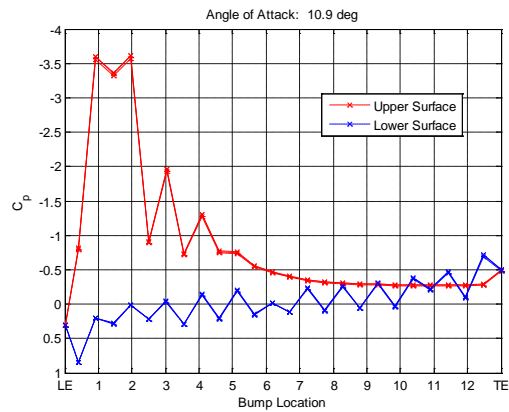


Figure B.345 C_p distribution, $Re = 500k$, $\alpha = 10.9^\circ$

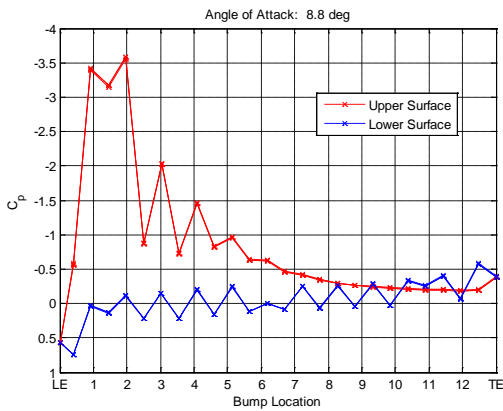


Figure B.343 C_p distribution, $Re = 500k$, $\alpha = 8.8^\circ$

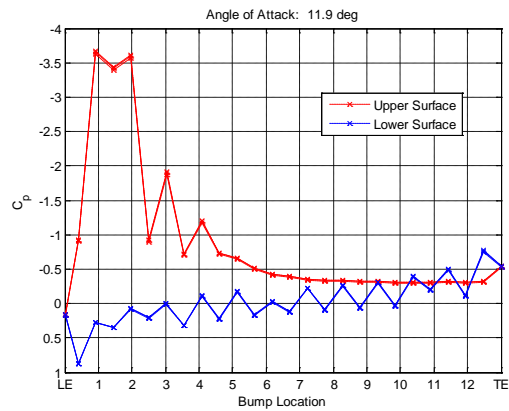


Figure B.346 C_p distribution, $Re = 500k$, $\alpha = 11.9^\circ$

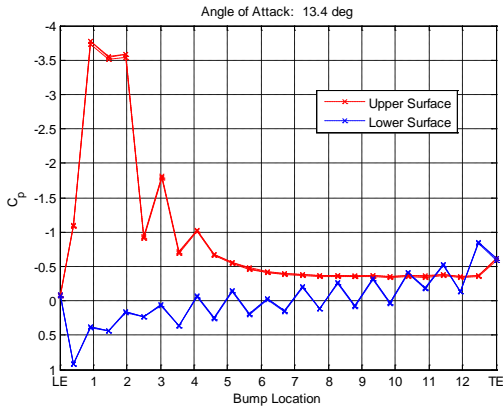


Figure B.347 C_p distribution, $Re = 500k$, $\alpha = 13.4^\circ$

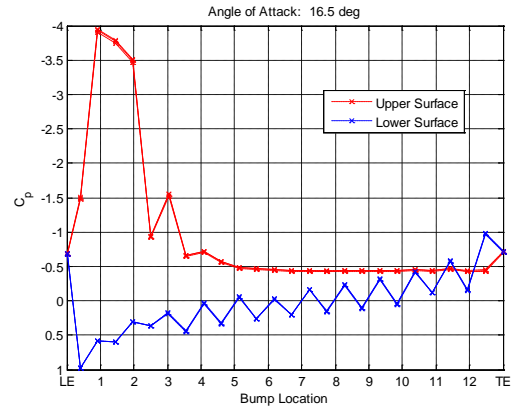


Figure B.350 C_p distribution, $Re = 500k$, $\alpha = 16.5^\circ$

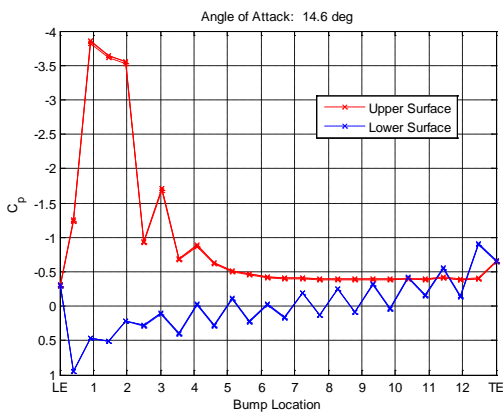


Figure B.348 C_p distribution, $Re = 500k$, $\alpha = 14.6^\circ$

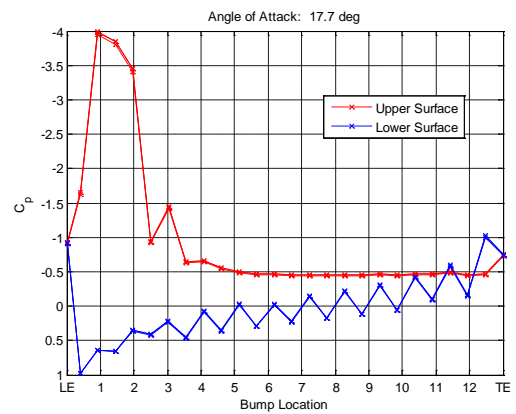


Figure B.351 C_p distribution, $Re = 500k$, $\alpha = 17.7^\circ$

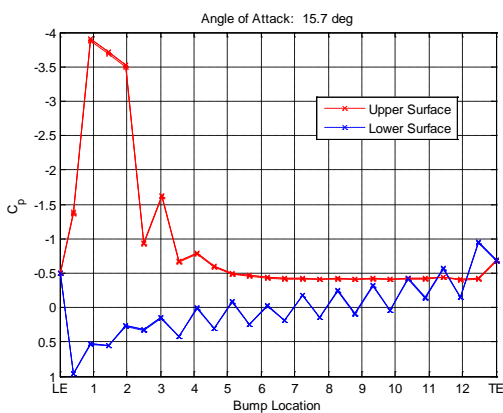


Figure B.349 C_p distribution, $Re = 500k$, $\alpha = 15.7^\circ$

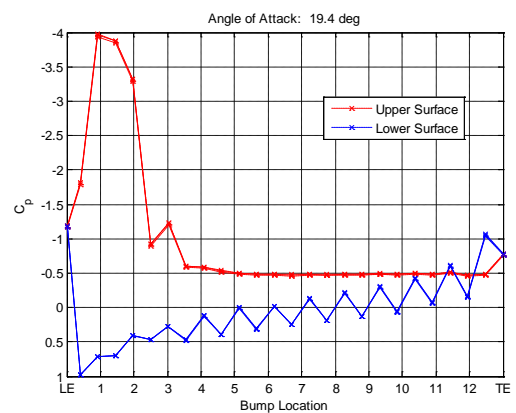


Figure B.352 C_p distribution, $Re = 500k$, $\alpha = 19.4^\circ$

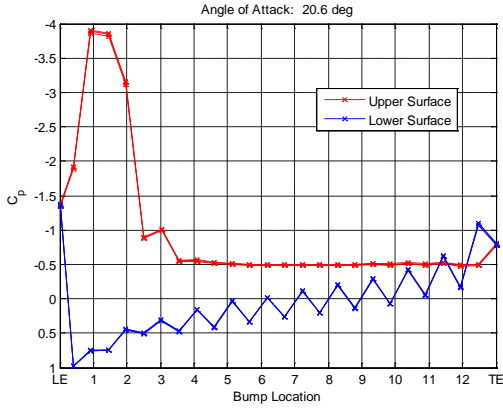


Figure B.353 C_p distribution, $Re = 500k$, $\alpha = 20.6^\circ$

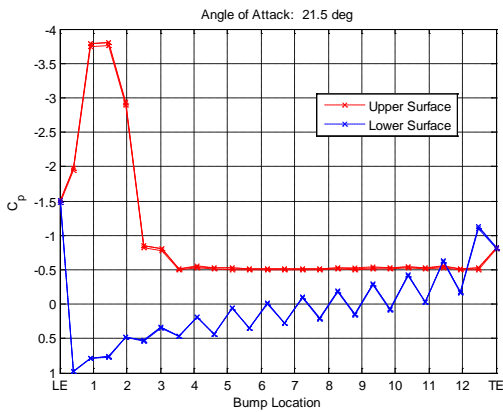


Figure B.354 C_p distribution, $Re = 500k$, $\alpha = 21.5^\circ$

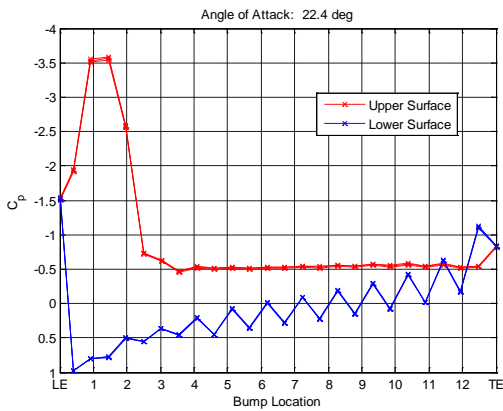


Figure B.355 C_p distribution, $Re = 500k$, $\alpha = 22.4^\circ$

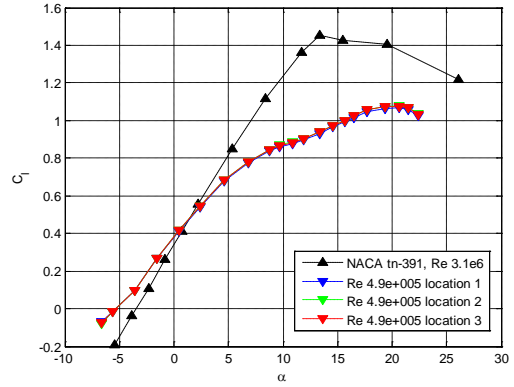


Figure B.356 $Re = 500k$ pre-averaged lift curves from 3 run locations

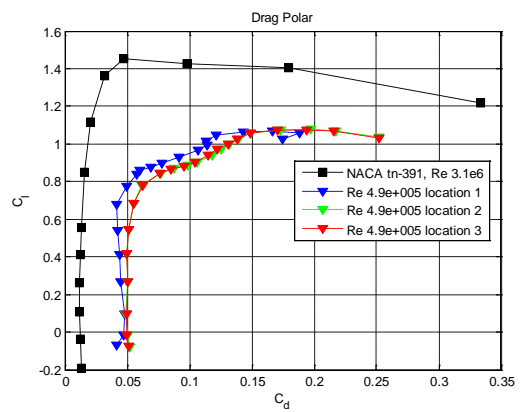


Figure B.357 $Re = 500k$ pre-averaged drag polars from 3 run locations

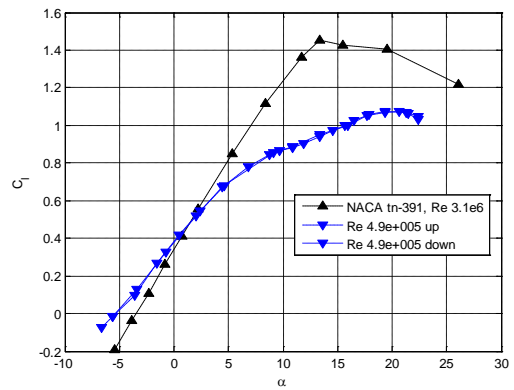


Figure B.358 $Re = 500k$ averaged lift curve with lift hysteresis

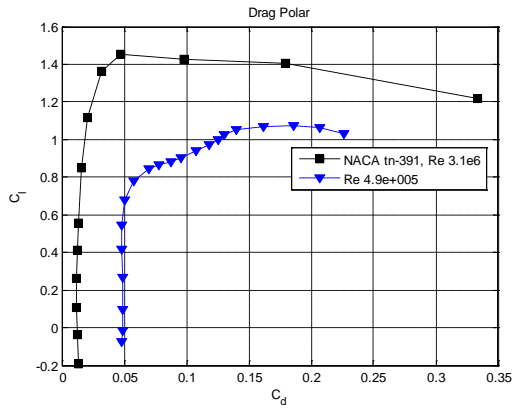


Figure B.359 $Re = 500k$ averaged drag polar

Copyright © Michael Andrew Thamann 2012

Appendix C MATLAB Code

C.1 Smooth Airfoil Integration Code Re < 500k

```
clc
clear all
close all
home = pwd;

c=.2032; % chord length in m
b=1; % unit span
rho = 1.225; % air density
nu = 1.564e-5; % air viscosity

% Read airfoil coordinate data from file
pts=dlmread('n4318.dat');
% Break into upper and lower pressure taps
xu(1:84,1:2)=pts(84:-1:1,1:2); % upper
xl(1:77,1:2)=pts(84:160,1:2); % lower
tap=dlmread('taps.dat');
tu(:,:)=tap(:,1:2);
tl(:,:)=tap(:,1:2:3);
% plot tap info
figure(1)
plot(xl(:,1),xl(:,2), 'k',xu(:,1),xu(:,2), 'k');
hold all;
axis([0 1 -.333 .333])
plot(tu(:,1),tu(:,2), 'rx');
plot(tl(:,1),tl(:,2), 'bx');
% false trailing edge
tu(14,:)= [1,0];
tl(14,:)= [1,0];
%% Initializing figures
open('naca_report_cl.fig'); % figure(2)
hold all
open('naca_report_drag_polar.fig'); % figure(3)
hold all
%% Get file location
path=uigetdir('Select data location');
cd(path)

% Plot pressure coefficients against the airfoil
% airfoil zeros
V_af0=dlmread('zero.txt');
disp(' ')
disp('.....airfoil zero data loaded.....')
disp(' ')
P_af0 = (V_af0-2.5)*1000; % .3 psi trans (output to Pa)
qinf_0 = P_af0(25); % in Pa

%% Analyze all test runs
for j=1:2
    if j==1
        for k=1:3
            % read in aoa for up increments
            aoau=dlmread('aoa_up.txt');
            aiu = sort(aoau);
```

```

for i=1:length(aiu)
figure(i+3)
% Plot the pressure coefficients
V=zeros(23,1);
% Read pressure data files
V(:)=dlmread([num2str(aiu(i)),'_d',num2str(k),'_u',...
'.txt']);
V_m = V(25);
P(:,i) = (V(:)-2.5)*1000-P_af0'; % .3 psi trans in Pa
qinf(i) = (V_m-2.5)*1000-qinf_0; % .3 psi trans in Pa

Cp = P(:,i)./qinf(i);
Cpte = (Cp(13)+Cp(25))/2;

dpu = [Cpte Cp(13) Cp(12) Cp(11) Cp(10) Cp(9) Cp(8)...
Cp(7) Cp(6) Cp(5) Cp(4) Cp(3) Cp(2) Cp(1)];
dpl = [Cp(1) Cp(14) Cp(15) Cp(16) Cp(17) Cp(18)
Cp(19) Cp(20) Cp(21) Cp(22) Cp(23) Cp(24) Cp(25)...
Cpte];
% plot pressure distribution
plot(tu(:,1), fliplr(dpu(1,:)), '--rx', tl(:,1),...
dpl(1,:), '--bx')
hold all
grid on
set(gca, 'YDir', 'reverse', 'XTickLabel', {'LE', '1', '2', ...
'3', '4', '5', '6', '7', '8', '9', '10', '11', '12', ...
'TE'}, 'XTick', [0 0.0769231 0.1538462 0.2307693...
0.3076924 0.3846155 0.4615386 0.5384617...
0.6153848 0.6923079 0.769231 0.8461541 0.9230772...
1]);
title(['Angle of Attack: ', num2str(aiu(i)-.6), ' deg'])
legend('Upper Surface', 'Lower Surface', 'Location', ...
'Best')
xlabel('Tap Location')
ylabel('C_p')

% Determine Cl, and Cd

dimXu=flipdim(tu(:,1),1);
dimYu=flipdim(tu(:,2),1);
dimXl=tl(:,1);
dimYl=tl(:,2);
X = [dimXu;dimXl(2:14)];
Y = [dimYu;dimYl(2:14)];
int = [dpu';dpl(1,2:14)'];

cd(home)
M = [X,Y,int];
Mi = LE_data(M,pts,i);
cd(path)

CL = trapz(Mi(:,1),Mi(:,3)*cosd(aiu(i)-.6))+...
trapz(Mi(:,2),Mi(:,3)*sind(aiu(i)-.6));

```

```

    % wake drag
    cd(home)
    [cdu,q_w,p_d,dz] = Drag1(aiu,i,k,path);
    wake(:,i)=p_d;

    q_wake(i,k) = q_w;
    CDw(i,k) = cdu;
    ai(i,k)=aiu(i)-.6;
    CLs(i,k)=CL;

    % reset taps
    clear tu tl
    tu(:,:)=tap(:,1:2);
    tl(:,:)=tap(:,1:2:3);
    tu(14,:)=[1,0];
    tl(14,:)=[1,0];
end
end
% plot data
uinf = sqrt(2*mean(qinf)/rho);
Re = (c*uinf)/nu;
% lift curve
figure(2);
h = plot(ai(:,1),CLs(:,1),'-bv');
set(h, 'MarkerFaceColor', get(h, 'Color'));
h = plot(ai(:,2),CLs(:,2),'-gv');
set(h, 'MarkerFaceColor', get(h, 'Color'));
h = plot(ai(:,3),CLs(:,3),'-rv');
set(h, 'MarkerFaceColor', get(h, 'Color'));
legend('NACA tn-391, Re 3.1e6', ['Re ', num2str(Re, '%1.1e')], ...
    ' location 1', ['Re ', num2str(Re, '%1.1e')], ...
    ' location 2', ['Re ', num2str(Re, '%1.1e')], ...
    ' location 3', 'location', 'best')
% drag polar
figure(3);
h = plot(CDw(:,1),CLs(:,1),'-bv');
set(h, 'MarkerFaceColor', get(h, 'Color'));
h = plot(CDw(:,2),CLs(:,2),'-gv');
set(h, 'MarkerFaceColor', get(h, 'Color'));
h = plot(CDw(:,3),CLs(:,3),'-rv');
set(h, 'MarkerFaceColor', get(h, 'Color'));
legend('NACA tn-391, Re 3.1e6', ['Re ', num2str(Re, '%1.1e')], ...
    ' location 1', ['Re ', num2str(Re, '%1.1e')], ...
    ' location 2', ['Re ', num2str(Re, '%1.1e')], ...
    ' location 3', 'location', 'best')
% average aerodynamic coefficients
CLsu = mean(CLs,2);
CDwu = mean(CDw,2);
output=[ai(:,1),CLsu,CDwu];
disp('      aoa      Cl      Cd      ');
disp('-----');
disp(output);
% Plot averages
% lift curve
cd(home)
lift_curve = open('naca_report_cl.fig');

```

```

hold all
plot(ai(:,1),CLsu,'-.bv','markerface','b');
% drag polar
open('naca_report_drag_polar.fig');
hold all
plot(CDwu,CLsu,'-.bv','markerface','b');
legend('NACA tn-391, Re 3.1e6',['Re ',num2str(Re,'%1.1e')],...
      'location','best')
else
% lift hysteresis
% read in aoa for up increments
% Plot pressure coefficients against the airfoil
cd(path)
%%%%%%%%%%%%%%%%%%%%%%%%%%%%%%%%%%%%%%%%%%%%%%%%%%%%%%%%%%%%%%%%%%%%%%%%
% airfoil zeros
V_af0=dlmread('zerod.txt');
disp(' ')
disp('.....airfoil zero data loaded.....')
disp(' ')
P_af0 = (V_af0-2.5)*1000; % .3 psi trans (output to Pa)
qinf_0 = P_af0(25); % in Pa
%%%%%%%%%%%%%%%%%%%%%%%%%%%%%%%%%%%%%%%%%%%%%%%%%%%%%%%%%%%%%%%%%%%%%%%%
aoad=dlmread('aoa_down.txt');
aid = sort(aoad);
for i=1:length(aid)
% Plot the pressure coefficients
Vh=zeros(23,1);
% Read pressure data files
Vh(:)=dlmread([num2str(aid(i)),'_d','.txt']);
V_m = Vh(25);
Ph(:,i) = (Vh(:)-2.5)*1000-P_af0'; % .3 psi trans in Pa
qinfh(i) = (V_m-2.5)*1000-qinf_0; % .3 psi trans in Pa

Cp = Ph(:,i)./qinfh(i);
Cpte = (Cp(13)+Cp(25))/2;

dpu = [Cpte Cp(13) Cp(12) Cp(11) Cp(10) Cp(9) Cp(8)...
      Cp(7) Cp(6) Cp(5) Cp(4) Cp(3) Cp(2) Cp(1)];
dpl = [Cp(1) Cp(14) Cp(15) Cp(16) Cp(17) Cp(18) Cp(19)...
      Cp(20) Cp(21) Cp(22) Cp(23) Cp(24) Cp(25) Cpte];

% Determine Cl hysteresis
dimXu=flipdim(tu(:,1),1);
dimYu=flipdim(tu(:,2),1);
dimXl=tl(:,1);
dimYl=tl(:,2);
X = [dimXu;dimXl(2:14)];
Y = [dimYu;dimYl(2:14)];
int = [dpu';dpl(1,2:14)'];

cd(home)
M = [X,Y,int];
Mi = LE_data_h(M,pts);
cd(path)

```



```

        CL = trapz(Mi(:,1),Mi(:,3)*cosd(aid(i)-.6))+...
            trapz(Mi(:,2),Mi(:,3)*sind(aid(i)-.6));
        aih(i)=aid(i)-.6;
        CLh(i)=CL;

        % reset taps
        clear tu tl
        tu(:,:)=tap(:,1:2);
        tl(:,:)=tap(:,1:2:3);
        tu(14,:)=[1,0];
        tl(14,:)=[1,0];
    end
    figure(lift_curve)
    plot(aid-.6,CLh,':bv','markerface','b');
    legend('NACA tn-391, Re 3.1e6',['Re ',num2str(Re,'%1.1e')],...
        ' up'],['Re ',num2str(Re,'%1.1e'),' down'],'location',...
        'best')
end
end
cd(path)
save('final_data')
cd(home)

function [cdu,q_w,p_d,dz] = Drag1(aiu,i,k,path)
cd(path);
c = .2032;
% dy in inches
dz = [0;2.875;4.5625;5.625;6.5;6.6875;6.875;7.0625;7.3125;7.6875;...
    8.1875;8.8125;9.5625;10.5625;11.8125;13.75];
dz = dz*.0254; % dy in m
V_d = dlmread([num2str(aiu(i)),'_d',num2str(k),...
    '_u_Mean-and-Zero.txt'],'',2,0);
V_d = V_d(:,1);
p_conv = [.7689; .7673; .7705; .7711; .7711; .7696; .7676; .7694;...
    .7684; .7706; .7603; .7639; .7614; .7611; .7616; .7619];
% wake pressures in Pa
p_d = p_conv.*V_d*249.08890833;
q_w = (p_d(1)+p_d(16))/2;
wake_int = (2/c)*(sqrt(p_d/q_w)-(p_d/q_w));
cdu = trapz(dz,wake_int);
end

function Mi = LE_data(M,pts,i)

    Mi=M;
    pts(84,1:2)=[0 0];

    tempx1=[Mi(13,1):-0.001:Mi(14,1)];
    tempy1=interp1(pts(1:84,1),pts(1:84,2),tempx1,'cubic');
    tempx2=[Mi(14,1):0.001:Mi(15,1)];
    tempy2=interp1(pts(84:end,1),pts(84:end,2),tempx2,'cubic');

    P=polyfit(Mi(11:14,2),Mi(11:14,3),2);
    tempCP1=polyval(P,tempy1);

```

```

P=polyfit(Mi(14:17,2),Mi(14:17,3),2);
tempCP2=polyval(P,tempy2);

figure(i+3)
plot(tempx1,tempCP1,'r.-',tempx2,tempCP2,'b.-')
set(gca,'YDir','reverse')

Mi=[Mi(1:13,:) ; tempx1(2:end)' tempy1(2:end)' tempCP1(2:end)';...
    Mi(14, :); tempx2(2:end)' tempy2(2:end)' tempCP2(2:end)';...
    Mi(15:end, :)];
end

function Mi = LE_data_h(M,pts)

Mi=M;
pts(84,1:2)=[0 0];

tempx1=[Mi(13,1):-0.001:Mi(14,1)];
tempy1=interp1(pts(1:84,1),pts(1:84,2),tempx1,'cubic');
tempx2=[Mi(14,1):0.001:Mi(15,1)];
tempy2=interp1(pts(84:end,1),pts(84:end,2),tempx2,'cubic');

P=polyfit(Mi(11:14,2),Mi(11:14,3),2);
tempCP1=polyval(P,tempy1);

P=polyfit(Mi(14:17,2),Mi(14:17,3),2);
tempCP2=polyval(P,tempy2);

Mi=[Mi(1:13,:) ; tempx1(2:end)' tempy1(2:end)' tempCP1(2:end)';...
    Mi(14, :); tempx2(2:end)' tempy2(2:end)'
tempCP2(2:end)';Mi(15:end, :)];
end

```

C.2 Smooth Airfoil Integration Code $Re = 500k$

```

clc
clear all
close all
home = pwd;

c=.2032; % chord length in m
b=1; % unit span
rho = 1.225; % air density
nu = 1.564e-5; % air viscosity

% Read airfoil coordinate data from file
pts=dlmread('n4318.dat');
% Break into upper and lower pressure taps
xu(1:84,1:2)=pts(84:-1:1,1:2); % upper
xl(1:77,1:2)=pts(84:160,1:2); % lower
tap=dlmread('taps.dat');
tu(:,:)=tap(:,1:2);
tl(:,:)=tap(:,1:2:3);
% plot tap info

```

```

figure(1)
plot(xl(:,1),xl(:,2), 'k',xu(:,1),xu(:,2), 'k');
hold all;
axis([0 1 -.333 .333])
plot(tu(:,1),tu(:,2), 'rx');
plot(tl(:,1),tl(:,2), 'bx');
% false trailing edge
tu(14,:)= [1,0];
tl(14,:)= [1,0];
%% Initializing figures
open('naca_report_cl.fig'); % figure(2)
hold all
open('naca_report_drag_polar.fig'); % figure(3)
hold all
%% Get file location
path=uigetdir('Select data location');
cd(path)

%% Plot pressure coefficients against the airfoil
% airfoil zeros
V_af0=dlmread('zero.txt');
disp(' ')
disp('.....airfoil zero data loaded.....')
disp(' ')
P_af0 = (V_af0-2.5)*1000; % .3 psi trans (output to Pa)
P_af0(1)= .5*(V_af0(1)-2.5)*6894.75729; % 1 psi trans (output to Pa)
P_af0(2)= .5*(V_af0(2)-2.5)*6894.75729; % 1 psi trans (output to Pa)
P_af0(3)= .5*(V_af0(3)-2.5)*6894.75729; % 1 psi trans (output to Pa)
P_af0(4)= .5*(V_af0(4)-2.5)*6894.75729; % 1 psi trans (output to Pa)
P_af0(5)= .5*(V_af0(5)-2.5)*6894.75729; % 1 psi trans (output to Pa)
qinf_0 = P_af0(25); % in Pa

%% Analyze all test runs
for j=1:2
    if j==1
        for k=1:3
            % read in aoa for up increments
            aoau=dlmread('aoa_up.txt');
            aiu = sort(aoau);
            for i=1:length(aiu)
                figure(i+4)
                % Plot the pressure coefficients
                V=zeros(23,1);
                % Read pressure data files
                V(:)=dlmread([num2str(aiu(i)),'_d',num2str(k),'_u',...
                    '.txt']);
                V_m = V(25);
                P(:,i) = (V(:)-2.5)*1000-P_af0'; % .3 psi trans in Pa
                % 1 psi trans (output to Pa)
                P(1,i)= .5*(V(1)-2.5)*6894.75729-P_af0(1);
                P(2,i)= .5*(V(2)-2.5)*6894.75729-P_af0(2);
                P(3,i)= .5*(V(3)-2.5)*6894.75729-P_af0(3);
                P(4,i)= .5*(V(4)-2.5)*6894.75729-P_af0(4);
                P(5,i)= .5*(V(5)-2.5)*6894.75729-P_af0(5);
                qinf(i) = (V_m-2.5)*1000-qinf_0; % .3 psi trans in Pa
            end
        end
    end
end

```

```

Cp = P(:,i)./qinf(i);
Cpte = (Cp(13)+Cp(25))/2;

dpu = [Cpte Cp(13) Cp(12) Cp(11) Cp(10) Cp(9) Cp(8)...
       Cp(7) Cp(6) Cp(5) Cp(4) Cp(3) Cp(2) Cp(1)];
dpl = [Cp(1) Cp(14) Cp(15) Cp(16) Cp(17) Cp(18)...
       Cp(19) Cp(20) Cp(21) Cp(22) Cp(23) Cp(24) Cp(25)...
       Cptel];
% plot pressure distribution
plot(tu(:,1), fliplr(dpu(1,:)), '--rx', tl(:,1),...
     dpl(1,:), '--bx')
hold all
grid on
set(gca, 'YDir', 'reverse', 'XTickLabel', {'LE', '1', '2', ...
     '3', '4', '5', '6', '7', '8', '9', '10', '11', '12', ...
     'TE'}, 'XTick', [0 0.0769231 0.1538462 0.2307693...
     0.3076924 0.3846155 0.4615386 0.5384617...
     0.6153848 0.6923079 0.769231 0.8461541 0.9230772...
     1]);
title(['Angle of Attack: ', num2str(aiu(i)-.6), ' deg'])
legend('Upper Surface', 'Lower Surface', 'Location', ...
     'Best')
xlabel('Tap Location')
ylabel('C_p')

% Determine Cl, and Cd

dimXu=flipdim(tu(:,1),1);
dimYu=flipdim(tu(:,2),1);
dimXl=tl(:,1);
dimYl=tl(:,2);
X = [dimXu;dimXl(2:14)];
Y = [dimYu;dimYl(2:14)];
int = [dpu;dpl(1,2:14)'];

cd(home)
M = [X,Y,int];
Mi = LE_data(M,pts,i);
cd(path)

CL = trapz(Mi(:,1),Mi(:,3)*cosd(aiu(i)-.6))+...
     trapz(Mi(:,2),Mi(:,3)*sind(aiu(i)-.6));

% wake drag
cd(home)
[cdu,q_w,p_d,dz] = Drag1(aiu,i,k,path);
wake(:,i)=p_d;

q_wake(i,k) = q_w;
CDw(i,k) = cdu;
ai(i,k)=aiu(i)-.6;
CLs(i,k)=CL;

% reset taps
clear tu tl

```

```

        tu(:,:)=tap(:,1:2);
        tl(:,:)=tap(:,1:2:3);
        tu(14,:)=[1,0];
        tl(14,:)=[1,0];
    end
end
% plot data
uinf = sqrt(2*mean(qinf)/rho);
Re = (c*uinf)/nu;
% lift curve
figure(2);
h = plot(ai(:,1),CLs(:,1),'-bv');
set(h, 'MarkerFaceColor', get(h, 'Color'));
h = plot(ai(:,2),CLs(:,2),'-gv');
set(h, 'MarkerFaceColor', get(h, 'Color'));
h = plot(ai(:,3),CLs(:,3),'-rv');
set(h, 'MarkerFaceColor', get(h, 'Color'));
legend('NACA tn-391, Re 3.1e6', ['Re ', num2str(Re, '%1.1e')], ...
    ' location 1', ['Re ', num2str(Re, '%1.1e')], ...
    ' location 2', ['Re ', num2str(Re, '%1.1e')], ...
    ' location 3'], 'location', 'best')
% drag polar
figure(3);
h = plot(CDw(:,1),CLs(:,1),'-bv');
set(h, 'MarkerFaceColor', get(h, 'Color'));
h = plot(CDw(:,2),CLs(:,2),'-gv');
set(h, 'MarkerFaceColor', get(h, 'Color'));
h = plot(CDw(:,3),CLs(:,3),'-rv');
set(h, 'MarkerFaceColor', get(h, 'Color'));
legend('NACA tn-391, Re 3.1e6', ['Re ', num2str(Re, '%1.1e')], ...
    ' location 1', ['Re ', num2str(Re, '%1.1e')], ...
    ' location 2', ['Re ', num2str(Re, '%1.1e')], ...
    ' location 3'], 'location', 'best')
% average aerodynamic coefficients
CLsu = mean(CLs, 2);
CDwu = mean(CDw, 2);
output=[ai(:,1),CLsu,CDwu];
disp('      aoa      Cl      Cd      ');
disp(' -----');
disp(output);
% Plot averages
% lift curve
cd(home)
lift_curve = open('naca_report_cl.fig');
hold all
plot(ai(:,1),CLsu,'-bv','markerface','b');
% drag polar
open('naca_report_drag_polar.fig');
hold all
plot(CDwu,CLsu,'-bv','markerface','b');
legend('NACA tn-391, Re 3.1e6', ['Re ', num2str(Re, '%1.1e')], ...
    'location', 'best')
else
% lift hysteresis
% read in aoa for up increments
% Plot pressure coefficients against the airfoil
cd(path)

```

```

%%%%%%%%%%%%%%%%%%%%%%%%%%%%%%%%%%%%%%%%%%%%%%%%%%%%%%%%%%%%%%%%%%%%%%%%
% airfoil zeros
V_af0=dlmread('zerod.txt');
disp(' ')
disp('.....airfoil zero data loaded.....')
disp(' ')
Ph_af0 = (V_af0-2.5)*1000; % .3 psi trans (output to Pa)
% 1 psi trans (output to Pa)
Ph_af0(2)= .5*(V_af0(2)-2.5)*6894.75729;
Ph_af0(2)= .5*(V_af0(2)-2.5)*6894.75729;
Ph_af0(3)= .5*(V_af0(3)-2.5)*6894.75729;
Ph_af0(4)= .5*(V_af0(4)-2.5)*6894.75729;
Ph_af0(5)= .5*(V_af0(5)-2.5)*6894.75729;
qinfh_0 = Ph_af0(25); % in Pa
%%%%%%%%%%%%%%%%%%%%%%%%%%%%%%%%%%%%%%%%%%%%%%%%%%%%%%%%%%%%%%%%%%%%%%%%
aoad=dlmread('aoa_down.txt');
aid = sort(aoad);
for i=1:length(aid)
% Plot the pressure coefficients
Vh=zeros(23,1);
% Read pressure data files
Vh(:)=dlmread([num2str(aid(i)),'_d','.txt']);
V_m = Vh(25);
Ph(:,i) = (Vh(:)-2.5)*1000-Ph_af0'; % .3 psi trans in Pa
% 1 psi trans (output to Pa)
Ph(1,i)= .5*(Vh(1)-2.5)*6894.75729-Ph_af0(1);
Ph(2,i)= .5*(Vh(2)-2.5)*6894.75729-Ph_af0(2);
Ph(3,i)= .5*(Vh(3)-2.5)*6894.75729-Ph_af0(3);
Ph(4,i)= .5*(Vh(4)-2.5)*6894.75729-Ph_af0(4);
Ph(5,i)= .5*(Vh(5)-2.5)*6894.75729-Ph_af0(5);
qinfh(i) = (V_m-2.5)*1000-qinfh_0; % .3 psi trans in Pa

Cp = Ph(:,i)./qinfh(i);
Cp(25)=Cp(22);
Cp(24)=Cp(21);
Cp(21) = (Cp(20)-Cp(24))*0.75+Cp(24);
Cp(22) = (Cp(21)-Cp(24))*(2/3)+Cp(24);
Cp(23) = (Cp(22)-Cp(24))*0.5+Cp(24);
Cpte = (Cp(13)+Cp(25))/2;

dpu = [Cpte Cp(13) Cp(12) Cp(11) Cp(10) Cp(9) Cp(8)...
Cp(7) Cp(6) Cp(5) Cp(4) Cp(3) Cp(2) Cp(1)];
dpl = [Cp(1) Cp(14) Cp(15) Cp(16) Cp(17) Cp(18) Cp(19)...
Cp(20) Cp(21) Cp(22) Cp(23) Cp(24) Cp(25) Cpte];

% Determine Cl hysteresis

dimXu=flipdim(tu(:,1),1);
dimYu=flipdim(tu(:,2),1);
dimXl=tl(:,1);
dimYl=tl(:,2);
X = [dimXu;dimXl(2:14)];
Y = [dimYu;dimYl(2:14)];
int = [dpu';dpl(1,2:14)'];

cd(home)

```

```

M = [X,Y,int];
Mi = LE_data_h(M,pts);
cd(path)

CL = trapz(Mi(:,1),Mi(:,3)*cosd(aid(i)-.6))+...
      trapz(Mi(:,2),Mi(:,3)*sind(aid(i)-.6));
aih(i)=aid(i)-.6;
CLh(i)=CL;

% reset taps
clear tu t1
tu(:,:)=tap(:,1:2);
t1(:,:)=tap(:,1:2:3);
tu(14,:)=[1,0];
t1(14,:)=[1,0];
end
figure(lift_curve)
plot(aid-.6,CLh,':bv','markerface','b');
legend('NACA tn-391, Re 3.1e6',['Re ',num2str(Re,'%1.1e')],...
      ' up'],['Re ',num2str(Re,'%1.1e'),' down'],'location',...
      'best')
end
end
cd(path)
save('final_data')
cd(home)

function [cdu,q_w,p_d,dz] = Drag1(aiu,i,k,path)
cd(path);
c = .2032;
% dy in inches
dz = [0;2.875;4.5625;5.625;6.5;6.6875;6.875;7.0625;7.3125;7.6875;...
      8.1875;8.8125;9.5625;10.5625;11.8125;13.75];
dz = dz*.0254; % dy in m
V_d = dlmread([num2str(aiu(i)),'_d',num2str(k),...
      '_u_Mean-and-Zero.txt'],'',2,0);
V_d = V_d(:,1);
p_conv = [.7689; .7673; .7705; .7711; .7711; .7696; .7676; .7694;...
      .7684; .7706; .7603; .7639; .7614; .7611; .7616; .7619];
% wake pressures in Pa
p_d = p_conv.*V_d*249.08890833;
q_w = (p_d(1)+p_d(16))/2;
wake_int = (2/c)*(sqrt(p_d/q_w)-(p_d/q_w));
cdu = trapz(dz,wake_int);
end

function Mi = LE_data(M,pts,i)

Mi=M;
pts(84,1:2)=[0 0];

tempx1=[Mi(13,1):-0.001:Mi(14,1)];
tempy1=interp1(pts(1:84,1),pts(1:84,2),tempx1,'cubic');
tempx2=[Mi(14,1):0.001:Mi(15,1)];
tempy2=interp1(pts(84:end,1),pts(84:end,2),tempx2,'cubic');

```

```

P=polyfit(Mi(11:14,2),Mi(11:14,3),2);
tempCP1=polyval(P,tempy1);

P=polyfit(Mi(14:17,2),Mi(14:17,3),2);
tempCP2=polyval(P,tempy2);

figure(i+3)
plot(tempx1,tempCP1,'r.-',tempx2,tempCP2,'b.-')
set(gca,'YDir','reverse')

Mi=[Mi(1:13,:) ; tempx1(2:end)' tempy1(2:end)' tempCP1(2:end)';...
    Mi(14,:); tempx2(2:end)' tempy2(2:end)' tempCP2(2:end)';...
    Mi(15:end,:)];
end

function Mi = LE_data_h(M,pts)

Mi=M;
pts(84,1:2)=[0 0];

tempx1=[Mi(13,1):-0.001:Mi(14,1)];
tempy1=interp1(pts(1:84,1),pts(1:84,2),tempx1,'cubic');
tempx2=[Mi(14,1):0.001:Mi(15,1)];
tempy2=interp1(pts(84:end,1),pts(84:end,2),tempx2,'cubic');

P=polyfit(Mi(11:14,2),Mi(11:14,3),2);
tempCP1=polyval(P,tempy1);

P=polyfit(Mi(14:17,2),Mi(14:17,3),2);
tempCP2=polyval(P,tempy2);

Mi=[Mi(1:13,:) ; tempx1(2:end)' tempy1(2:end)' tempCP1(2:end)';...
    Mi(14,:); tempx2(2:end)' tempy2(2:end)'
tempCP2(2:end)';Mi(15:end,:)];
end

```

C.3 Bumpy Airfoil Integration Code $Re < 500k$

```

clc
clear all
close all
home = pwd;

c=.2032; % chord length in m
b=1; % unit span
rho = 1.225; % air density
nu = 1.564e-5; % air viscosity

% Read airfoil coordinate data from file
pts=dlmread('bumpy-4318.dat');
% Break into upper and lower pressure taps
xu(1:558,1:2)=pts(558:-1:1,1:2); % upper
xl(1:558,1:2)=pts(558:1115,1:2); % lower

```



```

tap=dlmread('bumpy_taps.dat');
tu(:,:)=tap(1:26,:);
tl(:,:)=tap(26:51,:);
% plot tap info
figure(1)
plot(xl(:,1),xl(:,2), 'k',xu(:,1),xu(:,2), 'k');
hold all;
axis equal
plot(tu(:,1),tu(:,2), 'rx');
plot(tl(:,1),tl(:,2), 'bx');

%% Initializing figures
open('naca_report_cl.fig'); % figure(2)
hold all
open('naca_report_drag_polar.fig'); % figure(3)
hold all
%% Get file location
path=uigetdir('Select data location');
cd(path)

%% Plot pressure coefficients against the airfoil
% airfoil zeros
V_af0=dlmread('zero.txt');
disp(' ')
disp('.....airfoil zero data loaded.....')
disp(' ')
P_af0 = (V_af0-2.5)*1000; % .3 psi trans (output to Pa)
qinf_0 = P_af0(50); % in Pa

%% Analyze all test runs
for j=1:2
    if j==1
        for k=1:3
            % read in aoa for up increments
            aoau=dlmread('aoa_up.txt');
            aiu = sort(aoau);
            for i=1:length(aiu)
                figure(i+4)
                % Plot the pressure coefficients
                V=zeros(50,1);
                % Read pressure data files
                V(:)=dlmread([num2str(aiu(i)), '_d', num2str(k), '_u', ...
                    '.txt']);
                V_m = V(50);
                P(:,i) = (V(:)-2.5)*1000-P_af0; % .3 psi trans in Pa
                qinf(i) = (V_m-2.5)*1000-qinf_0; % .3 psi trans in Pa

                Cp = P(:,i)./qinf(i);
                Cpte = (Cp(49)+Cp(25))/2;

                dpu = [Cpte;Cp(25:-1:1)];
                dpl = [Cp(1);Cp(26:49);Cpte];

                % plot pressure distribution
                plot(tu(:,1),dpu(:,1), '--rx',tl(:,1),dpl(:,1), '--bx')
                hold all
            end
        end
    end
end

```

```

grid on
set(gca,'YDir','reverse','XTickLabel',{'LE','1','2',...
    '3','4','5','6','7','8','9','10','11','12',...
    'TE'},'XTick',[0 0.0769231 0.1538462 0.2307693...
    0.3076924 0.3846155 0.4615386 0.5384617...
    0.6153848 0.6923079 0.769231 0.8461541 0.9230772...
    1]);
title(['Angle of Attack: ',num2str(aiu(i)-.6),' deg'])
legend('Upper Surface','Lower Surface','Location',...
    'Best')
xlabel('Bump Location')
ylabel('C_p')

% Determine Cl, and Cd

X = [tu(1:26,1);tl(2:26,1)];
Y = [tu(1:26,2);tl(2:26,2)];
int = [dpu;dpl(2:26)];

M = [X,Y,int];

CL = trapz(M(:,1),M(:,3)*cosd(aiu(i)-.6))+...
    trapz(M(:,2),M(:,3)*sind(aiu(i)-.6));

% wake drag
cd(home)
[cdu,q_w,p_d,dz] = Drag1(aiu,i,k,path);
wake(:,i)=p_d;

q_wake(i,k) = q_w;
CDw(i,k) = cdu;
ai(i,k)=aiu(i)-.6;
CLs(i,k)=CL;

% reset taps
clear tu tl
tu(:,:)=tap(1:26,:);
tl(:,:)=tap(26:51,:);
end
end
% plot data
uinf = sqrt(2*mean(qinf)/rho);
Re = (c*uinf)/nu;
% lift curve
figure(2);
h = plot(ai(:,1),CLs(:,1),'-bv');
set(h,'MarkerFaceColor',get(h,'Color'));
h = plot(ai(:,2),CLs(:,2),'-gv');
set(h,'MarkerFaceColor',get(h,'Color'));
h = plot(ai(:,3),CLs(:,3),'-rv');
set(h,'MarkerFaceColor',get(h,'Color'));
legend('NACA tn-391, Re 3.1e6',['Re ',num2str(Re,'%1.1e'),...
    ' location 1'],['Re ',num2str(Re,'%1.1e'),...
    ' location 2'],['Re ',num2str(Re,'%1.1e'),...
    ' location 3'],'location','best')
% drag polar

```

```

figure(3);
h = plot(CDw(:,1),CLs(:,1),'-.bv');
set(h, 'MarkerFaceColor', get(h, 'Color'));
h = plot(CDw(:,2),CLs(:,2),'-.gv');
set(h, 'MarkerFaceColor', get(h, 'Color'));
h = plot(CDw(:,3),CLs(:,3),'-.rv');
set(h, 'MarkerFaceColor', get(h, 'Color'));
legend('NACA tn-391, Re 3.1e6', ['Re ', num2str(Re, '%1.1e')], ...
      'location 1', ['Re ', num2str(Re, '%1.1e')], ...
      'location 2', ['Re ', num2str(Re, '%1.1e')], ...
      'location 3'], 'location', 'best')
% average aerodynamic coefficients
CLsu = mean(CLs,2);
CDwu = mean(CDw,2);
output=[ai(:,1),CLsu,CDwu,];
disp('      aoa      Cl      Cd      ');
disp('-----');
disp(output);
% Plot averages
% lift curve
cd(home)
lift_curve = open('naca_report_cl.fig');
hold all
plot(ai(:,1),CLsu,'-.bv', 'markerface', 'b');
% drag polar
open('naca_report_drag_polar.fig');
hold all
plot(CDwu,CLsu,'-.bv', 'markerface', 'b');
legend('NACA tn-391, Re 3.1e6', ['Re ', num2str(Re, '%1.1e')], ...
      'location', 'best')
else
% lift hysteresis
% read in aoa for up increments
% Plot pressure coefficients against the airfoil
cd(path)
%%%%%%%%%%%%%%%%%%%%%%%%%%%%%%%%%%%%%%%%%%%%%%%%%%%%%%%%%%%%%%%%%%%%%%%%
% airfoil zeros
V_af0=dlmread('zerod.txt');
disp(' ')
disp('.....airfoil zero data loaded.....')
disp(' ')
P_af0 = (V_af0-2.5)*1000; % .3 psi trans (output to Pa)
qinf_0 = P_af0(50); % in Pa
%%%%%%%%%%%%%%%%%%%%%%%%%%%%%%%%%%%%%%%%%%%%%%%%%%%%%%%%%%%%%%%%%%%%%%%%
aoad=dlmread('aoa_down.txt');
aid = sort(aoad);
for i=1:length(aid)
% Plot the pressure coefficients
Vh=zeros(23,1);
% Read pressure data files
Vh=dlmread([num2str(aid(i)),'_d','.txt']);
V_m = Vh(50);
Ph(:,i) = (Vh-2.5)*1000-P_af0; % .3 psi trans in Pa
qinfh(i) = (V_m-2.5)*1000-qinf_0; % .3 psi trans in Pa

Cp = Ph(:,i)./qinfh(i);
Cpte = (Cp(49)+Cp(25))/2;

```

```

dpu = [Cpte; Cp(25:-1:1)];
dpl = [Cp(1); Cp(26:49); Cpte];

% Determine Cl hysteresis

X = [tu(:,1);tl(2:26,1)];
Y = [tu(:,2);tl(2:26,2)];
int = [dpu;dpl(2:26)];

M = [X,Y,int];

CL = trapz(M(:,1),M(:,3)*cosd(aid(i)-.6))+...
      trapz(M(:,2),M(:,3)*sind(aid(i)-.6));
aih(i)=aid(i)-.6;
CLh(i)=CL;

% reset taps
clear tu tl
tu(:,:)=tap(1:26,:);
tl(:,:)=tap(26:51,:);
end
figure(lift_curve)
plot(aid-.6,CLh, ':bv', 'markerface', 'b');
legend('NACA tn-391, Re 3.1e6', ['Re ', num2str(Re, '%1.1e'), ...
    ' up'], ['Re ', num2str(Re, '%1.1e'), ' down'], 'location', ...
    'best')
end
end
cd(path)
save('final_data')
cd(home)

function [cdu,q_w,p_d,dz] = Drag1(aiu,i,k,path)
cd(path);
c = .2032;
% dy in inches
dz = [0;2.875;4.5625;5.625;6.5;6.6875;6.875;7.0625;7.3125;7.6875;...
      8.1875;8.8125;9.5625;10.5625;11.8125;13.75];
dz = dz*.0254; % dy in m
V_d = dlmread([num2str(aiu(i)), '_d', num2str(k), ...
    '_u_Mean-and-Zero.txt'], '', 2, 0);
V_d = V_d(:,1);
p_conv = [.7689; .7673; .7705; .7711; .7711; .7696; .7676; .7694;...
    .7684; .7706; .7603; .7639; .7614; .7611; .7616; .7619];
% wake pressures in Pa
p_d = p_conv.*V_d*249.08890833;
q_w = (p_d(1)+p_d(16))/2;
wake_int = (2/c)*(sqrt(p_d/q_w)-(p_d/q_w));
cdu = trapz(dz,wake_int);
end

```

C.4 Bumpy Airfoil Integration Code $Re = 500k$

```
clc
clear all
close all
home = pwd;

c=.2032; % chord length in m
b=1; % unit span
rho = 1.225; % air density
nu = 1.564e-5; % air viscosity

% Read airfoil coordinate data from file
pts=dlmread('bumpy-4318.dat');
% Break into upper and lower pressure taps
xu(1:558,1:2)=pts(558:-1:1,1:2); % upper
xl(1:558,1:2)=pts(558:1115,1:2); % lower
tap=dlmread('bumpy_taps.dat');
tu(:,:)=tap(1:26,:);
tl(:,:)=tap(26:51,:);
% plot tap info
figure(1)
plot(xl(:,1),xl(:,2),'k',xu(:,1),xu(:,2),'k');
hold all;
% axis([0 1 -.333 .333])
axis equal
plot(tu(:,1),tu(:,2),'rx');
plot(tl(:,1),tl(:,2),'bx');

%% Initializing figures
open('naca_report_cl.fig'); % figure(2)
hold all
open('naca_report_drag_polar.fig'); % figure(3)
hold all
%% Get file location
path=uigetdir('Select data location');
cd(path)

%% Plot pressure coefficients against the airfoil
% airfoil zeros
V_af0=dlmread('zero.txt');
disp(' ')
disp('.....airfoil zero data loaded.....')
disp(' ')
P_af0 = (V_af0-2.5)*1000; % .3 psi trans (output to Pa)
P_af0(2)= .5*(V_af0(2)-2.5)*6894.75729; % 1 psi trans (output to Pa)
P_af0(3)= .5*(V_af0(3)-2.5)*6894.75729; % 1 psi trans (output to Pa)
P_af0(4)= .5*(V_af0(4)-2.5)*6894.75729; % 1 psi trans (output to Pa)
P_af0(5)= .5*(V_af0(5)-2.5)*6894.75729; % 1 psi trans (output to Pa)
qinf_0 = P_af0(50); % in Pa

%% Analyze all test runs
for j=1:2
    if j==1
        for k=1:3
            % read in aoa for up increments
```

```

aoau=dlmread('aoa_up.txt');
aiu = sort(aoau);
for i=1:length(aiu)
    figure(i+4)
    % Plot the pressure coefficients
    V=zeros(50,1);
    % Read pressure data files
    V(:)=dlmread([num2str(aiu(i)),'_d',num2str(k),'_u',...
        '.txt']);
    V_m = V(50);
    P(:,i) = (V(:)-2.5)*1000-P_af0; % .3 psi trans in Pa
    % 1 psi trans (output to Pa)
    P(2,i)= .5*(V(2)-2.5)*6894.75729-P_af0(2);
    P(3,i)= .5*(V(3)-2.5)*6894.75729-P_af0(3);
    P(4,i)= .5*(V(4)-2.5)*6894.75729-P_af0(4);
    P(5,i)= .5*(V(5)-2.5)*6894.75729-P_af0(5);
    qinf(i) = (V_m-2.5)*1000-qinf_0; % .3 psi trans in Pa

    Cp = P(:,i)./qinf(i);
    Cpte = (Cp(49)+Cp(25))/2;

    dpu = [Cpte;Cp(25:-1:1)];
    dpl = [Cp(1);Cp(26:49);Cpte];

    % plot pressure distribution
    plot(tu(:,1),dpu(:,1),'--rx',tl(:,1), dpl(:,1),'--bx')
    hold all
    grid on
    set(gca, 'YDir', 'reverse', 'XTickLabel', {'LE', '1', '2', ...
        '3', '4', '5', '6', '7', '8', '9', '10', '11', '12', ...
        'TE'}, 'XTick', [0 0.0769231 0.1538462 0.2307693...
        0.3076924 0.3846155 0.4615386 0.5384617...
        0.6153848 0.6923079 0.769231 0.8461541 0.9230772...
        1]);
    title(['Angle of Attack: ',num2str(aiu(i)-.6),' deg'])
    legend('Upper Surface', 'Lower Surface', 'Location',...
        'Best')
    xlabel('Bump Location')
    ylabel('C_p')

    % Determine Cl, and CCCd
    X = [tu(1:26,1);tl(2:26,1)];
    Y = [tu(1:26,2);tl(2:26,2)];
    int = [dpu;dpl(2:26)];

    M = [X,Y,int];

    CL = trapz(M(:,1),M(:,3)*cosd(aiu(i)-.6))+...
        trapz(M(:,2),M(:,3)*sind(aiu(i)-.6));

    % wake drag
    cd(home)
    [cdu,q_w,p_d,dz] = Drag1(aiu,i,k,path);
    wake(:,i)=p_d;

```

```

        q_wake(i,k) = q_w;
        CDw(i,k) = cdu;
        ai(i,k)=aiu(i)-.6;
        CLs(i,k)=CL;

        % reset taps
        clear tu tl
        tu(:,:)=tap(1:26,:);
        tl(:,:)=tap(26:51,:);
    end
end
% plot data
uinf = sqrt(2*mean(qinf)/rho);
Re = (c*uinf)/nu;
% lift curve
figure(2);
h = plot(ai(:,1),CLs(:,1),'-.bv');
set(h, 'MarkerFaceColor', get(h, 'Color'));
h = plot(ai(:,2),CLs(:,2),'-.gv');
set(h, 'MarkerFaceColor', get(h, 'Color'));
h = plot(ai(:,3),CLs(:,3),'-.rv');
set(h, 'MarkerFaceColor', get(h, 'Color'));
legend('NACA tn-391, Re 3.1e6', ['Re ', num2str(Re, '%1.1e')], ...
    ' location 1'], ['Re ', num2str(Re, '%1.1e')], ...
    ' location 2'], ['Re ', num2str(Re, '%1.1e')], ...
    ' location 3'], 'location', 'best')
% drag polar
figure(3);
h = plot(CDw(:,1),CLs(:,1),'-.bv');
set(h, 'MarkerFaceColor', get(h, 'Color'));
h = plot(CDw(:,2),CLs(:,2),'-.gv');
set(h, 'MarkerFaceColor', get(h, 'Color'));
h = plot(CDw(:,3),CLs(:,3),'-.rv');
set(h, 'MarkerFaceColor', get(h, 'Color'));
legend('NACA tn-391, Re 3.1e6', ['Re ', num2str(Re, '%1.1e')], ...
    ' location 1'], ['Re ', num2str(Re, '%1.1e')], ...
    ' location 2'], ['Re ', num2str(Re, '%1.1e')], ...
    ' location 3'], 'location', 'best')
% average aerodynamic coefficients
CLsu = mean(CLs, 2);
CDwu = mean(CDw, 2);
output=[ai(:,1), CLsu, CDwu];
disp('      aoa      Cl      Cd      ');
disp(' -----');
disp(output);
% Plot averages
% lift curve
cd(home)
lift_curve = open('naca_report_cl.fig');
hold all
plot(ai(:,1),CLsu,'-.bv', 'markerface', 'b');
legend('NACA tn-391, Re 3.1e6', ['Re ', num2str(Re, '%1.1e')], ...
    'location', 'best')
% drag polar
open('naca_report_drag_polar.fig');
hold all
plot(CDwu,CLsu,'-.bv', 'markerface', 'b');

```

```

        legend('NACA tn-391, Re 3.1e6', ['Re ', num2str(Re, '%1.1e')], ...
            'location', 'best')
else
    % lift hysteresis
    % read in aoa for up increments
    % Plot pressure coefficients against the airfoil
    cd(path)
    %%%%%%%%%%%%%%%%%%%%%%%%%%%%%%%%%%%%%%%%%%%%%%%%%%%%%%%%%%%%%%%%%%%%%%%%%
    % airfoil zeros
    V_af0=dlmread('zerod.txt');
    disp(' ')
    disp('.....airfoil zero data loaded.....')
    disp(' ')
    Ph_af0 = (V_af0-2.5)*1000; % .3 psi trans (output to Pa)
    Ph_af0(2)= .5*(V_af0(2)-2.5)*6894.75729; % 1 psi trans (in Pa)
    Ph_af0(3)= .5*(V_af0(3)-2.5)*6894.75729; % 1 psi trans (in Pa)
    Ph_af0(4)= .5*(V_af0(4)-2.5)*6894.75729; % 1 psi trans (in Pa)
    Ph_af0(5)= .5*(V_af0(5)-2.5)*6894.75729; % 1 psi trans (in Pa)
    qinfh_0 = Ph_af0(50); % in Pa
    %%%%%%%%%%%%%%%%%%%%%%%%%%%%%%%%%%%%%%%%%%%%%%%%%%%%%%%%%%%%%%%%%%%%%%%%%
    aoad=dlmread('aoa_down.txt');
    aid = sort(aoad);
    for i=1:length(aid)
        % Plot the pressure coefficients
        Vh=zeros(50,1);
        % Read pressure data files
        Vh(:)=dlmread([num2str(aid(i)), '_d', '.txt']);
        V_m = Vh(50);
        Ph(:,i) = (Vh(:)-2.5)*1000-Ph_af0; % .3 psi trans (in Pa)
        % 1 psi trans (output to Pa)
        Ph(2,i)= .5*(Vh(2)-2.5)*6894.75729-Ph_af0(2);
        Ph(3,i)= .5*(Vh(3)-2.5)*6894.75729-Ph_af0(3);
        Ph(4,i)= .5*(Vh(4)-2.5)*6894.75729-Ph_af0(4);
        Ph(5,i)= .5*(Vh(5)-2.5)*6894.75729-Ph_af0(5);
        qinfh(i) = (V_m-2.5)*1000-qinfh_0; % .3 psi trans (in Pa)

        Cp = Ph(:,i)./qinfh(i);
        Cpte = (Cp(49)+Cp(25))/2;

        dpu = [Cpte; Cp(25:-1:1)];
        dpl = [Cp(1); Cp(26:49); Cpte];

        % Determine Cl hysteresis
        X = [tu(:,1);tl(2:26,1)];
        Y = [tu(:,2);tl(2:26,2)];
        int = [dpu;dpl(2:26)];

        M = [X,Y,int];

        CL = trapz(M(:,1),M(:,3)*cosd(aid(i)-.6))+...
            trapz(M(:,2),M(:,3)*sind(aid(i)-.6));
        aih(i)=aid(i)-.6;
        CLh(i)=CL;

        % reset taps
        clear tu tl

```



```

        tu(:,:)=tap(1:26,:);
        tl(:,:)=tap(26:51,:);
    end
    figure(lift_curve)
    plot(aid-.6,CLh,':bv','markerface','b');
    legend('NACA tn-391, Re 3.1e6',['Re ',num2str(Re,'%1.1e'),...
        ' up'],['Re ',num2str(Re,'%1.1e'),' down'],'location',...
        'best')
    end
end
cd(path)
save('final_data')
cd(home)

function [cdu,q_w,p_d,dz] = Drag1(aiu,i,k,path)
cd(path);
c = .2032;
% dy in inches
dz = [0;2.875;4.5625;5.625;6.5;6.6875;6.875;7.0625;7.3125;7.6875;...
    8.1875;8.8125;9.5625;10.5625;11.8125;13.75];
dz = dz*.0254; % dy in m
V_d = dlmread([num2str(aiu(i)),'_d',num2str(k),...
    '_u_Mean-and-Zero.txt'],'',2,0);
V_d = V_d(:,1);
p_conv = [.7689; .7673; .7705; .7711; .7711; .7696; .7676; .7694;...
    .7684; .7706; .7603; .7639; .7614; .7611; .7616; .7619];
% wake pressures in Pa
p_d = p_conv.*V_d*249.08890833;
q_w = (p_d(1)+p_d(16))/2;
wake_int = (2/c)*(sqrt(p_d/q_w)-(p_d/q_w));
cdu = trapz(dz,wake_int);
end

```

Copyright © Michael Andrew Thamann 2012

References

- [1] S. A. Cambone, K. Krieg, P. Pace, and L. Wells, "Unmanned Aircraft Systems Roadmap 2005-2030," Department of Defense 2005.
- [2] J. R. Clapper, J. J. Young, J. E. Cartwright, and J. G. Grimes, "Unmanned Systems Roadmap 2007-2032," Department of Defense 2007.
- [3] J. R. Clapper, J. J. Young, J. E. Cartwright, J. G. Grimes, S. C. Payton, S. J. Stackley, *et al.*, "FY2009-2034 Unmanned Systems Integrated Roadmap," Department of Defense 2009.
- [4] M. E. Dempsey, ""Eyes of the Army" U.S. Army Roadmap for Unmanned Aircraft Systems 2010-2035," U.S. Army Unmanned Aircraft System Center of Excellence 2010.
- [5] J. A. Winnefeld and F. Kendall, "Unmanned Systems Integrated Roadmap FY2011-2036," Department of Defense 2011.
- [6] (2012). *AeroVironment, Inc.* Available: www.avinc.com/
- [7] (2012). *BAE Systems.* Available: www.baesystems.com
- [8] T. J. Harris, "Constrained Volume Packing of Deployable Wings for Unmanned Aircraft," Master's, Mechanical Engineering, University of Kentucky, 2011.
- [9] P. B. S. Lissaman, "Low-Reynolds-Number Airfoils," *Annual Review of Fluid Mechanics*, vol. 15, p. 239, 1983.
- [10] J. H. McMasters and M. L. Henderson, "Low Speed single Element Airfoil Synthesis," *Technical Soaring*, vol. 6, p. 1, 1980.
- [11] R. D. Braun, H. S. Wright, M. A. Croom, J. S. Levine, and D. A. Spencer, "The Mars airplane: a credible science platform," in *Aerospace Conference, 2004. Proceedings. 2004 IEEE*, 2004, p. 408 Vol.1.
- [12] T. McDaniel, "Flying Machine," United States Patent US001905298, 1933.
- [13] B. K. Bain and e. al, "Inflatable Airplane," United States Patent US003106373, 1963.
- [14] B. W. Cooke, "Wind-Tunnel Investigation of the Aerodynamic and Structural Deflection Characteristics of the Goodyear Inflatoplane," National Advisory Committee for Aeronautics, Washington, D.C.1958.
- [15] D. Cadogan, W. Graham, and T. Smith, "Inflatable and Rigidizable Wings for Unmanned Aerial Vehicles," presented at the 44th AIAA/ASME/ASCE/AHS/ASC Structures, Structural Dynamics and Materials Conference, Norfolk, VA, 2003.
- [16] *ILC Dover, Inc.* Available: <http://www.ilcdover.com/>
- [17] A. D. Simpson, "Design and Performance of UAV's with Inflatable Wings," Master's, Mechanical Engineering, University of Kentucky, 2008.
- [18] D. Cadogan, T. Smith, M. Mackusick, and F. Uhelsky, "Morphing Inflatable Wing Development for Compact Package Unmanned Aerial Vehicles," in *45th AIAA/ASME/ASCE/AHS/ASC Structures, Structural Dynamics & Materials Conference*, ed: American Institute of Aeronautics and Astronautics, 2004.
- [19] J. Jacob, S. Smith, and A. Simpson, "Inflatable and Warpable Wings for Meso-Scale UAVs," in *Infotech@Aerospace*, ed: American Institute of Aeronautics and Astronautics, 2005.
- [20] J. D. Jacob, A. Simpson, and S. Smith, "Design and Flight Testing Inflatable Wings with Wing Warping," *SAE Transactions Journal of Aerospace*, 2005.
- [21] J. Lumpp, A. Santhanakrishnan, M. Mackusick, S. Scarborough, D. Cadogan, S. Smith, *et al.*, "Flying on Air: UAV Flight Testing with Inflatable Wing Technology," in *AIAA 3rd "Unmanned Unlimited" Technical Conference, Workshop and Exhibit*, ed: American Institute of Aeronautics and Astronautics, 2004.

- [22] D. Reasor, S. Smith, R. LeBeau, and J. Jacob, "Flight Testing and Simulation of a Mars Aircraft Design Using Inflatable Wings," in *45th AIAA Aerospace Sciences Meeting and Exhibit*, ed: American Institute of Aeronautics and Astronautics, 2007.
- [23] A. Simpson, J. Jacob, and S. Smith, "Flight Control of a UAV with Inflatable Wings with Wing Warping," in *24th AIAA Applied Aerodynamics Conference*, ed: American Institute of Aeronautics and Astronautics, 2006.
- [24] M. Usui, "Aeromechanics of Low Reynolds Number Inflatable/Rigidizable Wings," Master's, Mechanical Engineering, University of Kentucky, 2004.
- [25] M. Drela, "Xfoil: An analysis and design system for low Reynolds number airfoils," in *Low Reynolds Number Aerodynamics*, ed New York: Springer-Verlag, 1989.
- [26] M. Drela and H. Youngren, "XFOIL," ed, 2008.
- [27] A. Santhanakrishnan and J. Jacob, "Effect of Regular Surface Perturbations on Flow Over an Airfoil," in *35th AIAA Fluid Dynamics Conference and Exhibit*, ed: American Institute of Aeronautics and Astronautics, 2005.
- [28] J. R. Sparks, "Experimental Flow Visualization for Corrugated Airfoils at Low Reynolds Number Including Development of a Pitch and Plunge Fixture," Master's, Mechanical Engineering, University of Kentucky, 2011.
- [29] D. A. Reasor, "Numerical Simulation of Two Flow Control Approaches for Low Reynolds Number Applications," Master's, Mechanical Engineering, University of Kentucky, 2007.
- [30] D. A. Reasor and R. P. LeBeau, "Numerical Investigation of the Effects of Bumps on Inflatable Wing Profiles," in *AIAA Region III Student Conference*, ed University of Notre Dame: American Institute of Aeronautics and Astronautics, 2007.
- [31] D. Takahashi and R. LeBeau, "Computational Investigation of Flow over Inflatable Airfoils at Multiple Reynolds Numbers," in *49th AIAA Aerospace Sciences Meeting including the New Horizons Forum and Aerospace Exposition*, ed: American Institute of Aeronautics and Astronautics, 2011.
- [32] R. LeBeau, D. Reasor, T. Gilliam, A. Schloemer, T. Hauser, and T. Johansen, "Numerical Comparison of Flow over Bumpy Inflatable Airfoils," in *47th AIAA Aerospace Sciences Meeting including The New Horizons Forum and Aerospace Exposition*, ed: American Institute of Aeronautics and Astronautics, 2009.
- [33] T. A. Johansen, "Optimization of a Low Reynold's Number 2-D Inflatable Airfoil Section," Master's, Mechanical Engineering, Utah State University, 2011.
- [34] R. Innes, "Computational Fluid Dynamic Study of Flow Over an Inflatable Aerofoil," Loughborough University, UK2006.
- [35] T. M. Seigler, "Dynamics and Control of Morphing Aircraft," Doctoral, Mechanical Engineering, Virginia Polytechnic Institute and State University, 2005.
- [36] D. Neal, M. Good, C. Johnston, H. Robertshaw, W. Mason, and D. Inman, "Design and Wind-Tunnel Analysis of a Fully Adaptive Aircraft Configuration," in *45th AIAA/ASME/ASCE/AHS/ASC Structures, Structural Dynamics & Materials Conference*, ed: American Institute of Aeronautics and Astronautics, 2004.
- [37] T. M. Seigler, D. A. Neal, J.-S. Bae, and Daniel J. Inman, "Modeling and Flight Control of Large-Scale Morphing Aircraft," *Journal of Aircraft*, vol. 44, pp. 1077-1087, 2007/07/01 2007.
- [38] M. I. Friswell and D. J. Inman, "Morphing Concepts for UAVs," presented at the 21st Bristol UAV Systems Conference, 2006.
- [39] W. F. Phillips, "Minimizing Induced Drag with Geometric and Aerodynamic Twist on a Wing of Arbitrary Planform," 2003.

- [40] W. F. Phillips, "Lifting-Line Analysis for Twisted Wings and Washout-Optimized Wings," *Journal of Aircraft*, vol. 41, 2004.
- [41] J. D. Jacob, "On The Fluid Dynamics of Adaptive Airfoils," presented at the ASME International Mechanical Engineering Congress and Exposition, Anaheim, CA, 1998.
- [42] R. Krashanitsa, D. Silin, S. Shkarayev, and G. Abate, "Flight Dynamics of a Flapping-Wing Air Vehicle," *International Journal of Micro Air Vehicles*, vol. 1, pp. 35-49, 03/01/ 2009.
- [43] (2000-2012). Festo. Available: www.festo.com
- [44] Festo, "Smartbird," ed, 2011.
- [45] E. B. Doepke, "Design and Flight of a Wing Warping Wing for Autonomous Flight Control," Master's, Mechanical Engineering, University of Kentucky, 2012.
- [46] F. E. D. Culick and H. R. Jex, "Aerodynamics, Stability, and Control of the 1903 Wright Flyer," in *Proceedings of the Symposium on the 80th Anniversary of the Wright Flyer*, ed: Smithsonian Institution, 1984.
- [47] G. D. Padfield and B. Lawrence, "The Birth of Flight Control: An Engineering Analysis of the Wright Brothers' 1902 Glider," *The Aeronautical Journal*, 2003.
- [48] O. Wright and W. Wright, "Flying Machine," United States Patent US000821393, 1906.
- [49] J. Jacob, A. Santhanakrishnan, N. Pern, and K. Ramakumar, "Enabling Flow Control Technology for Low Speed UAVs," in *Infotech@Aerospace*, ed: American Institute of Aeronautics and Astronautics, 2005.
- [50] M. Abdulrahim, H. Garcia, and R. Lind, "Flight Testing a Micro Air Vehicle Using Morphing for Aeroservoelastic Control," in *45th AIAA/ASME/ASCE/AHS/ASC Structures, Structural Dynamics & Materials Conference*, ed: American Institute of Aeronautics and Astronautics, 2004.
- [51] M. Abdulrahim, H. Garcia, and R. Lind, "Flight Characteristics of Shaping the Membrane Wing of a Micro Air Vehicle," *Journal of Aircraft*, vol. 42, pp. 131-137, 2005/01/01 2005.
- [52] M. Abdulrahim and R. Lind, "Modeling and control of micro air vehicles with biologically-inspired morphing," in *American Control Conference, 2006*, 2006, p. 6 pp.
- [53] K. E. Boothe, "Dynamic Modeling and Flight Control of Morphing Air Vehicles," Master's, Aerospace Engineering, University of Florida, 2004.
- [54] H. Garcia, M. Abdulrahim, and R. Lind, "Roll Control for a Micro Air Vehicle Using Active Wing Morphing," in *AIAA Guidance, Navigation, and Control Conference and Exhibit*, ed: American Institute of Aeronautics and Astronautics, 2003.
- [55] O. Bilgen, K. B. Kochersberger, D. J. Inman, and V. Giurgiutiu, "Macro-fiber composite actuators for a swept wing unmanned aircraft," *Aeronautical Journal*, vol. 113, pp. 385-395, 2009.
- [56] O. Bilgen, K. B. Kochersberger, D. J. Inman, and O. J. Ohanian, "Novel, Bidirectional, Variable-Camber Airfoil via Macro-Fiber Composite Actuators," *Journal of aircraft*, vol. 47, pp. 303-314, 2010.
- [57] B. Etkin, *Dynamics of Atmospheric Flight*. Mineola, NY: Dover Publications, Inc., 2000.
- [58] W. F. Phillips, *Mechanics of Flight*, 2nd ed. Hoboken, NJ: Wiley, 2004.
- [59] B. Stevens and F. Lewis, *Aircraft Control and Simulation*: Wiley-Interscience, 2003.
- [60] "USAF Stability and Control Digital DATCOM," ed: McDonnell Douglas Astronautics Company, 1978.
- [61] "Tornado," ed: Redhammer Consulting Ltd, 2010.
- [62] M. Drela and H. Youngren, "Athena Vortex Lattice," ed, 2006.
- [63] (2012). *Cloud Cap Technology*. Available: www.cloudcaptech.com/
- [64] B. Vaglienti. (2007). *Setup and Tuning of Piccolo Control Laws for 2.0.x*.

- [65] J. B. Barlow, W. H. Rae, and A. Pope, *Low-Speed Wind Tunnel Testing*, 3rd ed. New York, NY: Wiley, 1999.
- [66] S. Tavoularis, *Measurement in Fluid Mechanics*. New York, NY: Cambridge University Press, 2005.
- [67] E. N. Jacobs and R. N. Pinkerton, "Tests of NACA Airfoils in the Variable Density Wind Tunnel, Series 43 and 63," National Advisory Committee for Aeronautics, Washington, D.C. NACA-TN-391, 1931.

Vita

Michael Andrew Thamann

Born December 2nd 1986 in Cincinnati, OH

Raised in Fort Wright, KY

EDUCATION

BS, Cum Laude, Mechanical Engineering, University of Kentucky, Lexington, KY

PROFESSIONAL/RESEARCH EXPERIENCE

Graduate Research Assistant

- University of Kentucky College of Engineering, Lexington, KY: *May 2009 – Present*

Graduate Advisor

- Boundary Layer UAV Experiment Characterizing Atmospheric Turbulence, University of Kentucky College of Engineering, Lexington, KY: *Aug 2011 – Present*
- Kentucky Institute of Aerospace Education, Lexington, KY: *Sep 2010 – Present*
- UK AIAA Design Build Fly, Lexington, KY: *Aug 2009 – May 2010*

Material Testing Engineer

- Rapid Quality Manufacturing, West Chester, OH: *Dec 2009 – Jan 2010*

Technical Co-op

- GE Aviation, Evendale, OH: *May 2009 – Aug 2009*
- GE Aviation, Evendale, OH: *Aug 2008 – Dec 2008*
- GE Aviation, Madisonville, KY: *Jan 2008 – May 2008*
- GE Aviation, Madisonville, KY: *May 2007 – Aug 2007*

AWARDS AND AFFILIATIONS

- Graduate Fellowship
- Association for Unmanned Vehicle Systems International – member since *Aug 2011*
- American Institute of Aeronautics and Astronautics – member since *Oct 2009*
 - Design Build Fly Graduate Advisor
 - Design Build Fly Aerodynamics Team Leader
- Best Presentation in Section Winner 37th DCASS
- Engineer in Training Certificate
- Dean's List – University of Kentucky College of Engineering (*F05, S06, S07, F07, F09*)
- Academic Excellence Scholarship
- Computer Science, Engineering, and Mathematics Scholarship

PRESENTATIONS/PUBLICATIONS

Experimental determination of aerodynamic characteristics of the inflatable NACA 4318 airfoil for deployable UAV systems

- Presented: 37th Dayton-Cincinnati Aerospace Sciences Symposium - 3/6/2012
- Winner: Best Presentation in section

Photometric and Videometric Measurements for Design of Deployable Wings

- Accepted for: 53rd AIAA/ASME/ASCE/AHS/ASC Structures, Structural Dynamics, and Materials Conference – 4/23 – 26/2012
- Not presented due to travel restrictions, resubmitted for 2013

KIAE Design Competition: State Wide Wing Design Competition

- Presented: 34th Annual Kentucky Aviation Conference - 9/10/2010